TECHNISCHE UNIVERSITÄT MÜNCHEN
Helmholtz Zentrum München

Development of a Biophysical Treatment Planning System for the FRM II Neutron Therapy Beamline

Sylvia Garny

Vollständiger Abdruck der von der Fakultät für Physik der Technischen Universität München zur Erlangung des akademischen Grades eines

Doktors der Naturwissenschaften (Dr. rer. nat.)

genehmigten Dissertation.

Vorsitzender:	Univ.-Prof. Dr. J. L. van Hemmen
Prüfer der Dissertation:	
	1. Hon.-Prof. Dr. H. G. Paretzke
	2. Univ.-Prof. Dr. W. Petry

Die Dissertation wurde am 7.8.2008 bei der Technischen Universität München eingereicht und durch die Fakultät für Physik am 19.1.2009 angenommen.

Contents

1 Introduction 1

2 Radiation biophysics of neutrons, photons and their secondaries 5
2.1 Physical and chemical radiation effect 5
2.2 Biological radiation effects 7
2.2.1 Cellular radiation effect 8
2.2.2 Repair 9
2.2.3 Oxygen effect 12
2.2.4 Radiobiological effectiveness 14
2.3 Medical considerations of neutron therapy 16
2.3.1 Tumour classification 17
2.3.2 Volume definitions 18
2.3.3 Early and late radiation effects 21
2.3.4 Dose volume histogram 22
2.4 Radiobiological weighting 23
2.4.1 Review of literature 23
2.4.2 Biological weighting of doses in a voxel phantom 24

3 Description of treatment facility 29
3.1 Beamline characteristics 29
3.2 Treatment specifications 31

4 Neutron and photon transport calculation with GEANT4 including a voxel phantom 37
4.1 GEANT4 37
4.1.1 Fundamentals of the Monte Carlo simulation 38
4.1.2 Geometry 39

4.1.3 Physics 40
4.1.4 Book-keeping of results 43
4.1.5 Primary particles 44
4.1.6 Random number generation 46
4.1.7 Output of results 47
4.1.8 Parallelisation of calculations 48
4.2 Geometry of the voxel phantom 48
4.2.1 HMGU-voxel model 50
4.2.2 Voxel phantom representation within GEANT4 50

5 Validation of GEANT4 radiation transport calculations 53
5.1 Ambient Dose equivalent 53
5.1.1 Geometry of the ambient dose equivalent sphere 54
5.1.2 Calculation of the flux distribution and comparison with MCNP results 54
5.1.3 Calculation of the ambient dose equivalent 55
5.1.4 Conclusions 60
5.2 Calculation of BSS-response functions 61
5.2.1 Geometry implementation 61
5.2.2 Re-binning of cross sections 62
5.2.3 Calculation of the 6” sphere response function 65

6 Measurement of neutron spectra at the FRM II treatment facility by means of Bonner sphere spectrometry 67
6.1 Measurement principle 67
6.2 Deconvolution with MSANDB 69
6.3 Measurements 72
6.3.1 Experimental setup 73
6.3.2 Measured count rates 74
6.4 Calculation of the response matrix 75
6.5 Reconstruction and comparison of neutron-flux spectra 78
6.5.1 Unfolding with MSANDB 78
6.5.2 Comparison with other measurements and calculations 83
6.6 Conclusions 86

7 Calculation of neutron and photon depth dose profiles 87
7.1 Water phantom 87
7.1.1 Geometry of the water phantom 88
7.1.2 Description of the experiment 90
7.1.3 Calculated primary neutron depth dose curves 90
7.1.4 Calculated primary photon depth dose curves 97
7.1.5 Calculated secondary particle spectra in ICRU-tissue 99
7.1.6 Conclusions 99
7.2 Voxel phantom 102
7.2.1 Description of the irradiation geometry 102

7.2.2 The neutron dose distribution pattern 103
7.2.3 Dose volume histogram 105
7.2.4 Neutron dose and biologically weighted dose 108
7.2.5 Conclusions 110

8 Summary and conclusions 115

References 117

A Description of radiobiophysical quantities 129
A.1 Absorbed dose 129
A.2 KERMA 129
A.3 Ambient dose and ambient dose equivalent 130
A.4 Linear energy transfer (LET) 130
A.5 Quality factor 131

B Basic physics of primary and secondary particles in matter 133
B.1 Photons 133
B.2 Neutrons 141
B.3 Electrons and positrons 149
B.4 Protons and heavier ions 157
B.5 Particle tracks and relaxation 159

C Cross sections 163

D Energy rebinning of cross sections 167

E Supplementary remarks to the Bonner sphere measurements 169
E.1 Derivation of the activation 169
E.2 Sum of Bonner sphere response 170
E.3 Measurement vectors 170
E.4 Supplementary figures to the unfolding process 171
E.5 The unfolded FRM II neutron spectrum 175
E.6 The ^{3}He-BSS-response matrix 177

F Supplementary remarks to calculations in the water phantom 179
F.1 Description of experiment 179
F.2 Statistical analysis of depth dose curves 181
F.3 Neutron flux inside waterphantom 183

G Supplementary data for calculations in the voxel phantom 185

Acknowledgments 191

List of Tables

2.1 Dependency of the RBE on survival level and neutron energy 15
2.2 Tumour assessment after the TNM-system 17
2.3 Classification of remission 18
2.4 Stage levels 18

4.1 Special ion processes and models for hadrons in GEANT4 41
4.2 Neutron processes in GEANT4 42

5.1 Specification of tissue equivalent material in GEANT4 54
5.2 Specification of PE in GEANT4 61
5.3 Response of 2 mm gold foil (Comp. MCNP/GEANT4) 65

6.1 Total neutron flux at patient treatment position 84

7.1 Specification of perspex in GEANT4 88

A.1 Quality-factor-LET-relationship 131

B.1 Nuclear photo reactions 140

E.1 The FRM II neutron spectrum 175

G.1 Atomic material composition of voxel phantom 186
G.2 Voxel-Organ-ID to material number 187

List of Figures

2.1 Schematic sketch of direct and indirect effect of radiation on the DNA . 6
2.2 Schematic mammalian cell survival 9
2.3 Survival of Chinese hamster cells in different stages of the cell cycle . . 10
2.4 Recovery factor of Chinese hamster cells for neutrons and photons . . . 11
2.5 Dose rate dependence of surviving fraction 12
2.6 OER for different kinds of radiations 13
2.7 Survival of human cells after different types of irradiation 15
2.8 RBE over LET for three different levels of survival 15
2.9 Measured RBE(LET) of different doses on different cell lines 16
2.10 Schematic view of the treatment volumes and their margins 19
2.11 Direct dose volume histogram 22
2.12 Cumulative dose volume histogram 22
2.13 Tentative RBE-LET dependence 25
2.14 Tentative RBE-energy dependence for protons in water 26

3.1 Plan view of the MEDAPP facility at the FRM II 30
3.2 Top view of the moderator tank 30
3.3 Multileaf collimator of the medical beamline 32
3.4 Patient treatment couch and beam exit window 33
3.5 Results of neutron therapy for two applications 34

4.1 Example of a 2D-view of a simple GEANT4 geometry 39
4.2 Distribution of a primary particle source of a homogeneous, circular beam 45
4.3 HMGU-voxel models 49
4.4 Voxel model in GEANT4 51

5.1 Geometry of ambient dose equivalent calculations 55

5.2 GEANT4-calculated neutron flux in 1 cm depth of the 30cm PE sphere 56
5.3 Photon ambient dose equivalent calculated with GEANT4 57
5.4 Neutron dose equivalent calculated with GEANT4 58
5.5 Qualityfactor-Energy dependence 59
5.6 Neutron ambient dose equivalent calculated with GEANT4 60
5.7 Comparison of cut and diff method to calculate the BSS-response . . . 62
5.8 Gold capture cross section 63
5.9 Neutron flux inside 6” sphere (Comp. MCNP/GEANT4) 64
5.10 Neutron flux and response of 6” sphere (Comp. MCNP/GEANT4) . . 66

6.1 Decay of ^{198}AU 69
6.2 Picture of Bonner spheres 72
6.3 Geometry of Cd-tin and gold foil 73
6.4 Normalised measured count rates 74
6.5 Geometry of 1.3” sphere 76
6.6 Response matrix of BSS with gold foil detector 77
6.7 Start spectra for MSANDB 79
6.8 Unfolded neutron spectra – dependence on start spectra 80
6.9 Unfolded neutron spectra – dependence on number of iterations 81
6.10 Unfolded neutron spectra – dependence on 1.3” sphere and bare foil . . 82
6.11 Beam geometry 83
6.12 Unfolded neutron spectra – comparison with [16] 85

7.1 Geometry of water phantom in GEANT4 89
7.2 Simulated geometry of the treatment room at the FRM II 89
7.3 Water phantom inside treatment room 90
7.4 Measured depth dose curves in water phantom 91
7.5 Normalised calculated depth dose curves of neutrons 92
7.6 Fraction of absorbed dose of secondary particles 92
7.7 Comparison of depth dose curve in voxelised/simple geometry 93
7.8 Comparison of depth dose curve of different spectra 94
7.9 Neutron spectra in different depth of the water phantom 95
7.10 Depth dependency of mean neutron energy and total neutron flux . . . 96
7.11 Lateral dose distribution of the FRM II neutron beam 96
7.12 FRM II photon spectrum 98
7.13 Photon depth dose curves (Comp. measurements/calculations) 99
7.14 Secondary particle spectra in ICRU-tissue 100
7.15 Neutron and photon depth dose curves in water phantom (meas/cal) . 101
7.16 Anatomy of salivary glands 102
7.17 Geometry of the real treatment beam and the simulations 103
7.18 Absorbed and evaluated depth dose curves in voxel phantom 104
7.19 Absorbed lateral dose curves in water phantom 105
7.20 Dose-volume-histograms of the salivary glands 106
7.21 Dose-volume-histogram - influence of RBE 107
7.22 Absorbed dose inside the voxel phantom, phantom slices 109

7.23 Absorbed dose (total + photon) inside the voxel phantom 110
7.24 Absorbed neutron dose inside the voxel phantom; contour plot (x,y) . . 111
7.25 Absorbed neutron dose inside the voxel phantom; contour plot (slice, primary neutrons) 112
7.26 Absorbed dose inside the voxel phantom; contour plot (slices) 113

A.1 LET in water 130
A.2 Quality-factor-LET-Relationship 131

B.1 Photon interaction probabilities and cross sections 134
B.2 Relative interaction probability of photons 135
B.3 Relative angular distribution of photoelectrons 135
B.4 Geometry of the Compton scattering 136
B.5 Distribution of the Compton-photon and -electron angle 138
B.6 Compton photon- and electron-spectrum 138
B.7 Total compton cross section by Klein-Nishina 138
B.8 KERMA of the different charged secondary particles of the neutrons . . 142
B.9 Neutron cross sections in oxygen 143
B.10 Reactor fuel element 144
B.11 Secondary particle spectra of neutrons 148
B.12 Track structures of photons and neutrons 149
B.13 Probability of ionisation/excitation after electron energy loss 150
B.14 Electron cross sections in water vapour 152
B.15 Mass collision and mass radiation stopping power for electrons 152
B.16 Schematic picture and simulation of an electron track 154
B.17 Range of electrons 155
B.18 Calculated track of a 800 keV-electron in water 156
B.19 Stopping power of different particles in water 158
B.20 Range of electrons, protons and alphas in water, muscle, bone and lead 160
B.21 Electron, proton and alpha tracks in water vapour and water 161

C.1 Cross sections for neutrons in hydrogen 163
C.2 Cross sections for neutrons in carbon 164
C.3 Cross sections for neutrons in nitrogen 164
C.4 Cross sections for neutrons in gold 165

E.1 Sum of response functions of all 16 Bonner spheres 170
E.2 Measured gold activations at the patient treatment position 171
E.3 Measured gold activations at the radiography position 171
E.4 Unfolded neutron spectra – dependence on start spectra 172
E.5 Unfolded neutron spectra – dependence on iteration number 173
E.6 Unfolded neutron spectra – dependence on iteration number, log-plot . 174
E.7 ^{3}He-BSS-response matrix 177

F.1 Statistical analysis of depth dose curves 182
F.2 Neutron spectra in different depth of the water phantom 183

F.3 Neutron spectra in different depth of the water phantom, linear plot . . 183

CHAPTER

1

Introduction

Shortly after the discovery of the neutron in 1932 by J. Chadwick, R. Stone started with its clinical and therapeutical application: between 1936 and 1943 he irradiated over 250 patients [25]. The first euphoria soon vanished when unexpected and severe late effects appeared. Therefore, neutron therapy was not resumed after the Second World War. In 1959, fundamental research was performed at Hammersmith Hospital, London, on the radiobiological effects of neutrons on tissue [25]. It was discovered that Stone unintentionally overdosed many of his patients because of the much smaller or even missing fractionation effect of neutrons as compared to photons, which was not known to him at the time. In 1966, neutron therapy was restarted again and first successes could soon be reported [25]. Afterwards, many tumour centres used nuclear reactors or accelerators to irradiate patients with neutrons. In parallel to technical developements of the irradiation facilities, dose planning and dose application was improved. Further radiobiological studies resulted in recommendations of tumour treatment cases where neutrons have an advantage over standard photon therapy [25].

In Munich, neutrons have been used for radiation therapy since 1985 and about 1000 patients with different types of tumours were treated at the first research reactor in Garching until its closure on July the 28th, 2000 [127]. Since April 2005 it is possible to perform radiation treatment again and several patients have already been irradiated at the new Research Neutron Source Hans-Maier Leibnitz (FRM II). This new reactor was designed to have a greater neutron flux, primarily at low neutron energies. These low energy neutrons are converted with two uranium plates to high energy neutrons for the medical application at beamline 10 (full description in chapter 3.1). Filters are used to change the characteristics of the neutron spectrum and the neutron-to-photon ratio, to make them similar to the characteristics of the beam of the first reactor. Therefore, medical knowledge acquired with the first reactor can be applied for the treatment at the FRM II. The main differences between the earlier and the current facility are the increase in total neutron flux, which is 4.5 times as high, and the enlargement of the field size, which is six times as large [65]. Therefore, treatment time decreases, improving treatment conditions and quality.

In principle, neutron depth dose curves resemble those of photons, displaying an exponential decrease with depth, the slope depending on the energy of the neutrons. The deeper the treatment areal is located, the higher the neutron energy has to be, to provide an optimal treatment. Therefore, application of neutrons at the FRM II is restricted to superficial tumours, while those located deeper in the human body should be treated with accelerator-produced neutrons (see appendix B.2.1). Neutrons were found to have an advantage in treatment for several kinds of superficial tumours, depending on their biological characteristics. The different biological effects of radiation on tissue are presented and discussed in chapter 2. Particularly salivary gland tumours respond well to neutron radiation while the chances for tumour control after surgery or photon irradiation are usually low (see chapter 3.2).

Currently, measured depth dose curves in water together with the experience from former treatments are being used as a basis for the treatment planning at the FRM II. In order to improve treatment quality, this planning system had to be further developed. With the present work, the essential basis for a computer-based treatment planning is provided. The main aim was to implement a treatment planning program based on a well known Monte Carlo system which is not only able to calculate the physical energy dose deposited by the FRM II neutron and photon beam but also to provide the means for biological dose weighting for the different end points of concern: tumor cell inactivation, complications and late effect risks.

For the present work, GEANT4 was chosen as the Monte Carlo program to be used. Because no benchmark excercises existed at the beginning of this work for transport of neutrons down to meV, major efforts were made to test GEANT4 before it could be used for this treatment planning system (see chapter 5). This was done for two cases. First, the ambient dose equivalent was calculated with GEANT4 and compared in detail with other published data (section 5.1). Secondly, response-functions were calculated for Bonner spheres and were compared to calculations performed with another well known transport code, MCNP (Mares, priv. com.)(section 5.2). In order to provide a sound experimental basis for the dose calculations, the neutron spectrum at the place of patient treatment at the FRM II was then measured with a Bonner sphere system using gold foils as thermal neutron detectors (see chapter 6). For this purpose, the required response functions for all detectors of the spectrometer were calculated with GEANT4 (chapter 6.4). This response matrix was then used to unfold the neutron spectrum at the patient treatment position. The resulting neutron spectrum as well as the total neutron flux was compared to a spectrum that had been obtained earlier with MCNP and measured with threshold probes [16] and the total flux measured in a water bath [16]. The neutron spectrum obtained with the Bonner sphere measurement was then used for the GEANT4 dose calculations in a water phantom together with a precalculated photon spectrum [16](chapter 7). The resulting simulated depth dose curves in the water phantom were compared to measurements performed by [65], and reasonable agreement was found. This was also the case when the water phantom was voxelised, demonstrating that a voxel phantom can principally be implemented in the GEANT4 code. The human voxel phantom “Regina” from Zankl et al [107] was finally implemented in GEANT4 as a test case for the treatment planning for a real patient (section 4.2). Depth dose distributions in the voxel phantom for the neutron and photon spectrum of the FRM II were calculated (section 7.2.2). Furthermore, to demonstrate its principle applicability in the system, biological effect assessment was included for three different types of radiation sensitivity or endpoints given here with hypothetical weighting functions (section 7.2.4). In summary, this thesis describes the development and successful testing of the first neutron therapy treatment program with biophysical effect weigthing functions in a voxelised phantom.

CHAPTER

2

Radiation biophysics of neutrons, photons and their secondary particles

To understand radiation effects on a human being, not only the pure physical interactions of different particles with target atoms (described in appendix B) have to be considered, but also the way the energy is deposited in the tissue and its biological consequences. Depending on the particle's type, energy and other properties as well as on properties of the tissue, a tissue reacts differently to the irradiation. In this chapter, several known properties of biological radiation effects as well as some of the medical background are explained.

2.1 Physical and chemical radiation effect

The purely physical energy deposition to a target takes less than a picosecond and is followed by a prechemical and chemical phase, which takes from pico- to a microsecond, respectively [67]. For these following stages, it is important to consider where the interaction did exactly take place. One possibility is that a molecule which is important for the cell's function is hit directly. The deoxyribonucleic acid (DNA) is the most prominent example here. Another possibility is that a different, typically smaller molecule (e.g. water, which makes up 70-80% of the weight of a cell) is affected. Such a molecule or its fragments can, if they are mobile enough, interact indirectly with other molecules afterwards. Therefore, both direct and indirect radiation actions have to be considered (see figure 2.1). Which of the two possible types dominates depends on the type of radiation inducing the effect. For thin-ionising gamma, electron and positron radiation, the indirect effect on DNA dominates, whereas densely ionising particles like

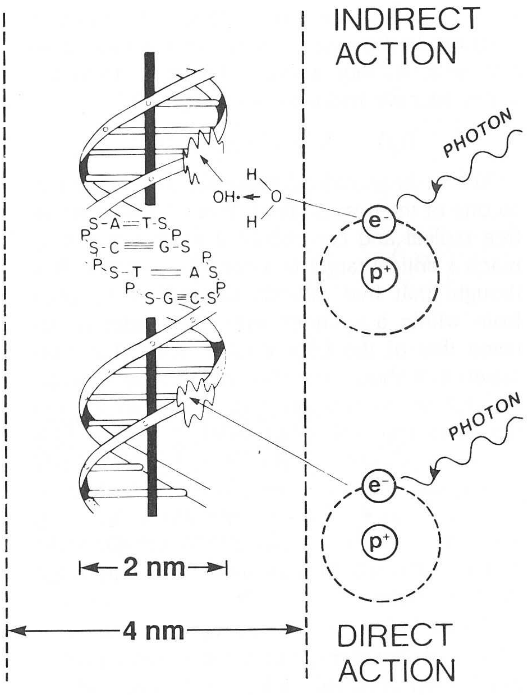

Figure 2.1: *Schematic sketch of direct and indirect effect of radiation on the DNA:*
S=sugar
P=phosphate group
A=adenine
T=thymine
C=cytosine
G=guanine
Direct action takes place at the DNA directly whereas indirect action affects small substrates (e.g. water), which can indirectly damage the DNA via chemical interaction [40]

neutrons and hadrons tend to cause more direct effects on DNA [40].
The most important molecule for the indirect action pathway is the H_2O molecule, mainly because it is most abundant, but also because its fragments are very small and fast in diffusion (diffusion constant $D \approx 5 \cdot 10^{-5} \frac{\mathrm{cm}^2}{\mathrm{s}}$ [40], which means they can go about $1\,\mathrm{\AA}$ in a picosecond). The molecule is primarily excited or ionised and H_2O^*, H_2O^+ and free electrons are produced. Their reaction leads then to the formation of H_3O^+, OH, e^-_{aq}, H, H_2 in the prechemical phase (see [121] and [81]):

$$
\begin{aligned}
\mathrm{H_2O^+ + H_2O} &\rightarrow \mathrm{H_3O^+ + OH} \\
\mathrm{H_2O^*} &\rightarrow \begin{cases} \mathrm{H_2O^+ + e^-} & \textit{ionisation} \\ \mathrm{H + OH} & \textit{molecular dissociation} \end{cases}
\end{aligned}
$$

The thermalised charged electron polarises the surrounding H_2O molecules (dipoles) and gets hydrated (denoted by e^-_{aq}). After some picoseconds, diffusion starts to play a role. The free radicals e^-_{aq}, OH and H can reach the DNA (or be scavenged in the matrix) and cause an indirect damage there. On the other hand, they react with each other to produce other free radicals or cellular toxins like H_2O_2 (from [121]):

$$\begin{aligned}
\mathrm{OH} + \mathrm{OH} &\rightarrow \mathrm{H_2O_2} \\
\mathrm{OH} + \mathrm{e}^-_{\mathrm{aq}} &\rightarrow \mathrm{OH}^- \\
\mathrm{OH} + \mathrm{H} &\rightarrow \mathrm{H_2O} \\
\mathrm{H_3O}^+ + \mathrm{e}^-_{\mathrm{aq}} &\rightarrow \mathrm{H} + \mathrm{H_2O} \\
2\mathrm{e}^-_{\mathrm{aq}} + 2\mathrm{H_2O} &\rightarrow \mathrm{H_2} + 2\mathrm{OH}^- \\
\mathrm{e}^-_{\mathrm{aq}} + \mathrm{H} + \mathrm{H_2O} &\rightarrow \mathrm{H_2} + \mathrm{OH}^- \\
\mathrm{H} + \mathrm{H} &\rightarrow \mathrm{H_2}
\end{aligned}$$

These processes occur until all radicals are bound in nonreactive molecules. The long term damage strongly depends on the type of molecules that are affected from the reactions and the spatial-temporal patterns of these damages. Important early direct and indirect damages to the DNA are single or double strand breaks or the loss of a base pair.

2.2 Biological radiation effects

Biological radiation effects develop a couple of microseconds after the radiation interaction. Some important effects are: single, double or complex strand breaks of the DNA, damage or loss of a base, denaturation, intra- or inter-molecular crosslinks, DNA-protein crosslinks as well as changes of proteins. Mid- and long-term effects are the disturbance of the cell cycle after some minutes to allow for repair. If many cells of an organ are affected the function of that organ can be changed (e.g. intestinal tract, nervous system) so that after some days and/or after some weeks severe malfunction of the organ (e.g. lung fibrosis) can occur. After many years there is still the possibility of the development of late effects like cancer or cataracts. Changes in the genetic material which affect the genes of progenies can manifest themselves even generations after the irradiation took place. On the whole, two possible ways are open to a cell which is damaged severely: cell death (a cell which cannot reproduce more than fifty progeny cells is called dead) or survival with mutations of the genome, which can cause future failure of the proper organ's function [40].

Medical effects of radiation on humans (and animals) can be categorised into two groups: deterministic and stochastic effects. A **deterministic** effect appears only at doses larger than a certain threshold and the severeness is dose dependent. An example is the reddening of the skin after radiation exposure as well as the acute radiation syndrome. A **stochastic** effect has completely different characteristics. The dose affects the probability of the damage, but there is no threshold. The severity is not dose-dependent, which is the most important difference to the deterministic damage. The most prominent example of a stochastic effect is the induction of a later tumour or of genetic defects. Furthermore, the latter displays a much longer latency period between exposition and incidence of the disease.

The cells of a human body are exposed to many kinds of cellular toxins every day, but only seldom such severe damages are possible after irradiation. Most times, the cell is able to repair the damage – for example a DNA strand break – with the help of the other strand. Single strand breaks are easily repaired in this way, but if both DNA-strands are affected over more than a few base pairs (a double strand break can be defined as two single strand breaks within less than, say 10 base pairs of the DNA), the repair can be much more complicated and not always possible. The cell can then go into apoptosis (= programmed cell death) and be replaced by a neighbouring cell. This is one way to ensure the function of the whole organ. In what way the neighbouring cells take part in this process is still under research [40, 121].

The impact of radiation on cells is both its power and its weakness. With the effects described above, the goal of hitting almost all tumour cells and destroying them is often achievable. On the other hand, there will always be healthy tissue surrounding the tumour, which cannot be spared. DNA-mutations can also be caused by radiation there. In most cases, changes in the genotype are of minor consequences to the organ and the human. But in the course of time, such damages could be accumulated. Hits can activate oncogenes, which could promote tumour formation and growth. This can also be caused by other factors like viruses, smoking or UV-radiation. Another undesirable influence of radiation could be to enhance the development of tumour cells by deactivating the corresponding suppressor genes. This could lead to proliferation, which is one of the outstanding attributes of a tumour, to divide without any control, and much faster than normal tissue cells [40].

Within certain models, one tries to quantify all of these important effects of radiation [40]. The main problems are the quantitative description of the huge number of interlinked repair and recovery pathways, which the cells and organs follow to protect themselves from these environmental impacts.

2.2.1 Cellular radiation effect

Biological effects of radiation on cells have been studied in very many cell-culture in-vitro experiments (among others: [11, 12, 13]). The so called plating efficiency PE (60-80% for some cells, usually even smaller) is needed as a correction factor when describing the survival in a cell experiment. It is defined by [40]:

$$\mathrm{PE} = \frac{\text{Number of growing cells}}{\text{Number of planted cells}}$$

$$\text{survival} = \frac{\text{Number of dividing cells after irradiation with} \geq 50 \text{ progeny}}{\text{Number of planted cells} \cdot \mathrm{PE}}$$

The survival is usually plotted as a function of the dose. In several models, it is attempted to describe these experimental data and interprete them mechanistically. Figure 2.2 schematically displays some of the parameters of the two most important models used in radiation therapy. On the right side (B), the **multitarget-model** is shown. The reciprocal of the slope at low doses D_1 (= dose at which the survival has dropped to 1/e) describes mainly the effect of a single event whereas the reciprocal of the final decline D_0 describes that of multiple events. The wide shoulder of the

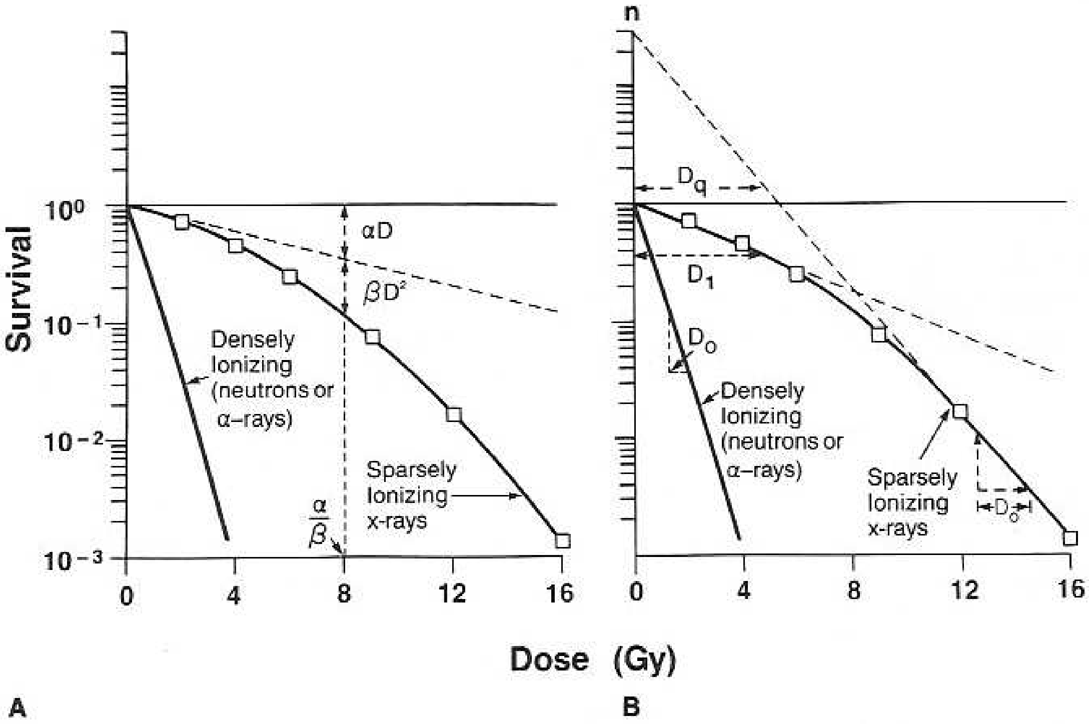

Figure 2.2: *Mammalian cell survival with the parameters of two different explanation models (discussion see text) [40]*

survival curves for thin-ionising radiation is reflected in a "quasi-threshold" dose D_q or an extrapolation number n (from [40]):

$$n = \exp\left(\frac{D_q}{D_0}\right)$$

Today the **linear-quadratic model** (figure 2.2, A, on the left side) is favoured for describing survival in radiation therapy. The logarithm of survival is given by a term which is proportional to the dose and one which is proportional to the square of the dose (from [40]):

$$S = e^{-\alpha D - \beta D^2}$$

For $D = \alpha/\beta$, the effects of the linear and the quadratic component are equal. The main disadvantage of this model is that it does not mirror the trend observed in experiments at very large doses. The theoretical survival curve keeps on bending downwards and does not flatten out to a more linear behaviour on a logarithmic axis as is the case for the experimental data.

2.2.2 Repair

From the point of view of cell survival, recovery and repair, radiation damage can be divided into three categories: lethal, sublethal and potentially lethal damage. In the

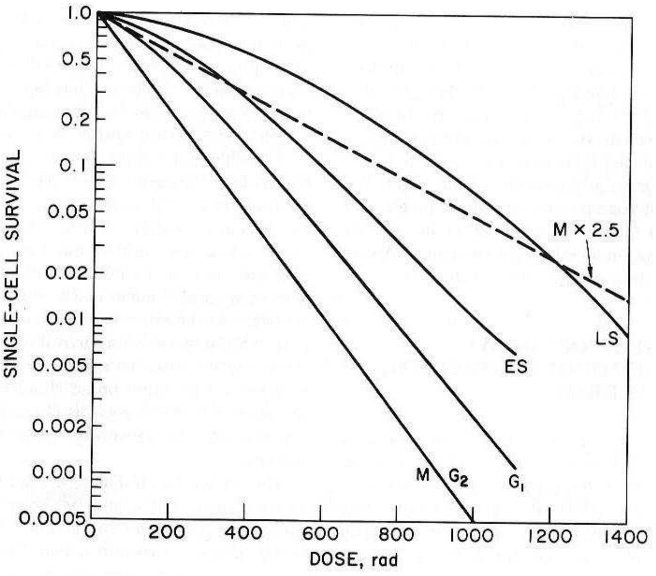

Figure 2.3: *Cellular survival of Chinese hamster cells in-vitro in different stages of the cell cycle [40]:*
LS = *late synthesis*
ES = *early synthesis*
M = *mitosis*
G1 = *postmitotic gap-phase*
G2 = *premitotic gap-phase*

first case, the damage leads inevitably to cell death. With **potentially lethal damage** (PLD), different behaviour of the cell can be observed, depending on the type and properties of radiation which causes the effect. The environment of the cell during and directly after the irradiation has crucial influence on the cell survival. In the case of photon irradiation for example, in-vitro repair (detected by higher levels of survival) is observed if the cells are allowed to keep on growing together in a united cell structure for another 6 to 12 hours after irradiation. This can be compared to the consequences of an irradiation with densely ionising radiation (neutrons, ions), where no such effect is visible. Because only limited manipulation of the cells' environment can be controlled (particularly if they remain inside an organ), **sublethal damage** (SLD) is better analysed. It was shown in fractionation experiments that many different processes in tissue are running in parallel: repair, re-assortment, re-population and re-oxygenation [40].

The main process against sublethal damage is **repair**. Furthermore, radiation sensitivity of cells strongly depends on the cell's status within the cell cycle (see figure 2.3). During mitosis (cell division) and G_2 (after the reduplication of the chromatin) the cell's survival curve is steepest, corresponding to the highest radiosensitivity regarding inactivation. On the other hand, in G_0 (not shown in the figure), when the cell is resting, the sensitivity is very low (see also discussion to figure 2.5). Inside a human being, the cells of different tissues are not synchronised. Therefore, when irradiated, mainly cells which are in M and G_2 are killed, which leads to a partial synchronisation (this can be shown in-vitro [40]). However, in a living body, the cells get redistributed throughout the whole cell cycle after few cycles. This effect is called **re-assortment**. This is important for radiation therapy because it is the reason why the cells of a tumour do not get synchronised. Additionally, the time spans of the different stages of the cell cycle vary for different cell lines.

However, the proliferating tumour has a growth advantage over healthy tissue cells: because its cells divide more often, areas where tumor cells were killed by radiation

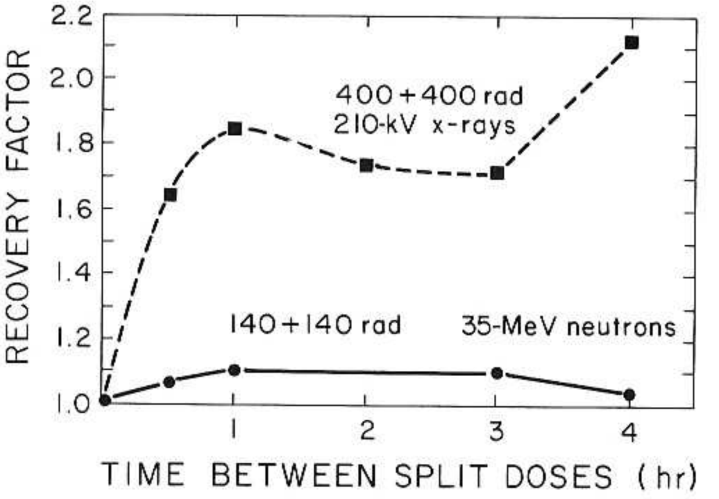

Figure 2.4:
Dose-fractionation experiment with Chinese hamster cells: comparison between neutron and photon irradiation [40]

are swiftly **repopulated**. This is also possible in some special healthy tissues, which also display high rates of cell division. An example is the epithelial layer, which is exposed to a rather heavy abrasion and is therefore bound to be replaced regularly by the underlying stem cells. But in most cases, this behaviour of repopulation has to be borne in mind for fractionation of dose in therapy, in particular when mixed neutron and photon fields are used. On the other hand, healthy tissue benefits from the **reoxygenation** of the tumour (see also chapter 2.2.3). When tumour cells are killed, the available oxygen is often able to diffuse into areas of the tumour which were hypoxic before and re-oxygenate a part of the tumour in this way, making it more sensitive to radiation again.

In order to describe the effect of a single exposure to radiation and that of fractionated exposure with the same dose, the **recovery factor** was defined:

$$\text{recovery factor} = \frac{\text{survival after the same fractionated dose}}{\text{survival after the same single dose}}$$

In figure 2.4 the recovery factor is plotted for two different types of radiation: photons and neutrons. With neutrons, only a minor influence of the fractionation is visible, whereas photon irradiation strongly depends on the interval between (and on the number of) irradiations. This has to be taken into account when planning a treatment irradiation. With photons but not for neutrons, the dose rate is also very important. Many cells display a rise in sensitivity for higher dose rates (HDR), but for some, the opposite is observed. This effect depends on the length of the cell cycle, the radiosensitivity of the respective stem cells and the ability of the tissue to adapt to the trauma of irradiation. For low dose rates (LDR), a broad spectrum of sensitivities is observed (see figure 2.5). This behaviour leads to two kinds of cells which are radioresistant. One are the proliferating cells. Statistically, in an in-vitro experiment, they are most often in the less radiosensitive S-phase, because it takes the longest time in the cell cycle to reduplicate the chromatin. On the other hand, there are the cells which divide extremely slowly. They are usually in late G_1 or even G_0 (recovery); both stages are rather radioresistant in cell experiments.

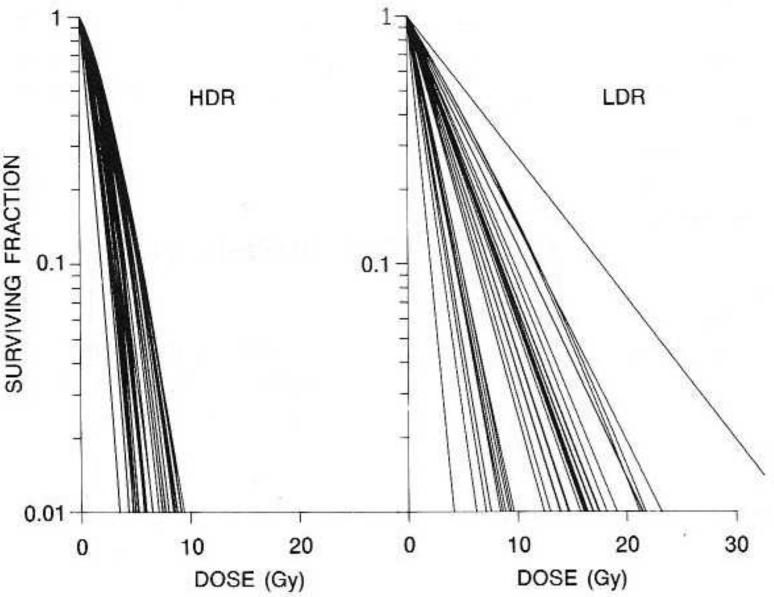

Figure 2.5:
Survival of several different cell types after irradiation with different dose rates [40]:
HDR = high dose rate
LDR = low dose rate

For every type of tumour, the best fractionation pattern has to be found, depending on cell growth, radiosensitivity and type and properties of radiation. It has to be mentioned that acute radiation effects and therapeutic long term effects, which are undesirable complications in healthy tissue, are not bound to behave in the same way with respect to the different irradiation and target parameters.
For therapeutic application, the linear-quadratic model described by the factors α, β and the number n of fractions is sometimes used to express a “Biological Effective Dose”:

$$\mathrm{D_{bio\ eff}} = \mathrm{D_{tot}} \cdot (\text{rel. effectiveness}) - \text{corrections}$$

$$\frac{\text{bio. effect}}{\alpha} = \mathrm{nD} \cdot (1 + \frac{\mathrm{D}}{\alpha/\beta}) - \frac{\ln 2}{\alpha} \cdot \mathrm{N_{cell\text{-}doubling}}$$

The biologically effective dose can then be described by the biological effect with the model parameters α and β, the prescribed dose D per fraction and the number of cell doublings N. A correction term for the alteration of the number of cells caused by proliferation can also be included.

2.2.3 Oxygen effect

The level of oxygenation can have a major influence on the effect of radiation in tissue. Thin-ionising radiation, like photons for example, displays more severe effects under aerobic than under anaerobic conditions. This kind of radiation usually deposits its dose mainly via the indirect effect (see explanation to figure 2.1). Small molecules like water or oxygen get exited or ionised by the photons and/or their secondary electrons, which also leads to a production of free and very reactive radicals. One possible reaction in the case of oxygen is the following:

$$\mathrm{O_2} \rightarrow \mathrm{O^{\cdot}} + \mathrm{O^{\cdot}}$$

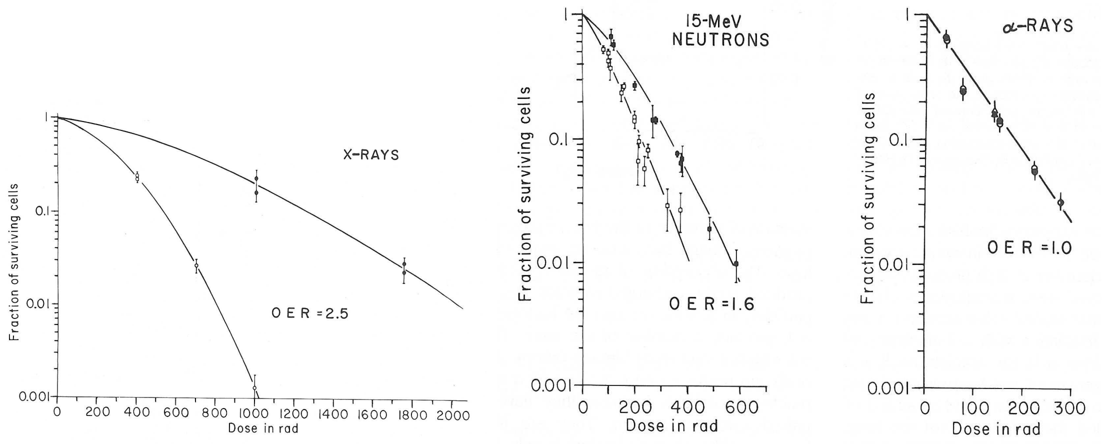

Figure 2.6: *OER for different kinds of radiations (low and high LET) [40]*

These oxygen radicals can then react with molecules of the water reaction-chain, which are also produced. Because of their high power to react with other molecules, oxygen radicals are very dangerous for a cell. Furthermore, they form bonds with the open ends of direct DNA-breaks or with other radicals, thereby damaging the DNA or fixing existing damage. Sometimes, the cell is not able to repair the loss of information then. Densely ionising radiation, like alpha particles or the heavy backscattering-nuclei of neutrons, for example, deposits its dose mainly via direct action. Therefore, the existence of oxygen essentially does not (or only slightly) change the effect of this kind of radiation. Neutrons, which mainly deposit their dose via protons, lie in between these two extremes. To quantify the oxygen effect, the **oxygen enhancement ratio** (OER) was defined [40] as the ratio of doses needed to produce the same final effect in presence/absence of external oxygen:

$$\mathrm{OER} = \left.\frac{\text{dose without } O_2}{\text{dose with } O_2}\right|_{\text{same effect}}$$

The OER is nearly one for those types of radiation which are not sensitive to the level of oxygen and greater than one for those which are (see figure 2.6). In similar in-vitro experiments, the dependence on the level of oxygenation was also studied in detail. It was found that the effect is already sensitive to very low levels of oxygen and when 2% oxygenation are reached, it is practically indistinguishable from conditions under normal aeration (which is 21% oxygen) [40]. Therefore, OER-values, which were determined in-vitro with 21% oxygenation can be applied for cells inside a human body, where the oxygenation is usually about 4%. The oxygen effect is very disadvantageous for common radiation therapy with photons: the tumour, often growing very fast and sometimes at places where its cells are not native, often does not have a good blood circulation and may therefore be badly oxygenated. Whole areas can have little oxygen, or even none at all, which can be an acute or chronic condition. These areas are far from the next blood vessel. By diffusion, oxygen can only reach places that are no further than about 70 μm away from a blood vessel [40]. Outside that radius that a small area of hypoxic cells exists, to be followed by necrotic, anaerobe cells at even larger distances. With standard photon therapy, tumour cells of these areas are much less sensitive to irradiation than the surrounding healthy tissue, which is usually well oxygenated. Because the prescribed therapeutic dose is limited in practice by the response of healthy tissue, only a part of the tumour cells are inactivated and local control of the tumour can be lost. If the total dose is divided into several partial doses, which is called **fractionation**, the tumour is usually **re-oxygenated** between the single irradiations because oxygen can diffuse from the blood vessels into the hypoxic areas. Therefore, more tumour cells can be killed in this way than with a single dose irradiation. This is one way to circumvent the differences in the oxygen effect. The other way is to change the quality of the radiation and take neutrons or heavy ions to treat necrotic tumours. The OER of these types of radiations is closer to one than for photons (see figure 2.6), which means that the biological effect depends less on the level of oxygenation of the tumour. The degree of re-oxygenation differs strongly between different kinds of tumour (carcinoma, sarcoma,...), depending on the level of cell proliferation rate and on the spread of the tumour. If a tumour displays only scarce re-oxygenation, heavy ion therapy offers the only other choice. Therefore it is very important to classify the tumour correctly (see chapter 2.3.1) in order to select the best treatment possible and to decide if the additional expenses of hadron therapy will pay off.

2.2.4 Radiobiological effectiveness

The quality of a type of radiation can be characterised by its LET-distribution, the linear energy loss per tracklength (see definition in appendix A.4). It has to be mentioned that the LET is not the ideal quantity for the characterisation, but the one which is used traditionally [66]. A better approach would be to use a quantity based on charged particle track structure data (e.g. Z^2/β^2), which does not only take the energy density along the track into account but also the radial energy density. Taking only the average of the LET-distribution is a loss of information. It would be useful to have more details on the actual energy deposition processes. In this work the local LET is used exemplarily as a first approach (without restricting further progress).

There has always been a demand to quantify the biological effect of hadron radiation in tissue compared to that of photons, which has a long history and much experience in therapy [52, 56]. The quantity of **relative biological effectiveness** RBE was defined as the ratio of the dose of a reference radiation D_{ref} (today: 250 kV X-ray) to that of the measured type D_{m} that give the same effect [45]:

$$\mathrm{RBE} = \left.\frac{\mathrm{D_{ref}}}{\mathrm{D_m}}\right|_{\text{same effect level}}$$

Total dose values, dose rate, fractionation, primary energy of the irradiation, cell type, oxygen level, regarded biological/medical endpoint, level of effect and LET have an influence on the RBE. In figure 2.7, the influence of initial neutron energy on the level of survival can be seen, which leads to very different values of RBE depending also on dose (see table 2.1). The RBE is furthermore used in clinical practise to characterise the biological effects of hadron radiation. Often the RBE is plotted as a function of

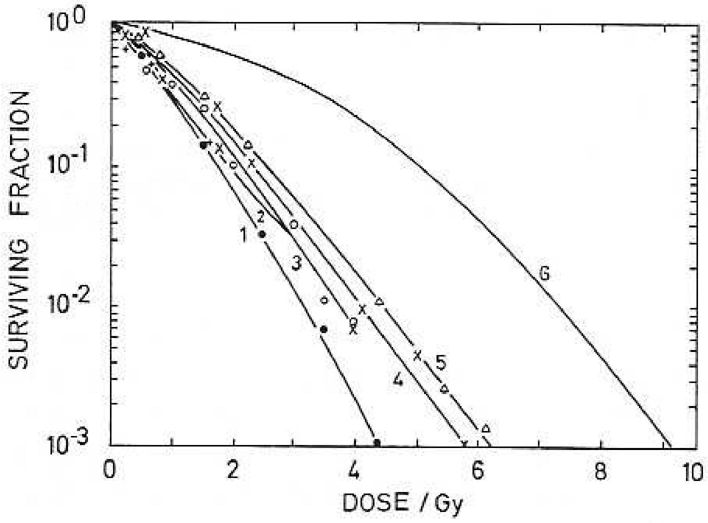

Figure 2.7: *Survival of human cells after different types of irradiation [67]:*

1. fission neutrons
2. 3 MeV neutrons
3. (20 MeV-$\alpha \rightarrow$ Be) neutrons
4. (15 MeV-d $\rightarrow$ Be) neutrons
5. 15 MeV neutrons
6. X-rays

Table 2.1: *Dependency of the RBE on the choice of survival level and neutron energy*

survival	RBE of fission-n	RBE of 15MeV-n
70%	5.3	2.7
1%	2.3	1.6

the LET (see figure 2.8). The location of the peak is often explained to be caused by the diameter of the DNA, the energy density and overkill at higher LET levels. But such a function is strictly only applicable for one specific cell line and one type of radiation. For other cells, the peak can be at another LET value or the height may be different. Looking at different cell lines, one cannot see a common trend for the RBE-LET-dependence (see figure 2.9). Difficulties can also arise from different types of reference radiation used in some experiments (200 keV-X-ray, ^{60}Co, ^{137}Cs), which

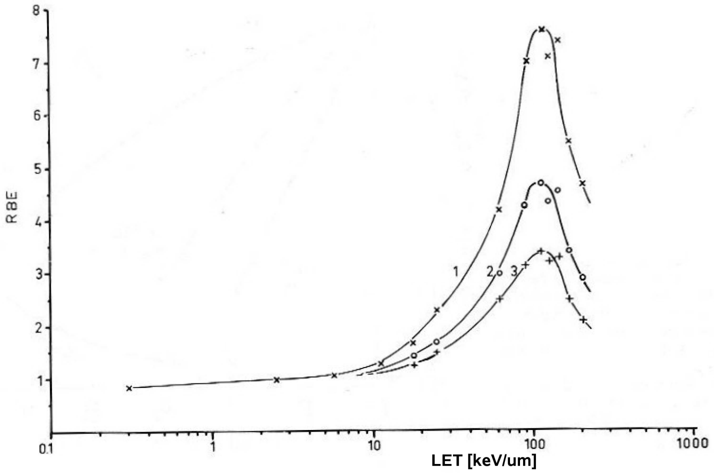

Figure 2.8: *RBE over LET for three different levels of survival: 0.8, 0.1, 0.01 [40]*

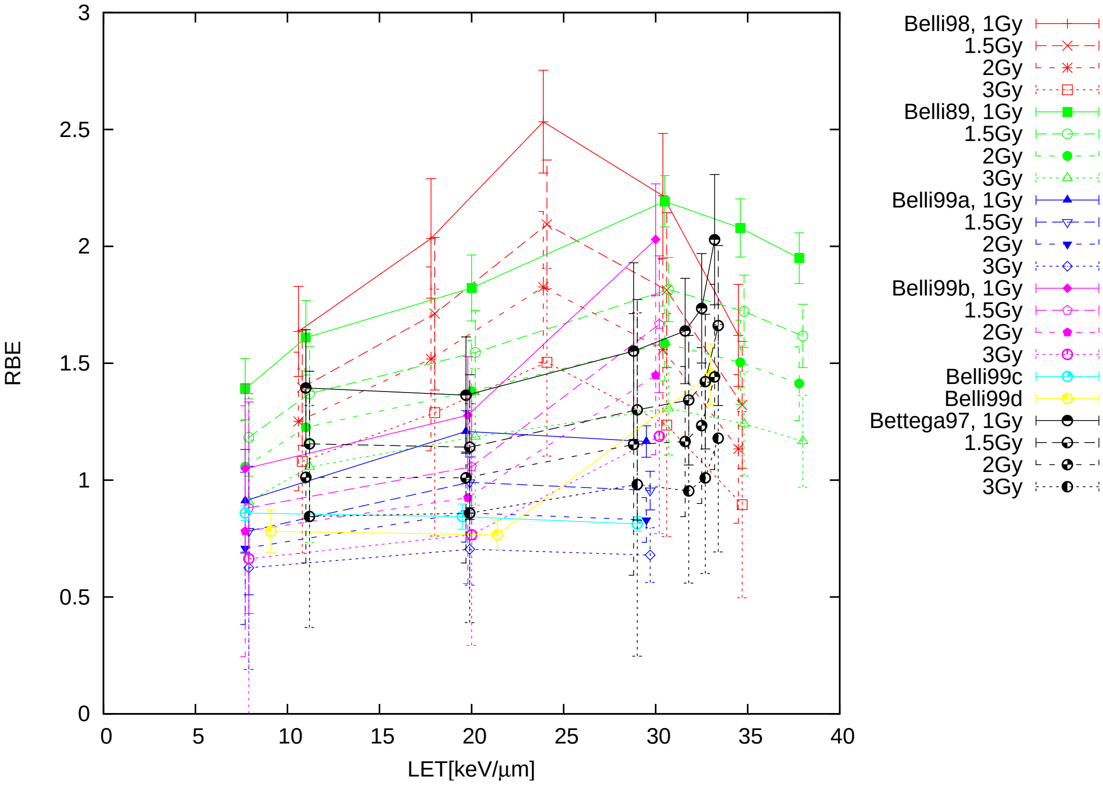

Figure 2.9: *RBE versus LET calculated from survival curves of different doses on different cell lines and for different reference radiations (all points at 1.5 Gy and 3 Gy were shifted by* $0.2\,keV/\mu m$ *to higher LET-values to be able to distinguish the different errorbars):*
Belli98 *[12] and* ***Belli89*** *[13]: V79 Chinese hamster cells, compared to photons of* 200 kV *X-ray*
Belli99a-d *[11]: human cells (tumour: a=SCC25 (sensitive), b=SQ20B (resistant); healthy tissue: c=HF19, d=M/10), compared to photons of* ^{60}Co *(for c:* ^{137}Cs*)*
Bettega *[14]: C3H10T1/2 mouse cells, compared to photons of* ^{60}Co

are known to have different biological effectiveness, too. Belli et al. [11] concluded from their data that protons and alpha particles display different biological behaviour at the same LET for cell inactivation, but this could not be proven to be a common trend for all cell lines by Goodhead et al.[38]. RBE-relationships for the inactivation of chromosome aberrations were studied among others by [22, 131, 108, 109, 80].

2.3 Medical considerations of neutron therapy

For the practical application of neutron radiation in therapeutic tumour treatment of a patient not only questions connected with reactor physics have to be answered, but also biophysical ones. The optimum of therapeutic treatment planning can only be achieved if the best form of treatment and radiation quality as well as the most

Table 2.2: *Tumour assessment after the TNM-system [106]*

T	is	“carcinoma in situ” (early cancer that has not spread to neighbouring tissue)
	0	No evidence of primary tumour
	1	small ($\leq$ 2 cm)
	2	big ($>$ 2 cm)
	3	reaching organ boundary or $>$ 5 cm
	4	neighbour organs invaded
	x	Primary tumour cannot be evaluated
N	0	No regional lymph node involvement (no cancer cells found in the lymph nodes)
	1	regional
	2	extended or both sides
	3	very extended ($>$ 6 cm or fixed)
	x	Regional lymph nodes cannot be evaluated
M	0	No distant metastasis (cancer has not spread to other parts of the body)
	1	Distant metastasis (cancer has spread to distant parts of the body)
	x	Distant metastasis cannot be evaluated
G	1	Tumour well-differentiated (Low grade)
	2	Moderately differentiated (Intermediate grade)
	3	Poorly differentiated (High grade)
	4	Undifferentiated (High grade)
	x	Grade cannot be assessed (Undetermined grade)
R	0	histological clean
	1	microscopic remaining tumour
	2	macroscopic remaining tumour
	x	remaining tumour cannot be assessed

suitable size and shape of the beam is chosen, considering all radiation characteristics mentioned earlier. In order to classify the type, size and spread of a tumour, different concepts for tumour and volume descriptions are used. These are shortly described in the next sections.

2.3.1 Tumour classification

The main intention of tumour classification is to establish a system that can be used to compare tumour treatment outcomes between different patients and thus quantify the results of different treatment possibilities. A tumour has to be described not only in its size and position, but also in its type and aggressiveness as well as in the invasion ability into other tissues (see table 2.2). This information is achieved by physical examinations, imaging studies (X-ray, CT, MRI, PET), laboratory tests (blood samples), pathology reports of the histological results and surgical reports [59].

The first step towards tumour classification is the so-called typing, where the location and source tissue of the tumour is determined. Medically, this is also apparent in the tumors name, where carcinomas, sarcomas or lymphomas are differentiated for example. The malignity or aggressiveness of the tumour is determined by the so-called grading/staging. This goes from level I (differentiated) to level IV (undifferentiated). The best known classification system is the TNM system. T stands for the volume and invasion ability of the primary tumour, N for local metastasis (in lymph nodes) and M for distant metastasis. For N there is often the additional information on the number of afflicted lymph nodes and the number of tested ones. For example, breast cancer T3 N2 M0 refers to a large tumour that has spread outside the breast to nearby lymph nodes, but not to other parts of the body. Prostate cancer T2 N0 M0 means that the tumour is located only in the prostate and has not spread to the lymph nodes or any other part of the body [59].
Furthermore, G was introduced to quantify the grading and R for the existence of remaining tumour parts after surgical removal [106]. The success of a therapy can be classified by specifying the remission (see table 2.3). Additionally there are five stage levels (see table 2.4) which tumours classified in the TNM system correspond to. Criteria for stages differ for different types of cancer. For example, bladder cancer T3 N0 M0 is stage III, however, colon cancer T3 N0 M0 is stage II [59].

Table 2.3: *Classification of remission [106]*

Remission	CR	complete remission
	PR	partial remission (> 50%)
	MR	minimal remission (25 - 50%)
	NC	no change (< 25%)
	P	Progression

Table 2.4: *Stage levels*

Stage 0	Carcinoma in situ (early cancer that is present only in the layer of cells in which it began)
Stage I, II and III	Higher numbers indicate more extensive disease: greater tumour size, and/or spread of the cancer to nearby lymph nodes and/or organs adjacent to the primary tumour.
Stage IV	The cancer has spread to another organ.

2.3.2 Volume definitions

From the medical point of view, it is important to know which volume is part of the tumour and therefore has to be irradiated. For safety purposes, margins are added, in order to be sure to hit the whole tumour volume with the application of radiation.

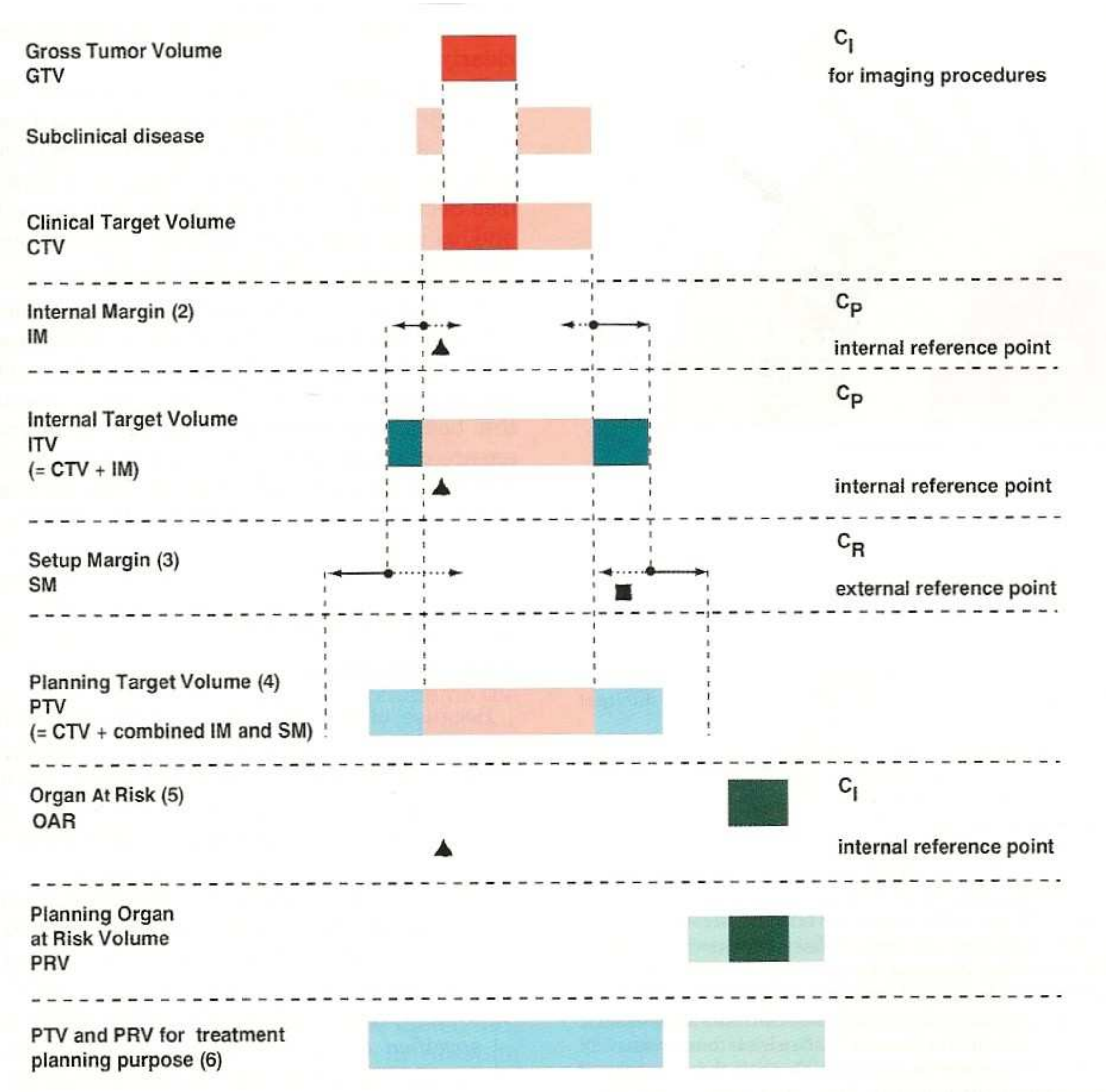
Gross Tumor Volume
GTV
C_I
for imaging procedures
Subclinical disease
Clinical Target Volume
CTV
Internal Margin (2)
IM
C_P
internal reference point
Internal Target Volume
ITV
(= CTV + IM)
C_P
internal reference point
Setup Margin (3)
SM
C_R
external reference point
Planning Target Volume (4)
PTV
(= CTV + combined IM and SM)
Organ At Risk (5)
OAR
C_I
internal reference point
Planning Organ
at Risk Volume
PRV
PTV and PRV for treatment
planning purpose (6)

Figure 2.10: *Schematic view of the volumes and their margins; internal and setup margin can be asymmetric and are combined, not added directly [57]*
right column: point of reference and coordinate system

On the other hand, the healthy tissue surrounding the tumour should be spared as far as possible. The exact definition of tumour and organ at risk [57] is therefore of great importance (see figure 2.10 for illustration).
The **gross tumour volume** is constituted of the primary tumour (GTV-T) and the metastasis in the lymph channel (GTV-N) and in other tissue (GTV-M). Here the density of tumour cells is very high ($> 10^6/\text{mm}^3$). Therefore the afflicted tissue can clearly be defined in the examination methods. The exact size, however, is often depending on the chosen imaging technique (for example different standard clinical methods like endoscopy or imaging with CT). In order to meet the aim of the death of the whole tumour without remission, a certain predefined dose has to be applied to the GTV. Because of the fractionation, the whole treatment often takes several weeks to finish. In this time, the tumour can change in shape and position. Therefore, the GTV should be determined thoroughly at the beginning and then be controlled regularly during treatment to ensure the fulfilment of total cell killing. If necessary, dose application has to be adapted by change of beamsize and aim or in extreme cases, the whole treatment planning has to be repeated.
Furthermore, the **clinical target volume** (CTV) is defined clinically and anatomically. Again two kinds are differentiated: tumour-neighbouring volumes (CTV-T, e.g. microscopical expansions of the GTV) or tumour-distant tissue (CTV-N/M, v.a. lymph nodes). There, tumour cell density is usually smaller than $10^3/\text{mm}^3$, but nevertheless, not treating this region often leads to tumour remission. In standard examination methods, the CTV is often not detectable and is therefore called subclinical volume. The oncologist has to define this volume with the help of probability tables, which list the occurrence of tumour cells outside the GTV from experimental data.
Surrounding the tumour in this fashion, it is still necessary to include certain margins, depending on the irradiation technique. The volume defined in this way is called **planning target volume** (PTV) and is used as basis for treatment planning. This accounts for several types of errors which would occur if the smaller CTV would be irradiated instead of the PTV. Basically, there are two sources of uncertainty in radiation therapy. One is caused by the tumour and the patient themselves: the uncertainty in size, shape and position (caused by physiological movement). These are covered by the concept of the internal margin (IM). The other uncertainty arises from the problem of reproducibility of the patient position in relation to the beam and is accounted for with the setup margin (SM). Uncertainty of the treatment machine, errors at the transport from the CT to the treatment position and finite accuracy of patient position particularly at fractionated treatment play a role here. Both margins have to compensate both systematic and random errors of correlated and uncorrelated kind. A simple addition of both margins (which is equal to a linear superposition) leads to a PTV which is much to big and therefore the limits of toleration for healthy tissue can be reached. A better approach is the quadratic addition, treating systematic and random errors separately and combining them later, comparing them with experimental data:

$$\begin{aligned}\Sigma &= (\Sigma^2_{setup} + \Sigma^2_{organmotion} + \Sigma^2_{delineation})^{1/2} \quad \textit{systematic}\\ \sigma &= (\sigma^2_{setup} + \sigma^2_{organmotion})^{1/2} \quad \textit{random}\end{aligned}$$

Using models and experiments, Stroom at al. (in [57]) found a margin of $2\Sigma + 0.7\sigma$ for example. In general, such an exact mathematical calculation is not possible because all single uncertainties are not exactly known. Therefore, the margin is often defined by estimations which are based on experience. The boundaries are defined by the closeness of organs at risk, where the dose is not allowed to exceed a certain limit.

After the treatment planning, the treated volume (TV) is determined from the obtained dose plans. It consists of all those volumes which are irradiated with at least the minimal tumour dose. This dose was previously pre-assigned by the physician taking radiation resistance of the tumour into account. To evaluate side effects and local recurrence (which is also described by the tumour complication probability = TCP, see section 2.4.1), this volume is of great importance. To compare the treated volume with the original target volume (the PTV), the so-called conformity index CI is defined:

$$\mathrm{CI} = \frac{\mathrm{TV}}{\mathrm{PTV}}$$

The ideal aim of treatment planning is a CI of unity, but this can often not be reached because of closeness of organs at risk. However, the index can be used to quantify treatment planning optimisation. Furthermore, there is the irradiated volume with a size depending on the irradiation technique. All areas which are irradiated with a dose that is relevant for side effects are combined here. The relevance is defined by the normal tissue tolerance (NTCP= normal tissue complication probability, see 2.4.1) being significantly greater than zero.

The boundary of the beams is defined by one or more organs at risk (OAR). These are organs which are either very radiation sensitive or very important for survival (often both). The sensitivity can again be derived from the NTCP and is often determined from clinical observations. There are different models from which the NCTP can be derived. One of them is the functional subunit concept, which classifies organs into a serial and a parallel group. For parallel organs, the size of the irradiated volume alone determines the sensitivity (an example is the lung). In serial organs, the sum of hits is essential, which is equivalent to the amount of dose deposited at one position, independent of its size (an example is the spinal cord). For treatment planning, an uncertainty margin is added here in analogy to the internal and the setup margin.

2.3.3 Early and late radiation effects

For treatment planning, not only the removal of the tumour is important, but also the minimalisation of side effects of the radiation in healthy tissue. These often limit the total dose and field sizes of the treatment. In order to cure the patient, some side effects are unavoidable, but they should be kept as small as possible. The most common early side effects are reddening of the skin and disfunction of salivary gland or other mucosa, which are directly in the beam. This can lead to dryness in the mouth (xerostomia) for example. These disfunctions, induced by irradiation of healthy tissue, can be temporarily or permanent. Late effects like secondary tumours can also be caused by irradiating healthy tissue, but on the other hand also by missing the primary tumour (either because of organ movement or because the treatment fields were too small). In that part of the tumour volume which received insufficient dose, the tumour can reappear, often in a more aggressive form. This process is called recurrence and should be avoided at all costs.

2.3.4 Dose volume histogram

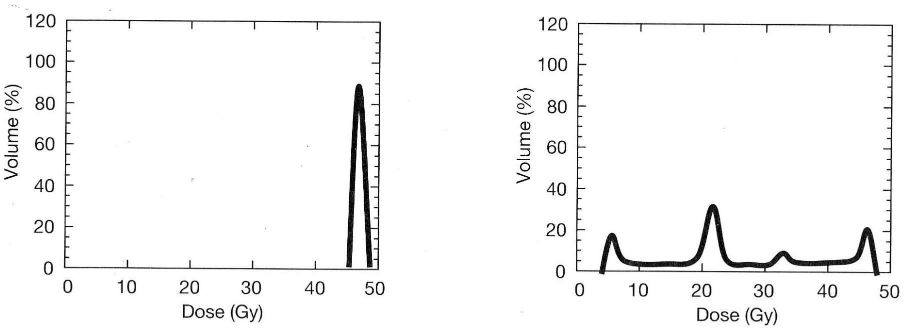

Figure 2.11: *Direct DVHs for a four field prostate treatment for the target volume (left) and a critical organ (right, rectum) [101]*

A calculated 3D treatment plan contains the information of dose at all points inside the patient. This is a large amount of information, so a histogram is used to sum the dose in each organ depending on the fraction of organ volume, the so-called dose-volume-histogram (DVH). In this condensation, the spacial information is lost. There are two ways to plot the result, as direct or as cumulative diagram [101].

In figure 2.11 an example of a direct DVH is shown. For the PTV, the ideal plot would be a delta-function at the dose prescribed by the physician. For a real case (in figures 2.11 and 2.12, a four field prostate treatment), a broadening of the peak can be observed. For critical organs, the DVH may result in an expanded distribution, where different peaks mark fractions of the volume which get a certain dose.

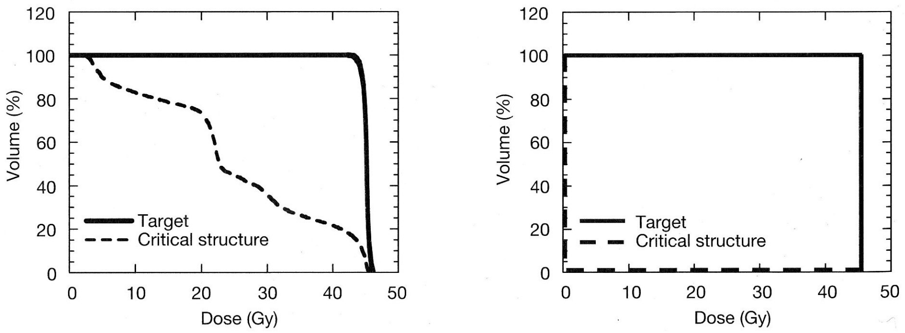

Figure 2.12: *Cumulative DVHs for a four field prostate treatment on the left and ideal case shown on the right [101]*

In figure 2.12, an example of a cumulative DVH is shown. There, the ideal case is plotted on the right side, the prostate case on the left side. The ideal would be that 100% of the target volume get all of the prescribed dose while 0% of the critical organ get any dose. This cannot be reached in the real case, though it is the aim of treatment planning to get as near as possible to this.

2.4 Radiobiological weighting

The aim of radiation therapy is to damage cells by energy deposition in such a way that they are not able to divide anymore and die. The perfect therapy would kill all of tumour cells while sparing all healthy cells surrounding the tumour. This aim cannot be reached with any available form of therapy, using radiation or not. Therefore it is of great importance to know as much as possible about the damage inflicted upon the tumour and the surrounding tissue in order to assess and, if possible, improve it. Different concepts have been designed to calculate not only the physical energy deposition of radiation but also the biological reaction of the cells. The effects of high-LET radiation like heavy ions and neutrons have mostly been analysed in comparison to low LET radiation like photons or electrons (see chapter 2.2.4 on RBE). The different behaviour has to be measured and quantified and included into the calculation process of biological assessed dose. In the next section, a short survey of biological radiation effect assessment is given, followed by a description of the weighting implemented for the calculations in this thesis.

2.4.1 Review of literature

For photon irradiation there are different ways to quantify and investigate cell damage. Tumour killing can be described by the **tumour control probability** (TCP) following Källmann [43] using, for example, a Poisson-ansatz:

$$\mathrm{TCP} = \prod_{\mathrm{i}} 2^{-\exp(\mathrm{x_i})} \quad , \quad \mathrm{x_i} = \mathrm{e} \cdot \gamma \left(1 - \frac{\mathrm{d_i}}{\mathrm{D_{50}}}\right) + \ln \frac{\mathrm{v_i}}{\mathrm{V_{PTV}}}$$

Here, $\mathrm{d_i}$ is the dose of the volume element $\mathrm{v_i}$ of the planning target volume $\mathrm{V_{PTV}}$. For the dose $\mathrm{D_{50}}$ a 50% control probability is necessary and γ is the gradient of the dose-effect function in the inflexion point. Other definitions are possible and reasonable, depending on the radiation effect which is considered. An example is the TCP based on survival of stem cells to investigate cell density and dose inhomogeneity [129].

On the other hand, the damage of healthy tissue was quantified using the **normal tissue complication probability** (NTCP), which is described in a model by Lyman in the following way [72]:

$$\mathrm{NTCP} = \frac{1}{\sqrt{2\pi}} \int_{-\infty}^{\mathrm{t}} \exp\left(-\frac{\mathrm{t}^2}{2}\right) \mathrm{dt}$$

$$\mathrm{t} = \frac{\mathrm{D} - \mathrm{TD_{50}(v)}}{\mathrm{m} \cdot \mathrm{TD_{50}(v)}} \quad , \quad \mathrm{v} = \frac{\mathrm{V}}{\mathrm{V_{ref}}}$$

Here, D is the homogeneous dose in the volume V and $\mathrm{V_{ref}}$ is the reference volume. $\mathrm{TD_{50}(v)}$ is the tolerance dose which causes complication in the part v of the volume with a probability of 50%. The gradient parameter m and the tolerance dose $\mathrm{TD}_{50}(\mathrm{v})$ have to be determined by adjustment to measurement curves. There also exist other ways of description of the NTCP [17, 43, 23], which will not be discussed here.

Other ways to evaluate a dose plan is the minimum/maximum-criterion, where the minimum and maximum dose inside the tumour volume are prescribed as well as the the median and the homogeneity of the dose distribution, the relative residual volume dose[1] and the success probability E which consists of a combination of TCP and NTCP. There are also attempts to combine all of these parameters in a quantification parameter B [43] to simplify and accelerate the assessment of a dose plan.

Neutron irradiation is not a standard application in tumour therapy and therefore, the numbers of patients treated worldwide are orders of magnitude smaller than for photon therapy. In both TCP and NTCP the probabilities of complications or control have to be included from experience. Because of the relatively small number of cases, this is not possible for neutron therapy. Therefore another way can be tried, reverting to the basics of radiation effects in a cell: the linear-quadratic model (see chapter 2.2.1). Cell survival is often described in the following way [93, 86]:

$$\mathrm{S} = \mathrm{S}_0 \mathrm{e}^{-(\alpha \mathrm{D} + \beta \mathrm{D}^2)}$$

Note that the parameters α, β depend slightly on the dose D and strongly on the dose rate $\dot{\mathrm{D}}$ and the LET of the particle. To calculate cell survival in the irradiated volume with this ansatz, the coefficients α and β have to be known from relevant cell experiments which have to be corrected for all differences to the real irradiation situation for all particles and energies. This is not done at the moment. But in principle, this ansatz can be used not only for cell killing, but also for other secondary effects such as secondary tumour induction and induction of complications.

2.4.2 Biological weighting of doses in a voxel phantom

Absorbed dose D alone is not a useful quantity to describe radiation biological effects. In radiation protection, therefore, absorbed dose is weighted with a radiation weighting factor $\mathrm{w_R}$, accounting for the relative efficiency of a given quality of the radiation field to induce the medical endpoint “somatic late effects” at doses and dose rates compatible with radiation protection practices, legislations and regulations. The resulting product $\mathrm{D} \cdot \mathrm{w_R}$ in an organ tissue was given the new name *equivalent dose* H with the new special name of “Sievert” for the same unit J/kg (as absorbed dose).

In radiation therapy, one is dealing with higher absorbed doses in many tissues/organs and with more relevant medical endpoints. Thus, the radiation protection concept cannot be adopted directly but has to be modified. The modifications concern the endpoints and the numerical values of the weighting factor. Here, the endpoints

a) inactivation of tumour cells,

b) induction of complications in healthy tissues,

---

[1] Dose which is deposited in those organs and tissues which are classified as less important

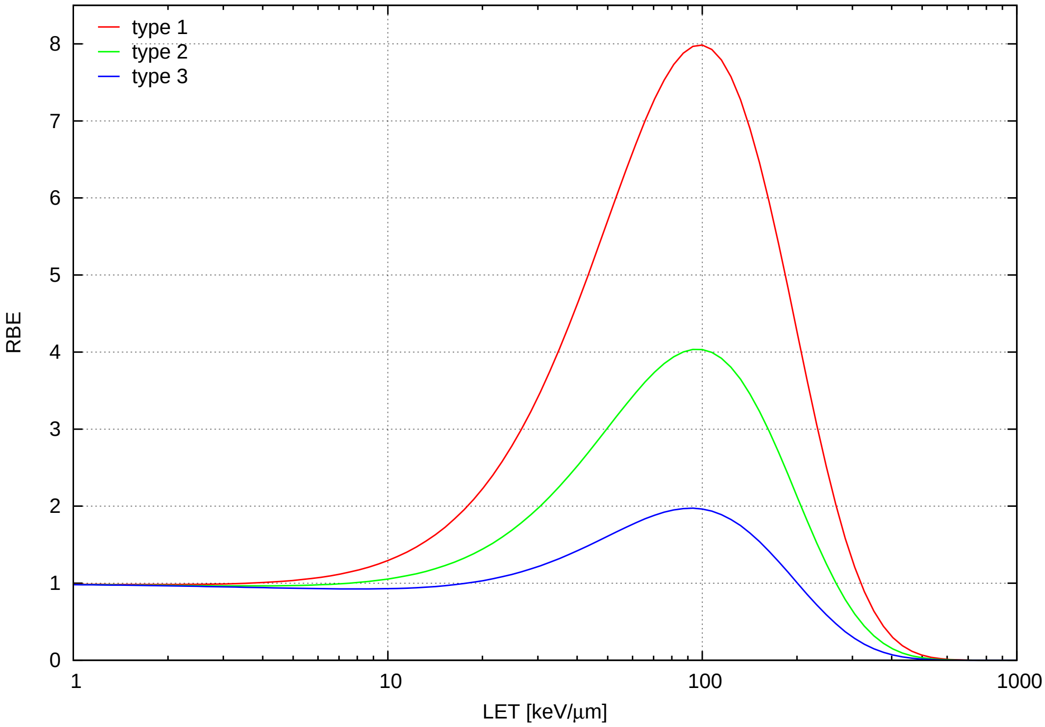

Figure 2.13: *Tentative RBE-LET dependence for three different types of radiation actions (example models for: 1: late effects, 2: inactivation of healthy tissue (complications), 3: induction of secondary tumours)*

c) induction of late somatic effects in healthy tissues

will be considered. One needs numerical functions for all three endpoints and as a function of radiation quality, oxygenation, tissues, etc. These functions are not known presently and their discussion is outside the scope of this work. Here, only reasonable approximations were made to demonstrate the principal capability of the developed treatment planning programme to account for these influencing factors.

In addition, there are generally two possibilities to account for these different efficiencies:

i) direct forward calculations for each single constituent of the local moderated radiation field in the irradiated body, or

ii) accounting for the radiative differences or RBEs of the respective radiation fields relative to the local properties of used photon fields, for which large experiences were collected and published in literature.

Here, only this latter option is discussed.

The methods to quantify tumour treatment success described in the preceeding section are not easily applicable for standard neutron therapy. However, direct specification of cell killing by neutrons is not necessary to assess the effect of the neutron dose applied.

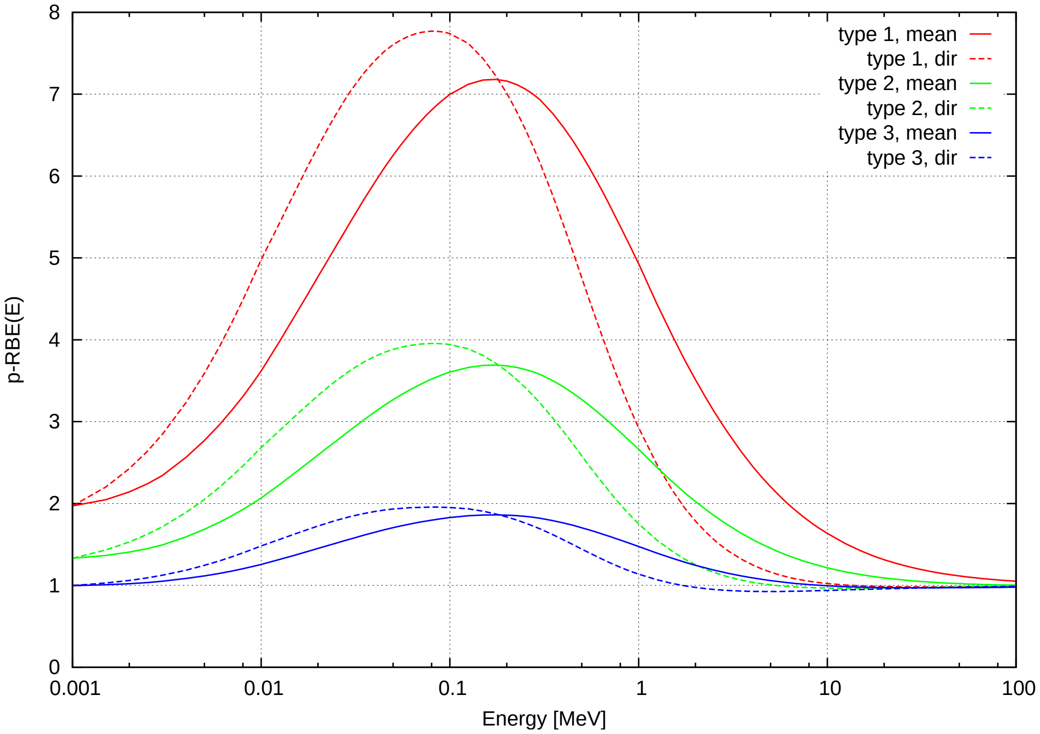

Figure 2.14: *Tentative RBE-energy dependence for protons in water for the three different types of radiation actions shown in figure 2.13: comparison for direct and mean calculation*

There exists much experience in photon therapy, so it is a reasonable approach to convert the calculated neutron dose to a photon dose equivalent, which can be evaluated in the same way as standard photon therapy. This would lead to the use of a quantity similar to the RBE at appropriate dose levels, which describes the ratio of dose necessary to achieve the same effect as a reference radiation (see chapter 2.2.4). In this case, it would be more precise to use high energy photons (for example the bremsstrahlung spectrum of a linear accelerator), which are used for the photon treatment, as reference radiation. This approach is complicated by the RBE's dependency on several parameters, like the type of endpoint evaluated, the level of the effect, the dose, dose rate and LET of the particles and many more.

Some of these parameters can be taken into account by including them in the calculation process. The dose and LET at the position of dose deposition are known in all steps of the calculation. In figure 2.13, examples of tentative RBE-LET-dependences for the three types of radiation effects at appropriate dose levels are shown. They can be interpreted as radiation effects for the induction of late effects (red) and inactivation (complications) of healthy (green) and tumour cells (blue), for example. All of these curves have additionally a dose dependency and can be different for different particles, which has been neglected here. The maximum is not always located at 100 keV/μm for example (see section 2.2.4). The dose-dependency as well as different RBE-LET-curves for different kinds of particles can easily be taken into account and it is also possible to include different tissue radiation sensitivity as well as tissue dependent LET-values for each particle. In analogy to the approach used in the ambient dose equivalent calculation for the quality factor (see chapter 5.1.3) a mean RBE-energy dependence was calculated from these curves (see figure 2.14 for protons for example). This was introduced into the dose-calculation inside the voxel phantom (see chapter 7.2). In practice, an individualised computer model of the irradiated body part of a patient has to be produced from his/her Dicom-CT-images.

CHAPTER

3

Description of treatment facility

The scientific research reactor FRM II in Garching is primarily designed to supply a high flux of thermal neutrons for diffraction, spectroscopy, radiography and secondary particle production (e.g. positrons). However, these neutrons are not suitable for direct neutron therapy as they do not deposit much energy in greater depth (BNCT is outside the scope of this work). Therefore, before entering into beamline number 10, the thermal neutrons are converted by two plates of enriched uranium inside the heavy water (D_2O) tank to get a new, unmoderated high-energy fission spectrum [126]. The neutrons are then channelled into a beam tube through the biological shield (consisting of light water in the pool and 1 m heavy concrete) and various shielding and filtering layers to the patient treatment couch at a distance of almost 6 m from the converter plates (see figure 3.1). The beam can be shaped with the help of a multileaf collimator (see figure 3.1), which is placed at the very end of the beam tube. This collimator has to be shielded, which is done with the help of a fourfold shutter inside the beam tube. The following chapters describe the beamline characteristics in detail and give a short introduction to the problems and opportunities of neutron therapy.

3.1 Beamline characteristics

In the research reactor FRM II, one fuel element of 8.1 kg highly enriched uranium (93% ^{235}U) is placed inside a heavy water tank (D_2O) which is surrounded with light water (H_2O)(see figures 3.1 and 3.2). The duration of a duty cycle is 60 days with a constant thermal power of 20 MW (this corresponds to a source strength of $1.5 \cdot 10^{18}$ n/s). The emitted fission neutrons are moderated inside the heavy water tank. There, two converter plates (containing together 489 g of ^{235}U, thermal power 80 kW)

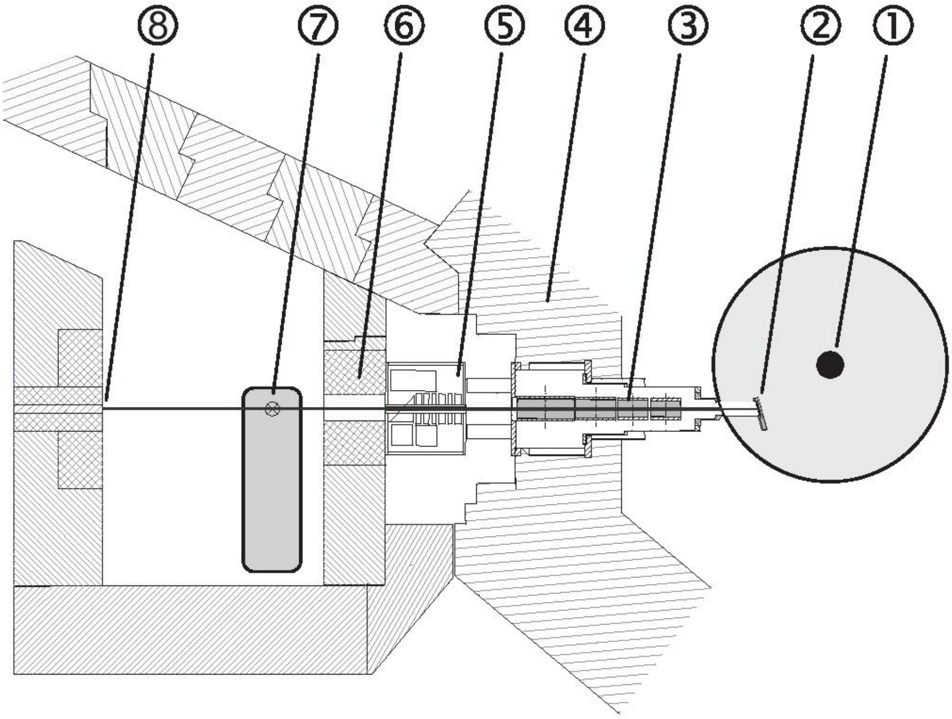

Figure 3.1: *Plan view of the MEDAPP facility at the FRM II [16]:*
1: reactor core; 2:converter plates in the D_2O *tank (grey); 3: beam tube and shutters; 4: biological shield; 5: filter bench (fixed* B_4C *epoxy, fixed lead, optional lead and PE); 6: multi leaf collimater (MLC); 7: irradiation cite; 8: beam dump*

capture part of the thermal neutrons to produce new unmoderated fission neutrons. A part of those enter into beamline SR10. On its way to the beam exit point into the treatment room, the beam is changed by several structural elements, filters (boron-plastic filter for the thermal neutrons, lead filter of 3.5 cm thickness for photons) and the multileaf collimator. These elements also produce further photons. The filters were chosen to resemble the FRM I conditions as closely as possible to simplify CE

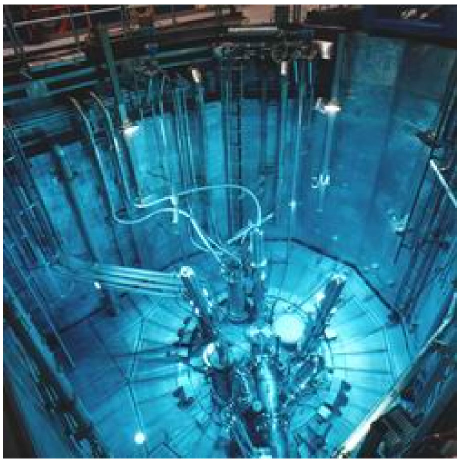

Figure 3.2: *Top of the moderator tank, viewed from the edge of the operating basin filled with light water [31]*

and TÜV certification processes. The collimator can shape the beam's cross section shape with 40 leaves (20 upper and lower leave, respectively) of 1.5 cm lateral width. The maximal beam cross section is a $20 \cdot 30\,\mathrm{cm}^2$ rectangle (see figure 3.3). Each leaf is 50 cm thick in the direction of the beam: 10 cm Fe, 30 cm PE and 10 cm Pb. Its cross section is 1.5 cm times 10 cm (no overdrive is possible). The sequence of beam passage is Fe → PE → Pb. The purpose of the three layers is to filter the primary neutrons as well as primary photons and the secondary particles produced inside the filter itself. The reference point was chosen at the place of patient treatment, 100 cm from the beam exit wall which in turn is 593 cm from the converter plates.

At the beam entrance side of the collimator, two ionisation chambers measure the dose rate of the total beam. These beam monitors integrate the received dose over the treatment time and shut off the radiation when the prescribed dose is reached. The correlation between this designated dose and the monitor units which have to be preselected was determined by Kampfer [65] in the course of the basic dosimetry measurements. The correlation between field size and shape, dose in water phantom and number of monitor units was also measured.

The patient treatment couch is optimised to consist of materials which cannot be easily activated by inelastic neutron collisions. Therefore, metal is avoided where possible or shaped in a way that omits the beam. Even the operating device of the treatment couch is built out of wood. A laser system is installed to define the horizontal and vertical beam centre. Furthermore, a light field can be used to visualise the beam's cross section on the patient's surface in order to position him correctly. Because of the large beam penumbra (measured and discussed in detail in [65, 16]), the neutron flux at the edge of the light field is 50% of that in the centre for a field size of $9 \cdot 9\,\mathrm{cm}^2$.

Between the treatment room and the radiography site, there is a window in the wall which can be closed by a beam shutter if necessary (see figure 3.1). Because of the beam divergence, the beam size at the radiography position is about $30 \cdot 30\,\mathrm{cm}^2$. Inside the radiography room a flexible frame is installed. With this frame the sample (or Bonner sphere) can be placed at the necessary position.

3.2 Treatment specifications

The FRM II MedApp (medical application) spectrum (see figure 6.1) at beamline SR10 has a mean energy of about 1.9 MeV. Therefore, the application is constrained to superficially situated tumours, similar to the former FRM-RENT-I beam [127]. The main part of tumours treated there were relapses of head-and-neck tumours, melanomas, salivary gland tumours (all curatively) and local relapses of mamma-carcinomas (most times palliatively). The focus for the FRM II medical applications will also lie on these kinds of treatments.

For many decades, neutron therapy has been studied at different centres throughout the world and neutrons were found to have an advantage over photons for slowly-growing and well-differenciated tumours [25]. Examples of results of two studies are shown in figure 3.5, for salivary gland tumours and for head-and-neck cancers. For the salivary gland tumour good results were found with neutrons and a much better local

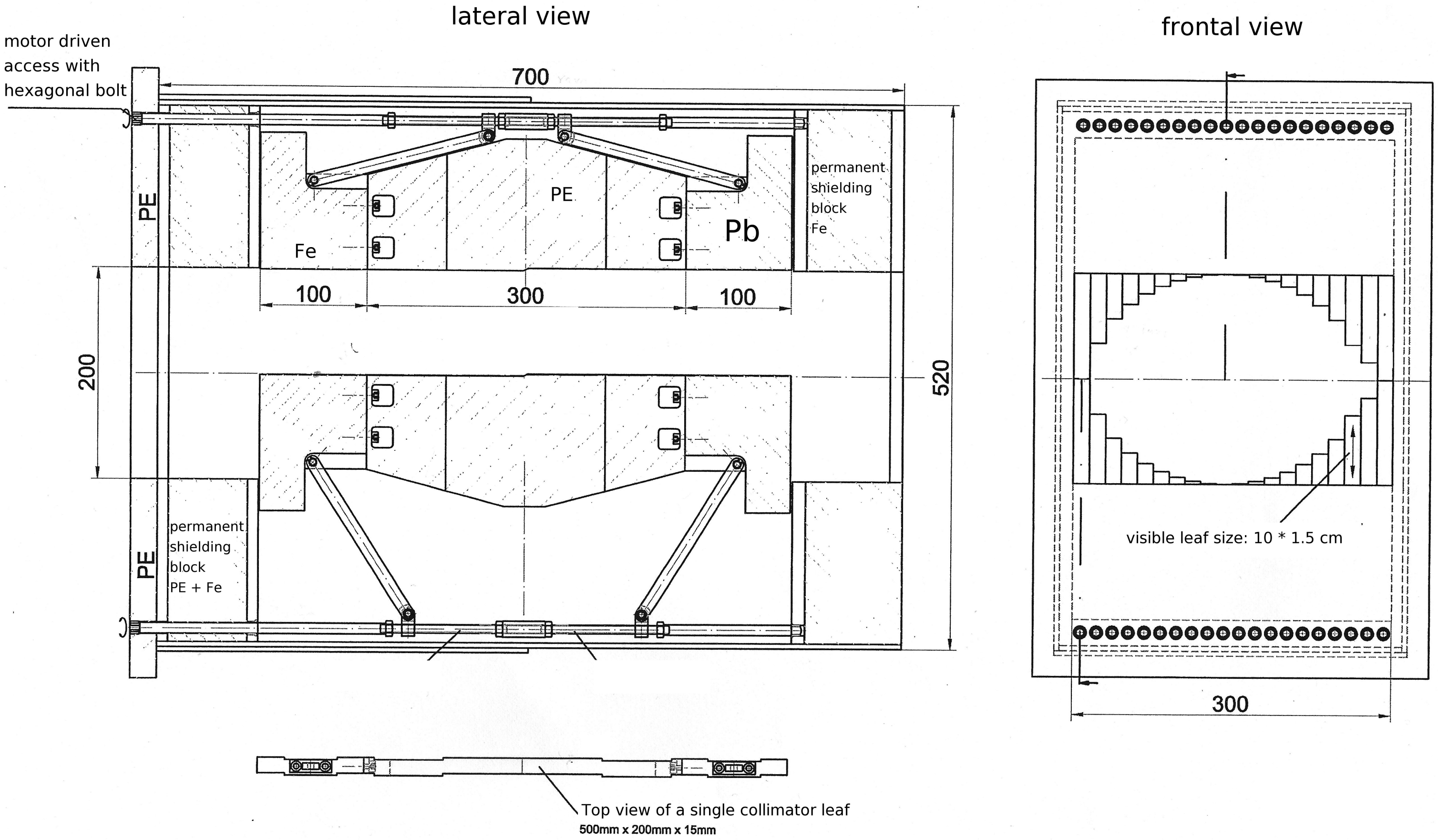
lateral view
motor driven
access with
hexagonal bolt
700
PE
PE
Fe
Pb
permanent
shielding
block
Fe
100
300
100
200
520
permanent
shielding
block
PE + Fe
PE
frontal view
visible leaf size: 10 * 1.5 cm
300
Top view of a single collimator leaf
500mm x 200mm x 15mm

Figure 3.3: *Multileaf collimator of the medical beamline: schematic design (in mm); for a description see text (Waschkowski, priv. com.)*

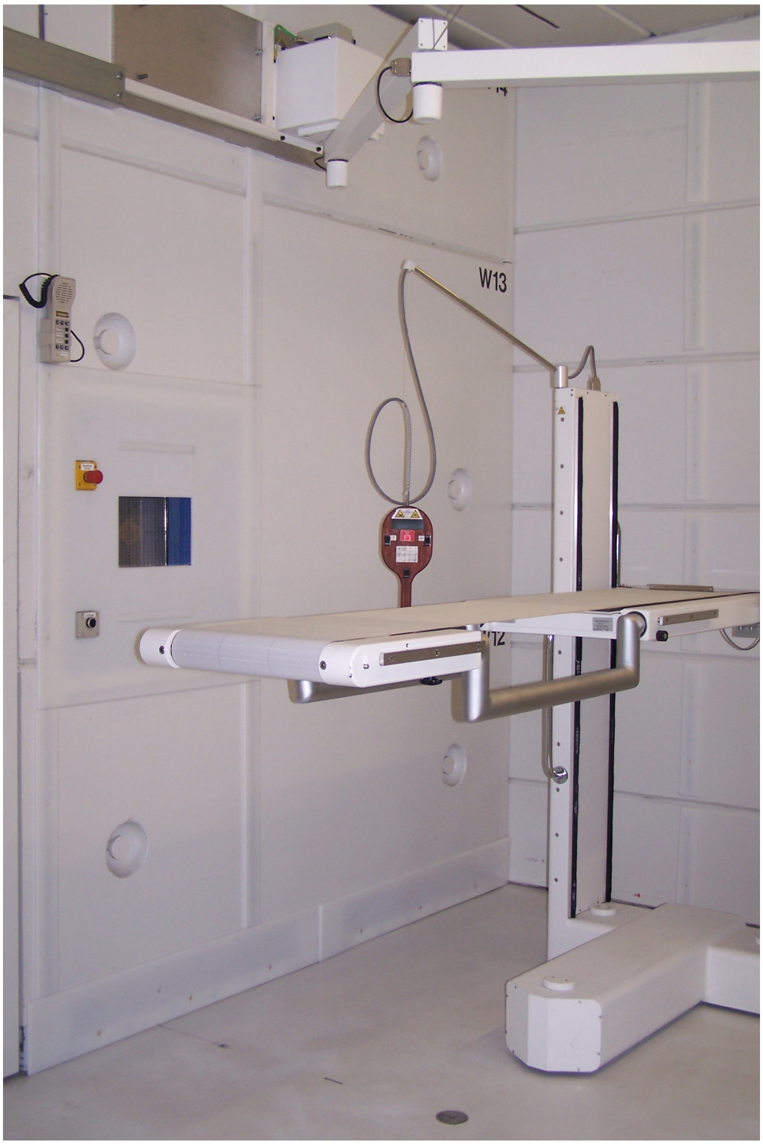

Figure 3.4: *View of the patient treatment couch; on the left, the beam exit window can be seen as well as the wooden hand panel for the couch in the centre.*
(Wagner, priv. com.)

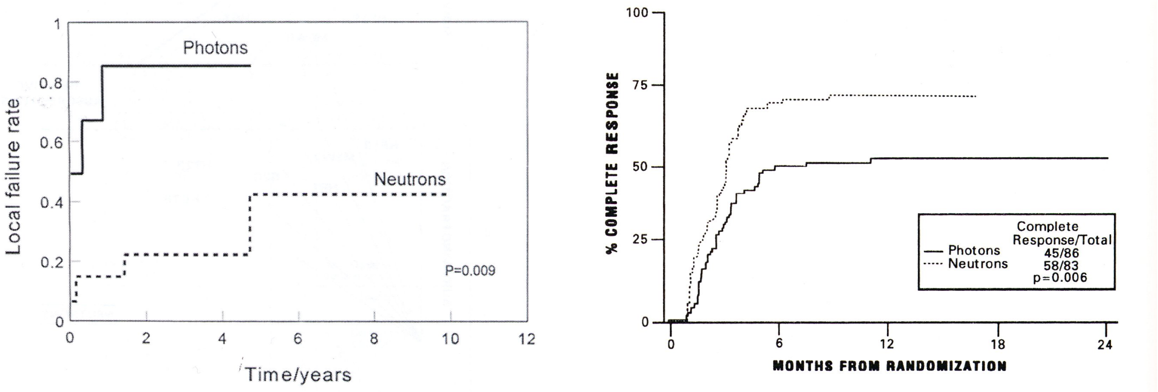

Figure 3.5:
left: *Neutron therapy of unresectable salivary gland tumours. Probability of local-regional control failure with initial failure rate as starting points [128]*
right: *Actuarial tumour clearance curves for patients with advanced head and neck cancer - the percentage of patients with complete regression of all the tumour after the initial treatment vs the time since radiation[88]*

control was reached compared to standard photon therapy [128]. Similar results were also obtained at the FRM (Wagner, priv. com.). Neutrons also showed an advantage over surgical removal in some cases, particularly if clear resection margins could not be guaranteed. However, this initial success was not reflected in the 10-year survival, where there was no significant difference in the success of treatments by neutrons and photons. In both cases, a high metastatic failure rate was observed. In the case of head-and-neck tumours on the other hand, no significant improvement over photon therapy could be found, although the response for neutrons was better than for photons [88]. But this did not result in better tumour control and there was an increase in late effects. Therefore, patients with these kind of tumours should be carefully selected. This result can be applied to most application of neutrons, as radiobiological advantages of neutrons (discussed in chapter 2) can change rapidly throughout the tissue of the application area and during treatment time span. Therefore, the initial overall advantage may be lost for some patients. However, older studies often included cases of poor technical applications and therefore results (mainly for side effects) may be different for new up-to-date possibilities.

At the FRM II, usually a boost treatment is applied by Molls/Kneschaurek (Klinik und Poliklinik für Strahlentherapie und Radiologische Onkologie Klinikum rechts der Isar, Technische Universität München). This means that in addition to 40-50 Gy total dose with photons from a normal linear accelerator, about 10 Gy energy-dose of neutrons is applied (in 5 fractions with 2 Gy each). This procedure can minimise side effects like severe reddening of the skin (= acute erythema), which are often observed for neutrons and which are usually more severe than with photons.

In addition to the clinical tumour treatment, studies on neutron capture therapy could be performed at the FRM II. A prominent example is the Boron-Neutron-Capture-Therapy, which has long been under investigation. The idea is that with the help of special molecules, boron is applied and concentrated inside the tumour. The whole area is then irradiated externally by low energy neutrons, which are captured by the boron to produce alpha particles ($^{10}\mathrm{B}(\mathrm{n},\alpha)^{7}\mathrm{Li}$). These alpha-particles have only small energies (about 1.5 MeV) and therefore deposit their energy locally and primarily inside the tumour if a higher concentration of boron was accumulated there than in the surrounding healthy tissue. The main drawback is, that up to this moment, it has not been possible to find a suitable molecule for the selective boron transport into the tumour (the same is the case for other atoms showing similar neutron capture characteristics).

CHAPTER

4

Neutron and photon transport calculation with GEANT4 including a voxel phantom

For the neutron transport simulation, the Monte Carlo program GEANT4 [4] was used. It can calculate dose and flux for many primary particle fields. It is shortly described in the first section. For the treatment simulation in this work a voxel phantom [107] was used, which is described together with its implementation in GEANT4 environment in the second section.

4.1 GEANT4

The GEANT4-code is a toolkit rather than a fixed radiation transport computer program [4]. The user has to implement the details of the geometry, physics and recording himself. The user has to make sure that he choses the right modules to fit the relevant problem. For some parts there are graphical ways to detect mistakes and errors on first sight, or at least warning messages when something does not fit in the simulations, while for other parts test calculations are necessary for debugging. This definitely applies to the physical models and the data that cannot be displayed graphically but are fundamental for the whole transport simulation. In particular, low-energy neutron physics apparently has not been used often before and data from literature are scarce. Therefore, a detailed study of the neutron physics at low energies had to be performed in advance of dealing with the actual problem (see chapter 5). A great advantage of the design of GEANT4 is that the user has the possibility to adapt the program exactly to the problem he wants to simulate, looking closely at the points of interest for his task while simplifying others to speed up calculations.

In the following paragraphs the toolkit GEANT4 (version 4.8.2) is introduced and discussed in selected detail.

4.1.1 Fundamentals of the Monte Carlo simulation

GEANT4 is a Monte Carlo program, simulating a particle track with the help of random numbers and interaction probabilities based on cross sections. The cross sections are either precalculated in advance using theoretical models or read from data files like the ENDF/B-VI files for neutrons. The mean free path (or interaction length) of a particle with energy E is defined by:

$$\lambda(E) = \left(\sum_i \left[n_i \cdot \sigma(Z_i, A_i, E) \right] \right)^{-1}$$

where i is running over all kinds of atoms making up the material of the local target volume, n_i is the density of atoms of the species i in the relevant volume, σ is the total interaction cross section of the atom i and the term in parenthesis is the macroscopic cross section (which, thus, is defined as the reciprocal of the mean free path).
In GEANT4, like in many other Monte Carlo programs (e.g. EGS4 [91]), the differential approach to particle transport is used. This is less complicated for inhomogeneous materials than the direct approach. The material-independent number n_λ of mean free paths that a particle travels before the next interaction is given by:

$$n_\lambda = \int_{x_1}^{x_2} \frac{dx}{\lambda(x)}$$

with the path length x, which depends on the material. Therefore λ is also position-dependent. If n_r is the number of mean free path lengths that lie between the present location and the point of the next event, its distribution function is given by:

$$P(n_r < n_\lambda) = 1 - e^{-n_\lambda}$$

Therefore, the total number of mean free paths n_λ can be sampled with the help of a equally distribited random number $\eta \epsilon [0, 1[$ which samples from $P(n_r < n_\lambda)$ to give

$$n_\lambda = -\log \eta$$

After each step Δx, the remaining number of mean free path lengths is calculated by:

$$n'_\lambda = n_\lambda - \frac{\Delta x}{\lambda(x)}$$

until the relevant step given by $s(x) = n_\lambda \cdot \lambda(x)$ is the shortest and is therefore taken to determine the next interaction. In this way, all processes which depend on the energy of the particle (discrete as well as continuous) inflict a limit on the stepsize. A precondition for this procedure is that the particle cross section does not change much along the stepsize (which is equal to the energy loss being small). The smaller the

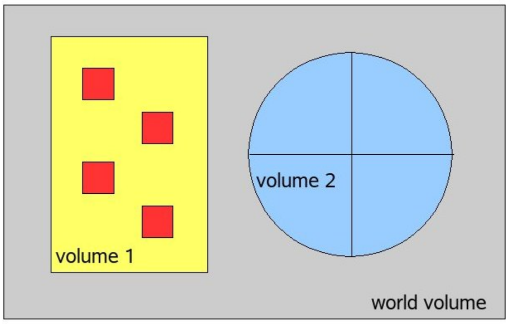

Figure 4.1: *Example (2D-view) of a simple geometry of two "volumes" (yellow cuboid and blue cylinder) inside the "world volume" (gray cuboid). Inside the yellow cuboid, there are four red parametrised "daughter volumes" (also cuboids), and inside the blue cylinder, there are four replicas totally filling the blue "mother volume".*

stepsize, the more exact is the simulation, at cost of computing time. A compromise between the increase of the computing time and the deviation from the assumption of a constant cross section is imposed in GEANT4 by not allowing the residual range of the particle to decrease by more than 20 % during a single step. This works well for energies above 0.5 MeV, but is expensive in terms of computing time for lower energies. Therefore a lower limit for the stepsize was introduced additionally [36].

4.1.2 Geometry

In GEANT4, the geometry is described and implemented object by object, quite similar to a real construction process. The point to start is the so called **world volume**, an artificial volume which hosts all the others. Into this the required objects are placed, defining shape and material along with other properties.

Defining a **material** can be accomplished in several ways. The most simple one is to take a predefined material from the NIST-database [92]. Alternatively, elements can be built by defining their atomic numbers and specific masses. A specific material can then be created out of these elements, either by declaring the bonding number of the constituent molecules or by defining the mass fraction of each element. The second possibility is useful when the exact molecular composition is not known. Furthermore the density, the state of aggregation and the temperature can be defined.

The next step is to build a **solid volume**, which describes the shape and size of the object. There are over 20 listed solids, e.g. a sphere or a torus, which can be chosen. Their essential quantities, like the size of edges or angles have to be defined. Further changes can be applied by boolean operations, adding or subtracting volumes from each other. A special case are the boundary represented solids (BREPS), which are defined by a description of their boundaries.

After the geometrical definition, a material has to be added (this is mandatory) and a magnetic field, a sensitive detector or a user defined limit can be supplemented to get the **logical volume**. The **physical volume** is an instance of the logical, placed in the so called mother volume translated, rotated or even in multiple copies. This **mother volume** is either the world volume, which hosts the basic parts, or one of its daughters or "granddaughters" (see example in figure 4.1). In this way a hierarchic tree is built that is searched for the next volume a particle traverses. There are several ways to check for forbidden volume overlaps, the most simple one being a flag that generates

output on the overlap-state if switched on for a physical volume. More sophisticated ones are extra programs like DAVID or OLAP, that have graphical tools for investigation.
There are special classes to handle repeated volumes (so called **replicas**), which are better described by the mother volume being divided into multiple identical subvolumes (for example the blue cylinder and its segments ion figure 4.1) and **parametrised volumes**, which are almost independent placements of a volume inside the mother volume. The latter can differ not only in the place, but also in rotation, material and even the size of geometrical dimensions. The user has to define such changes explicitly.
There is another special kind of parametrisation for voxelised geometries in which box-shaped volumes fill a container completely. This is called **G4PhantomParameterisation**. In this case the navigation is simplified, since the navigator can calculate the voxel in which a particle is located by simple arithmetic. Integer division of the current coordinate vector $(\mathrm{x}, \mathrm{y}, \mathrm{z})$ by the voxelsize in the corresponding direction $(\mathrm{xSize}, \mathrm{ySize}, \mathrm{zSize})$ gives a triplet of integer numbers $(\mathrm{nx}, \mathrm{ny}, \mathrm{nz})$, which can be used together with the total number of voxels in the three directions $(\mathrm{xNo}, \mathrm{yNo}, \mathrm{zNo})$ to calculate the copynumber of the voxel, i.e. the linear location in the computer memory:

$$\mathrm{copyNo} = \mathrm{nz} \cdot \mathrm{xNo} \cdot \mathrm{yNo} + \mathrm{nx} \cdot \mathrm{yNo} + \mathrm{ny}$$

With this copynumber, the access to the next voxel is simple and fast, whereas in the more general case, the navigator would have to search all the other daughtervolumes of the relevant volume's mother to find the next voxel, which is a very slow process for a geometry with millions of voxels.
With all these repeated volumes, large and complicated geometries can be built in a simple way, thus saving computing time and memory space.

4.1.3 Physics

In the following section, the physics used in the calculations is described [36]. Special emphasis is put on neutron physics, although many other particles (photons, electrons, secondary ions, etc.) play a role in this context.

In GEANT4 all particles can be transported in silico. The basic principle is always the same: every particle has different interaction processes attached to itself. In each step the SteppingManager asks each of these processes to suggest an interaction length (also the transportation process, which calculates the distance to the next boundary). This is done with the help of random numbers (see section 4.1.6) and the respective interaction cross sections, which are either included in tabulated form (e.g. ENDF/B-VI files) or calculated beforehand out of theoretical models. The process suggesting the shortest steplength is selected as the next process to happen. The particle is transported, the suggested steplength and the process is undertaken (sometimes using further random numbers to calculate the energy and momentum of secondary particles). Some processes are not included in this pattern, for example because there is no spatial translation connected to them. This is e.g. the case for radioactive decay, which is a so called “ProcessAtRest”. Another example are continuous processes like continuous

ion	**G4 process name**	**G4 model name**
proton	G4ProtonInelasticProcess	G4BinaryCascade
deuteron	G4DeuteronInelasticProcess	G4LEDeuteronInelastic
triton	G4TritonInelasticProcess	G4LETritonInelastic
alpha	G4AlphaInelasticProcess	G4LEAlphaInelastic
He3	G4HadronElasticProcess	G4LElastic

Table 4.1: *Special ion processes and models; for all listed ions* `G4hIonisation` *and* `G4HadronElasticProcess` *(model=* `G4LElastic` *) were used in addition.*

energy loss (using a restricted stopping power), which are executed before the discrete ones are dealt with.

Electromagnetic physics

The electromagnetic physics includes interaction processes for photons, electrons and positrons. Defined processes are Compton scattering, photoelectric effect, pair production (which is called gamma conversion) and muon-pair production for photons, ionisation and delta ray production, Bremsstrahlung and positron annihilation for electrons and positrons. For charged particles there is a common multiple scattering process (see below). There are special classes for the low energy range which include Rayleigh scattering and the adaption of the other processes to low energies taking the atomic shell structure into account [36]. For photons, electrons and positrons the low energy extensions [19] were used in the calculations presented here with the default cutoff set to 1mm. In every material, this value is translated into an energy below which continuous slowing down approximation is used.

Hadronic physics

For hadrons the layout is different. Every particle has a cross section data set (sometimes a group of particles shares the same), which is based on parametrised models taken from the GEANT3-GHEISHA package (called low and high energy models), explicit datasets (e.g. ENDF/B-VI for neutrons) or theoretical models (e.g. the Bertini cascade). With this cross section data set the steplength-proposal is done. On the other hand there are models which handle the reaction itself. These two can be used independently, depending on the focus of the calculation.

There are various kinds of physical processes for **charged hadrons**, for example ionisation, elastic and inelastic scattering. Each of them can be represented by different kinds of models, which are valid in different ranges of energies. For instance, in the case of inelastic high energy proton scattering the `G4LEProtonInelastic` process or the Bertini Cascade can be used (the Bertini Cascade for example is valid in the range of ∼100 MeV to some GeV). These models can be arranged in such a way that the physics is described most conveniently in the considered energy range, balancing computing speed and correctness of the result.

G4Hadron∼Process	**energy**	**G4-model**	**G4NeutronHP-dataset**
Elastic	< 4eV	G4NeutronHPThermalScattering	ThermalScatteringData
	< 20 MeV	G4NeutronHPElastic	ElasticData
	> 19 MeV	G4LElastic	–
Inelastic	< 20 MeV	G4NeutronHPInelastic	InelasticData
	> 19 MeV	G4BinaryCascade	–
Fission	< 20 MeV	G4NeutronHPFission	FissionData
	> 19 MeV	G4LFission	–
Capture	< 20 MeV	G4NeutronHPCapture	CaptureData
	> 19 MeV	G4LCapture	–

Table 4.2: *Neutron processes together with the corresponding neutron models and* `G4NeutronHP` *-dataset used for response calculation*

For the calculations for this thesis, all ions were treated with `G4hIonisation`, `G4HadronElasticProcess` and `G4MultipleScattering`, which deal with ionisation, elastic scattering and multiple scattering, respectively. For some ions there are special inelastic processes (see table 4.1). For generic ions (all ions which are not otherwise defined) there is a different ionisation routine, `G4ionIonisation`. The inelastic processes are dealt with by `G4HadronInelasticProcess`, using two cross section data sets: `G4TripathiCrossSection` and `G4IonsShenCrossSection`, and one model: `G4BinaryLightIonReaction`.

For **neutrons**, the ENDF/B-VI files [42] from Los Alamos [20] are selected for the steplength-proposal. These datasets are directly included in GEANT4 in the G4NDL 3.10 library, which is only adapted to another data-pattern more suitable for GEANT4 input (lin-lin-interpolation; [36]). Low energy processes together with the corresponding low energy models (based on the G4NDL 3.10 library) were used to build the neutron physics list. A detailed listing for neutron models and datasets is given in table 4.2.
A special case for neutrons is the low energy thermal scattering. In this thesis this elastic process was relevant for calculations in water and polyethylene because of their large hydrogen content. In the H_2O molecule, the OH-bond can undergo torsional harmonic oscillations (hindered rotations) and internal vibrations at very low energies, whereas in the $(CH_2)_n$ molecule several vibrational modes, depending on the surrounding bonds, occur. Since the vibrations and oscillations are temperature-dependent, the scattering cross section is also depending on temperature. To take this effect into account a special thermal scattering dataset and model has to be included for neutron energies smaller than 4 eV.

Multiple scattering for charged particles

The multiple scattering algorithm for charged particles in GEANT4 was implemented by Urbán based on the Lewis theory [77]. Unlike the Molière formalism which can only give the angular distribution after a step, the Lewis theory also gives the moments of the spatial distribution. Urbán's implementation simulates the scattering and calculates path length corrections and lateral displacement. The algorithm is needed when the comparison of proposed steplengths is done. All physical processes give their proposal in true pathlength t (that is the path length of an actual particle due to physical interactions like multiple scattering), while the limit of the next boundary in the geometry is a geometrical pathlength z (that is the shortest distance between the endpoints of a step, $z \leq t$). So t is transferred to z to select the next kind of interaction (see chapter 4.1.1). Afterwards this transition has to be reversed because the energy loss and scattering computations are done with the true pathlength. The multiple scattering algorithm plays a role again at the final translocation of the particle, where the mean lateral displacement and its correction are determined. Before the translocation a check on the geometrical boundaries ensures that the particle did not cross into the next volume by these corrections. Several step limitations were included to ensure the physical correctness of spatial geometries. Thus, backscattering directly behind a boundary is possible whereas passing through a volume in one step is prohibited. Special focus also lies on the first step of a particle after its creation. Another limit is imposed by the behaviour of the particle near boundaries. The last step in a volume is allowed to be only as large as the mean free path of the elastic scattering of the particle in the relevant material. This last limit is pre-set to be valid for electron and positron tracking, but this, as well as the range of this restriction, can be changed in adaption to the problem investigated.

4.1.4 Book-keeping of results

This section explains how the relevant data is collected and processed in different cases, which can be done in two different classes: in UserSteppingAction or in the sensitive detector.

The UserSteppingAction

In every step, the `G4UserSteppingAction`-routine is called. In this class the user can implement code to extract information on the step depending on self-defined criteria, process and save it. One example is the calculation of the ambient dose equivalent. In this case the deposited energy is read out at every step and divided by the mass of the relevant volume to get the deposited dose. This is then multiplied by the quality factor of the relevant particle at the respective energy to be able to calculate the ambient dose equivalent, which is this quantity $(D \cdot Q)$ summed up over all particles (gamma, electron, neutron, proton, alpha) and steps and finally devided by the total primary neutron flux. The same summation is done with the square of the dose-value $((D \cdot Q)^2)$. This additional value is needed to calculate not only the ambient dose equivalent but also to estimate the corresponding statistical variance at the end of the run (see chapter 4.1.7).

Sensitive Detector

A powerful and sophisticated tool in GEANT4 is the **sensitive detector manager** (`G4SDManager`) which can collect physical interaction data of every step, casting a spotlight on the present situation of the particle and its surroundings, the so called hit (`G4VHit`). The position, time and energy deposition of the step, the momentum and energy of the particle and geometrical information can be checked and collected in a so called hits-map (`G4THitsMap`). An object of the sensitive detector manager class is registered to a logical volume, defining in which part of the geometry the data should be collected. A so called **multifunctional detector** (`G4MultiFunctionalDetector`) is attached to the sensitive detector manager, uniting the different **scorers** which accumulate the specific data. Several different scorers can be attached to one multiple detector, covering the whole range of interesting physical quantities. Some scorers are already predefined in the GEANT4-package, like energy deposition (`G4PSEnergy-Deposit`), dose (`G4PSDoseDeposit`) or flux (`G4PSCellFlux`, `G4PSFlatSurfaceFlux`, etc.), and can be adapted to the particular problem. This was done for example in the case of dose or flux scoring to be able to calculate also the statistical error of the respective parameter (the procedure is the same as in G4UserSteppingAction-routine). The multifunctional detector builds a hits-map for every scorer there is, applying filters if stated. There are particle- (`G4SDParticleFilter`) and particle-with-energy filters (`G4SDParticleWithEnergyFilter`). These filters can be used to save data which are not only particle specific, but also energy discriminating. This was implemented for the flux-scoring, where the flux was scored energy-bin-wise with a predefined energy-grid. In every step the location within the geometry is checked to see if a process belongs to a logical volume with a sensitive detector. If this is the case, the specified data are collected in the hits-map(s). The hits-maps are accessible at the end of the run, giving the possibility to extract necessary information, process it further and export it in a suitable format (see chapter 4.1.7). For parametrised volumes, one hits-map per scorer for all copies of the logical volume is created, which consists of as many entries as there are parametrised volumes. These entries can be accessed separately at the end of the run, simplifying the administration of a large number of scoring volumes.

4.1.5 Primary particles

One of the three mandatory classes in GEANT4 which the user has to define is the generation of primary particles (`G4VUserPrimaryGeneratorAction`). In this class the user can define the type of the primary particle, its starting point (vertex), energy and momentum. The correctness of all quantities has to be assured. The next section shows how this was done in this thesis.

Homogeneous source distribution

In many cases there is a spread out beam which has to be homogeneous over the whole area. For all particles a starting point, the vertex, has to be defined. Assuming this point lies on the $(z = 0)$-plane and that the initial velocity vector of the particle is parallel to the positive z-direction, two possibilities for the beam-shape have to be

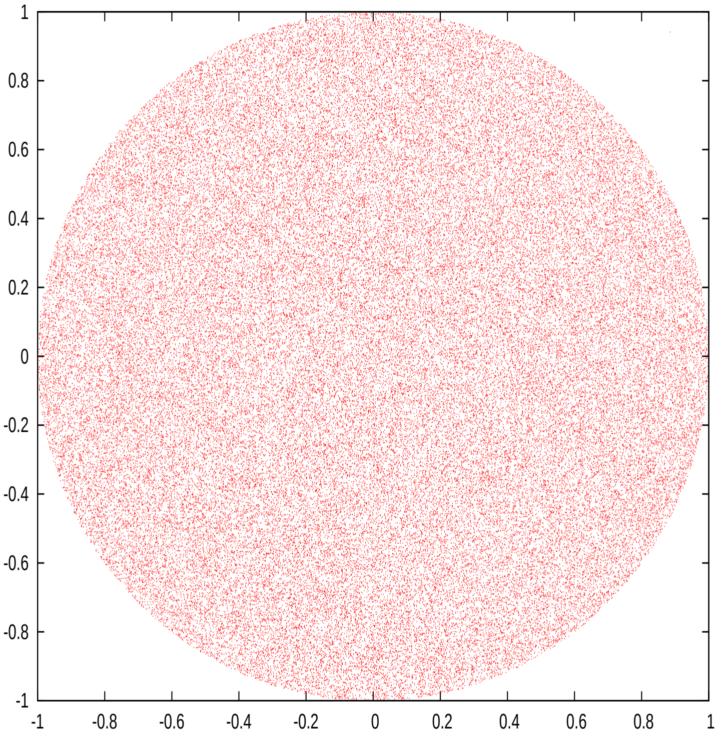

Figure 4.2: *Distribution of primary particles in x-y plane in the case of a homogeneous, circular beam*

considered in this context: a rectangular and a circular beam cross section. In the first case, the x and y coordinate of the vertex are just random numbers ($\eta \in [0, 1]$) shifted by -0.5, multiplied by the length of the beam cross section in x (xlength) and y direction, respectively.

$$x = (\eta - 0.5) \cdot xlength$$

If the beam is not centred, the coordinates are translated afterwards ($x = x - x_{translation}$). In the second case, the radius (r) and the angle (φ) of polar coordinates are sampled randomly (r = beamradius, $\varphi = \kappa$ and random numbers $\eta, \kappa \in [0, 1]$). Then x and y are calculated by taking the sin and cos respectively:

$$x = r\sqrt{\eta} \cdot \cos(2\pi \cdot \varphi)$$

$$y = r\sqrt{\eta} \cdot \sin(2\pi \cdot \varphi)$$

An example of a distribution calculated with this algorithm is shown in figure 4.2.

Simulation of the FRM II neutron and gamma spectra

The calculations in the water- and voxel phantom described later are performed with the input FRM II neutron and gamma flux spectrum. The neutron spectrum displays a distribution which is quite similar to a Watt-spectrum (see chapter 6.5). In order to simulate the spectrum, which is available in an energy-binned form, it is integrated and then normalised to one. The result is a probability distribution between zero and one, corresponding to the different amount of flux in each energy bin.

$$\mathrm{P(E)} \in [0,1[\quad , \quad \textit{discrete}$$

The energy of the primary particle is scored from this distribution with the help of a random number $\kappa \in [0,1[$.

$$\mathrm{P(E)} = \kappa \quad \Rightarrow \quad \mathrm{E} \in [\mathrm{E}^{\mathrm{i}}_{\mathrm{min}}, \mathrm{E}^{\mathrm{i}}_{\mathrm{max}}[$$

Within the bin, the spectrum is assumed to be homogeneous. The energy (E) is sampled randomly between the lower and the upper energy bin border.

$$E = E^i_{min} + \eta \cdot \Delta E^i \quad ; \quad \eta \in [0,1]$$

Conceptionally the same approach was applied to the initial gamma spectrum.

4.1.6 Random number generation

The random number generation is one of the most important parts of the Monte Carlo calculation as millions of good quality random numbers are needed during the simulation. In GEANT4, the `HEPRandom` module of the CLHEP-library is used [37], which is based on an algorithm by James [60]. Like in almost all other Monte Carlo codes, this is a pseudo random number generator which can be initialised e.g. with a time seed, ensuring automatically the independence of different runs.

There are several requirements for a good pseudo random number generator. The most important one is a good randomness, which is only fulfilled up to a certain number of random numbers. A good generator has a long period before it repeats itself. To work with a code using these numbers, it is necessary that the sequence of random numbers can be repeated, not only from the beginning, but also by saving some information and starting in the middle of a complicated simulation. A very important property is the ability to produce long disjoint subsequences that enable the user to make independent calculations which can be combined afterwards. The portability of the generator to different computer systems in order to exactly reproduce the results is convenient, but not always possible. Formerly, the efficiency of the algorithm was a very important point, but today, the function call for the random number is often the most time-consuming step. This can only be sped up when not a single number is returned, but a whole array.

Traditionally, pseudo random number algorithms were based on a single integer seed (32 bit), for example the multiplicative linear congruential generator (MLCG), which was first used in 1948 by Lehmer [73], which calculates the next random number $\mathrm{s_{i+1}}$ out of its predecessor $\mathrm{s_i}$:

$$\mathrm{s_{i+1}} = (\mathrm{a} \cdot \mathrm{s_i} + \mathrm{c}) \mod \mathrm{m}$$

with a, c and m integer constants to be carefully chosen in order to get good numbers. Two bits are usually lost to the sign of the number, so the maximum period is 2^{30} or 10^9 at most. Marsaglia [83] discovered the main weakness of this algorithm: d-tuples of the generated numbers form a lattice structure in a d-dimensional space in such a

way that they all lie on a certain limited number of hyperplanes, which is not the case for real independent random numbers.
Other simple generators use the Fibonacci algorithm [69]:

$$\mathrm{s_i = (s_{i-p} \odot s_{i-q}) \quad mod\ m}$$

where $p > q$ are integers giving the "lag" in the Fibonacci numbers and $\odot$ is an addition or subtraction.
These simple generators can be improved by bit-mixing for example, where two independent algorithms are combined to give longer periods. A new sequence of random numbers r is calculated from the two original sequences s and t by:

$$\mathrm{r_i = s_i \odot t_i}$$

with $\odot$ is again an addition or subtraction, followed by modulo 1. Newer algorithms are so called very long period (VLP) methods, which are using a table of a large number of random seed (produced with one simple generator) and a set of indices (produced with the help of another simple generator), which point to seeds in the table. The final random number is calculated from the indexed seeds and all used numbers are updated.
An example of such a generator is used in GEANT4: `RANMAR`, which was first described by Marsagli, Zaman and Tsang [84]. It consists of a Fibonacci generator with p=97 and q=33 together with $\odot = \{(\text{subtraction} + 1) \mod 1\}$ as operation. This is combined with an arithmetic sequence generator (again with subtraction as operation), all are `FORTRAN` codes. `RANMAR` provides a good distribution together with an incredibly long period of $2^{144} \approx 2 \cdot 10^{43}$. If disjoint subsequences are needed, $9 \cdot 10^8$ different ones with 10^{30} average length each can be generated. The random numbers are bit-identical on different computer systems, but very much memory (102 full words) is necessary to reproduce an arbitrary state of the random machine. Because internally a floating point representation is used, the random number generation is very fast, about a few μs per 1000 numbers (1.5/3.4 μs on an IBM 3090), depending on how many are called at once (the call of an array of 1000 numbers is faster than 1000 calls of a single number).
In GEANT4 other algorithms, e.g. `RANECU` by l'Ecuyer [78] can be used. Because these have no direct advantage needed in the course of this thesis, only HepJamesRandom was used.

4.1.7 Output of results

The output of GEANT4 is user-dependant. At the end of a run, which is finished when all secondary particle tracks, created by all predefined primaries, are terminated, a user-defined class (`G4RunAction`) enables the output of calculated values. The results from `G4UserSteppingAction` and from the `G4THitsMaps` (see section 4.1.4) can be accessed, processed and written in the appropriate format into a file. For all calculations the output-values (like dose or flux) were normalised to a standard input flux. This was defined as one primary particle per cross section of the beam. For a calculated dose

D, a cross section of the beam A and N primary particles the normalised dose is:

$$\frac{D}{\Phi} = \frac{D \cdot A}{N}$$

In the case of the dose calculations inside the water phantom, this quantity can be multiplied by the measured total neutron flux to get the real deposited dose (which can also be measured with ionisation chambers, see chapter 7). To calculate the variance of a certain result, for example the dose D, not only the sum of the deposited dose $D = \sum_i D_i$ (for all interactions i) but also the sum of its squares $D_2 = \sum_i (D_i)^2$ was saved. Together with the number of histories N (which is in all calculations treated here the same as the number of primary particles) the variance (Var) can be calculated in the following way:

$$\mathrm{Var} = \sqrt{\frac{\mathrm{D}_2}{\mathrm{D} \cdot \mathrm{D}} - \frac{1}{\mathrm{N}}}$$

Afterwards, this quantity is converted to a relative variance by division with the corresponding dose or flux value (here: $\mathrm{Var}_{\mathrm{rel}} = \mathrm{Var}/\mathrm{D}$).
Other data-processing is the format setting of the voxel phantom-dose matrix, the calculation of the dose-volume-histogram or of the Bonner sphere response (see chapter 6.4). The results are then written in ASCII-code into a file and from this histograms in various styles and shapes can be produced with GNUPLOT [3].

4.1.8 Parallelisation of calculations

In order to get acceptable statistics even with the small phantom voxel sizes, very many primary particles (or histories) have to be started: in the case of the voxel phantom, one million primary neutrons per square centimetre. The dose uncertainty in the beam is then below 3% for depths smaller than 4 cm and rising slowly with depth. But this calculation would take more than 16 days on one single PC. Therefore a simple parallelisation is performed using MPI (Message Passing Interface, [90]), a programming standard which can be used to exchange messages between different, parallelised computers. The algorithm used was presented by Sutherland [116]. The primary particles are divided between the available computer nodes and simulated independently. At the end of the run, the results of the different calculations are summed at the output node and can be processed further if necessary. It should be mentioned that for the parallelisation to work, each node must be initialised with a different random number to ensure the independence of the results. The algorithm works very well and the time scales linearly with the number of nodes [116]. Furthermore, this speed-up has no upper bound for a reasonable number of nodes, because the traffic between the nodes during the calculation is extremely small. This means that the calculations can be accelerated to the desired degree by using an approbriate number of nodes.

4.2 Geometry of the voxel phantom

A voxel is a small cuboid used to discretize and describe the image of an object (e.g. a person) in three dimensions in analogy to the pixel in two dimensions. A voxel phantom

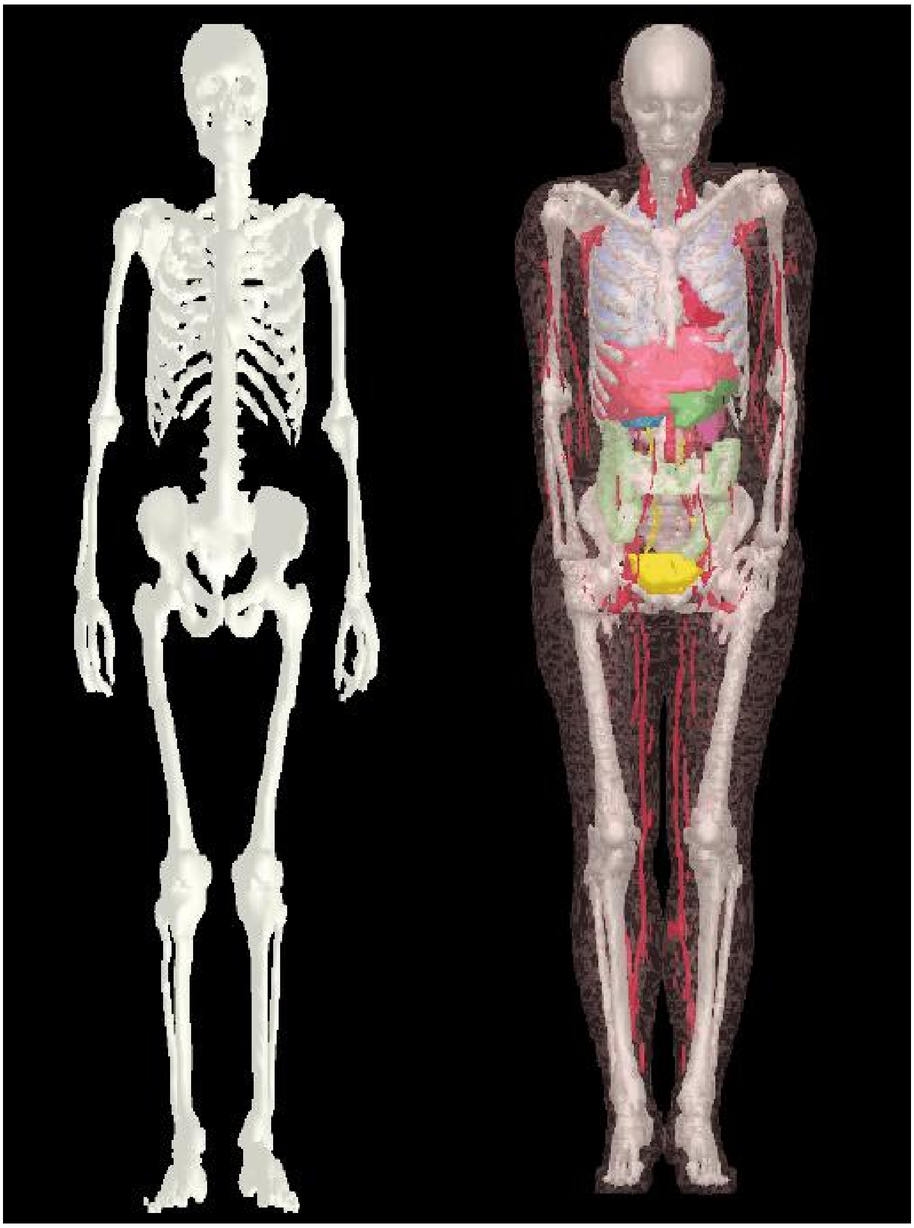

Figure 4.3: *Picture of reference voxel phantoms [132]:*
left*: skeleton view of Reference Male;*
right*: half-transparent view of Reference Female with organs depicted in different colours*

or voxel model is the voxel-representation of a person in a computer, consisting e.g. of one organ-ID for every voxel. In radiation protection, voxel phantoms are used e.g. for dose and risk assessment calculations. For this purpose, reference phantoms are under construction which are adapted to the ICRP 89-standards of weight and size for male and female [47]. For the dose calculations of this work one of these voxel phantoms (REGINA,[107]), which has been developed in the same institute, was used. Generally, it is possible to include real patient data in the same way as the voxel model if a fast and automatic segmentation code will be developed.

4.2.1 HMGU-voxel model

The voxel phantom was build by Zankl et al. [107] using CT-scans of real persons. The Hounsfield numbers of the CT-slices were translated to 141 organ-IDs (see table G.2) each referring to a voxel of $1.775 \cdot 1.775 \cdot 4.84\,\mathrm{mm}^3$ size, with the long side of the voxel going in the voxel phantom-axis direction. There are 299 columns, 137 rows and 337 slices. It represents an idealised female of 163 cm height and 60 kg weight. Starting from the real CT of a woman (Laura: 167 cm height, 59 kg), the size, position and sometimes material of a voxel was changed to fulfil the requirements of ICRP 89 [47], using anatomical books for guidance. In this way a Reference Female REGINA (and also a Reference Male REX) was constructed which will be adopted by the ICRP as standard humans in the near future. A skeleton view of Reference Male and a transparent view of the Reference Female is depicted in figure 4.3.

4.2.2 Voxel phantom representation within GEANT4

The voxel phantom REGINA was used as a first “patient” for the dose calculations with GEANT4. Because the intended application of the FRM II neutron beam is limited to the head and neck region for the moment, only the upper quarter of the voxel phantom was included in the calculations with 87 slices. Two ways to implement the voxel phantom into GEANT4 were tested. The first was using parametrised volumes and placing only those which are filled with tissue, omitting surrounding air. This is very RAM-economic (3 887 730 voxels compared to 14 255 124 in the original file. This is less than 30% of the memory needed for the whole phantom), but not very fast in the calculation. The normal way of findinf the next voxel has then to be used which searches in all voxels for the next one when a particle is at a boundary. The alternative way was to use the fast phantom parameterisation (see section 4.1.2), which places all voxels but calculates the present position using the information that all voxels are arranged in a rectangular grid. Therefore, this algorithm is much faster.

The material of the voxel at (x,y,z)-position is set according to the number given in the phantom’s datafile. In the process, the 142 organ IDs are projected onto 30 different materials which are then used in the calculations (see table G.1 for details on the atomic composition and table G.2 for organ to material conversion).

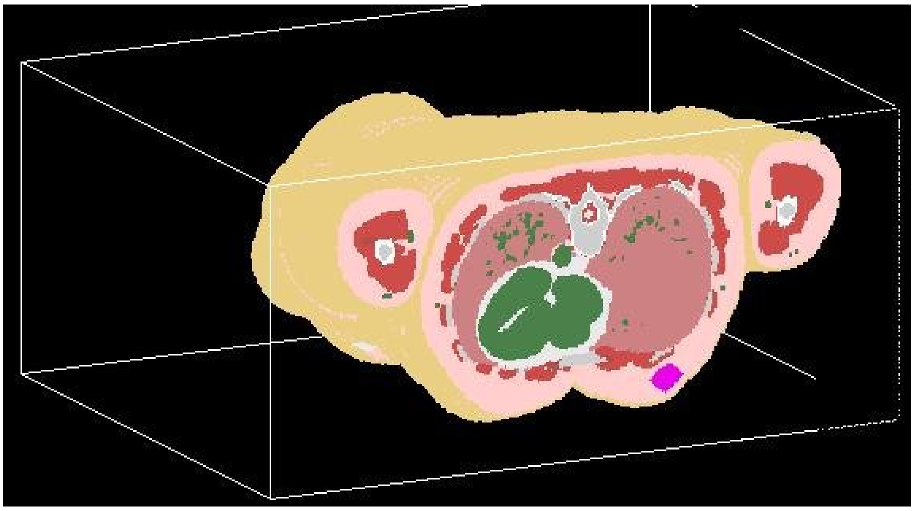

Figure 4.4: *Picture of the voxel phantom in* GEANT4 *used in this thesis; organs in different colours*

CHAPTER

5

Validation of GEANT4 radiation transport calculations

The Monte Carlo program GEANT4 can transport all charged and uncharged particles in matter. In chapter 4.1 the basics of the geometry and physics implementation were explained. So far, the main area of application were high energy hadron physics for the LHC and other accelerators at CERN [44, 74]. Only scarce information about neutron transport in the low energy regions and for medical application is available. Therefore, the neutron transport and dose calculations had to be thoroughly tested in the course of this thesis by comparing neutron fluxes and neutron doses calculated with GEANT4 with those published by the ICRU 57 [54] and calculated with MCNP (Mares/Leuthold, priv com. and [76]) in different geometries. The next chapters describe the calculations and results obtained for the ambient dose equivalent, a quantity used in radiation protection (see appendix A.3) and for a set of Bonner sphere detectors. The calculated response matrix was later used for unfolding the neutron spectrum at the FRM II. By comparing the calculated ambient doses with published data, not only the dose calculation was tested for GEANT4 but a way to implement the use of weighting functions applied to absorbed dose values was demonstrated and verified.

5.1 Ambient Dose equivalent

The ambient dose equivalent (definition see A.3) is a weighted radiation dose, depending both on the particle type which deposits the energy and on its kinetic energy. This is taken into account by the quality factor (definition see A.5) which connects the ambient dose and the ambient dose equivalent. Both the ambient dose equivalent and

the quality factor are thoroughly described and analysed in ICRU 57 [54].
In order to test the usefulness of the GEANT4 code for neutron calculations, the ambient dose equivalent in the ICRU sphere was calculated in the present work for photons and neutrons including the quality factor Q from ICRP 60 [46]. The results of the GEANT4 calculations are compared to those given in ICRU 57 that are based on MCNP calculations performed by various laboratories [113, 76].

5.1.1 Geometry of the ambient dose equivalent sphere

According to ICRU 57 the ambient dose equivalent is to be calculated in 1 cm depth of a sphere with radius 15 cm composed out of tissue equivalent (TE) material. This was represented in GEANT4 by placing a sphere of TE-Material (see table 5.1.1) with 30 cm diameter inside the world volume (which was filled with “vacuum” of density 10^{-25}g/cm^3). To score the ambient dose equivalent, a small tube (10 mm diameter, 2 mm thickness) out of the same material (TE) is placed in 1 cm depth of the sphere, the cross section facing the incoming beam. This beam illuminates the whole sphere homogeneously, parallel and in the direction of the connecting line between the scorer and the centre of the sphere (see figure 5.1).

atomic composition *	**physical quantities**
10.1% H	temperature = 300K
11.1% C	state of aggregation = solid (kStateSolid)
2.6% N	density = 1.0 g/cm^3
76.2% O	for energy loss purposes: ChemicalFormular = ”H_2O”

Table 5.1: *Specification of tissue equivalent (TE) material in* GEANT4*;*
**all with natural composition of isotopes, specifications in weight percent*

5.1.2 Calculation of the flux distribution and comparison with MCNP results

The basic quantity to be compared between the two neutron transport calculations is the neutron flux inside a defined volume. When comparing flux, mistakes in the geometry, material buildup or physics can usually be detected.
The neutron flux inside the dose-scorer was also calculated with MCNP in the course of the ambient dose equivalent calculations for the ICRU-report [54]. For the present comparison, the energy-binning-pattern from these MCNP calculations was adapted in GEANT4 to eliminate discrepancies induced by different binning. In each energy bin, the neutron flux between the upper- and lower bin-border was accumulated with a GEANT4-CellFlux-scorer (description see section 4.1.4). Overall, the agreement between the GEANT4 calculation and those done by MCNP was reasonable (see figure 5.2).

In GEANT4 versions earlier than 8.2 there was no way to include thermal scattering for

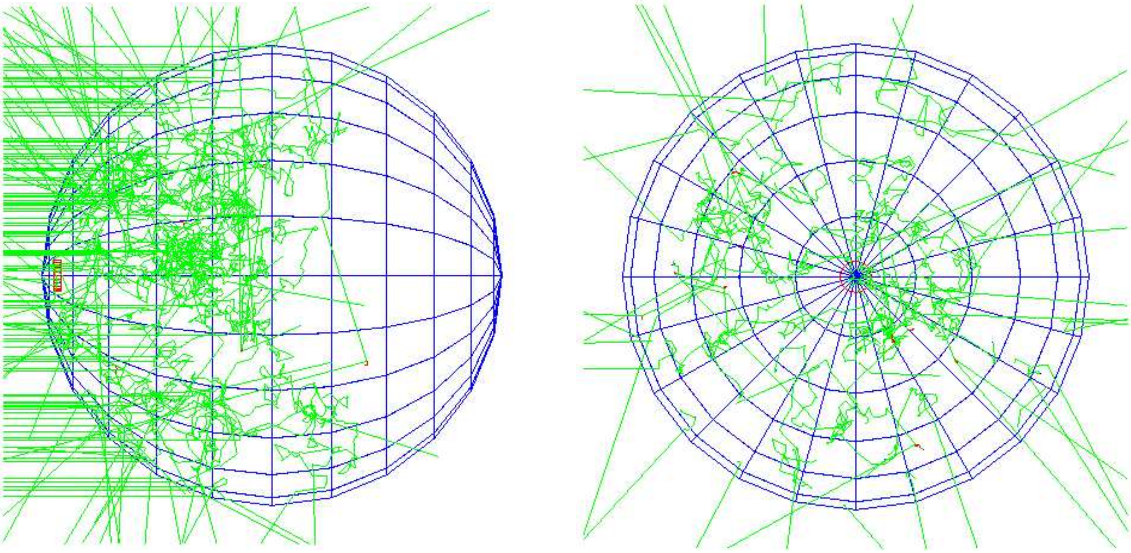

Figure 5.1: *Fifty 10 keV-neutrons incident on the ICRU-sphere; in red: magnified scorer (20 mm · 5 mm);* ***left:*** *lateral view, incoming beam from the left side;* ***right:*** *beam's eye view*

neutrons according to the S(α, β)-matrix (see chapter B.2.2). Therefore the molecular properties of the material for thermal elastic scattering below 4 eV were not taken into account. This is clearly visible to lead to wrong predictions of a decreased flux at very low energies (see green data points in figure 5.2). In version 4.8.2, thermal scattering for neutrons can be included and the agreement for low energies is much better now, as can be seen in figure 5.2 below 1 eV (blue data points).

5.1.3 Calculation of the ambient dose equivalent

The ambient dose equivalent per unit fluence for of photons, electrons and neutrons is listed in ICRU 57 for a wide range of energies (photons: 10 keV − 10 MeV, neutrons: 1 meV − 20 MeV). For the present computations, the ambient dose equivalent for photons and the ambient dose and ambient dose equivalent for neutrons were also calculated with GEANT4 for validation studies.

Ambient dose equivalent per unit fluence for photons

First, the ambient dose equivalent problem was tackled by taking photons as primary particles. The quality factor of photons and electrons is defined to be equal to one for all photon energies [54]. Photon physics (as simulated by GEANT4) has already been thoroughly tested, for example by Poon and Verhaegen [102], so the primary focus was on testing the geometry and individual installation.

The results of the GEANT4 calculations for photons over the whole energy range are shown in a double logarithmic plot in figure 5.3. Agreement for energies below 2 MeV is very good. For higher photon energies, the geometry described in ICRU 57 leads to a levelling out of the dose equivalent. This is due to the buildup effect near surfaces of

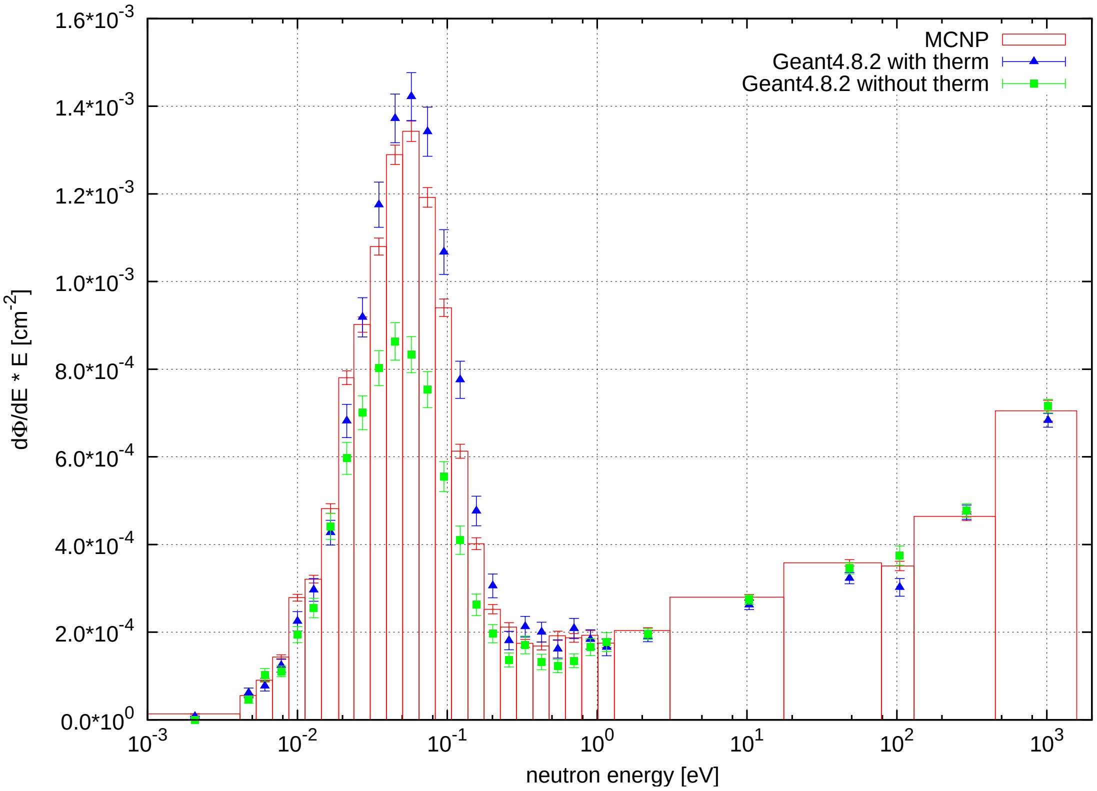

Figure 5.2: *Neutron flux of 1 keV primary neutrons inside the 2 mm thick scorer placed in 1cm depth of the 30 cm PE sphere; comparison between* GEANT4 *(this work) and* MCNP *calculations (**red**; V. Mares, HMGU-ISS, priv. com.); **blue triangles**:* GEANT4 *calculations including thermal upscattering; **green boxes**:* GEANT4 *calculations without thermal upscattering.*

materials with different electron densities (changing from a thinner (air/vacuum) to a denser material), like in this case from vacuum to TE-matter. Secondary electron equilibrium is not achieved near surfaces because there are more electrons leaving a small test volume inside the material than entering the volume from upstream neighbouring volumes. This leads to an initial increase in dose with depth close to the surface followed by the usual decrease. The higher the photon energy, the higher is the energy of the secondary electrons and the deeper these electrons penetrate. Therefore, the maximum of the deposited dose is reached in greater depth for higher primary photon energies. Looking at a particular depth (for example 1 cm, as is the case for the H*(10) calculation in the ICRU sphere) and varying the energy of the photons, leads to a shallow increase and then a decline of the dose deposited there with increasing photon energy. In ICRU 57 the given photon ambient dose equivalent data per unit fluence (for photons the ambient dose equivalent is equal to the ambient dose) increase for all photon energies higher than 100 keV, which is not consistent with the theoretical background described above. The given development would imply that there is some kind of buildup material in front of the sphere, for example an air column, which has a thickness varying with the primary energy of the photons. This geometry is clearly dif-

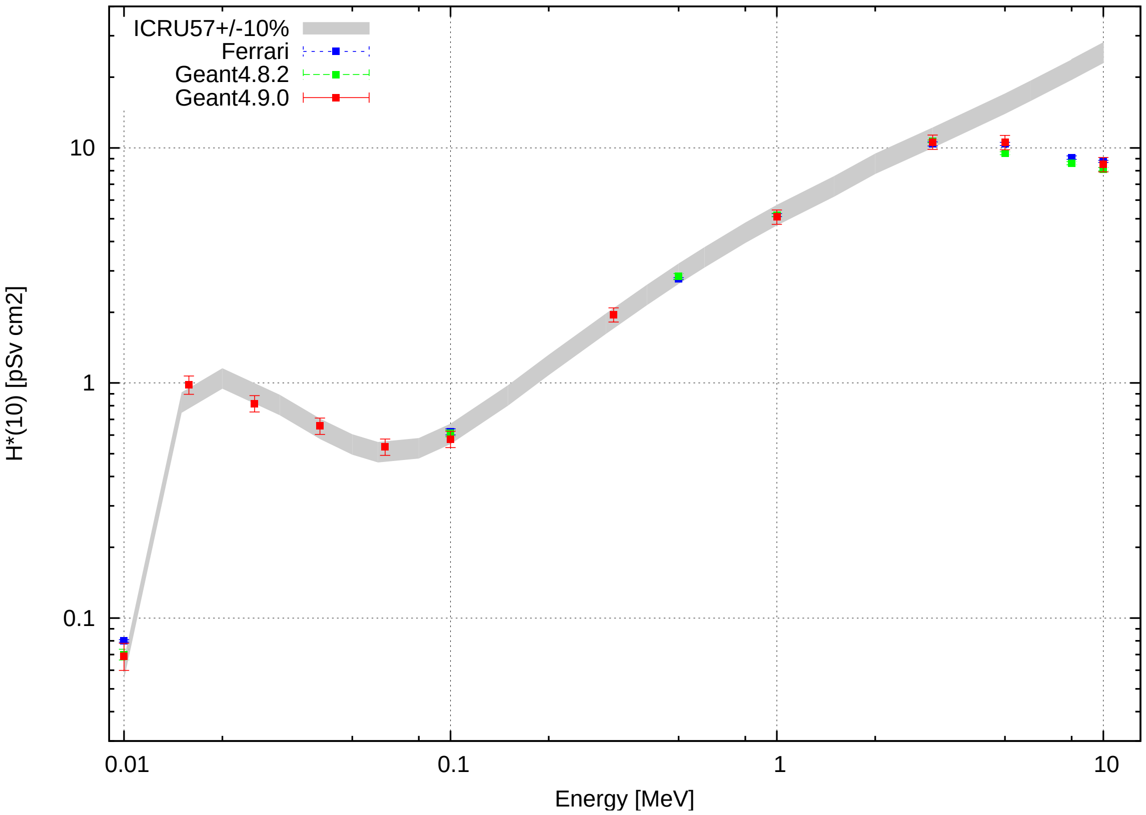

Figure 5.3: *Photon ambient dose equivalent calculated with* GEANT4 *(red: version 4.9.0, green: version 4.8.2) in comparison to data from* ICRU 57 *(in gray with* ±10% *uncertainty margin arising from variance between calculations [54]) and Ferrari [29, 30] (blue)*

ferent to the one described in the report (ICRU-sphere in vacuum). Therefore, values for the ambient dose equivalent above 2 MeV are not consistent with those calculated in the present work with GEANT4. Ferrari et al. [30] discussed this problem in detail and also points out that including a buildup material depending on the primary energy of the photons would destroy the required additivity of the ambient dose equivalent for which the geometry has to be the same for all energies. Evidently, the ICRU quantity should only be used for photons below 2 MeV.

Ferrari et al. also calculated the ambient dose equivalent over the whole energy range with the geometry described in ICRU 57, which was also used for the GEANT4 calculation of the present work. The results show good agreement with ICRU 57 data at lower energies, [29, 30]. At higher energies his data exhibits the expected decline. The results of the GEANT4-calculations are in accordance with the Ferrari-data also for higher energies (see figure 5.3, blue points for Ferrari and red/green points for GEANT4).

The peak at 25 keV is due to the change of the leading photon interaction from photo-effect to Compton scattering where only a fraction of the photon energy is transferred to the electron (the change of interaction can be seen in figure B.1). This demonstrates

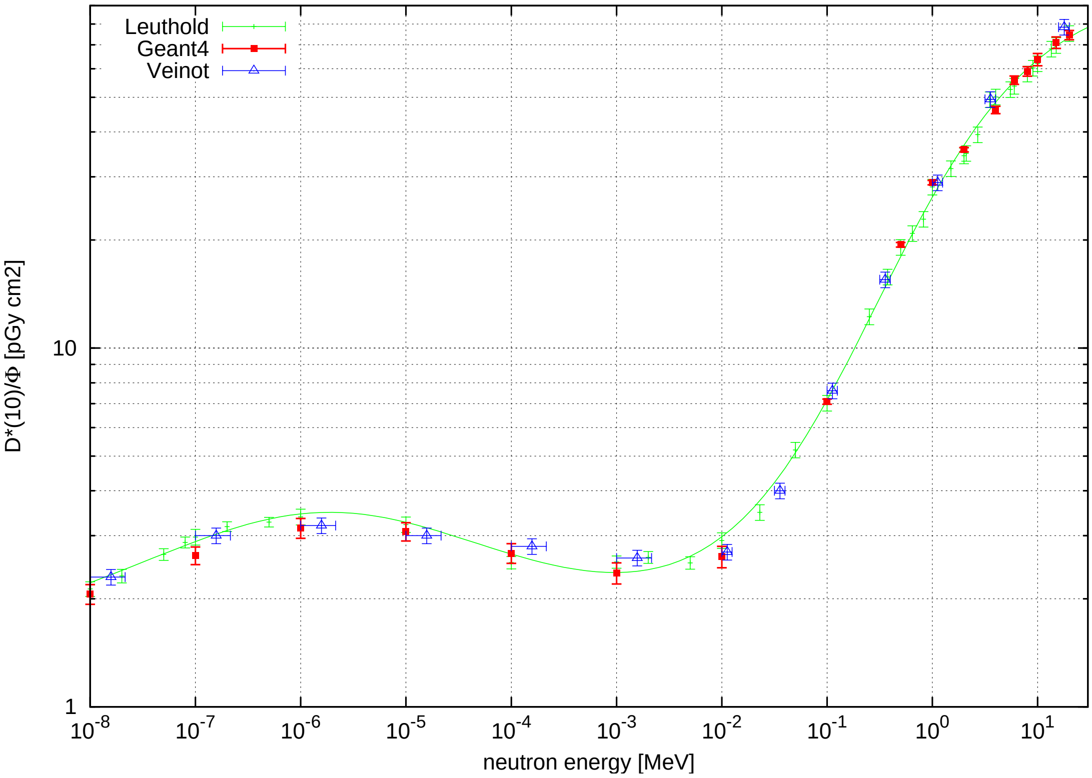

Figure 5.4: *Comparison of different calculations for the dose equivalent in 1 cm depth of the 30 cm* ICRU *sphere:* GEANT4 *(this work, red points), Leuthold (green points with spline interpolation,[76]) and Veinot (blue points, [123])*

that the geometry and material setting as well as the photon physics used in this thesis are correctly implemented in GEANT4.

Ambient dose and ambient dose equivalent of neutrons

The ambient dose for neutrons as primary field particles was also calculated with GEANT4 for validation tests.

This quantity is defined as the absorbed dose deposited by a parallel and aligned beam of neutrons in 1 cm depth of the ICRU-sphere divided by the flux of the incoming neutrons (see chapter A.3). Compared to calculated data by Leuthold et al. [76] and by Veinot [123] a remarkably good agreement can be obtained over the whole energy region (see figure 5.4).

The ambient dose equivalent was then calculated using the LET-relationships from ICRU 49 (protons and alphas [53]) and ICRU 73 (heavier ions: C, N and O [58]). With the option "multiple scattering" switched on, in the relevant energy range (lower than 15 MeV), the whole energy of a recoil or nuclear reaction ion is deposited in one step and not in many small steps as is the case with single step tracking (which is computationally much slower). This is sufficient as the range of these charged particles is less than 1 mm, which is the small compared to the resolution of the voxel. Therefore,

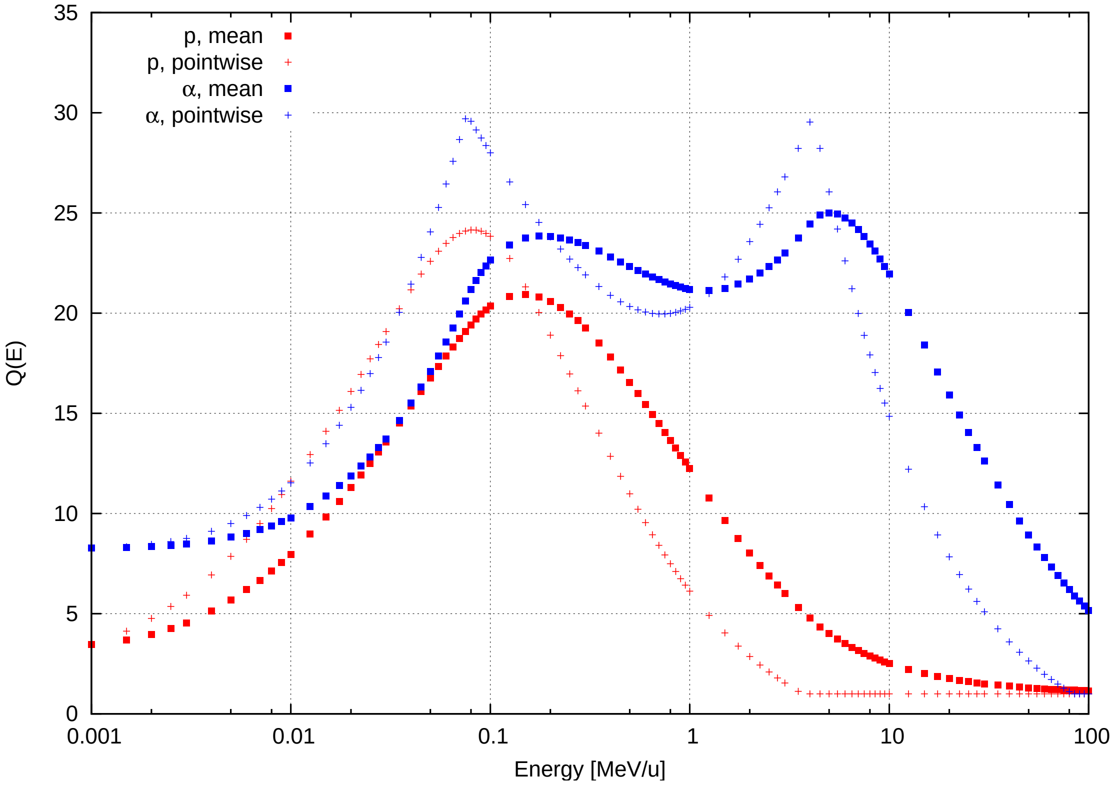

Figure 5.5: *Comparison of the pointwise (differential) and the mean (integrated) quality factor Q for protons (red cross and square) and alpha (blue cross and square)*

the quality factor Q-LET-dependency (see figure A.2), which is listed in ICRU 57, cannot be used because the LET is varying strongly during the slowing down of an ion. Thus, an averaged quantity of the quality factor had to be found, which can be applied in this case. For this purpose, a mean quality factor Q_{mean} was defined by averaging Q over the slowing down of an ion. For this, the Q(LET)-LET(E)-dependency was integrated from $\mathrm{E_{start}}$ to E=0 over all energies (P. Leuthold, HMGU-ISS, priv.com.).

$$Q_{mean}(E_{start}) = \frac{\int_{E_{start}}^{0} Q(LET(E))dE}{\int_{E_{start}}^{0} dE}$$

The difference between the pointwise and the mean Q_{mean} is shown in figure 5.5 for protons (red crosses and boxes) and alpha-particles (blue crosses and boxes). A shift to higher energies as well as a decrease of the maximum of the Q values can be seen for both protons and alphas.

Including this mean quality factor in the SteppingAction routine, the ambient dose equivalent H*(10) was calculated using the following equation (see definition of H*(10) in appendix A.3):

$$H^{*}(10) = \sum_{particles+steps} Q_{mean}(E_{start}) \cdot D$$

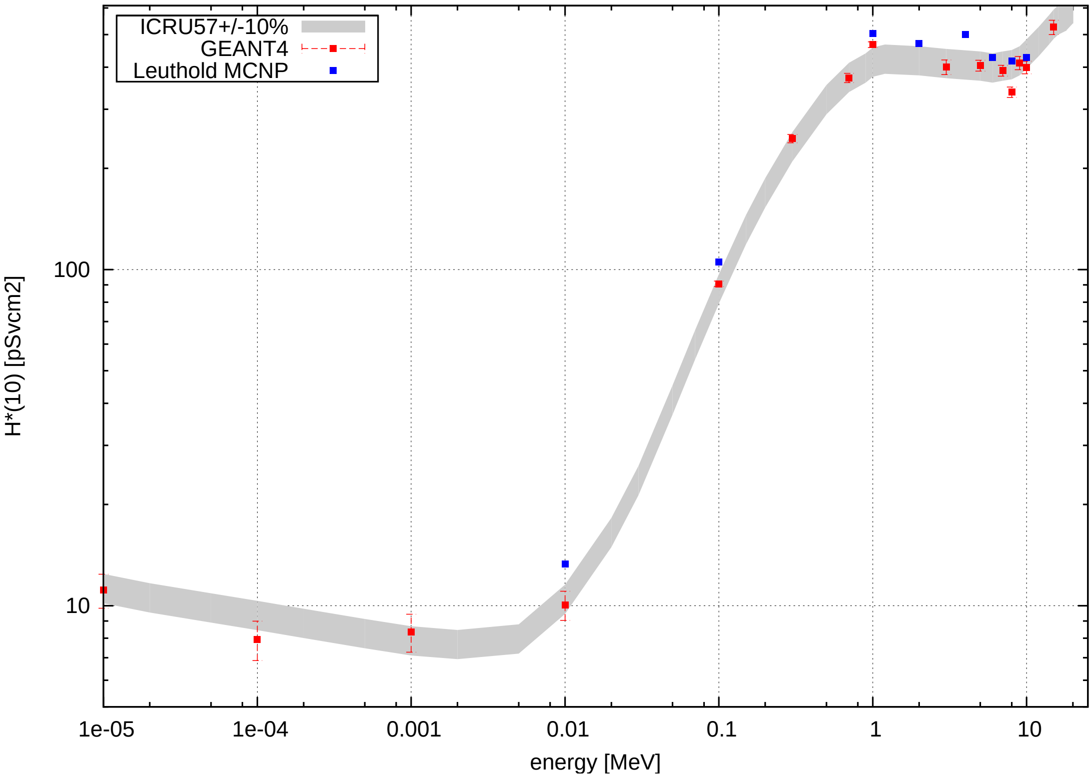

Figure 5.6: *Comparison of different calculations for the ambient dose equivalent in 1 cm depth in the* ICRU *sphere:* GEANT4 *(this work)*, ICRU *(with 10% uncertainty arising from variance between different calculations[54]) and Leuthold [76]*

where $Q_{mean}(E_{start})$ is this mean quality factor of the particle with starting energy E_{start} and D is the dose deposited by the particle in the relevant step (for ions $D = E_{start}/m$ with m being the mass of the scoring-tube). In figure 5.6 one can see the very good agreement of the GEANT4 calculation of the present work with the ICRU- as well as with the Leuthold-data [76] over the whole energy range.

5.1.4 Conclusions

For the first time, dose calculations with GEANT4 were performed for photons and neutrons below 20 MeV. The moderated neutron flux, photon ambient dose equivalent as well as the neutron ambient dose and ambient dose equivalent were calculated and good agreement with published data was found [32]. This verifies that GEANT4 is now apt to calculate neutron doses correctly also for low energy neutrons in the case of the used physic list.

In addition, it demonstrates that in GEANT4, the use of a weighting function is possible, e.g. to convert dose to any weighted dose. See for example chapter 7.2.4 , were biological weighting functions are introduced to convert absorbed dose to weighted dose in a voxel phantom.

5.2 Calculation of response functions for a Bonner sphere neutron spectrometer

The next step in the verification process was the calculation of a Bonner sphere response function and its comparison to data calculated with MCNP (V. Mares, HMGU-ISS, priv. com.). A Bonner sphere spectrometer system consists of several moderating polyethylene (PE) spheres of different diameters. Inside the spheres there is some kind of thermal neutron detector to measure thermal neutron flux, e.g. a gold foil. The simulated detector response of all possible primary energies is called a response function of the sphere. The calculation of the response functions for the set of Bonner spheres used at the FRM II was carried out with GEANT4 (see chapter 6.4), using the physic list described in chapter 4.1.3, that was also used for the ambient dose equivalent problem (see chapter 5.1). The results for the 6 inch sphere with the 23 μm gold foil used at the measurements and with a 2 mm gold foil as extreme scenario were compared to MCNP calculation (Mares, priv. com.) to verify the calculation process.

5.2.1 Geometry implementation

For the verification calculations two different target geometries were simulated in GEANT4. The first represents an extreme case for neutron flux absorption by a measurement device: a 2 mm thick gold foil. This gold foil had a diameter of 15 mm which fitted exactly into a cadmium tin with inner diameter 15 mm and an outer diameter of 16 mm. Furthermore, the tin had an inner height of 2 mm and an outer one of 3 mm, resulting in 0.5 mm Cd around the gold foil. This tin was placed in the middle of a 6” PE sphere ($\rho = 0.92\,\mathrm{g/cm^3}$).

The second geometry mirrors the exact geometry of the measuring system at the FRM II. There is an outer white PE sphere with density $\rho = 0.95\,\mathrm{g/cm^3}$ and radius 6” and an inner black sphere with $\rho = 0.96\,\mathrm{g/cm^3}$ and radius 1.3”. The gold foil was only 23 μm thick (for detailed description of the geometry see figure 6.3 and chapter 6.3.1). In both cases, the material atomic composition of PE was implemented according to table 5.2 with the densities given above.

The macroscopic thermal neutron absorption cross section for gold ($5.89\,\mathrm{cm^{-1}}$) is larger than that of ^{3}He ($0.23\,\mathrm{cm^{-1}}$). However, given the actual sizes of the gold foils used and that of a typical ^{3}He detector, the number of nuclear reactions induced by thermal neutrons (^{197}Au(n, γ)^{198}Au in the gold foil and ^{3}He(n, p)^{3}H in the ^{3}He-detector)

atomic composition*	physical quantities	
ratio of elements: H: 2 C: 1	temperature = 300K state of aggregation = solid (kStateSolid)	for energy loss purposes: ChemicalFormular = “(C_2H_4)_N_Polyethylene”

Table 5.2: *Specification of PE in* GEANT4*; hydrogen in PE* (TS_H_of_Polyethylene) *was used for thermal scattering; *all with natural composition of isotopes*

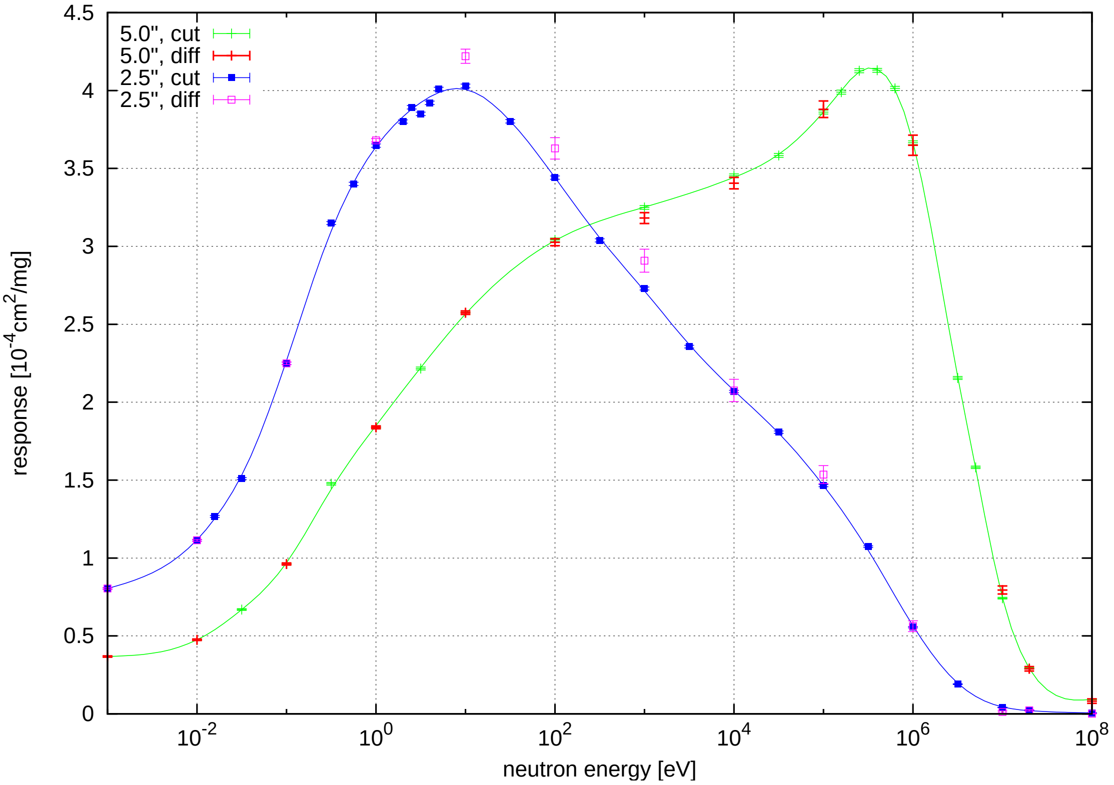

Figure 5.7: *Comparison of two methods to calculate the response: cutting the neutron flux below 0.251 eV (cut) or subtracting the neutron flux with and without Cd (diff) before folding with the cross section for two different sphere sizes: 2.5" and 5"*

is about a factor of 430 smaller in the gold foils compared to that in the ^{3}He-detector. Therefore, the gold foil activation cannot be simulated in silico directly in a reasonable amount of time, like it is done for the latter [82]. Instead, the neutron flux inside the Cd-tin was simulated, using the `G4SDParticleWithEnergyFilter` and the `CellFlux` scorer (for a detailed description of both, see chapter 4.1.4). Afterwards, this flux was folded with the capture cross section taken from G4ENDL 3.10 (which is the same as ENDF/B-VI [79]) in order to compute the number of activated ^{198}Au-atoms.
For the second geometry, Cd was not included in the calculation directly, but the thermal flux was determined by cutting the neutron flux spectrum at the right bin (below 0.251001 eV). The correctness of this approach was tested in the case of the 2.5" and the 5.5" sphere (see figure 5.7). The difference between the two approaches turned out to be less than 6%. This corresponds to a much lower difference when both methods are used to calculate the activation of a gold foil in a real neutron field, spanning the whole energy range.

5.2.2 Re-binning of cross sections

The response of the gold foil was calculated by multiplying the scored flux with the capture cross section of gold (^{198}Au). Therefore, the capture cross section and the neu-

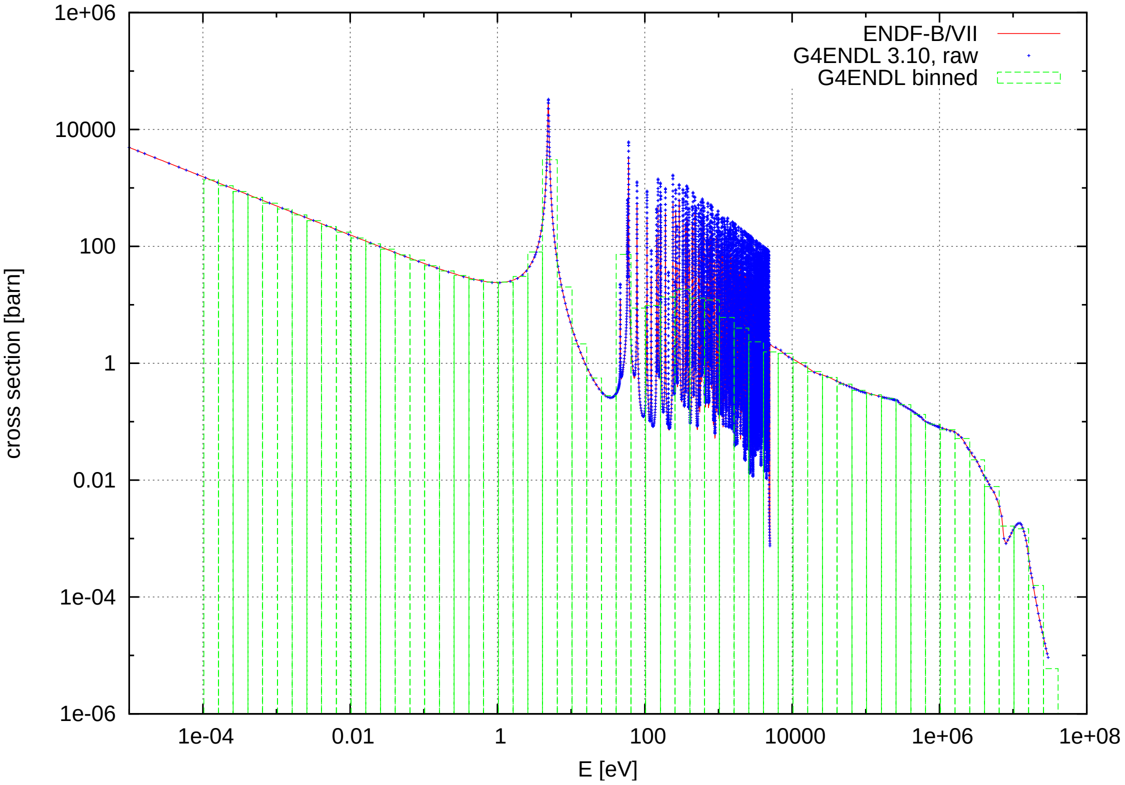

Figure 5.8: *Gold* (^{197}Au) *neutron capture cross section from ENDF/B-VII, pointwise (red, [79]),* G4ENDL 3.10 *pointwise (blue) and in the used bin-structure(green, with assumption of undisturbed flux (see text) using the CONBOLZ code (Rühm, priv. com.))*

tron flux at the place of the gold foil had to be in the same energy bin structure. For the flux calculations the chosen bin structure was 5 bins per decade from 0.100001 meV to 100.001 MeV. The little shift to higher energies was chosen to be able to compare the flux calculations with MCNP results, where the upper bin-border is always included and the lower excluded, which is just the opposite as in GEANT4. Another difference between the two codes was not accounted for: In MCNP, all particles with energy higher than the highest bin are added to this highest bin (the same is true for the lowest bin and particles with smaller energies), which is not the case in GEANT4 where these particles are discarded. However, this difference was not critical, because there are only few particles with such low energies and none with higher energies than the maximum bin, there being no upwards scattering at such high energies.

The gold capture cross section of Los Alamos [79] are given pointwise with a predefined interpolation pattern (log-lin and log-log), which was transferred in the GEANT4 neutron data library G4ENDL to linear-linear interpolation over the whole energy range. This G4ENDL capture cross section (σ) was re-binned into the energy binning (E_k) of the neutron fluence (ϕ) using the CONBOLZ code (Rühm, priv. com.; see appendix D and figure 5.8). In this way, the cross section σ_i^* in the new energy-binning [E_i,E_{i+1}] can be calculated from the point cross section $\sigma(E_k)$ and the corresponding

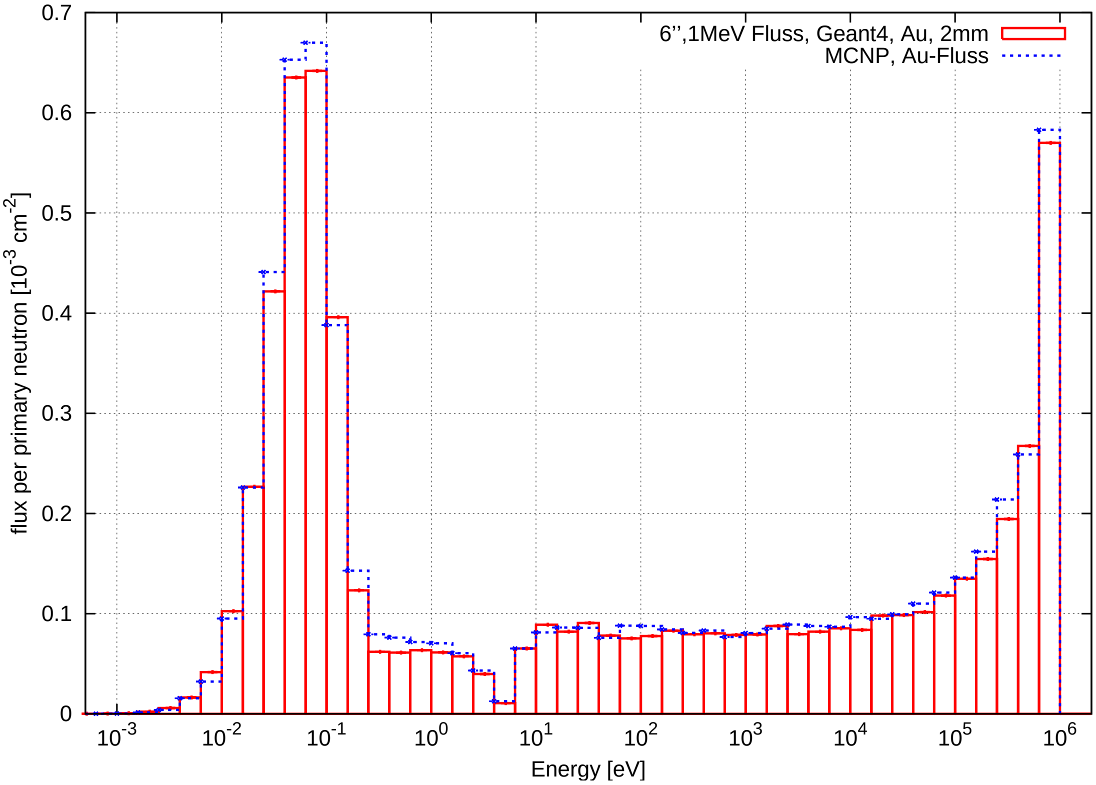

Figure 5.9: *Comparison of* GEANT4 *(this work) and* MCNP *(Mares, priv. com.) flux calculation for the 6" sphere, 1 MeV monoenergetic neutrons and 2 mm gold foil; the flux depression due to the gold resonance at 4.9 eV is clearly visible*

particle fluence $(d\phi/dE)_k$. The cross section σ_i^* in energy bin i is then:

$$\sigma_{\rm i}^* = \frac{\sum_{\rm k=1}^{\rm N} \left(\frac{\rm d\phi}{\rm dE}\right)_{\rm k} \cdot \sigma(\rm E_k)}{\sum_{\rm k=1}^{\rm N} \left(\frac{\rm d\phi}{\rm dE}\right)_{\rm k}} \tag{5.1}$$

with N being the number of cross section data points within the corresponding new energy bin.

Therefore, the characteristics of the neutron flux must be known. As is explained in appendix D, this problem is normally solved for neutrons by taking a so called thermalised spectrum, with the Boltzmann-peak at thermal energies and a 1/E shape from 0.125 eV upwards. Unfortunately, this is not a valid guess if there is a gold absorber of more than 5 μm thickness present. The resonance at 4.906 eV (see figure 5.8) absorbs so many neutrons, that the flux is depressed at the site of the foil. For thinner foils, this flux depression can be neglected, but in the case of the FRM II measurements (mean foil thickness 23 μm) it cannot. For the unfolding process only the thermal flux is required. In the measurement this is determined by subtracting the values measured with Cd from those measured without Cd present. In the GEANT4 calculation, the neutron flux is simulated and the response R calculated according to chapter 5.2.3:

$$\begin{aligned}\mathrm{R} = \mathrm{R}_{-\mathrm{Cd}} - \mathrm{R}_{+\mathrm{Cd}} \quad &\sim \quad \sum_{i=1}^{60} \phi_i^{-Cd} \cdot \sigma_i - \sum_{i=1}^{60} \phi_i^{+Cd} \cdot \sigma_i \\ &= \quad \sum_{i=1}^{60} (\phi_i^{-Cd} - \phi_i^{+Cd}) \cdot \sigma_i \;\approx\; \sum_{i=1}^{17} \phi_i^{-Cd} \cdot \sigma_i\end{aligned}$$

For the last step it is assumed that the Cd-tin absorbs all thermal particles while not disturbing the high energy flux (see 5.2.1 for further discussion and figure 5.7). The upper limit of energy bin 17 is 0.251001 eV, which is lower than the resonance energy of 4.906 eV. Therefore, the error introduced by this simplification is considered to be negligible.

5.2.3 Calculation of the 6” sphere response function

The response was calculated with GEANT4 at several monoenergetic energies for the primary neutrons for the 6“ sphere. The flux was calculated and normalised to standard flux (one neutron per sphere cross section). In the program, this was realised by dividing the calculated neutron flux by the number of simulated primary neutrons and by multiplying it with the cross section of the relevant sphere ($=\pi r^2$). The result was then multiplied by the number of gold atoms N_{197} of the normalised mass of 1 mg gold. These gold atoms are able to capture the neutrons and become activated to ^{198}Au.

In order to test the accuracy of the GEANT4-calculation, the neutron flux at the place of the gold foil was also calculated with MCNP with the 2 mm gold foil (Mares, priv. com.; see figure 5.9 and table 5.3) and for the real geometry (see figure 5.10, Mares, priv. com.). The response calculated for the 2 mm gold foil showed good agreement of GEANT4 and MCNP-calculation on the one hand and of the cut and difference-method on the other hand. This is remarkable as a thickness of 2 mm was chosen to represent the extreme case of a thick foil where flux depression of the neutrons cannot be ignored due to the large resonance of the gold absorber cross section at 4.9 eV. Furthermore, in MCNP, the number of ^{198}Au atoms produced was calculated directly (or, to be more precise, the number of capture reactions which lead to ^{198}Au was counted), which gave the same result as the flux-method. The same conclusion can be drawn from the simulations of the real geometry. Though the neutron flux displays some discrepancies

energy	GEANT4.8.2	MCNP
1 eV (cut)	$3.66 * 10^{-5}$	$3.93 * 10^{-5}$
(diff)	$3.67 * 10^{-5}$	$3.93 * 10^{-5}$
(cut)	$1.17 * 10^{-4}$	$1.10 * 10^{-4}$
1 MeV (diff)	$1.20 * 10^{-4}$	$1.13 * 10^{-4}$
(direct)	-	$1.11 * 10^{-4}$

Table 5.3: *Gold foil response calculated with GEANT4 and MCNP using a 2 mm thick gold foil as detector in a 6” sphere; 3 different calculation methods: difference of neutron flux with/without Cd folded with capture cross section, flux cut below 0.251 eV & folded and direct calculation of produced* ^{198}*Au*

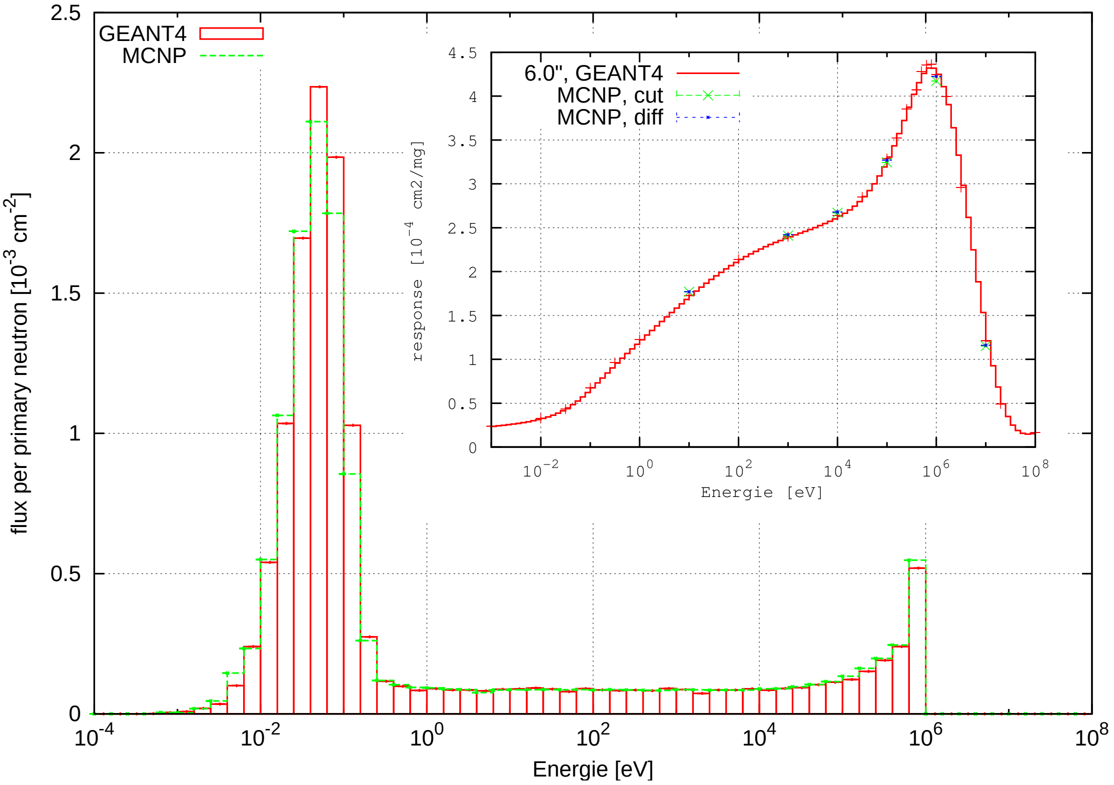

Figure 5.10: *Comparison of neutron flux at the place of the gold foil for 1MeV primary neutrons inside the 6" sphere.* ***Inset****: Comparison of Bonner sphere response with gold foil detector; calculated with* GEANT4 *(this work, red) and* MCNP *(Mares, priv. com.; in green with cut at 16th bin and blue with difference of flux with/without Cd (see also figure 5.7))*

(smaller than 6%) in this case (see figure 5.10), both response calculations with MCNP and GEANT4 are in very good agreement.

CHAPTER

6

Measurement of neutron spectra at the FRM II treatment facility by means of Bonner sphere spectrometry

Besides scintillation spectrometers (often out of organic stilbene: $C_{14}H_{12}$), time-of-flight measurements and hydrogen counters, Bonner sphere spectrometers are a commonly used instrument to measure neutron flux. Typically, they consist of a set of five to 20 polyethylene spheres with a thermal neutron counter inside. Depending on the amount of neutron flux, different detectors are used inside: active detectors like ^{3}He-counters for low intensity neutron flux and passive ones like activation foils in fields with high neutron flux. This is due to their different sensitivity for neutrons, which depends on the thermal neutron cross section involved. For ^{3}He the main reaction at low energies is inelastic (n,p)-scattering with a thermal cross section of 5328 b at 25.3 meV. An example of activation foils is gold with a thermal capture cross-section of 98.71 b at 25.3 meV.

In the case of the FRM II neutron therapy beamline, the expected flux is quite high ($3 \cdot 10^8 \frac{\text{neutrons}}{\text{cm}^2\text{s}}$). Therefore, a passive gold foil detector was used and the response matrix was pre-calculated for this detector set using GEANT4. The measured activation results were unfolded using MSANDB and the resulting spectrum compared to results from threshold probe measurements [16].

6.1 Measurement principle

The Bonner sphere spectrometers consist of a set of polyethylene (PE) spheres of different sizes (varying between 2 and 15 inches), which are placed in the neutron field to moderate the incoming neutrons. In the centre of each sphere a detector is placed which is sensitive to thermal neutrons. This sensitivity to thermal neutrons is achieved by choosing a detector material that has a very high inelastic cross section in the relevant thermal neutron energy range (below about 1eV), like ^{3}He, ^{6}Li, ^{10}B or ^{197}Au. If needed (for example by the unfolding algorithm), the epithermal neutrons can be eliminated by performing two measurements: one with, the other one without cadmium shielding of the detector and subtracting the two values. This is possible because the cadmium neutron capture cross section displays a steep edge at about 0.5 eV, capturing neutrons with lower energies while being almost transparent for neutrons with higher energies. Thus, subtraction of the two values provides the pure thermal neutron flux. The advantage of focusing on thermal neutrons and eliminating contributions from epithermal neutrons is the more pronounced difference in the resulting response functions of different detector/sphere combinations and thereby an improvement of the unfolding process.

In order to increase the sensitivity, a lead shell is inserted somewhere inside the PE-sphere which produces many secondary neutrons from the primary high energy ones (the basic reaction is Pb(n,xn)). The response of the purely PE spheres for high relative to low energy neutrons does increase with the sphere size, but for energies greater than 10 MeV, all spheres display a decline of the response (see figure 6.6 and [82]). On the other hand, the useful sphere size is often limited by the geometry of the neutron field which is to be measured. The flux is averaged over the whole sphere, therefore it is a pre-requisite that the flux is homogeneous over the whole cross section of all spheres used for the measurement. This is sometimes, for example in the case of a focused neutron beam for neutron therapy, only fulfilled for smaller sphere sizes. A further problem with big spheres is their mass, making them very heavy and laborious to handle. At least the first problem can be overcome by using a lead shell, which enables the measurements of high neutron energy fields (e.g. the field from cosmic rays, see [75]). The optimal depth and thickness for the lead shell have to be studied by calculating the response of the whole lead-PE system with a Monte Carlo program in advance, adapting the response to the requirements of the measurement.

The two possible detector types are active detectors, usually being very sensitive and passive ones, usually not so sensitive to thermal neutrons, but with the ability to measure greater flux. An example of an active detector is the ^{3}He-detector, where the $^3_2He(n,p)^3_1t$ reaction leads to protons and tritons. At higher energies also elastic scattering at the ^{3}He occurs. These particles ionise the ^{3}He-gas inside the measurement chamber, which can be used as a signal. Such detectors are usually operated in the proportional counter mode. The number of particles initiating these ionisation processes is simulated with a Monte Carlo program to give the response functions of the spheres together with the detector.

An example of a passive detector is a gold activation foil (^{197}Au). The neutrons are captured in the gold foil to produce ^{198}Au which decays via β^-decay to ^{198}Hg ($T_{1/2} = 2.69517\,d$; β^-- endpoint energy $E = 1.372\,\mathrm{MeV}$ and $E_\gamma = 411.8\,\mathrm{keV}$ for the photon which is emitted promptly (23 ps) and can be counted with a gamma detector; decay scheme see figure 6.1). The saturation activity A_∞ of the foil is measured in a 4π-proportional counter (countrate Z), correcting for time since irradiation (elapsed time

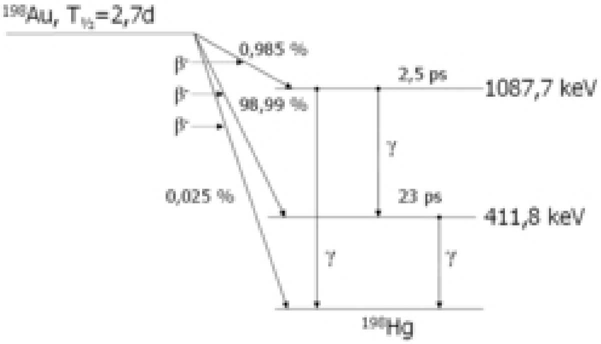

Figure 6.1: *Decay of* ^{198}Au *[1]*

$\mathrm{t_e}$), irradiation ($\mathrm{t_r}$) and measurement ($\mathrm{t_m}$) time when necessary (further explanations see chapter B.2.6):

$$\mathrm{A}_\infty = \frac{\lambda \mathrm{Z t_m}}{\mathrm{q}\varepsilon} \cdot \frac{\mathrm{e}^{\lambda \mathrm{t_e}}}{\left(1-\mathrm{e}^{-\lambda \mathrm{t_r}}\right)\left(1-\mathrm{e}^{-\lambda \mathrm{t_m}}\right)}$$

with emission probability q and detection efficiency ε. If the irradiation time and the measurement time are small compared to the half life ($t_r, t_m << T_{1/2}$) this becomes (derivation see E.1):

$$\mathrm{A}_\infty = \frac{\mathrm{Z}}{\mathrm{q}\varepsilon} \cdot \frac{\mathrm{e}^{\lambda \mathrm{t_e}}}{\lambda \mathrm{t_r}}$$

In this case, the activation of the gold foil is the process which is simulated by GEANT4 for the calculation of the response matrix, more precisely the number of ^{198}Au-atoms. In the end a measurement vector is obtained with the count rates of each sphere, containing gas-proportional counters or specific gold activities. This dataset is then to be unfolded with a deconvolution program, for example MSANDB to obtain an estimate of the incident neutron spectrum.

6.2 Deconvolution with MSANDB

The deconvolution program MSANDB [87] needs three main inputs, a measurement vector, a response matrix and a start spectrum. The response matrix consists of the response function of all used spheres/detector combinations and dose conversion coefficients if desired. The start spectrum can be an arbitrary spectrum, but to facilitate the unfolding process, it should be chosen in line with the physical properties of the expected spectrum (educated guess). All response functions and the start spectrum are bound to be given in the same energy binning (10 bins for every decade of energy). MSANDB takes the start spectrum and folds it with the response matrix to get a calculated vector. Then it compares this result with the measured data (χ^2-test). If the result is closer than a given value, it stops. Otherwise it modifies the start spectrum somewhat and repeats the process. This kind of iteration is done until the desired χ^2-value is reached or a predefined number of iterations were run (see chapter 6.2 for details on the unfolding algorithm). Investigations [115] have shown that the unfolding process depends only weakly on the start spectrum and that 300 to 500 iterations are best to give a spectrum which is not only reproducing the measured data satisfyingly

but also displays characteristics which are "physically" correct.
In appendix B.2.6 the saturation activation A_∞ for an activated foil in a homogeneous and time-constant neutron flux field $\Phi(E)$ is derived:

$$\mathrm{A}_\infty = \Phi\sigma\mathrm{N} = \mathrm{N}_{197}\int \Phi(\mathrm{E})\sigma(\mathrm{E})\mathrm{dE} = \mathrm{N}_{197}\sum_{\mathrm{j}} \Phi_\mathrm{j}\sigma_\mathrm{j}$$

with capture cross section $\sigma(E)$. This is only true for a bare foil in the neutron field. If the foil is placed inside a moderator (for example a polyethylene sphere), the flux is changed while passing through the PE. Therefore, the flux in the term $\Phi_j\sigma_j$ becomes a moderated flux and $\Phi_{i,j}\sigma_j = R_{i,j}\cdot\Phi_j$, with $R_{i,j}$ being the response of the sphere i to a standard neutron flux of energy $[E_j, E_{j+1}]$ [85]. So for the i-th sphere, one gets (the number of ^{197}Au atoms is usually already included into the derivation of $R_{i,j}$):

$$\mathrm{A}^\mathrm{k}_\infty = \sum_\mathrm{i} \mathrm{R}_{\mathrm{i,j}}\Phi_\mathrm{j} \qquad \Longleftrightarrow \qquad \tilde{\mathrm{A}} = \boldsymbol{R}\,\tilde{\Phi}$$

This matrix equations have to be solved using all measured foil data with the same neutron flux in order to reconstruct the real spectrum. This task is sometimes called the "inverse problem of spectrometry". Because there are only few measuring points (one for each sphere), but a large number of energy bins, this is a highly under-determined problem and, thus, has no unique solution. Unfolding programs try to find the best fit to all measured data, taking some restrictions and information into account. This is done in MSANDB in an iterative way (excluding e.g. negative flux by taking the logarithm), starting from a good-guess start spectrum $\mathbf{\Phi^0}$ (see [5, 85, 87] and Leuthold, priv. com.):

1) First, estimated start activities A_i^0 are calculated for each foil i, based on the assumed start spectrum $\mathbf{\Phi^0}$ and the elements of the pre-calculated response matrix line $\vec{R_i}$ for all energy bins j:

$$\mathrm{A}^0_\mathrm{i} = \sum_\mathrm{j} \mathrm{R}_\mathrm{ij}\Phi^0_\mathrm{j}$$

2) These calculated activities A_i^0 are then compared to the actually measured ones A_i^m and a correction factor is determined as follows:

$$\ln\mathrm{M} = \frac{\sum_\mathrm{i} \ln\left(\frac{\mathrm{A}^\mathrm{m}_\mathrm{i}}{\mathrm{A}^0_\mathrm{i}}\right)\cdot\left(\frac{\mathrm{A}^\mathrm{m}_\mathrm{i}}{\mathrm{s}^\mathrm{m}_\mathrm{i}}\right)^2}{\sum_\mathrm{i}\left(\frac{\mathrm{A}^\mathrm{m}_\mathrm{i}}{\mathrm{s}^\mathrm{m}_\mathrm{i}}\right)^2}$$

with $\mathrm{s}^\mathrm{m}_\mathrm{i}$ being the variances of the count-rates.

3) The next spectrum and activities are then calculated:

$$\Phi^1_j = M\cdot\Phi^0_j \qquad , \qquad A^1_i = M\cdot A^0_i$$

4) After the two introducing steps, the iterative process is started. With the help of a sensitivity function for each foil based on the current iteration, a weighting function $\mathrm{W}_{\mathrm{i,j}}^{\mathrm{k}}$ for that foil is obtained, which is based on the relative contribution of the flux Φ_j of the j-th energy bin to the calculated activation A_i^k of the foil i:

$$\mathrm{W}_{\mathrm{ij}}^{\mathrm{k}} = \frac{\mathrm{R}_{\mathrm{ij}}\Phi_{\mathrm{j}}^{\mathrm{k}}}{\mathrm{A}_{\mathrm{i}}^{\mathrm{k}}}$$

5) A correction function $\mathrm{M}_{\mathrm{j}}^{\mathrm{k}}$ for each energy bin is then calculated with these weighting factors $\mathrm{W}_{\mathrm{ij}}^{\mathrm{k}}$ and with the logarithmic ratio of the measured A_i^m and the calculated A_i^k activations:

$$\ln \mathrm{M}_{\mathrm{j}}^{\mathrm{k}} = \frac{\sum\limits_{\mathrm{i}} \mathrm{W}_{\mathrm{ij}}^{\mathrm{k}} \ln\left(\frac{\mathrm{A}_{\mathrm{i}}^{\mathrm{m}}}{\mathrm{A}_{\mathrm{i}}^{\mathrm{k}}}\right) \cdot \left(\frac{\mathrm{A}_{\mathrm{i}}^{\mathrm{m}}}{\mathrm{s}_{\mathrm{i}}^{\mathrm{m}}}\right)^2}{\sum\limits_{\mathrm{i}} \mathrm{W}_{\mathrm{ij}}^{\mathrm{k}} \left(\frac{\mathrm{A}_{\mathrm{i}}^{\mathrm{m}}}{\mathrm{s}_{\mathrm{i}}^{\mathrm{m}}}\right)^2}$$

6) The next iteration of the flux is obtained by application of these correction factors $\mathrm{M}_{\mathrm{j}}^{\mathrm{k}}$ to the current iteration of the flux and the activities:

$$\Phi_{\mathrm{j}}^{\mathrm{k+1}} = \mathrm{M}_{\mathrm{j}}^{\mathrm{k}} \cdot \Phi_{\mathrm{j}}^{\mathrm{k}} \qquad , \qquad \mathrm{A}_{\mathrm{i}}^{\mathrm{k+1}} = \mathrm{M}_{\mathrm{j}}^{\mathrm{k}} \cdot \mathrm{A}_{\mathrm{i}}^{\mathrm{k}}$$

7) There are two ways to finish the iteration. The first one is when a certain predefined number of iterations is reached, the second is when the relative change of the calculated activities at all energy bins is smaller than a specified value ε:

$$\frac{\chi^{\mathrm{k+1}}}{\chi^{\mathrm{k}}} - 1 \leqslant \varepsilon \qquad \text{with} \qquad \chi^{\mathrm{k}} = \sum_{\mathrm{i}} \left(\ln \frac{\mathrm{A}_{\mathrm{i}}^{\mathrm{m}}}{\mathrm{A}_{\mathrm{i}}^{\mathrm{k}}}\right)^2 \cdot \left(\frac{\mathrm{A}_{\mathrm{i}}^{\mathrm{m}}}{\mathrm{s}_{\mathrm{i}}^{\mathrm{m}}}\right)^2$$

On the whole, the relative uncertainty of the measurement $\frac{A_i^m}{s_i^m}$ is only important in cases where it is different for the different foils, otherwise it cancels out.

This iterative process is implemented in MSANDB using the computer language `FORTRAN`. Several input data are needed, which are read in via an input file: the response matrix, the measured activations (together with an overall normalisation factor if necessary), a start spectrum, the maximum number of iterations and/or the finish criterion ε.
To facilitate the unfolding process, the start spectrum should match the expected spectrum (educated guess), but this is not a mandatory requirement. If there are many similar measurement results (e.g. when the response functions overlap over a large range), MANSDB is usually able to unfold the spectrum even if the start spectrum is poorly chosen (see chapter 6.5.1). The program uses a common energy bin structure, determined by the response matrix binning. The maximum number of iterations (or the exit criterion ε) should be chosen in such a way that the resulting unfolded spectrum is still physically reasonable. MSANDB sometimes tends to produce many small peaks at unlikely energies, fitting the measured data the closest way which is mathematically

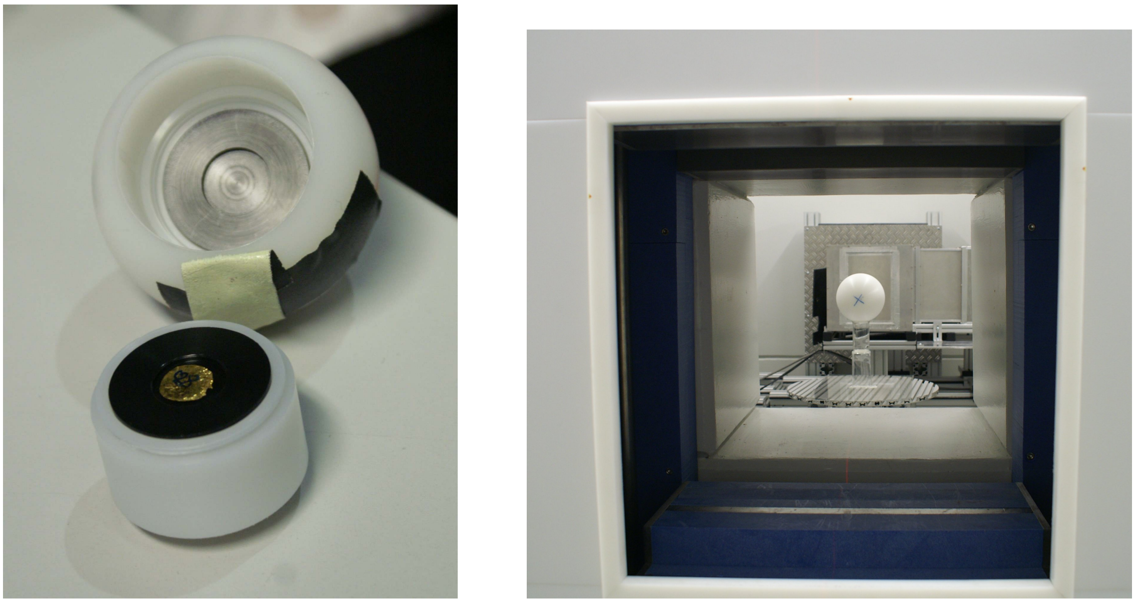

Figure 6.2: *Bonner spheres used at the FRM II measurements:* ***left****: 2.5" during preparation process;* ***right****: 6" in irradiation position at radiography site*

possible. Therefore the number of iterations were studied in [115] and in chapter 6.5.1, and a maximum number of about 600 was determined to be the best approach. The uncertainty of the spectrum in energy regions where response data is scarce (below about 1 eV and above 10 MeV) cannot be compensated by measurements. The only possible way to overcome this problem is to manufacture measurement systems with totally different responses, for example PE-spheres with an included lead shell for high energies (this is also discussed in chapter 6.4).

6.3 Measurements

The measurements with gold foils in the centre of the Bonner spheres took place at the FRM II (from December 12th to 15th 2006) with medical filtering, using 15 spheres (2.5" to 15", see chapter 6.3.1), a black inner sphere (used in all spheres to fill the space carved out for the ^{3}He-detector) and a device for holding the bare gold foil. There were two series: one at the patient treatment position, the other farther away from the beam at the position of the radiography facility (for an outline of the chamber geometry, see chapter 3.1). The first series included measurements with sphere sizes bare, 1.3" (black sphere) and diameters 2.5" to 9". Bigger spheres could not be illuminated entirely at this distance from the converter because of the limited beamsize and the inhomogeneity of the beam (see [65]). In the second series, measurements with diameters of 10" to 15" were also possible. Due to potential neutron-induced activation in lead, and the expected maximum of the spectrum at few MeV (with a steep decline for higher neutron energies; see fission spectrum of ^{235}U), no spheres with a lead shell were used.

Specification of the goldfoils	
inner diameter:	4.7 mm (±0.7 mm)
outer diameter:	10.3 mm (±0.6 mm)
thickness:	23 μm (±4 μm)
weight:	29.3 mg (±8.1 mg)

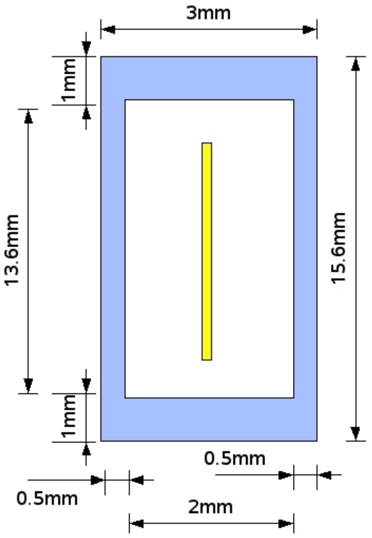

Figure 6.3: *Table of average parameters of the goldfoil's (^{197}Au) geometry and weight and a sketch of the geometry of the cadmium-tin (in blue), the goldfoil (not drawn to scale) is depicted in yellow*

6.3.1 Experimental setup

At the **patient treatment position**, the spheres where placed on top of the patient couch with the help of a plastic pail, a glass canister or a cardboard roll, depending on the size of the sphere, minimising scattering of neutrons in the direct vicinity of the spheres and foils, respectively. Attention was also paid that the patient couch was not irradiated. The bare gold foil was attached to a metal frame with the help of a thin thread in such a way that the metal was not illuminated by the beam. In all cases, the gold foil was perpendicular to the beam, 205 cm from the beam exit point of the wall (48.5 cm from the back wall), in the beam centre (145 cm over the floor). The resulting distance to the converter was 697 cm and to the collimator 218 cm. The beam shutters and the collimator were opened at maximum, which resulted in a beam-cross section of $20 \times 30\,\text{cm}^2$. Therefore, sphere sizes of 2.5, 3.0, 3.5, 4.0, 4.5, 5.0, 5.5, 6.0, 7.0, 8.0 and 9.0 inch could be used. The lateral flux decrease could be estimated from lateral dose measurements by Kampfer ([65], using beam expansion of 2-3° beam angle and a wall-distance of 205 cm relative to 100 cm) to be less than 5% between the central axis of the beam and a point 12 cm lateral from it. This corresponds to a sphere size of 9", which was the biggest sphere used in this measurement. At the **radiography facility position**, the spheres were also placed isocentrically onto the mounting system installed there (again with plastic pail, etc. to minimise scattering), at a distance of 905 cm to the converter plates. Because of the larger distance and the beam expansion, sphere sizes of 2.5, 3.0, 3.5, 4.0, 4.5, 5.0, 5.5, 6.0, 7.0, 8.0, 9.0, 10.0, 11.0, 12.0 and 15.0 inch could be used (the resulting flux decrease was again smaller than 5%).

The pure gold (^{197}Au) foil was ring-shaped (for the geometry see table in figure 6.3). The cadmium-tin used in half of the measurements to subtract the epithermal is also shown in figure 6.3 (together with its dimensions). The gold foil (or the tin with the gold foil inside) was placed inside a tube-shaped cavity (radius: 1.56 cm, thickness: 3 mm; neatly fitting the Cd-tin) in the middle of the black inner sphere (PE, density $= 0.96\,\text{g/cm}^3$), which has a diameter of 1.3" and two knobby ends to be exactly posi-

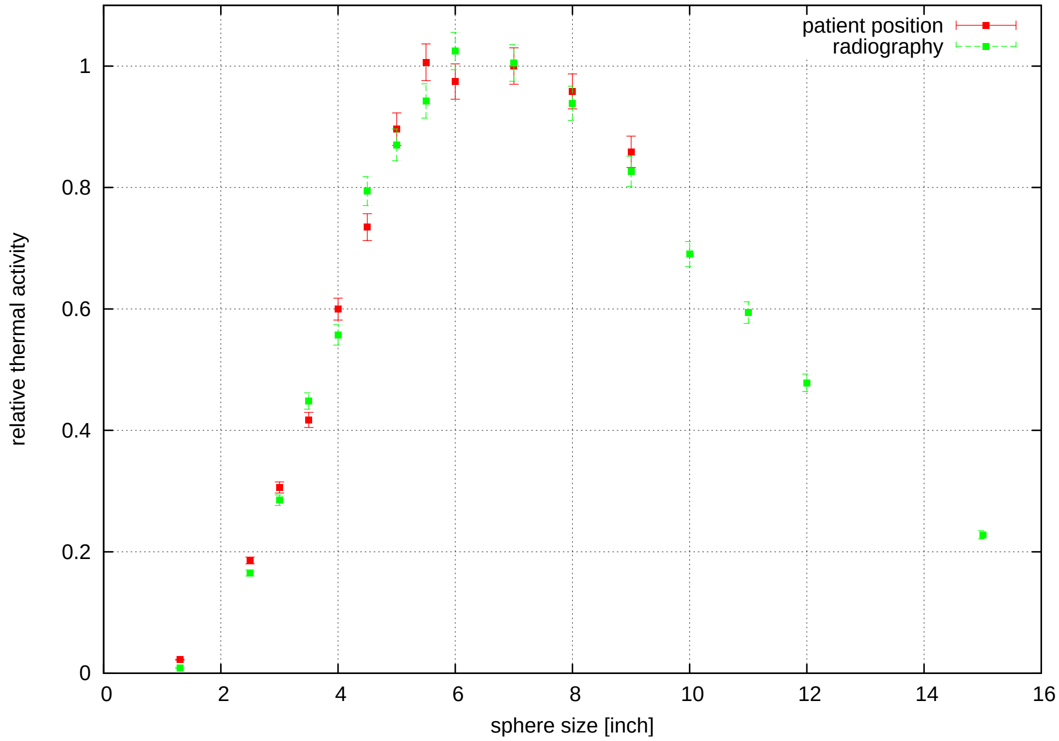

Figure 6.4: *Comparison of the two measurement vectors of the thermal neutron flux: difference of measurement with/without Cd normalised to the specific activity of the 7" sphere; errorbars give the variances of activation measurement (3%)*

tioned inside the white spheres (PE, density = 0.95 g/cm^3).
The activation of the gold foil was measured afterwards in a 4π-proportional counter, correcting for the time since irradiation. Both the irradiation and the measurement time were small compared to $T_{1/2}$(^{198}Au) and therefore did not need direct correcting (see chapter 6.1). The Au-activity was then normalised to unit mass of ^{197}Au, getting the specific activity per second and mg. All measurements were converted to the same monitor-value (M1=1265 MU in 500 s; MU = monitor units), which is a good indicator of the converter power (better than the direct converter power display, which is not precise enough), correcting to a value of 2.53 $\frac{\text{MU}}{\text{s}}$ for all measurements. In the end, all activities were transformed into the number of ^{198}Au -atoms produced, to obtain the same quantity that was pre-calculated in the response matrix.

6.3.2 Measured count rates

The raw data of the Bonner sphere measurements are plotted in figures E.2 and E.3 in the appendix, displaying both measurements with and without Cd at the patient treatment position and radiography position. The activation caused by thermal neutrons is calculated by subtracting the measured value with Cd from that without Cd. For a better comparison, both datasets in the patient and the radiogarphy room were normalised to the value of the 7 inch sphere (arbitrary selection) and plotted together in figure 6.4. Because the different-sized spheres do not represent a totally independent system of measurements all points of the two data sets have to lie on a smooth curve, which is actually the case within the measurement uncertainties. Also both sets should be similar, because they come from the same beam (there is just another beam-window to cross into the radiography-room). This is indeed the case for the measurements performed. For the 1.3" sphere and the bare foil the measured value became negative at the patient position (only for the bare foil at the radiography site), probably because the spectrum present at the site of measurement is almost a pure fission spectrum (the thermal component is at least two orders of magnitude lower than the maximum at about 2 MeV, see figure 6.12) resulting in very low activities for the small spheres and the bare foil (which only sees the thermal part). Therefore, perturbing effects have a greater importance for the smaller spheres than for the bigger ones. Another point is the correctness of the assumption that the Cd-tin absorbs all thermal neutrons while not changing the higher energy spectrum. While this is not critical in the presence of a large number of thermal neutrons, the relative error introduced can be high if only few thermal neutrons are present. In the case of the FRM II spectrum, the error introduced by the assumption of an ideal Cd-absorber is up to 6% for the small spheres (see figure 5.7).

Because of bad measurement results, both the bare foil and the 1.3" sphere measurement were repeated in the patient treatment room and a reasonable result for the 1.3" sphere could be obtained (in May 2008 with a good similarity to the radiography-measurement within uncertainties, see figure 6.4, F. Wagner, priv. com.), which was taken for the unfolding process. While the new measurements provided reasonable results for the activation of the gold foil inside the 1.3" sphere, they again failed to quantify the activity of the bare foil due to low counting statistics.

6.4 Calculation of the response matrix

The geometry of all the Bonner spheres ($\rho = 0.95\,\mathrm{g/cm^3}$, radii in inch: 2.5, 3.0, 3.5, 4.0, 4.5, 5.0, 5.5, 6.0, 7.0, 8.0, 9.0, 10.0, 11.0, 12.0, 15.0) with the space-filling inner black sphere ($\rho = 0.96\,\mathrm{g/cm^3}$, radius: 1.3", see figure 6.5) and the gold foil inside (geometry see table in figure 6.3) were implemented in GEANT4 in the way they were described in chapter 6.3.1. The spheres were simulated free in vacuum, without any of the supporting devices. Therefore a small error is introduced by neutron scattering in the environment, which was not considered.

For each sphere the response for 22 to 29 single energy points were calculated, focused on the maximum of the response and at places with a steep gradient. Along these points a spline function was then fitted with `SPLINE` (spline fit method from Wittmann, GSF; Mares, HMG-ISS, priv. com.) and the 111 necessary matrix points needed for MSANDB extracted with this program. The response function of all spheres and of the bare foil where read in together with the energy bin structure and appropriate dose conversion coefficients into a C^{++}-program which puts all data into the MSANDB format. This complete matrix was then transferred to binary format with `UMSBIB` (Mares,

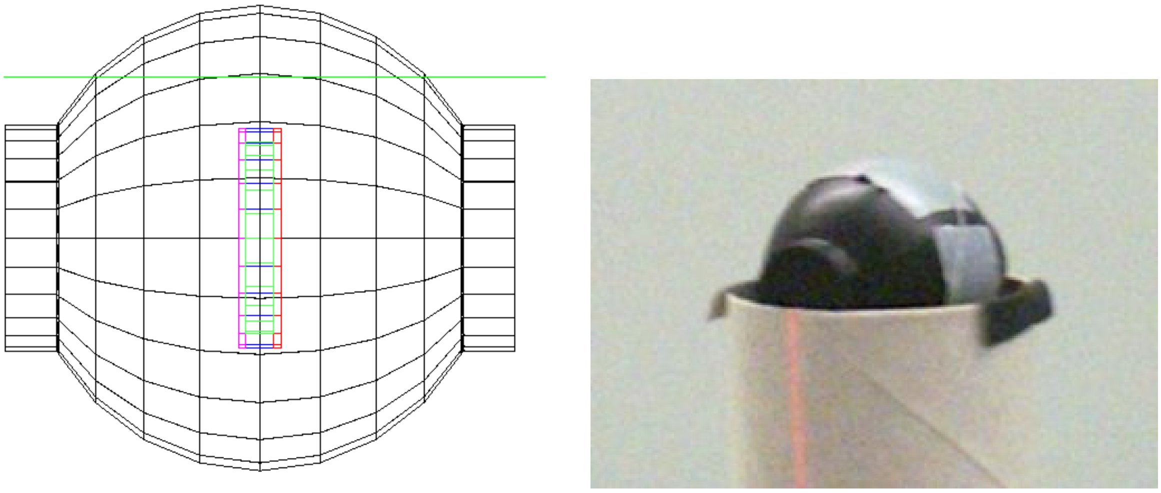

Figure 6.5: *1.3” inner sphere out of black PE, left:* GEANT4 *model with one neutron track and the Cd-tin inside, right: photo of irradiation geometry*

priv. com.). This matrix has been determined for the first time with GEANT4. The measured gold foil activations (transferred to number of ^{198}Au-atoms) can be unfolded with it by MSANDB (see chapter 6.5).

The response functions of all 16 spheres and of the bare foil are plotted in figure 6.6. The bare foil displays a steep decline at low energies where it is the only detector with any response at all. Basically, this response is equivalent to the cross section of ^{198}Au. Of all the foils which were irradiated inside a sphere, the response of the foil inside the 1.3” sphere is the one with its peak position at the lowest energy. The bigger the sphere, the higher lies the position of the peak. For sphere diameters larger than 8“, the maximum of the response functions declines and the energy of the peak position is increasing only very slowly in logarithmic scale.

Comparing the gold foil response with the response of the ^{3}He detector (see figure E.7 and [82]), a strong resemblance can be seen. The biggest difference is the height of the response matrix: peak heights are around $4 \cdot 10^{-4}\,\mathrm{cm}^2\mathrm{mg}^{-1}$ with gold foils compared to $0.7\,\mathrm{cm}^2\mathrm{mg}^{-1}$ for the ^{3}He detector. Another difference is a small shift to larger spheres: the response function of the 4” gold foil resembles more the response of the 4.5” than the 4” ^{3}He response. This is due to the higher PE content in the gold foil case caused by the different size of the detectors, which was compensated by the 1.3” black inner sphere for the gold foil measurement. The other characteristics of the response function are very similar.

It can clearly be seen in figure 6.6 that the response functions are overlapping and not all spheres are necessary for the unfolding process. On the other hand, using all spheres provides a certain amount of redundancy and error reduction, as was already discussed in chapter 6.3.2. Looking at the summed response of all spheres (see figure E.1) shows that the weak point of this kind of measurement are the region of thermal neutrons and the region above some MeV if no lead-shell-sphere is used. At least from the theoretical point of view, in these regions, the unfolding process is bound to fail

Figure 6.6: *Total response matrix of the Bonner sphere system with* $23\mu m$*-gold foil inside, calculated with* GEANT4*; sphere size in inch is shown as a parameter on each line*

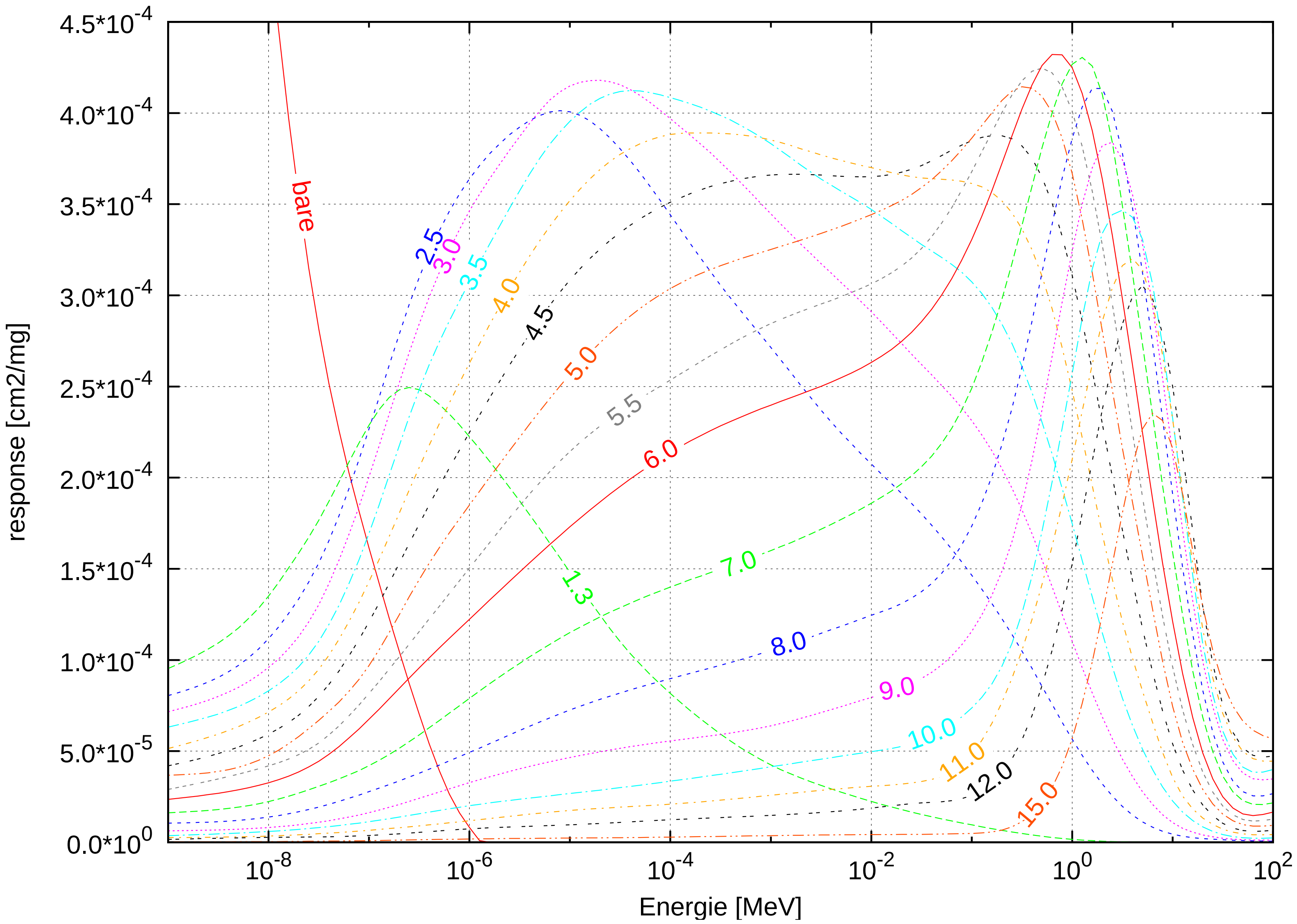

(or to fall back onto the start spectrum) because there is no response data available there. Nevertheless, in the case of determining the neutron energy flux at the FRM II in Garching, where the expected spectrum is similar to a Watt-spectrum with an additional epithermal and thermal part, the Bonner sphere spectrometer is a good instrument to measure the integral neutron flux.

In summary, GEANT4 was used to calculate the response matrix for the HMGU Bonner sphere system with gold foils as passive thermal neutron detectors [34]. This matrix was not available before and allows now the measurement and unfolding of the neutron spectrum at the therapy beamline (see below).

6.5 Reconstruction and comparison of neutron-flux spectra

In the previous chapters, the measurement of the gold foil activation and the determination of the Bonner sphere response matrix was explained in detail. These two data sets were entered into the unfolding process of MSANDB (for program description see chapter 6.2). Furthermore, the program needs a good-guess starting spectrum, which is studied and discussed among other factors in the first two following chapters. The unfolded neutron spectrum is also analysed for effects of the numbers of iterations and the influence of measurement uncertainties is outlined. In the last part, the results from the MSANDB-unfolding are compared to a neutron spectrum obtained by adapting a MCNP-simulation to threshold-probe measurements [16].

6.5.1 Unfolding with MSANDB

Investigation [115] have shown that the unfolding process is only weakly depending on the start spectrum, which is mainly due to the large overlap of the response functions over a large range. These functions give redundant information to the unfolding process whereas in areas of low response (at energies smaller than 1 eV and larger than 10 MeV) the start spectrum is almost not changed at all. About 500 iterations were determined to be best to give a spectrum which is not only reproducing the measured data satisfyingly but also displays characteristics which are physically correct (see also chapter 6.5.1 for discussion). That means that there are no artificial peaks at energies were peaks are not expected.
Three different start spectra were tested for the unfolding process (see figure 6.7). One (in the figure: cosmic+cut) is a start spectrum derived from the spectrum of secondary neutrons from cosmic rays [75], which was cut at about 12 MeV (steep decline), to resemble a fission spectrum. The second start spectrum used is a fission (or Watt) spectrum, with the usual triangular appearance in log-log representation. At low energies, a thermal peak was added (taken out of the cosmic spectrum), supplementing data in a region where again the unfolding is weak (primarily because the bare foil measurement failed). The last start spectrum tested (MSITER+MCNP) is the spectrum which

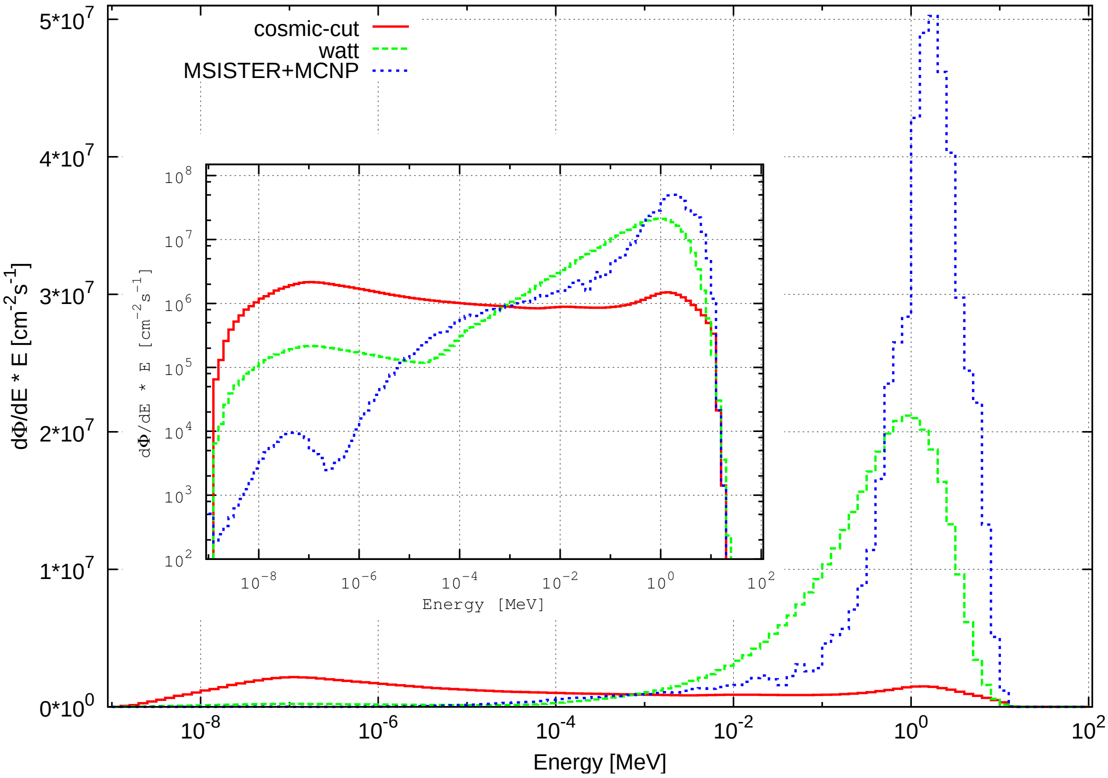

Figure 6.7: *Different start spectra used to unfold the neutron spectrum at the treatment location; for a detailed explanation see text; For the unfolding process, only the relative form is important, not the absolute values*

Breitkreutz [16] calculated with MCNP and adapted with the help of threshold measurements (with the program MSITER). In his work, this spectrum was compared to a transmission-calculated spectrum with good similarity. The three different start spectra were primarily taken to study the dependence of the unfolding process on the start spectrum and to ensure that differences between the (MSITER+MCNP)-spectrum and the unfolded one from the gold foil measurements are not caused by poor choice of the start spectrum. It should also be mentioned that the resulting spectrum is not dependant on the absolute values of the whole start spectrum but rather on the relative distribution.

The unfolding of measured activities with MSANDB is a highly under-determined process as there are only 11 (respectively 16) activity measurements, but 111 energy bins where the neutron flux has to be calculated. Therefore, the program makes some assumptions, for example that the flux is non-negative and that the flux of the measured field is homogeneous over all spheres.

The iteration process was terminated after 600 iterations, which was known ([115] and also tested) to give good results. In figure 6.8 the resulting unfolded spectra of two completely different start spectra are presented. There is the very good agreement of the unfolded spectra between 10 eV and 8 MeV. In this energy range, the deviation of

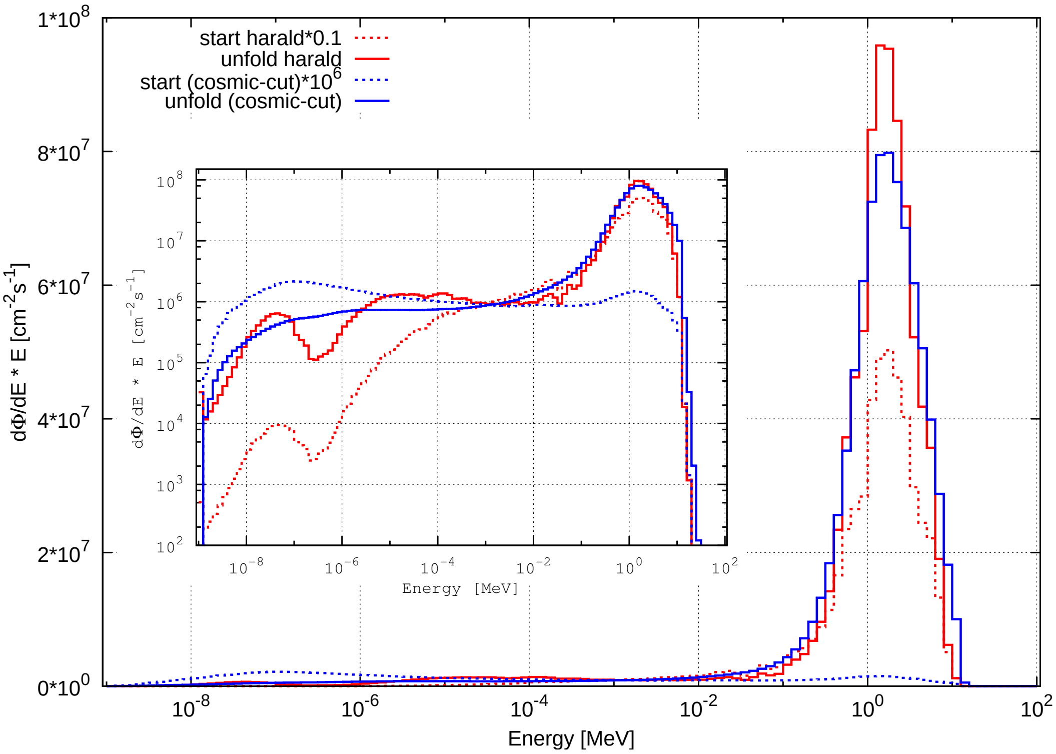

Figure 6.8: *Unfolded neutron spectrum with MSANDB with two different start spectra: one is the spectrum calculated and measured by Breitkreutz [16], the other a thermalised neutron spectra from cosmic rays, cut at about 12 MeV to mirror the edge of a fission spectrum*

the two unfolded spectra is less than 20% for almost all bins, whereas the start spectra differ by more than two orders of magnitude. The unfolding with the third start spectrum also produces comparable results (see figure E.4). Secondly, the MeV-peak is reproduced even when it was not so eminent in the start spectrum. Furthermore, there appears to be very little thermal neutron flux present. This was already known from the measured activities of the gold foil, where the foils in the small spheres and the bare foil displaye only very small activations (see section 6.3.2).

Another parameter analysed was the dependence of the spectrum on the number of iterations. This is shown in figure 6.9. Using the cosmic-ray spectrum, it can be seen that it takes only 5 iterations to reproduce a Watt-like spectrum. Further increasing the number of iterations causes the MeV peak to shift about 2 bins to lower energies and become narrower. As a consequence, the neutron flux around 10 keV decreases.

In the second plot it is shown what would happen if the iteration number is even further increased: a “ghost” peak at about 10 keV forms and the MeV peak is shifted to even lower energies and for a very large number of iterations gets split into two (see also figure E.6). The result is a spectrum which cannot be explained physically. The algorithm is not converging asymptotically, but has to be stopped after a reasonable number of iterations. The number chosen for unfolding the FRM II spectrum was 600, but a range of 100-1000 would also result in reasonable spectra.

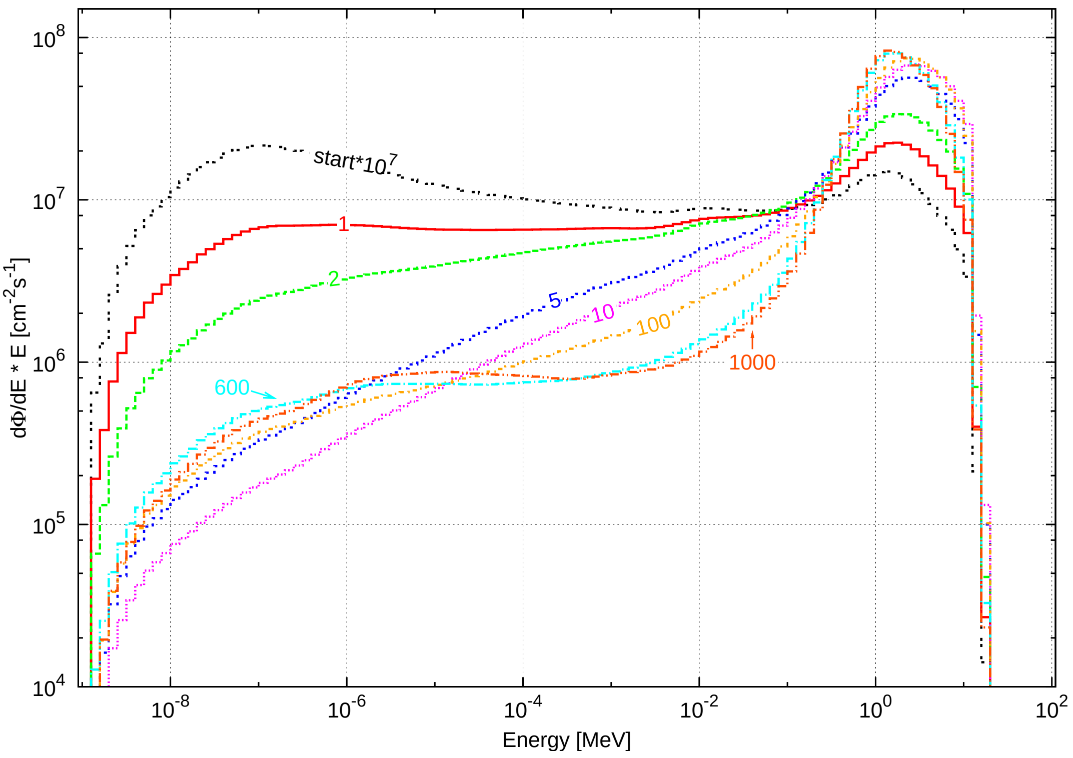

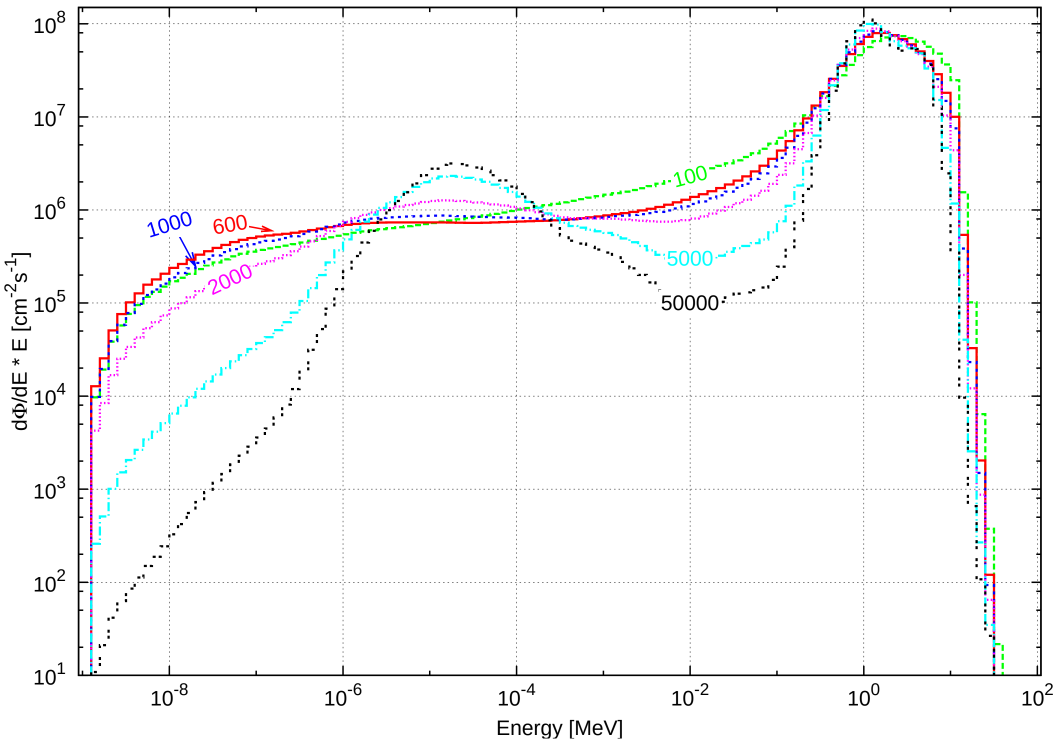

Figure 6.9: *Unfolded neutron spectrum with MSANDB, depending on different numbers of iteration steps (depicted as numbers on the lines); start spectrum is the thermalised neutron spectrum from cosmic rays, cut at about 12 MeV (see also figure 6.8)*

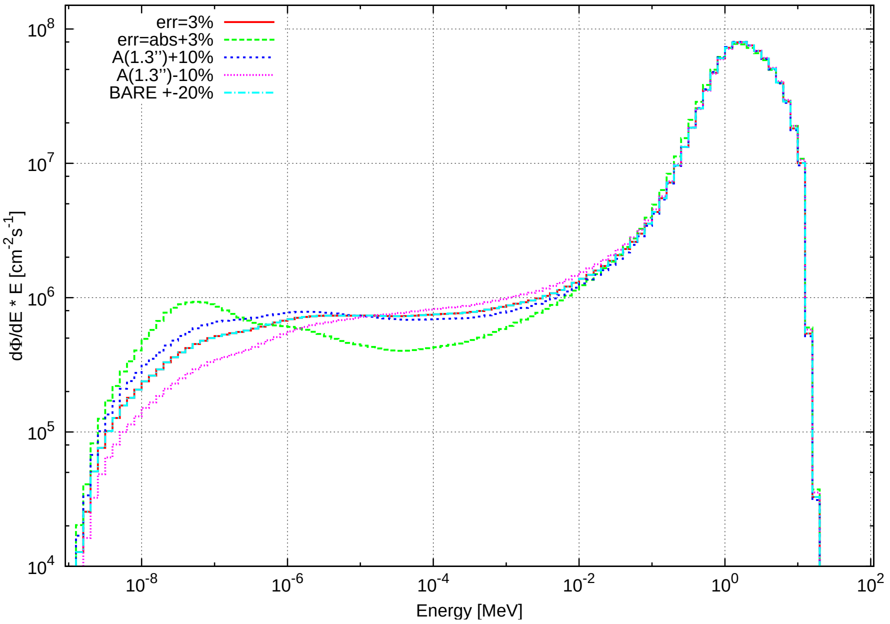

Figure 6.10: *Study of the dependence of the spectrum on the uncertainty and value of the 1.3" sphere and the bare foil*

In order to test the dependence of the unfolded spectrum on the activation of the bare foil and the foil in the 1.3" sphere, which are the only spheres with significant response to thermal neutrons, a sensitivity analysis was performed. Four artificial scenarios were tested:

- Adding an absolute error to the measurements of all spheres which amounts to 25% of the measured activation of the gold foil inside the 1.3"sphere (in figure 6.10: err=abs+3%)

- Increasing the absolute value of the count rate of the gold foil of the 1.3"sphere by 10% (in figure 6.10: A(1.3")+10%)

- Decreasing the absolute value of the gold foil of the 1.3"sphere by 10% (in figure 6.10: A(1.3")-10%)

- Introducing an artificial value for the bare foil with an assumed error of 20% (in figure 6.10: BARE +-20%)

The last point was introduced because reasonable (that is positive) activation could not be achieved though the measurement was repeated for the bare foil. On the whole, the MeV peak is stable, changing neither in position in the spectrum nor in absolute height. But it is visible that the lower part of the spectrum is depending on the exact values of the measurements. It also has to be mentioned that a change in the errors of the count rates of all spheres, if they are the same for all, does not change the outcome at all. This is due to the used algorithm of MSANDB, where the factor considering the uncertainty cancels if all are equal (see chapter 6.2).

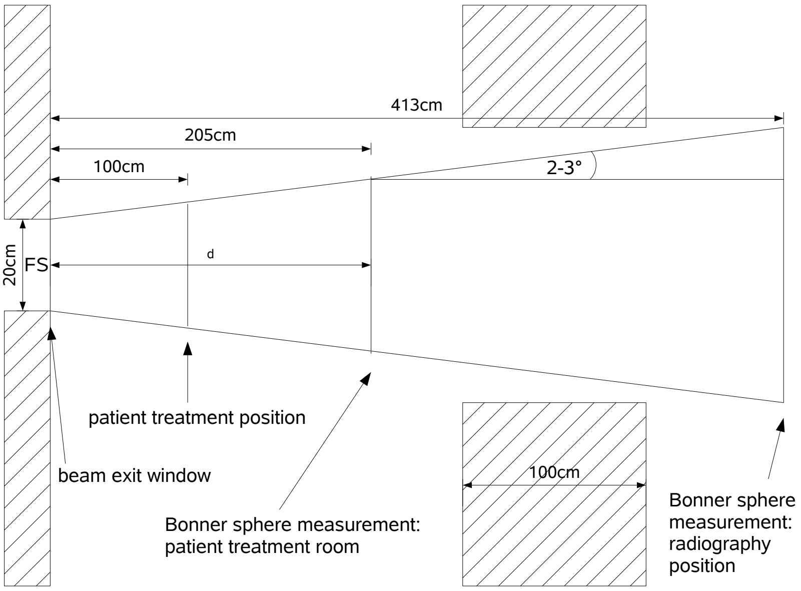

Figure 6.11: *Beam geometry at beamline SR10 at the FRM II with beam expansion*

6.5.2 Comparison with other measurements and calculations

The total neutron flux determined with the Bonner spheres inside the patient treatment room (for the exact measurement position see chapter 6.3.1) was determined to be $2.0{\cdot}10^8\,\mathrm{cm}^{-2}\mathrm{s}^{-1}(\pm5\%)$, depending only slightly on the used start spectrum and iteration number. For 600 iterations, the difference between the total flux for the different start spectra is smaller than 2%. At the radiography site, the total neutron flux was determined to be $1.1\cdot10^8\,\mathrm{cm}^{-2}\mathrm{s}^{-1}(\pm5\%)$.

Both values can be compared to the total flux measured with gold foils in a water phantom (waterbath-goldprobe method, [16]), which was shown to be the same as the one resultingfrom the treshold probe measurement by Breitkreutz. For the goldprobe measurement, a water phantom was used to thermalise fast neutrons and the resulting neutrons were captured by goldfoils. The water phantom was changed to simulate a isotropic point source by inserting a channel to let the neutrons enter into the middle of the phantom. Corrections for the anisotropic beam (it displays a strong preferential direction) and neutrons leaving the phantom at all sides and particularly through the entrance tunnel were included. A total neutron flux of $3.2(4)\cdot10^8\,\mathrm{cm}^{-2}\mathrm{s}^{-1}$ was determined at the position of patient treatment, which is at 100 cm distance from the exit window of the beam in the wall, in the isocentre of the beam (145 cm above the ground, [16]).

In order to compare this result with that obtained in the present work, the greater distance to the exit window has to be considered as well as the beam divergence of $2-3°$ (Wagner, priv. com.). If it is assumed that the total neutron flux is not affected by scattering in air and surrounding material, the flux at the different positions can easily be converted into each other (see figure 6.11):

$$\mathrm{flux}\cdot\mathrm{area}=\mathrm{const.}$$

location	**method**	**distance from window [cm]**	**flux** $[10^8\,cm^{-2}s^{-1}]$	**flux @100 cm** $[10^8\,cm^{-2}s^{-1}]$
pat. pos.	waterbath [16]	100	3.2	-
pat. room	BSS	205	2.0	3.0-3.4
rad. room	BSS	413	1.1	3.1-4.1

Table 6.1: *Summary of measured neutron flux at the beamline 10 at the FRM II: pat. pos.= patient treatment position, pat. room = patient treatment room, rad. room = radiography room, "flux @100 cm" = flux extrapolated to a distance of 100 cm from the beam exit window; for further details see text*

$$\mathrm{F_1} = \frac{\mathrm{A_2}}{\mathrm{A_1}} \cdot \mathrm{F_2} = \frac{(\mathrm{FS} + 2\mathrm{d_2} \cdot \tan(\alpha))}{(\mathrm{FS} + 2\mathrm{d_1} \cdot \tan(\alpha))} \cdot \mathrm{F_2}$$

with field size FS at the position of the beam exit window, and distance from this position $\mathrm{d_i}$. With the distance from the respective measurement position (205 cm and 413 cm compared to the treatment position at 100 cm, see chapter 6.3.1) and the measured flux (see above), the resulting flux is $(3.0 - 3.4) \cdot 10^8\,\mathrm{cm^{-2}s^{-1}}$ and $(3.1 - 4.1) \cdot 10^8\,\mathrm{cm^{-2}s^{-1}}$ (for $2 - 3°$) for the position in the treatment room and the radiography site, respectively. Strictly speaking, the assumption of negligible scattering does not hold for the real measurements. Particularly at the radiography site, the additional wall with the beam window probably introduces some scattering. On the whole, the total flux measured with the Bonner spheres is in good agreement with the waterbath measurement [16]. All results are summed in table 6.1.

In figure 6.12, the unfolded spectra obtained are combined in one plot. There, different numbers of iterations are depicted in different shades of gray. Furthermore, an impression of the variability of the resulting neutron spectra, depending on which of the three start spectra is used, can be seen in the width of the gray curves. This analysis was done with the activation data from the patient treatment room measurements. In addition, one spectrum measured in the patient treatment room and one at the radiography site are plotted together with the MCNP+MSITER neutron spectrum from [16], which has a total flux of $3.2 \cdot 10^8\,\mathrm{cm^{-2}s^{-1}}$. All spectra are normalised to a total neutron flux of $3.2 \cdot 10^8\,\mathrm{cm^{-2}s^{-1}}$, which was obtained by [16] with a very exact method for total flux measurement.

The most important result of the comparison is the good agreement of the spectra at high energies. Only for energies below 50 keV, the MCNP spectrum displays a higher neutron flux. At low energies, particularly at thermal energies, the spectra differ strongly. This is an energy range where the results of the Bonner sphere measurement are not unambiguous and therefore have to be handled with caution. But as on the one hand the neutron flux in this region is already at least 2 orders of magnitude smaller than that of the maximum and on the other hand this energy range is of lower importance for the patient dose calculation, the exact neutron flux distribution is irrelevant.

Figure 6.12: *Variability of the unfolded spectrum depending on iteration number and start spectrum together (in gray: shading indicates the number of iterations. The variability displays the different start spectra for the gold activation vector obtained in patient treatment room) with unfolded neutron spectrum of MSANDB inside the treatment room (this was used for further calculations: BSS-spectrum, pp (patient position, red)) and at the radiography site (BSS-spectrum, rad; green), together with the spectrum from Breitkreutz ([16], MCNP+MSITER, blue), all normalised to* $3.2 \cdot 10^8\,\mathrm{cm}^{-2}\mathrm{s}^{-1}$ *neutron flux.*

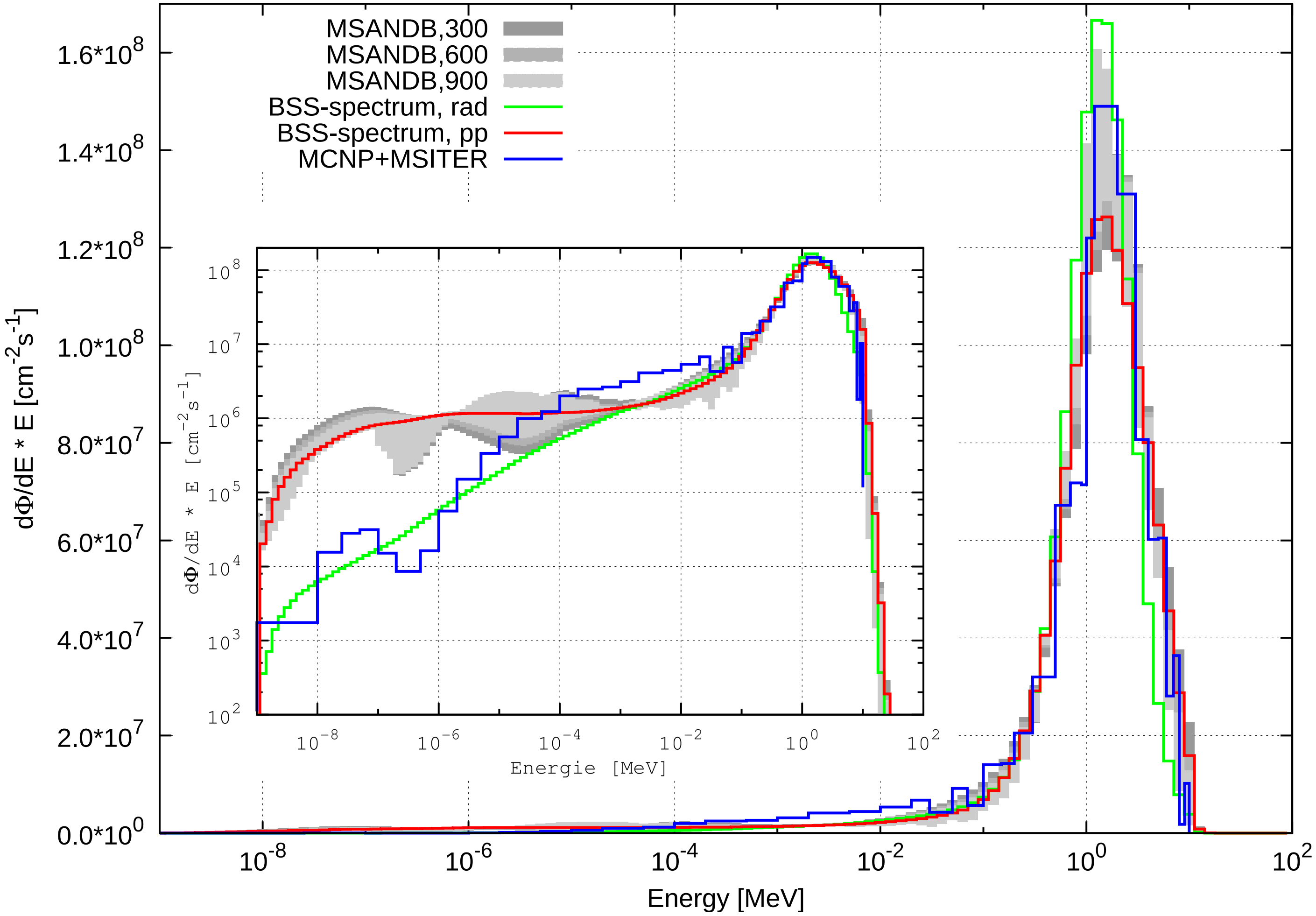

6.6 Conclusions

The neutron spectrum in the patient treatment room and the radiography site at the beamline SR10 of the FRM II was measured using a Bonner sphere spectrometer. The resulting spectra were compared to a spectrum determined by calculation with MCNP and unfolding of threshold probes [16]. Both agree well [33].

The stability of the unfolding process of MSANDB was tested for the number of iterations, different start spectra and dependency on certain measured activities in the 1.3" sphere and for the bare foil. Both are difficult to measure because of the low thermal neutron flux and are, thus, prone to errors. The overall result is a spectrum resembling a watt spectrum with possibly a small thermal peak in addition (though this was not used as a start spectrum). This neutron spectrum (called BSS-spectrum, pp, see figure 6.12) was used for further calculations in the water- and voxel phantom.

CHAPTER

7

Calculation of neutron and photon depth dose profiles

In the course of this work the first steps towards a detailed patient treatment planning program were done. The task was tackled in two steps. First depth dose profiles inside a water phantom were calculated and compared to measurements performed by Kampfer [65, 64, 63]. After this validation of the dose calculation, the patient dose calculation for a salivary gland tumour treatment was simulated using a voxel phantom. In addition, the means for biological dose weighting were introduced and tested in principle.

7.1 Water phantom

A water phantom is often used in radiation therapy to measure depth dose profiles and thereby characterise the beam. In the case of photon irradiation with a linear accelerator, a water phantom is usually used to do basic dosimetry. This was also the case for the FRM II beam, which consists of neutrons as well as photons. Depth dose and lateral dose curves were measured by Kampfer [64]. These measurements were simulated with GEANT4 in the course of this thesis and compared to the measured data. For this purpose, two different types of water phantoms were implemented in GEANT4 (see 7.1.1). One is a straightforward implementation of the real phantom, the other is a voxelised adaption. The second one was used to test the voxelisation algorithm and the calculation process in GEANT4 in a voxelised geometry. As primary neutron spectrum, the unfolded Bonner sphere spectrum obtained in the present work (see chapter 6.5.1) was used for both phantoms as well as another spectrum (by Breitkreutz, [16]).

Furthermore, a primary photon spectrum which was calculated by H. Breitkreutz [16] with MCNP was used to estimate the part of the dose that is caused by photons. This spectrum has a large uncertainty and the total photon flux had to be adapted (see chapter 7.1.4). Therefore, it might be that the calculated gamma depth dose agrees well but not excellently with the measured data.

7.1.1 Geometry of the water phantom

The experiment was performed with a water phantom consisting of a box of perspex filled with about 200 litre of water. It had a beam entry window (sealed with two aluminium plates) and a device for positioning the ionisation chambers. This water phantom was simulated in two different ways: by a solid box of water with little measurement chambers inside and in voxelised form consisting of over 10 millions of little water boxes. Both phantoms consisted of water and were put into a cubic container out of perspex with dimensions 63.5 × 63.5 × 52 cm^3 and 2.0 cm wall thickness (material definition see table 7.1). For the voxelised phantom, the dimensions were slightly enlarged to 64 × 64 × 52 cm^3 to simplify the voxelisation algorithm, and voxel sizes of 0.2 × 0.2 × 0.5 mm^3 were used in accordance with real CT-pixel and CT-slice dimensions. The perspex container has a window of 12 × 34 cm^2 size which is sealed with two aluminium plates of 1.5 mm thickness.

atomic composition *	physical quantities	
ratio of elements: C: 5 O: 2 H: 8	temperature = 300 K state of aggregation = solid (kStateSolid) density = 1.19 g/cm^3	for energy loss purposes: ChemicalFormula = "(C_2H_4)_N_Polyethylene"

Table 7.1: *Specification of perspex in* GEANT4*; hydrogen in water* (TS_H_of_Water) *was used for the thermal scattering of neutrons; *natural composition of isotopes*

A beam size of 9 × 9 cm^2 was chosen, similar to the experiment, and the beam was assumed to be homogeneous over the whole cross section without beam divergence.

The detector device inside the whole solid water box was simulated as a tube-shaped chamber with a radius of 0.376 cm and a height of 1.208 cm, resulting in a detector volume of 0.5365 cm^3 (material = water). It should be mentioned that in the simulation, no correction factors were needed because the described setting represents an undisturbed measurement in contrast to the real measurement by Kampfer [64]. The chambers were parametrised in such a way that the first chamber is placed at 0.5 cm depth in water, followed every centimetre by another detector chamber. This tube chamber corresponds well with the ionisation chamber used for the real measurements (volume 0.5 cm^3 [1 cm^3 for the PTB-chamber], shaped like a thimble, [64]). In total there are 40 measurement points which corresponds to a maximum measurement depth of 39.5 cm. In the case of the voxelised phantom, the parametrised tubes were removed and the depth-dose scoring was done directly inside the voxels.

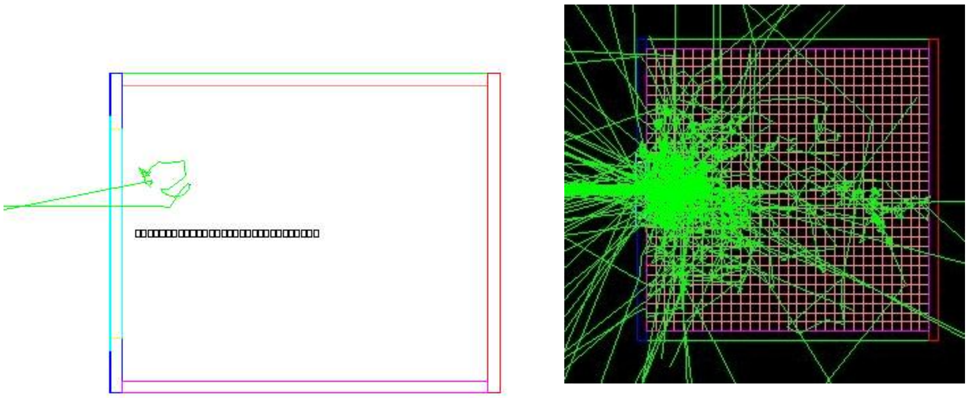

Figure 7.1: *The two types of simulation for the water phantom geometry:*
left*: simple box phantom with the measurement chambers inside (which are also out of water) with one incoming neutron track;*
right*: x-y-plane of the voxelised phantom with tracks from 100 primary neutrons of the FRM II beam. For visualisation purposes, 2 cm voxel size was used here*

In the voxelised geometry, the total absorbed dose and the absorbed dose caused only by primary and secondary photons and electrons is scored, simulating the real measurement, where both the neutron and photon doses were determined (see chapter 7.1.2). In the case of the simple geometry it was possible to collect more information: the total, neutron, proton, electron/positron and photon dose were all scored separately as well as the local moderated neutron fluences in the 58 energy bins. Therefore, a detailed analysis was possible for the neutron energy deposition.

For the simple geometry, the influences of the surrounding walls, floor and roof were also studied. The patient treatment room was implemented in a schematic way, using

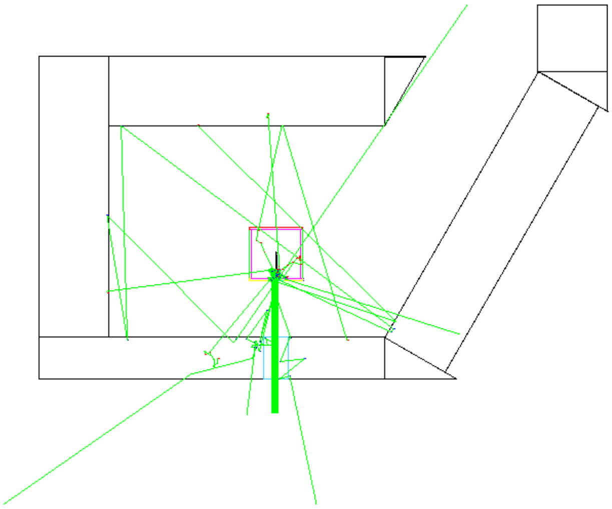

Figure 7.2: *Geometry of the walls at the beam line SR10 of the FRM II; wall material chosen was* G4-concrete*; thickness = 80/50 cm; $20 \times 30\,cm^2$ beam window; distance to floor/ceiling = 145 cm; 10 neutron tracks are shown*

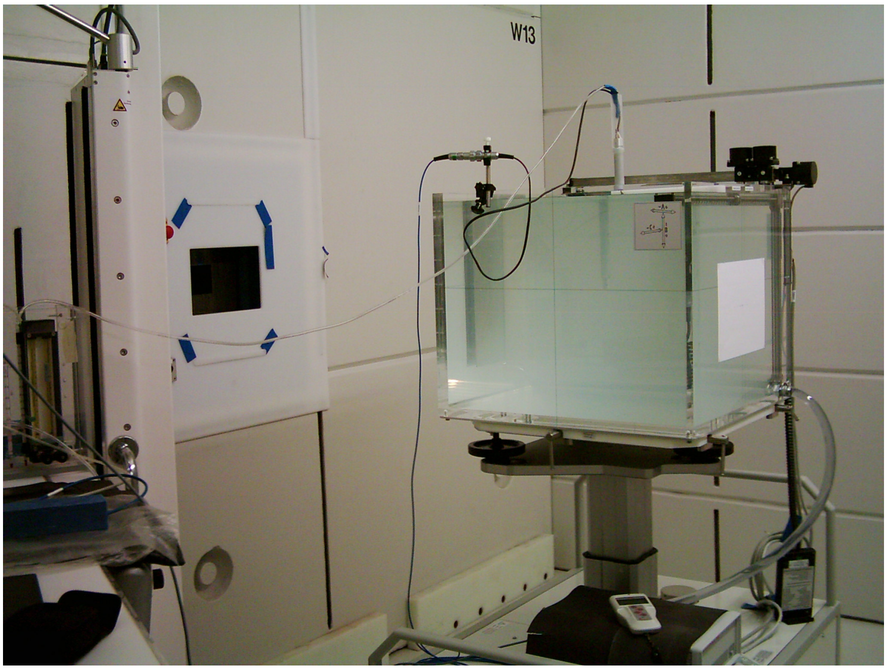

Figure 7.3: *Water phantom at the irradiation position. At the left side of the picture, the beam exit window can be seen [65].*

G4-concrete from the NIST-material database as wall material. The walls were simulated to be 80 (50) cm thick with a beam exit window of $20 \times 30\,cm^2$ size. In figure 7.2 a top-view of the simulated room is shown together with 10 neutron tracks using the unfolded BSS-spectrum.

7.1.2 Description of the experiment

For the measurement [64], the two ionisation chamber method described in [110] was utilised to separate the neutron and photon absorbed doses inside the water phantom. In principle, the two chambers must be of different sensitivity for neutrons. This is normally managed by taking one out of tissue equivalent (TE) material (with high hydrogen content) and the other out of material without hydrogen (Mg/Ar or a Geiger-Mueller counter (which is not possible with the intensive therapy beam)). In this case, a TE-chamber (EXTRADIN, T2) and a Mg/Ar-chamber (EXTRADIN, M2) were used [64]. The basic principles of the measurement are explained in appendix F.1 and the results are plotted in figure 7.4. The neutron to photon absorbed dose ratio for the beamline 10 with medical filtering was determined to be 2.7 at 2 cm depth inside a PE-phantom. This is in good agreement with the characteristics of the old RENT beam [64].

7.1.3 Calculated primary neutron depth dose curves

The total depth dose pattern of the FRM II neutron beam spectrum as determined with the Bonner spheres (see chapter 6.5.1) was calculated inside the tube-shaped measurement chambers and the voxels, respectively. The absolute absorbed dose value was determined by calculation of the energy deposited inside the chamber or voxel per pri-

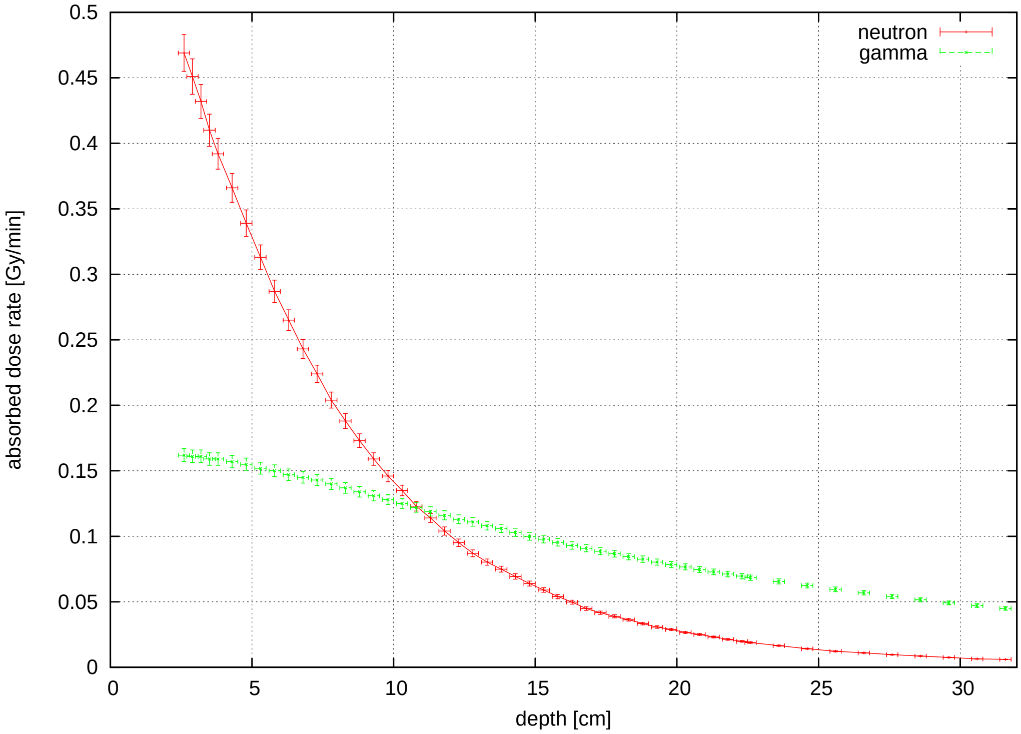

Figure 7.4: *Measured depth dose distribution of the therapeutical neutron-photon field at the FRM II in Garching, SR10; 3% uncertainty in dose measurement and 2 mm in position; already corrected for 2 mm measurement point displacement [64]*

mary neutron in GEANT4 and multiplication with the total flux of $3.2 \cdot 10^8\,\mathrm{cm}^{-2}\mathrm{s}^{-1}$ afterwards. This flux value was determined independently by a gold foil activation in a water phantom [16] and by the Bonner sphere measurement with a correction for distance to converter afterwards (see chapter 6.5.2).

In order to sample the neutrons in the calculation according to the measured spectrum, this spectrum was integrated and normalised. From this probability function, the primary neutrons were sampled using random numbers (see chapter 4.1.5 for a detailed description). In the measurement chambers of the simple geometry, the proton, electron, photon and neutron absorbed doses and for the voxelised geometry, the dose from low-LET particles (electrons, positrons, photons) was scored separately in addition to the total dose.

In figure 7.5 the calculated depth dose distribution of different monoenergetic primary neutron beams is depicted together with that using the measured FRM II neutron spectrum. This spectrum is a mixture of neutrons with energies between some eV's and about 10 MeV, peaking at about 2 MeV (see figure 6.12). Therefore, the depth dose curve does not resemble one of the other curves alone, but rather a mixture of all together. The same can be seen in figure 7.6, where the relative part of the dose for some secondary particles is plotted. For the FRM II spectrum, the largest part of the energy is deposited by protons. It is clearly visible that the quality and therefore also the depth dose behaviour of the FRM II spectrum consists of a mixture of neutrons with

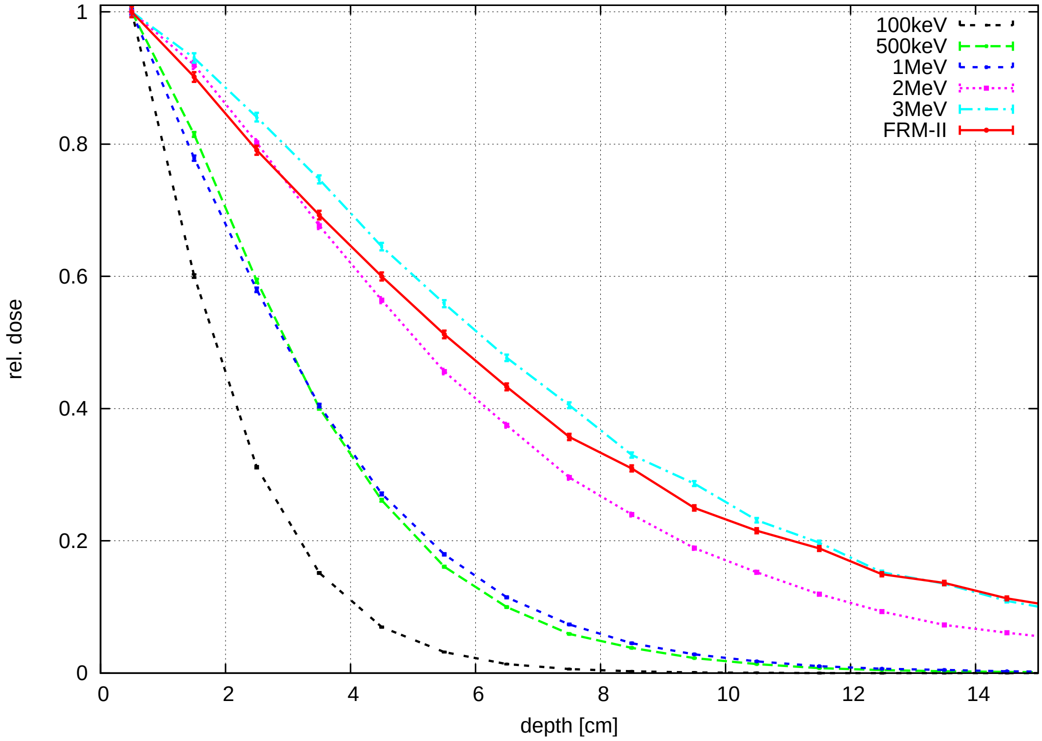

Figure 7.5: *Normalised depth dose curves for different monoenergetic primary neutron beams and the FRM II spectrum, calculated with GEANT4*

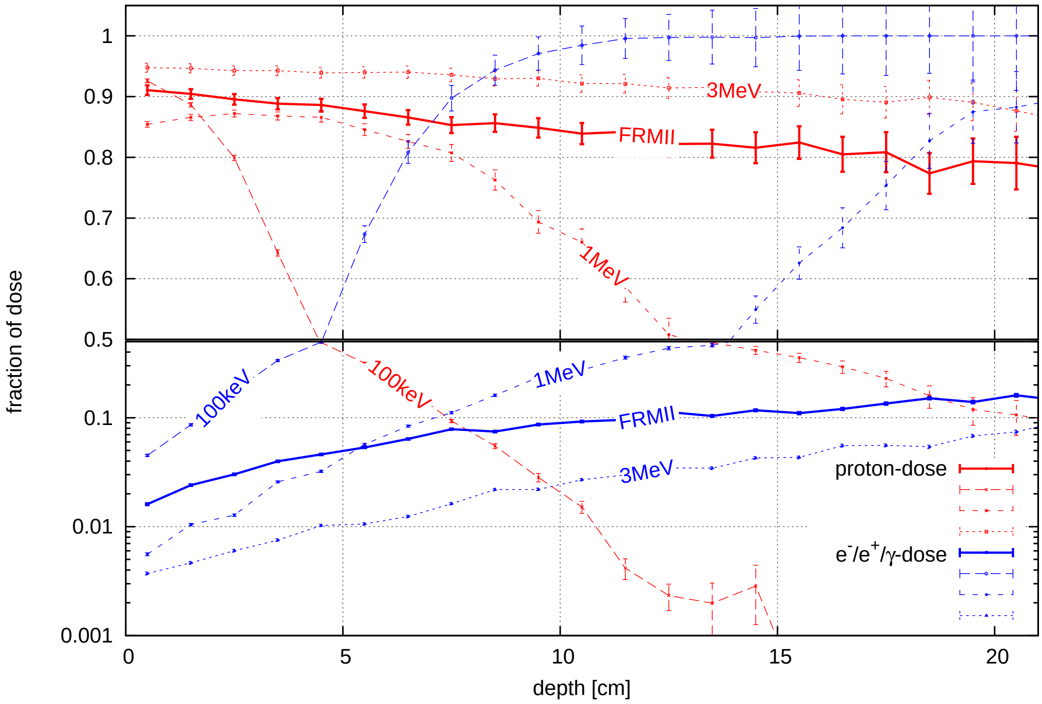

Figure 7.6: *Fraction of dose deposited by protons or low-LET radiation for different monoenergetic primary neutrons and the FRM II spectrum (note the change in scale of the y-axis)*

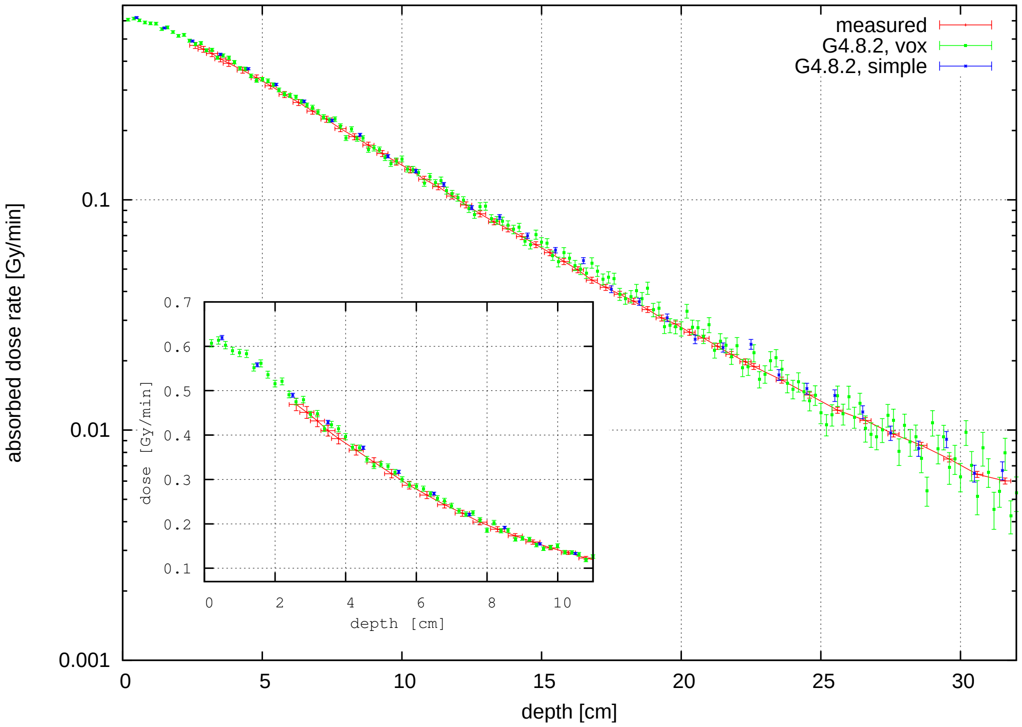

Figure 7.7: *Absolute neutron depth dose in the water phantom: comparison between voxelised (green, integration over 8 central voxels) and simple geometry (dark blue) calculated with* GEANT4 *together with the measurement of Kampfer [64]; The inset displays the neutron depth dose rate in a linear scale for the first 10 cm*

different energies. Close to the surface, the contribution of the secondary protons from the FRM II spectrum to absorbed dose is even smaller than that from 100 keV-neutrons and vice versa for the low-LET radiation. But as these neutrons get thermalised with depth, the proton and low-LET fraction of the FRM II depth dose tend to lie between that of the monoenergetic 1 and 3 MeV-neutrons. The fraction of dose for the different secondary particles close to the surface can be compared to the part of the KERMA, which is shown in figure B.8 in chapter B.2. There, it is also shown that the leading dose contribution is deposited by protons, followed by heavy recoil ions which were not scored separately here.

In figure 7.7, the calculated absorbed dose rates in the simple and the voxelised geometry are shown together with the measured depth dose curve (with logarithmic dose presentation, the inset with linear dose). The results of the simple and the voxelised geometry are in excellent agreement (see also appendix F.2). The latter was integrated over 4 voxels in lateral and 2 voxels in vertical direction around the central beam axis to get a better statistics (resulting in a dose collection volume of 0.16 cm^3 from 8 voxels). This demonstrates that the voxelisation algorithm (for a description see chapter 4.1.2) produces the same results as the non-voxelised calculation.

A second result displayed in the plot is the excellent agreement between the calculations and the measurements (see also appendix F.2). The decrease with depth of

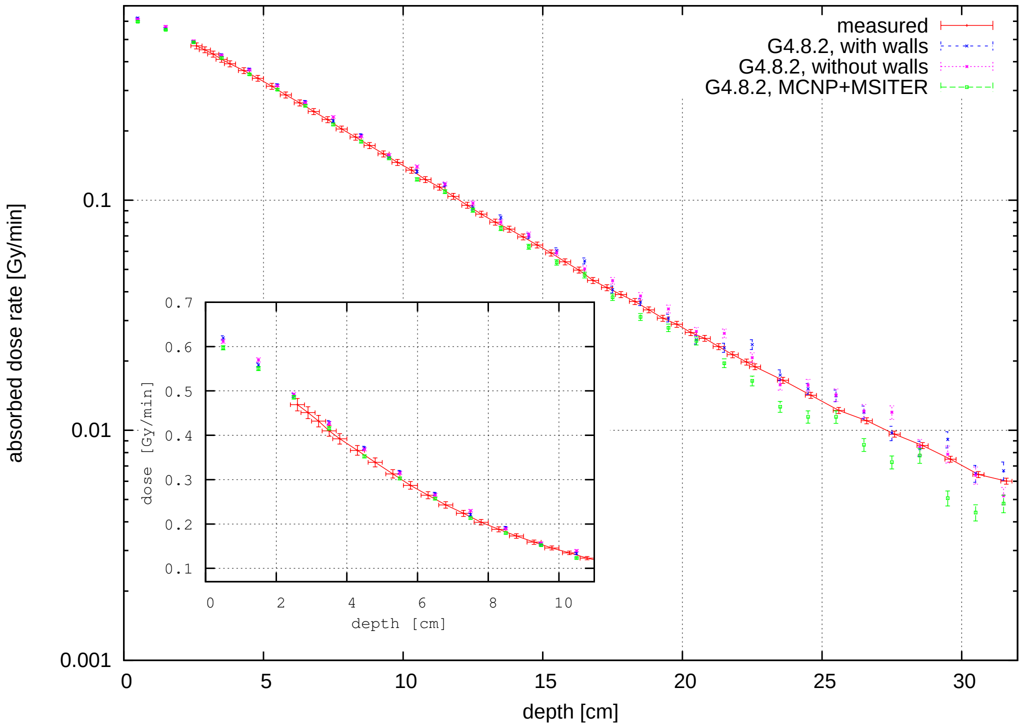

Figure 7.8: *Absolute neutron depth dose in the water phantom: comparison between Bonner sphere measured spectrum (BSS-spectrum, pp see chapter 6.12) with (blue) and without (pink) surrounding walls and the GEANT4-calculated depth dose curve of MCNP+MSITER-spectrum from [16] (green); The inset displays the neutron depth dose in linear scale for the first 10 cm*

both curves is very similar. Small differences between the measured and the calculated curves in terms of their absolute values are partly due to the different date of the measurement (the Bonner sphere measurement took place approximately 1 year after the depth dose measurement, resulting in a small converter plate burn-up of approximately 2% [16]) and for greater depths due to calculation statistics. The dependence of W_n on the neutron energy spectrum (see discussion in F.1) seems to be negligible as the depth dependence of the measured values (where the W_n dependence on energy was not included) is practically equal to the calculations where it is inherently considered. But small deviations may also be explained by this difference.

In figure 7.8 a further comparison is plotted between the GEANT4-calculated depth dose curve of the BSS-spectrum with and without walls as well as the GEANT4-calculated depth dose curve of the MCNP+MSITER-spectrum [16]. It can be seen that the influence of the surrounding walls is of minor importance: for small and median depths (up to 10 cm) it is less than 2%. For simplification, the boron fraction in the walls was not considered. Simulating it would decrease the deflected neutron part even further as boron is bound to capture a greater part of the thermal neutrons and the resulting influence on the depth dose would be even smaller than it is without it. Thus, it is not necessary to consider the treatment room when calculating the dose in

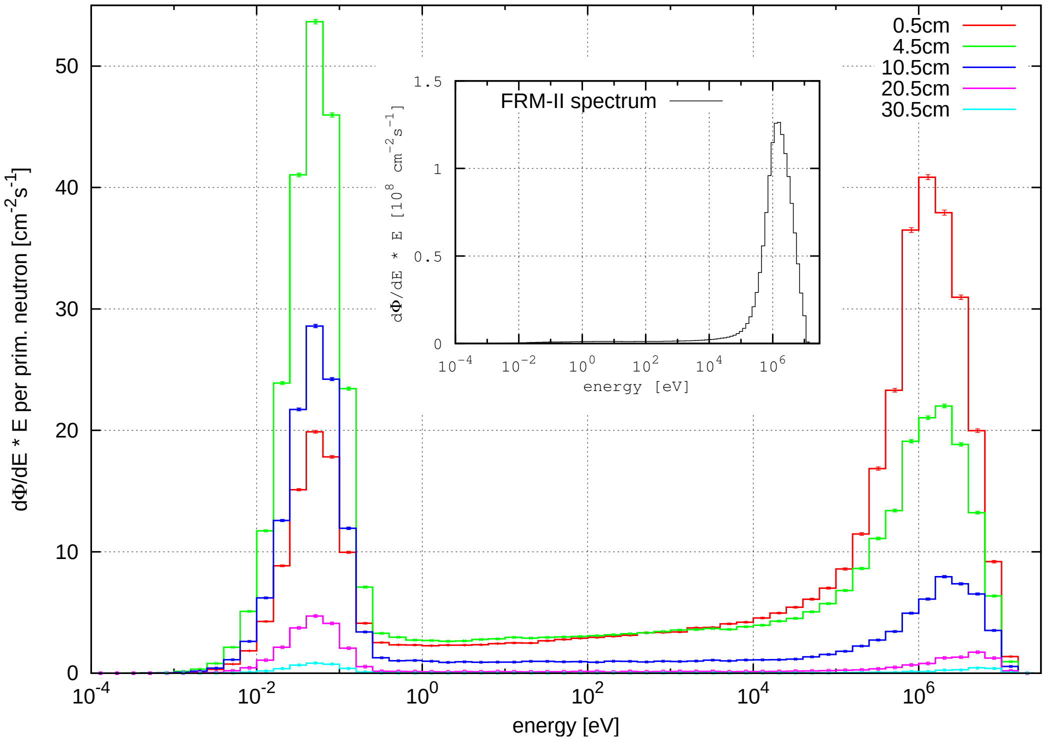

Figure 7.9: *Neutron spectra in different depth of the water phantom in fluence per primary neutron with the incident primary neutron spectrum (BSS-spectrum) in absolute scale as inset*

the voxel phantom or in a patient.

Besides the Bonner sphere spectrum, the spectrum determined with MCNP and threshold probes (MCNP+MSITER, [16]) was also used as input for a depth dose calculation with GEANT4. The difference between the two spectra was discussed in chapter 6.5.2. In the depth dose calculation, both spectra were treated in the same way, calculating the dose per primary neutron and multiplying this value with the total flux afterwards. Apparently, the MCNP-spectrum results in an almost identical depth dose curve, which is also well aligned with the water phantom measurements of Kampfer [64] (see also appendix F.2). The slight discrepancies may arise from the small differences in the spectra, primarily those of the high energy peak and the increase of neutron flux in the neutron energy region between 1 keV and 20 keV (for the bin at 2 keV, there are 90% more neutrons).

Another interesting quantity to study is the moderation of the FRM II neutron spectrum with depth in the water phantom (see figure 7.9). The inset shows the measured unfolded primary neutron flux (in lethargy presentation), which has practically no thermal part (see chapter 6.5.2). Comparing this with the spectra in different depths (0.5 cm, 4.5 cm, 10.5 cm, 20.5 cm, 30.5 cm), one can see that the neutrons are thermalised quickly. In 4.5 cm depth, the thermal Boltzmann-peak is already higher than the high-energy peak. These thermal neutrons scatter often inside the phantom, so that the total neutron flux is increased by more than 25% (compared to the value

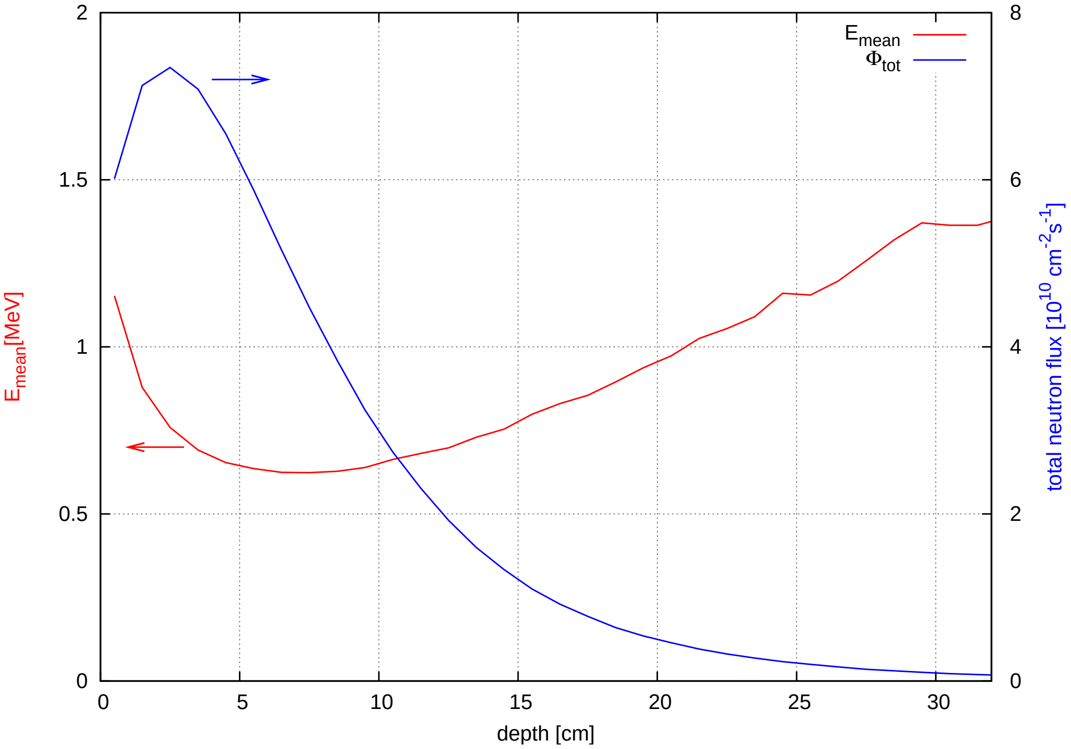

Figure 7.10: *Depth dependency of the mean neutron energy (left y-axis) and the total neutron flux (right y-axis) inside the water phantom*

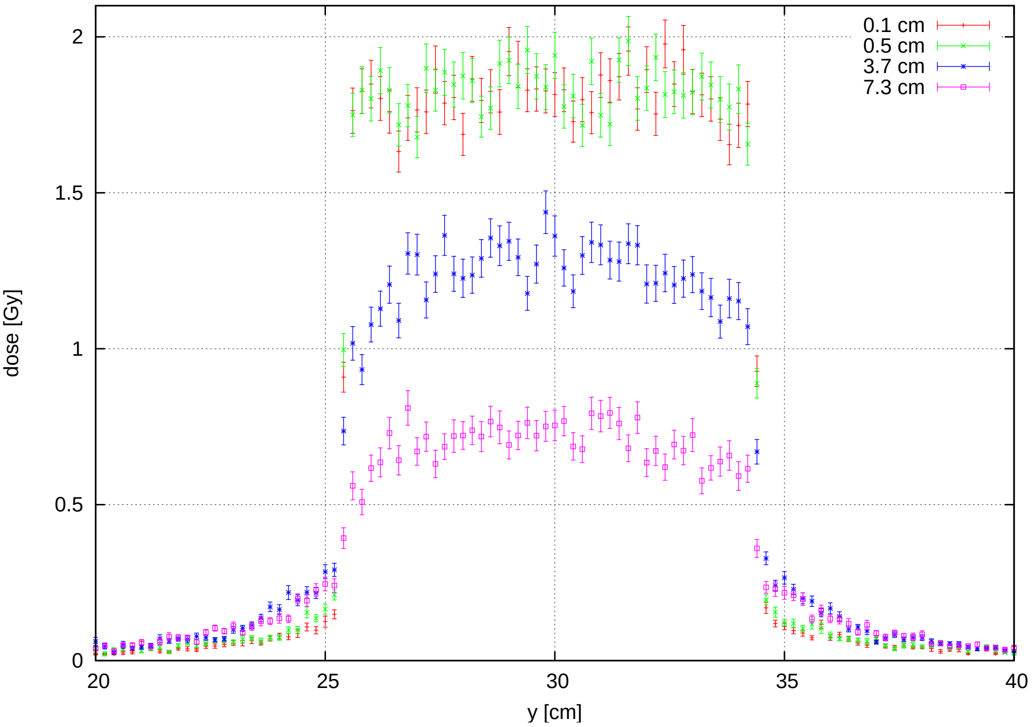

Figure 7.11: *Lateral dose distribution of the* $9 \times 9\,\mathrm{cm}^2$ *FRM II neutron beam in different depth inside the phantom after 3 minutes of irradiation with a total neutron flux of* $3.2 \cdot 10^8\, n/cm^2 s$*: 1 mm (red); 5 mm (green), 37 mm (blue), 73 mm (pink)*

at 0.5 cm depth) before it starts to decline for depths greater than 2.5 cm (see figure 7.10). That is also the reason why the fraction of depth dose deposited by low-LET particles is rising with depth in water (see figure 7.6). Thermal neutrons get captured and secondary photons with 2.225 MeV are released (see chapter B.2.4 for details on neutron interaction):

$$ {}^{1}_{1}\mathrm{H}(\mathrm{n},\gamma)\mathrm{d} \quad \text{with} \quad \mathrm{E}_\gamma = 2,225\mathrm{MeV} $$

On the other hand, the capture process concerns only low energy neutrons. Therefore, the spectrum is just thermalised to a certain degree. In greater depth the ratio of the peaks at high and low neutron energies is rising again, the spectrum is hardened. This can be clearly seen in figure F.2, where the spectra are plotted normalised to the thermal peak. For greater depths in the phantom, the ratio of the high energy to the thermal peak height is rising again. This is also the reason why the mean neutron energy is rising again after a steep decline within the first few centimetres (see figure 7.10).

In figure 7.11, it can also be seen that the neutrons are significantly scattered inside the water phantom and deposit their energy not only inside the beam profile but also in the surrounding tissue (see also figure 7.1 on scattering of neutrons). The sharp edges of the primary rectangular beam which can still be seen in the dose profile in the fist few millimetres are rounded off with depth so that e.g. in 7.3 cm depth, the dose declines over several centimetres. This beam spread is even more pronounced for the real beam, because the beam divergence of 2-3° as well as the penumbra of the different filters and collimators were not included in these calculations, but would further increase beam expansion.

7.1.4 Calculated primary photon depth dose curves

The FRM II treatment beam also consists of a photon part, which is caused by the interaction of neutrons with material inside the reactor core, the converter plates and the beamline. This primary photon spectrum has not yet been measured up to this moment. However, a MCNP calculation has been performed [16] starting from a position which has no influence on both the converter plates and the reactor core. The photons are then transported through the beamline up to the patient treatment position. Due to the lack of knowledge on starting particles at the source position, the validity of the resulting spectrum is poor. Furthermore, the simulation of delayed photons, released by activated material inside the beamline, is not possible with MCNP and the total photon flux is therefore about 40% to low (for a detailed discussion, see [15]). Nevertheless, this spectrum was used as a first clue to obtain information on the photon depth dose distribution.

The photon spectrum inside the water phantom was simulated in GEANT4 in the same way as the neutron spectrum, by calculating the probability functions (by integration and normalisation) and selecting the energy of the primary photons with a random number (see chapter 4.1.5). Both the simple and voxelised geometry were used and the result compared to the measured data from Kampfer [64]. It should be noted that the measured photon dose includes contributions from secondary photons produced by

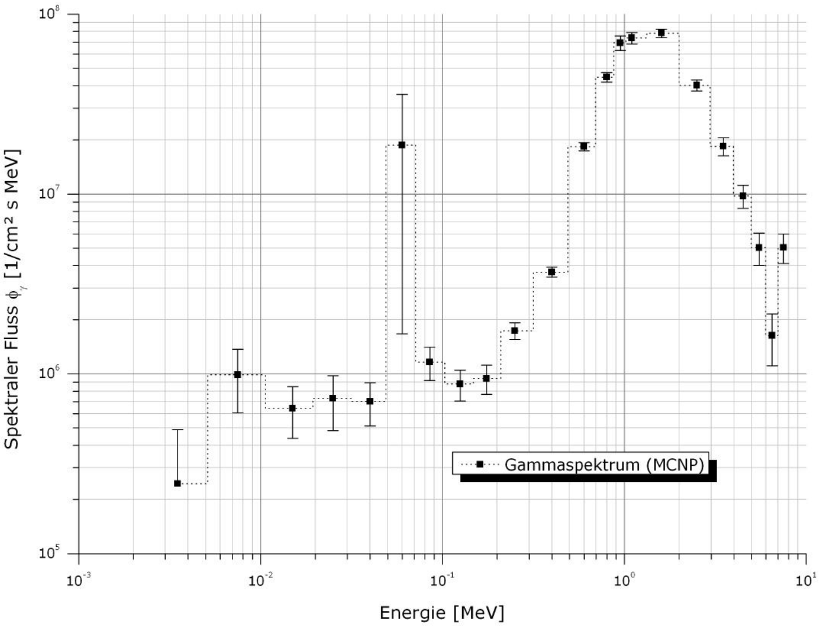

Figure 7.12: *FRM II photon spectrum, calculated by Breitkreutz with MCNP [16]*

the neutrons inside the water phantom as the two-ionisation-chamber method cannot distinguish between primary and secondary photons. The results are shown in figure 7.13. Again, the voxelised and simple geometry produce the same result (compare green and gray data), which verifies the voxelisation algorithm once more. Furthermore and similar to the neutron case, inclusion of the surrounding walls seems to have no effect again on the depth dose curves (compare green and black data).

In the plot, both the dose from primary photons and from secondary photons, which were caused by primary neutrons, are shown. Because the depth dose curve of the neutrons is consistent with the measured data both in relative and absolute terms, the secondary photon depth dose curve can also be assumed to be correct in absolute value. On the whole, the contribution from the secondary photons amounts to about 15% of the total photon dose in the first centimetres. On the other hand, figure 7.13 clearly shows that the summation of the calculated primary and secondary contribution leads to a curve which is somewhat lower than that measured (compare light blue and red data). It can be concluded, therefore, that the total primary photon flux which was calculated to be $1.8 \cdot 10^8\, cm^{-2}s^{-1}$ might be too low. For test purposes, the flux was therefore increased until the calculations matched the measurements. This adaption resulted in a best estimate of the photon flux of $2.9 \cdot 10^8\, cm^{-2}s^{-1}$. That means that the incident flux of photons and neutrons are rather similar. Furthermore it can be seen in the figure that the overall decline of the calculated depth-dose curve is somewhat shallower than the measured one (compare dark blue and red data). This suggests that the calculated spectrum [16] might have been harder than the spectrum present when the dose measurements by Kampfer [64] were performed. These discrepancies could arise from the poor original information available for the MCNP calculations. Nevertheless, the depth dose curve does not deviate much in the first 10 cm, so the spectrum can be used together with the adapted flux for the calculations in the voxel phantom.

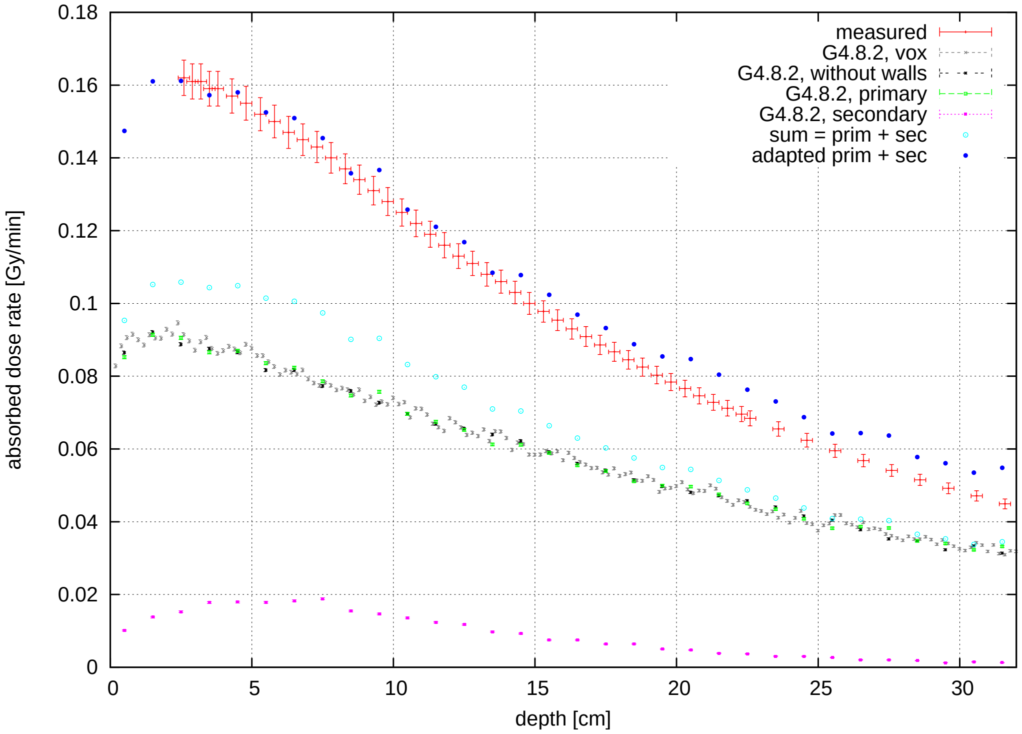

Figure 7.13: *Primary and secondary photon depth dose curves in comparison to measured [64] data;* GEANT4-*calcualtions in different geometries; for a detailed discussion, see text*

7.1.5 Calculated secondary particle spectra in ICRU-tissue

In the simple geometry, the water inside the phantom and the 40 measurement chambers was replaced by ICRU-tissue (definition see section 5.1.1). Then, the secondary particle spectra (protons and alpha-particles) were scored in different depth. The results are shown in figure 7.14, which can be compared to the neutron flux in different depth shown in figures 7.9 and F.3. Because of the incoming spectrum of neutrons, the proton and alpha spectra do not resemble the secondary particle spectra plottet in figure B.2.7, but display a wide distribution peaking at 3 MeV for protons and about 5 MeV for alpha-particles. The mean proton energy is slowly rising from 2.7 MeV in 0.5 cm depth to about 5 MeV in 40 cm depth while the total proton flux is decreasing strongly.

7.1.6 Conclusions

Primary photon and neutron spectra were used to calculate by Monte Carlo Transport simulation depth dose distributions inside a water phantom with GEANT4 [35]. The neutron spectrum used was that measured in the patient treatment room with a Bonner sphere system. For the photon spectrum, a spectrum was used that was calculated with MCNP [16] but which suffered from lack of sufficient input data. The results obtained in the GEANT4 calculation using this spectrum must therefore be interpreted with

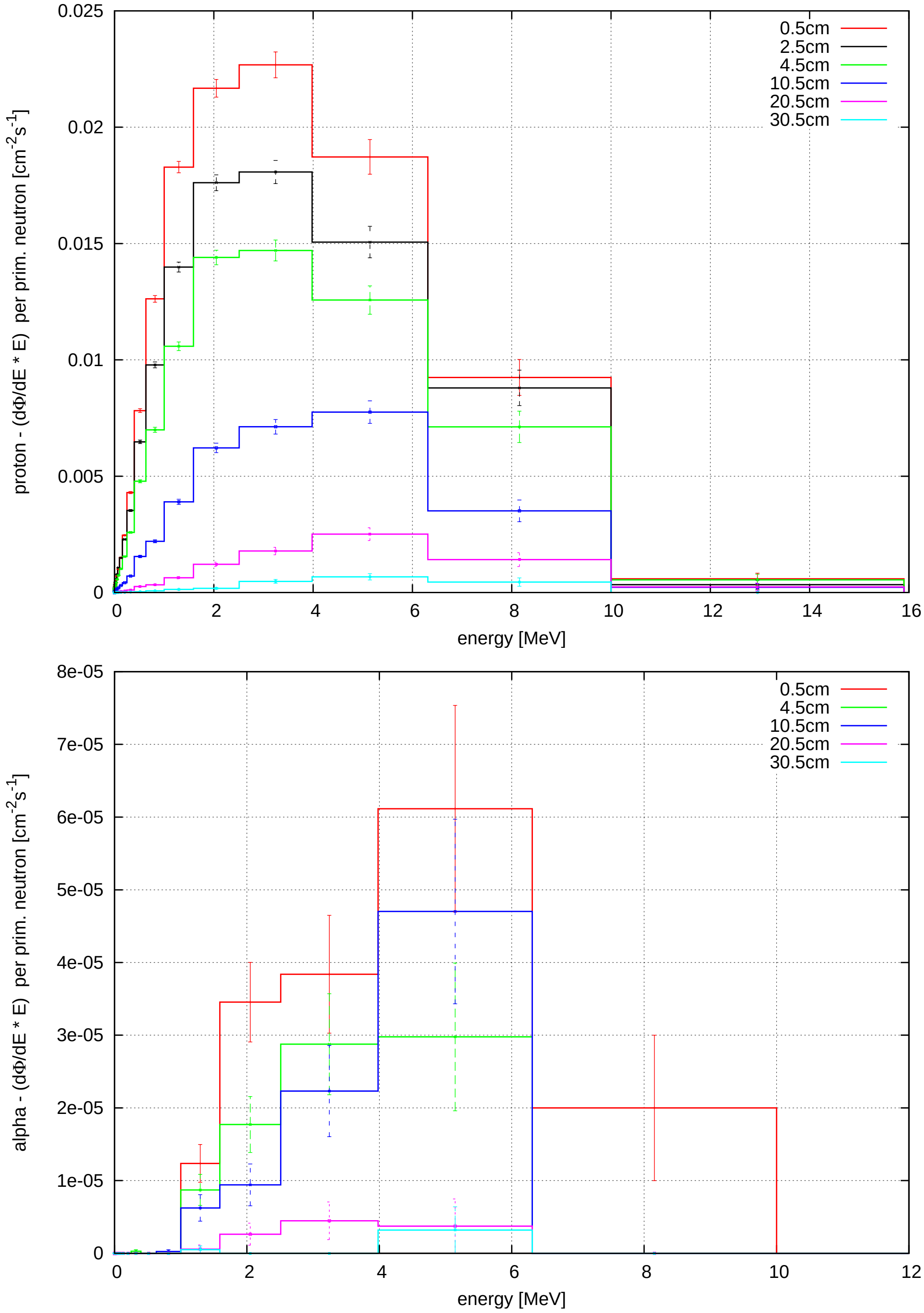

Figure 7.14: *Secondary particle spectra per primary neutron in different depth of the simple water phantom geometry (water was replaced by ICRU-tissue); top: protons, bottom: alpha*

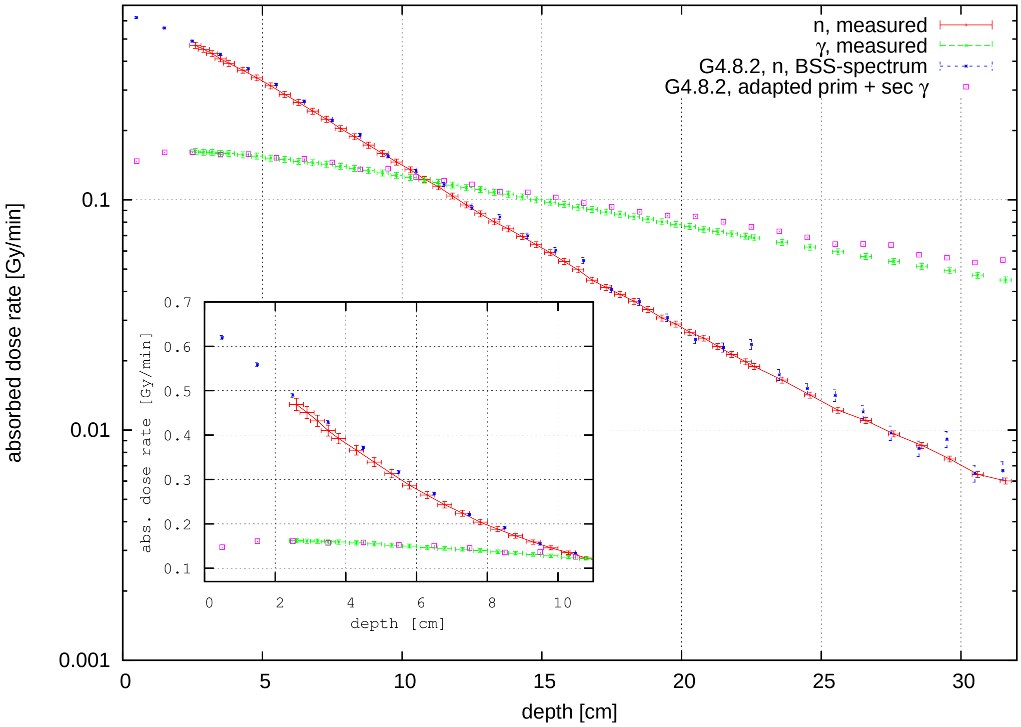

Figure 7.15: *Neutron and photon depth dose curves in comparison to measured data; the inset shows the dose deposition in the first 10 cm in linear scale; the measured total neutron flux of* $3.2 \cdot 10^8\, n/cm^2 s$ *was applied as well as the fitted photon flux of* $2.9 \cdot 10^8 cm^{-2} s^{-1}$

care. The main results are that GEANT4 calculations with the neutron spectrum measured with Bonner spheres at the FRM II and unfolded with MSANDB (see chapter 6) produce neutron depth dose curves which agree excellently with the measurements. For the primary photon spectrum calculated with MCNP [16], an adaption in total photon flux had to be done. The resulting photon depth dose curve agrees acceptably with the measurements. The resulting depth dose curves for neutrons and photons are combined in figure 7.15. Both the Bonner sphere system neutron spectrum and the calculated MCNP photon spectrum can therefore be used as an input for depth dose calculations in depths which are relevant for patient treatment planning in the head and neck region (see chapter 3.2 for details on application at the FRM II).

7.2 Voxel phantom

The calculation of the dose distributions for patient treatment planning and its biological consequence assessment with a Monte Carlo program such as GEANT4 requires not only the knowledge of the electron density like in normal treatment planning for photon irradiation with a linear accelerator but also the exact atomic composition of each irradiated tissue. Therefore, a voxelised description of the patient must be used, where the atomic and even isotopic composition in each voxel is known. This can be obtained by segmentation of patient CT-data. In the tissue segmentation, the Hounsfield-numbers (which are basically electron densities) are transferred into material information. This process cannot be performed fully automatically up to this date and significant user interaction is always needed. This is required because simple linear density-material relationships are not enough to distinguish between all tissues involved. Therefore, in this work a voxel phantom developed by Zankl et al [107] was used as a first example. This phantom was created for radioprotection purposes out of a CT-dataset that was obtained from real human data. The voxel phantom and its implementation in GEANT4 was described in section 4.2. In the next sections, a case of a salivary gland treatment is studied.

7.2.1 Description of the irradiation geometry

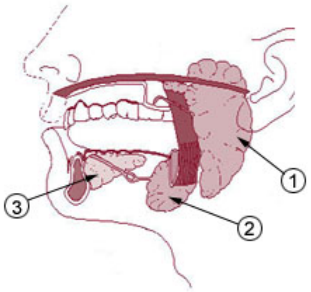

Figure 7.16: *The three salivary glands [2]:*
1) parotid gland
2) submandibular gland
3) sublingual gland

The chosen test case was a salivary gland treatment of the right submandibular gland (lower jar salivary gland, see figure 7.16). Because the real field size applied to the patient was almost a rectangle (see left side of figure 7.17), a rectangular beam with 6 cm · 7 cm cross section was simulated, coming from 270°, which corresponds to the right side of the patient. The isocentre was also placed in accordance to that of the real patient case using the skeletal structure as a guideline. Some approximations had to be made because the head-to-body angle for the voxel phantom was different to that for the real case (see figure 7.17). Nevertheless, the whole calculation algorithm could be tested in this way and a first assessment of the energy deposition pattern was possible. It should be noted that the field shape can easily be changed in the simulation to adapt it to the shape of the PTV (definition see section 2.3.2) if necessary. The total

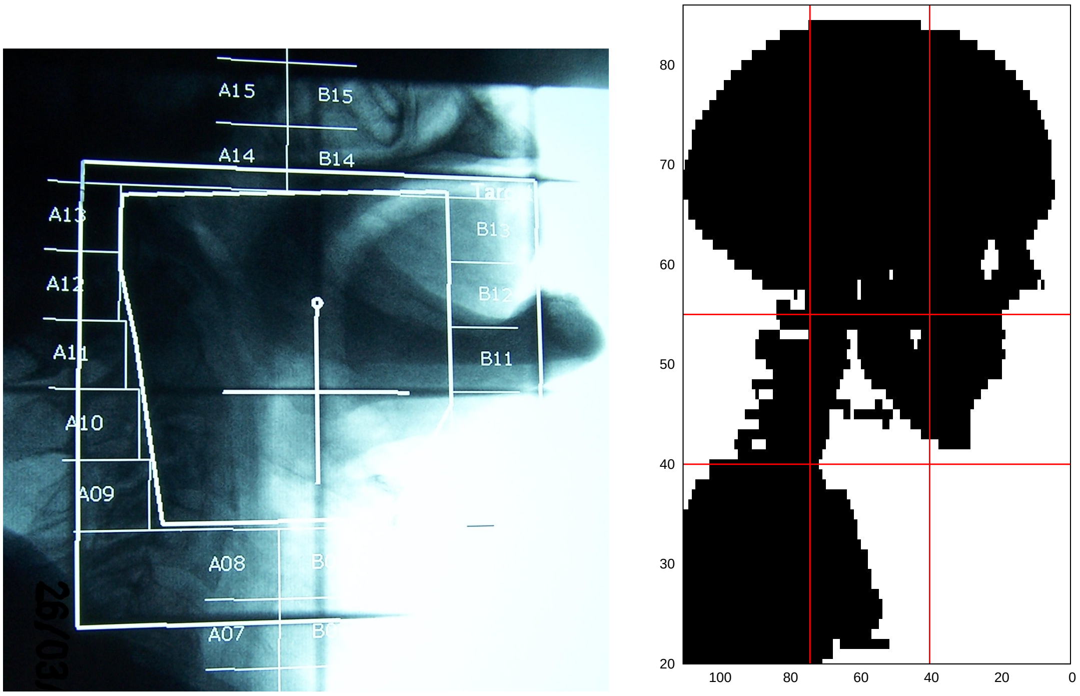

Figure 7.17: *Comparison of real treatment beam (control of beam field; left panel; Loeper, priv. com.) and simulated field in voxel phantom (bordered by red lines; right panel)*

primary neutron flux of $3.2 \cdot 10^8\, n/cm^2s$, which was already used for the water phantom calculations, was also used here together with the fitted incident primary photon flux of $2.9 \cdot 10^8\, \gamma/cm^2s$ (see discussion in section 7.1.4).

7.2.2 The neutron dose distribution pattern

The depth dose distribution of the setting described above was calculated with GEANT4 for the whole phantom. As a first overview, the depth dose curve of the central beam is compared to that obtained in the water phantom (see figure 7.18). The decrease of dose with depth is similar for both phantoms, but somewhat steeper for the voxel phantom because its atomic composition is different from water (for example, the hydrogen content (abundance) of adipose tissue (material number 28) is 62.5% compared to 66.7% in water). The change of material with depth in the voxel phantom is also seen in the figure (pink line). When the material changes, e.g. from 19 (skin) to 28 (adipose tissue) or to 21 (muscle), a change in the dose can also be seen. This can also be studied for the biologically weighted depth dose distribution, where the same material dependence is visible. For further discussion of the biologically weighted dose, see section 7.2.4.

In figure 7.19, the lateral absorbed dose distribution is shown for various depths inside the phantom. Comparing this with the lateral dose distribution in the water phantom (figure 7.11), the beam broadening can again be seen. Furthermore, a material effect is

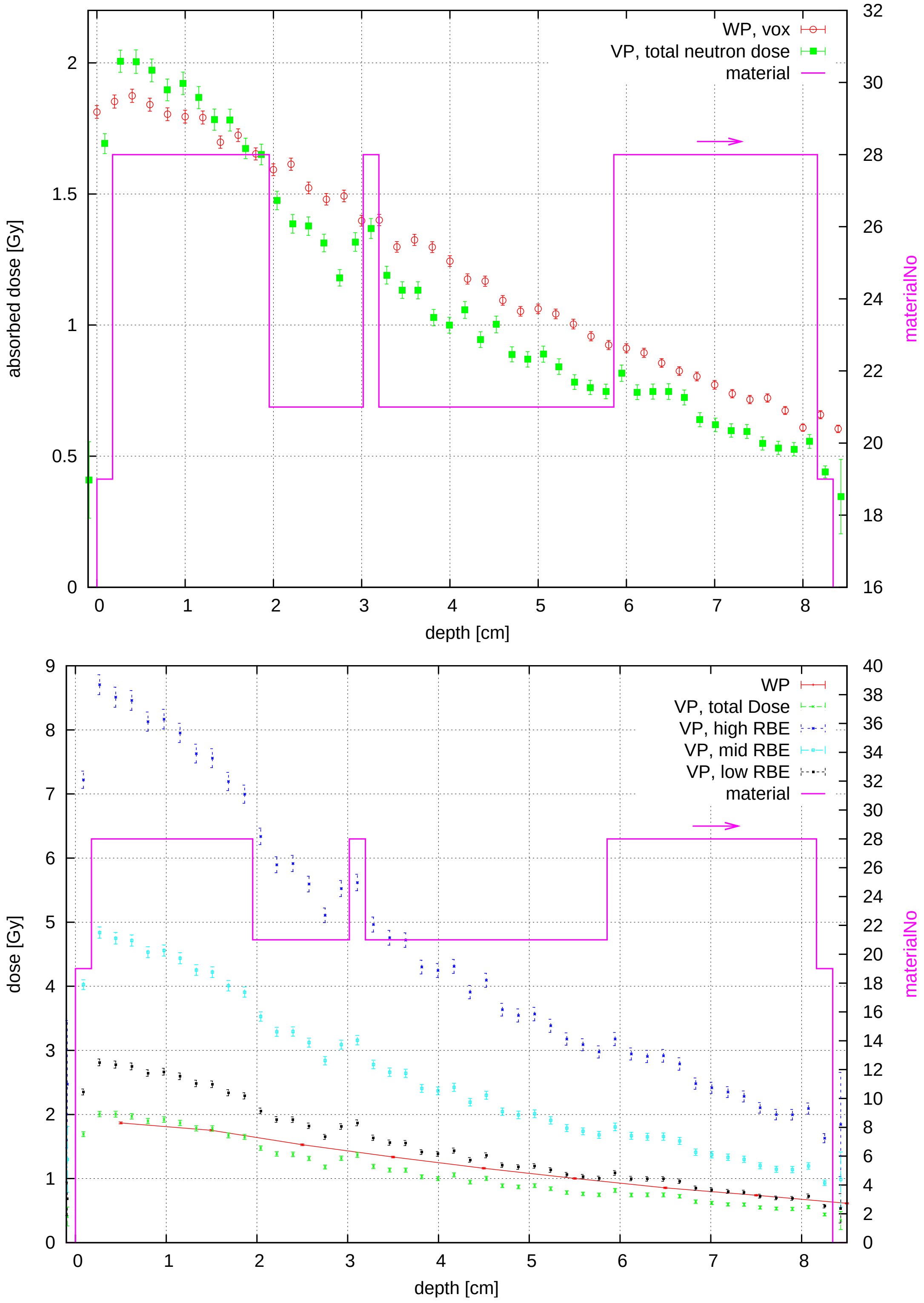

Figure 7.18: *Absorbed depth dose curves for the FRM II neutron beam in the voxel phantom at slice number 45 and row number 48 (which is in the beam centre) compared to those in the waterphantom (red): total energy absorbed dose (green) and evaluated doses (see figure 2.13): for type 1 (high response, dark blue), for type 2 (middle response, light blue), for type 3 (low response, black); All curves were calculated for 3 min irradiation with a primary neutron flux of* $3.2 \cdot 10^8$ *n/cm*^{2}*s (no primary photons)*

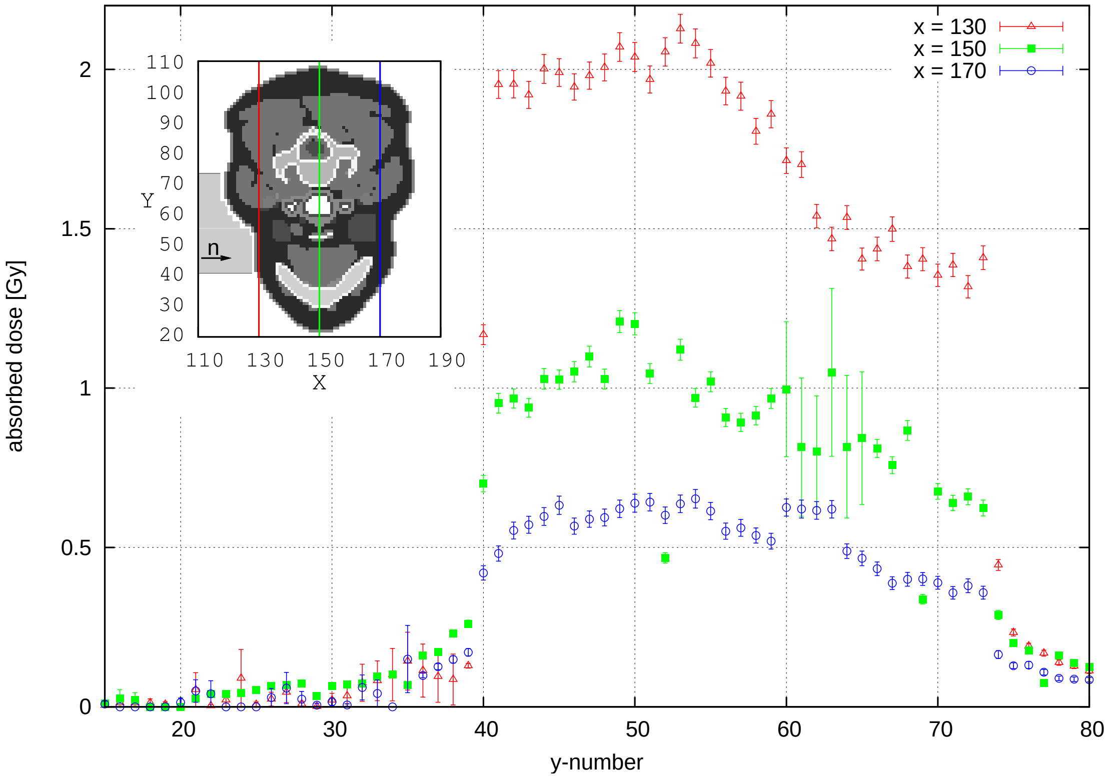

Figure 7.19: *Absorbed lateral dose distribution (column-wise) of the* $6 \times 7\,\mathrm{cm}^2$ *FRM II neutron beam in different depth inside the phantom after 3 minutes of irradiation with a total primary neutron flux of* $3.2 \cdot 10^8\ n/cm^2s$ *(no primary photons): row number 130 (red); 150 (green), 170 (blue) in slice number 44. The lateral beamsize is depiced in gray on the left side of the phantom from y=40 to y=74*

also visible. Towards the right side of the curves (higher y values), which corresponds to the back side of the phantom, the dose declines. This is caused by the phantom's uneven surface. Looking at the relevant slice (44), it can be seen that the neck starts to bulge in the relevant area. Therefore, the radiation is absorbed before reaching the relevant row number whereas on the left side of the curve, no such material is present (the voxels in row number 130 are basically the first voxels of tissue there). In the green curve (row number 150) an area of high statistical uncertainty can be seen between about y = 60 and y = 65. This is the area where the trachea is located and fewer particles interact with the air inside and deposit dose there. Behind this area, more energy is therefore deposited which can indeed be seen in the blue curve (row number 170).

7.2.3 Dose volume histogram

In patient treatment planning, another tool is used for plan quality assessment, i.e. the dose-volume-histogram (DVH, see section 2.3.4). In this histogram, the abundant spacial data is condensed into a plot giving the amount of volume of an organ irradiated

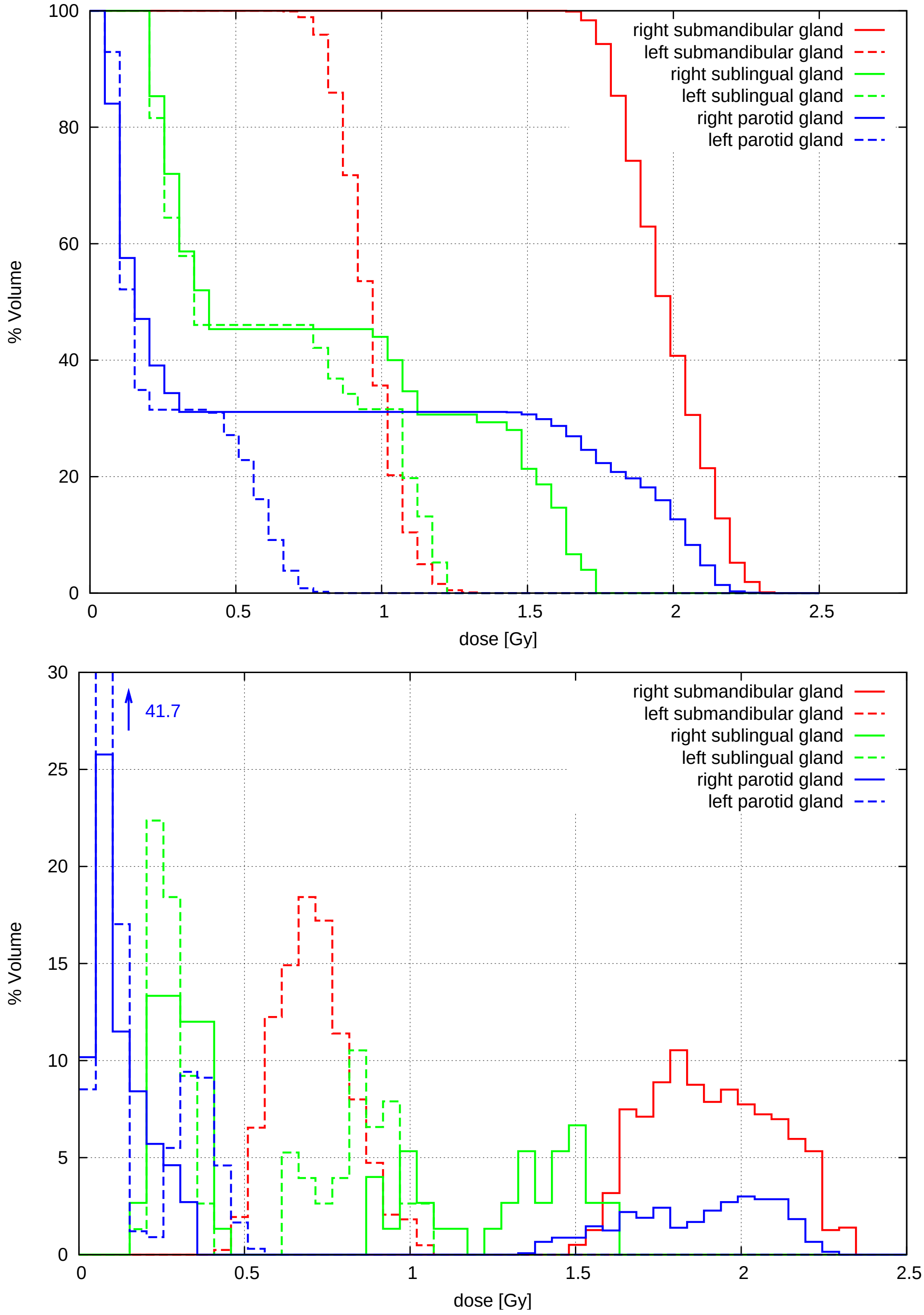

Figure 7.20: *Cumulative (top) and direct (bottom) dose-volume-histogram of the salivary glands after 3 min irradiation with the* $6 \times 7\,\mathrm{cm}^2$ *FRM II neutron beam, a total primary neutron flux of* $3.2 \cdot 10^8\ n/cm^2s$ *and a total primary photon flux of* $2.9 \cdot 10^8\ \gamma/cm^2s$ *(for position of isocentre see text)*

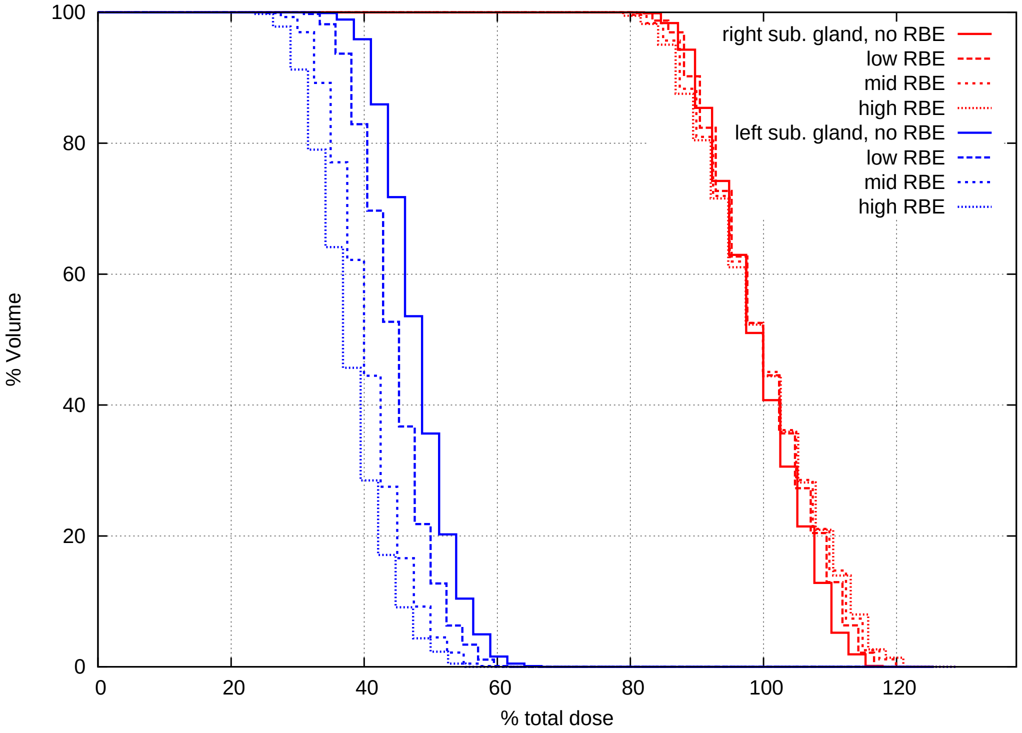

Figure 7.21: *Dose-volume-histogram of the left and right submandibular glands after 3 min irradiation with the* $6 \times 7\,\mathrm{cm}^2$ *FRM II neutron beam, a total primary neutron flux of* $3.2 \cdot 10^8\, n/cm^2 s$ *and a total primary photon flux of* $2.9 \cdot 10^8\, \gamma/cm^2 s$*, including the effect of dose weighting (for discussion see text)*

with a certain dose. In figure 7.20 the cumulative and direct DVH of the studied salivary gland case are depicted. Six organs are differentiated (see also anatomical drawing in figure 7.16): the healthy salivary glands of the patients' left side, the treated right submandibular gland and the right sublingual and parotid gland, which are also partly in the beam.

Figure 7.20, top, (cumulative DVH) shows that for the treated submandibular gland, the whole volume gets at least 1.63 Gy, and about 50% of the volume gets more than 2 Gy. This can also be derived from the direct DVH (figure 7.20, bottom), where it is shown that the ideal delta-curve discussed in section 2.3.4 is not obtained for the one-beam neutron irradiation. However, it should be mentioned that almost the same DVH would result from a pure photon irradiation from a linear accelerator, since it is characteristic for an exponentially declining depth-dose curve of a single field. For the other salivary glands of the right phantom side, it is evident from both figures that there is always some part of the volume which is directly exposed to the main beam and therefore gets considerable amount of dose (partucularly, this is can be seen in the direct DVH). The salivary glands of the left phantom side are somewhat shielded by the absorbing tissue in between and therefore get less dose on the whole.

In figure 7.21, the influence of dose weighting on the DVH of the left submandibular gland is indicated. For this plot, the artificial RBE-LET relationship discussed in section 2.4.2 was used to calculate a biologically weighted dose (for a detailed discussion on the dose weighting see section 7.2.4). It is visible that with higher RBE, the left submandibular gland, which is situated on the opposite side of the patient compared to the beam, gets less biologically weighted dose. This effect is caused by the photon part of the beam, which amounts to a higher fraction of the dose in the left compared to the right submandibular gland.

7.2.4 Neutron dose and biologically weighted dose

In figure 7.18, the depth dose curves for the three evaluated dose distributions discussed in section 2.4.2 for low, middle and high response, corresponding to the artificial RBE-LET-curves shown in figure 2.13 are displayed together with that for absorbed dose from the FRM II primary neutron spectrum. From these curves it can be seen that the dose increases by a factor of about 4.3, 2.3 and 1.4, respectively, for the three evaluated functions compared to the absorbed dose. From radiobiological experiments, it is known that the RBE of neutrons with TCP = 0.5 (TCP = tumor complication probability) varies between 1.61-1.95, depending on the depth in PE-phantom [71]. The RBE changes with the neutron spectrum [49], as can be seen in the plot as a small decrease in overall RBE with depth inside the phantom because of the beam hardening. It should be noted, however, that in the calculation, the dependence of the RBE on the dose was not yet included. In some experiments, cells displayed a decline of the RBE with increasing dose (see figure 2.9). So the rise of the RBE due to the hardening of the spectrum may be compensated for by the dose-effect. But this strongly depends on the exact RBE functions which have to be obtained first before a more detailed study is reasonable.

In figures 7.22, z-slices of the biologically weighted absorbed dose inside the voxel phantom are shown for the different evaluation functions of the RBE for a total primary neutron flux of $3.2 \cdot 10^8\, n/cm^2 s$. The increase in the biologically evaluated dose for higher RBE values can be seen as well as the dose decrease with depth inside the phantom. The low doses in hard bone material (edge-structure in the lower and upper part of the slice) may be due to the lower hydrogen content (31.2% element abundance compared to 62.5% in adipose tissue for example). Inside air cavities such as the trachea, the deposited dose is also reduced due to the low density and the lack of hydrogen. This can be seen in the middle part of the slice. In figure 7.23, the primary photon depth dose (for a total photon flux of $2.9 \cdot 10^8\, \gamma/\mathrm{cm}^2\mathrm{s}$) is shown together with the total dose from primary neutrons and photons (right panel, here neutrons are not weighted in any form). It can be seen that the total dose with primary photons is about 0.5 Gy higher than without them. This is particularly important for the healthy left salivary gland, because the depth dose of the photons is very shallow and therefore penetrates more into the tissue. This undesired effect will rise the dose to healthy tissues behind the tumour. However, it should be kept in mind that the RBE for photons is defined to be one for all energies, so this effect is less important if higher neutron RBEs are considered (see figure 7.21).

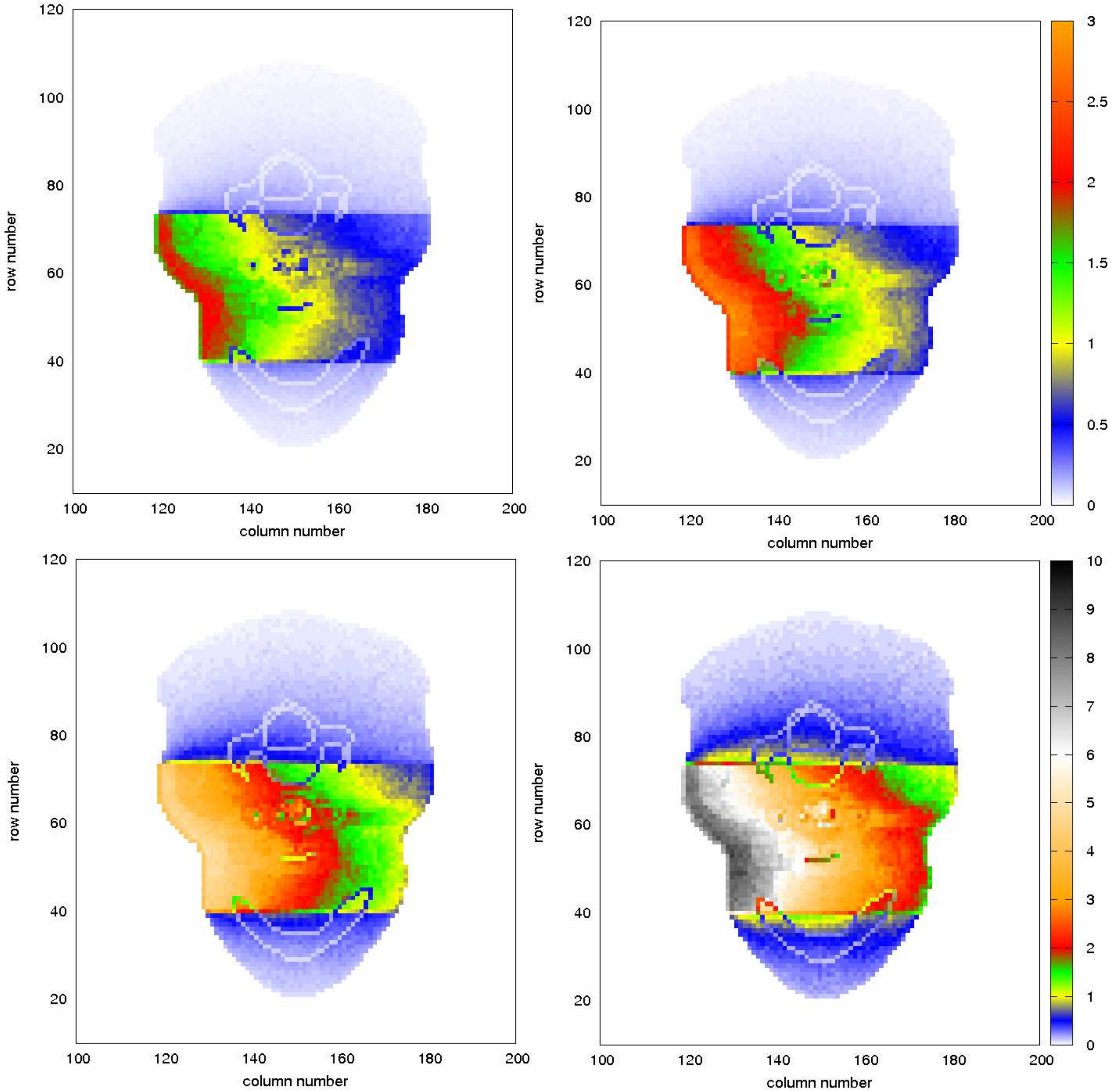

Figure 7.22: *Absorbed dose (in Gy or Sv) inside the voxel phantom after 3 min irradiation with the* $6 \times 7\,\mathrm{cm}^2$ *FRM II neutron beam and a total primary neutron flux of* $3.2 \cdot 10^8\, n/cm^2 s$ *(no primary photons included; for dose weighting see figure 2.13): top left: absorbed dose; top right: dose with low response weighting; bottom left: dose with middle response weighting; bottom right: dose with high response weighting;*

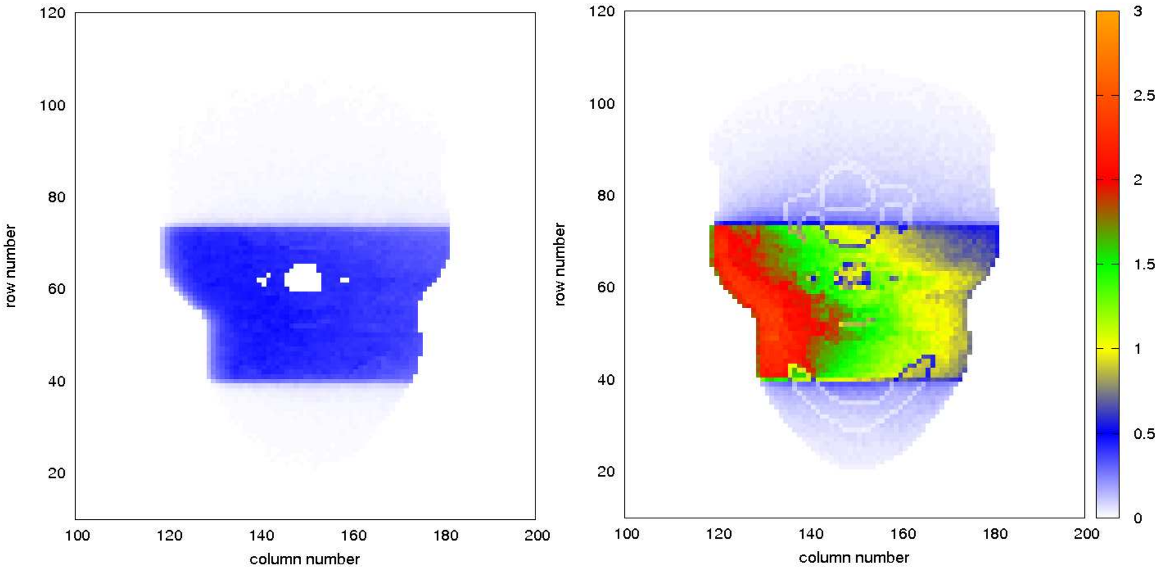

Figure 7.23: *Absorbed dose in Gy inside the voxel phantom after 3 min irradiation with the* $6 \times 7\,\mathrm{cm}^2$ *FRM II neutron beam and a total primary photon flux of* $2.9 \cdot 10^8\,\gamma/cm^2s$ *(left) and the total dose of the photons and of the neutron flux of* $3.2 \cdot 10^8\,n/cm^2s$ *(right, without weighting)*

7.2.5 Conclusions

In figures 7.25 and 7.24, slices of the voxel phantom with materials coded in grayscale is shown together with the relevant organs (salivary glands in red (right) and blue(left)). The dose is given on the same scale in contour lines in percent of the prescribed absorbed dose of 2 Gy. This representation is common in clinical usage, because it is possible to correlate the dose distribution directly with anatomical structures.

In the last sections it was shown for a sample case simulating a real application that a dose distribution for the neutron treatment at the FRM II can be calculated with GEANT4 [35]. The resulting dose matrix can be evaluated in different ways (depth dose curve, DVH, slice view) depending on the desired information. A biological radiation effect weighting can be included in the calculations as was done for three artificial RBE-LET-functions in the example. A dependence of this function on material and deposited dose is also possible, if biological data is available.

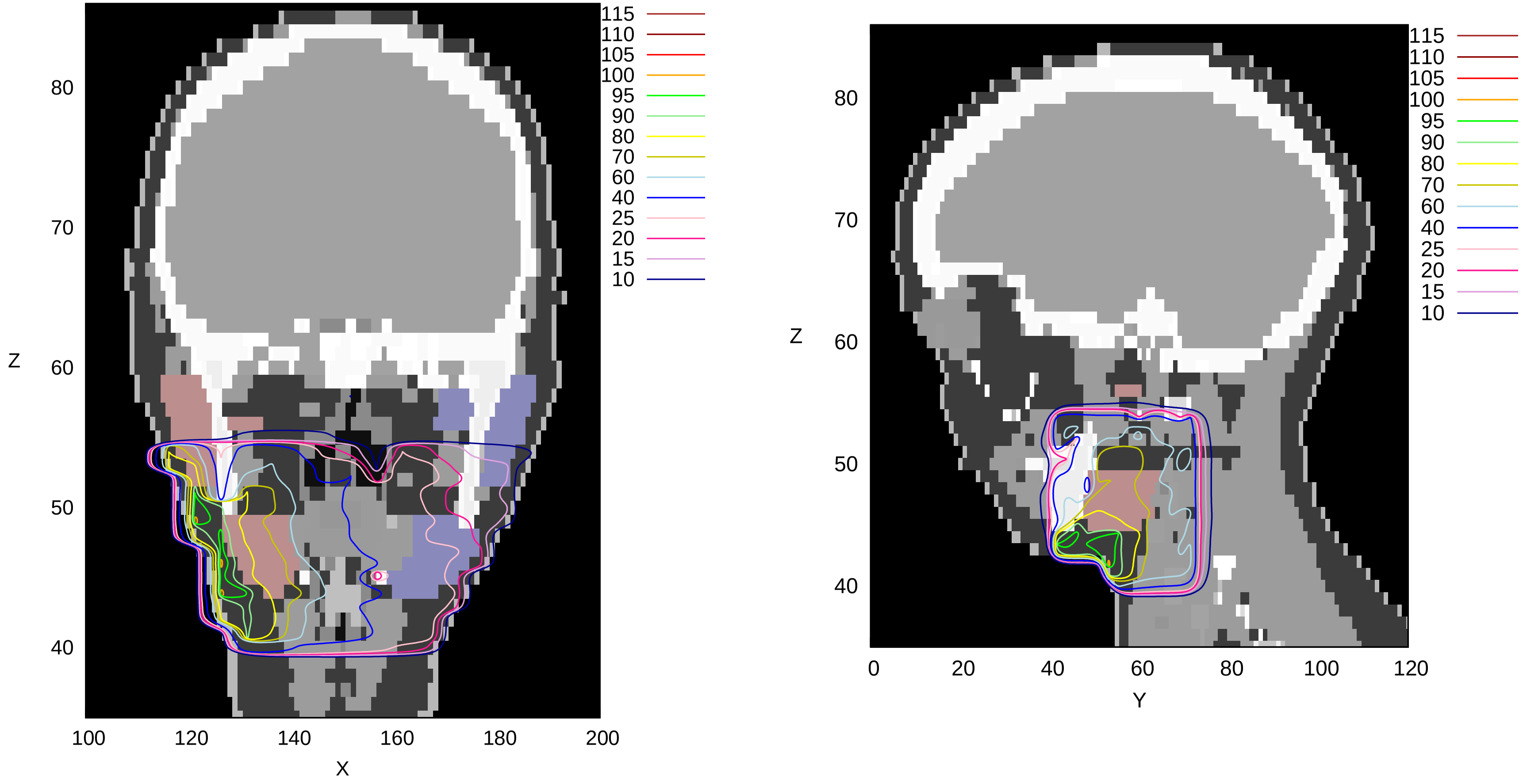

Figure 7.24: *Absorbed neutron dose inside voxel phantom after 3 min irradiation with the* $6 \times 7\,\mathrm{cm}^2$ *FRM II neutron beam and a total primary neutron flux of* $3.2 \cdot 10^8\,\mathrm{n/cm^2s}$ *(no primary photons included); contourline as percentage of the prescribed dose of* 2 Gy*;* ***left:*** *row number (x) 134;* ***right:*** *column number (y) 57; in red/blue, the right/left salivary glands are highlighted*

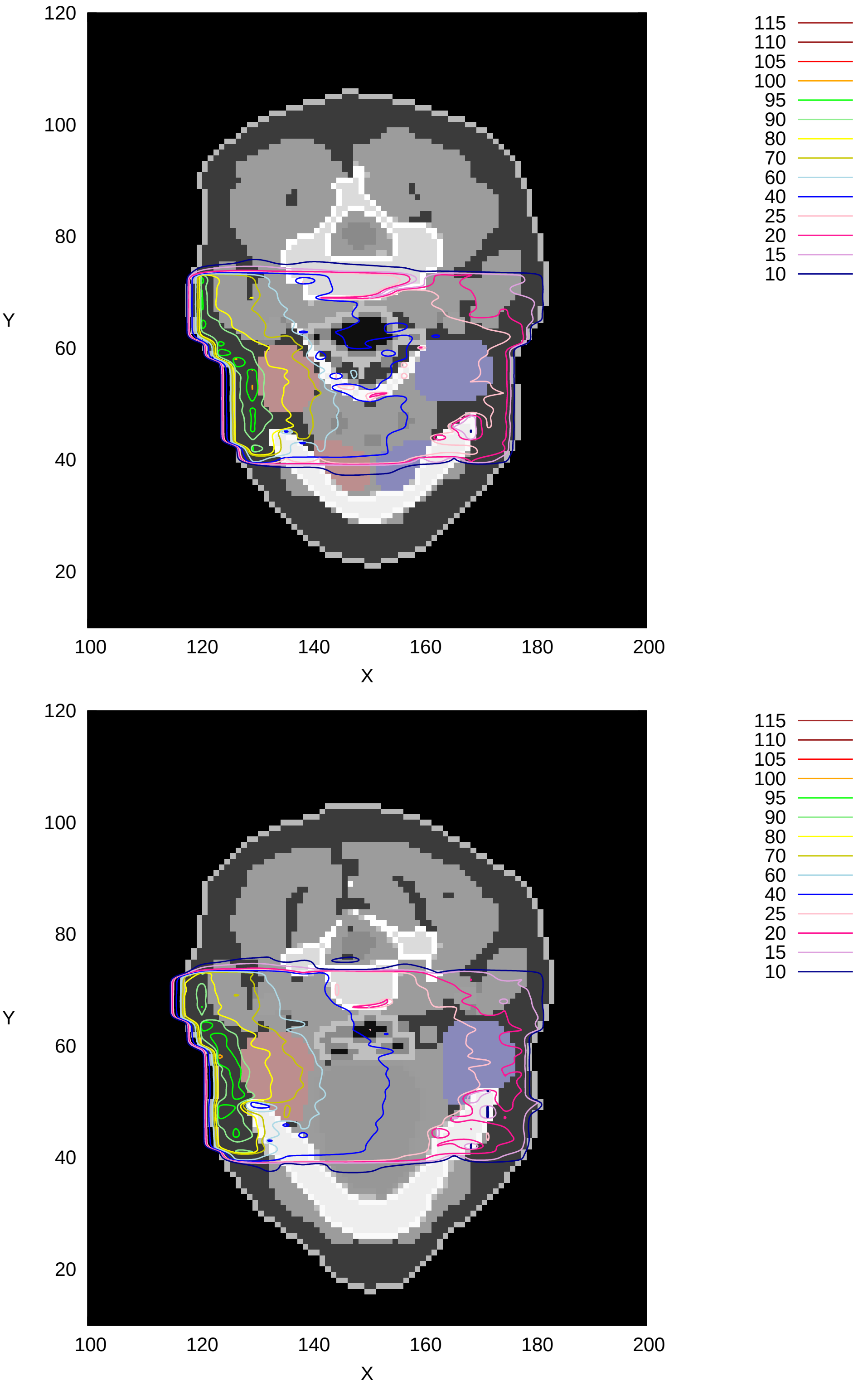

Figure 7.25: *Absorbed neutron dose inside voxel phantom after 3 min irradiation with the* $6 \times 7\,\mathrm{cm}^2$ *FRM II neutron beam and a total primary neutron flux of* $3.2 \cdot 10^8\ n/cm^2s$ *(no primary photons included); contourline as percentage of the prescribed dose of 2 Gy; slices 45 (top) and 47 (bottom); in red/blue, the right/left salivary glands are highlighted*

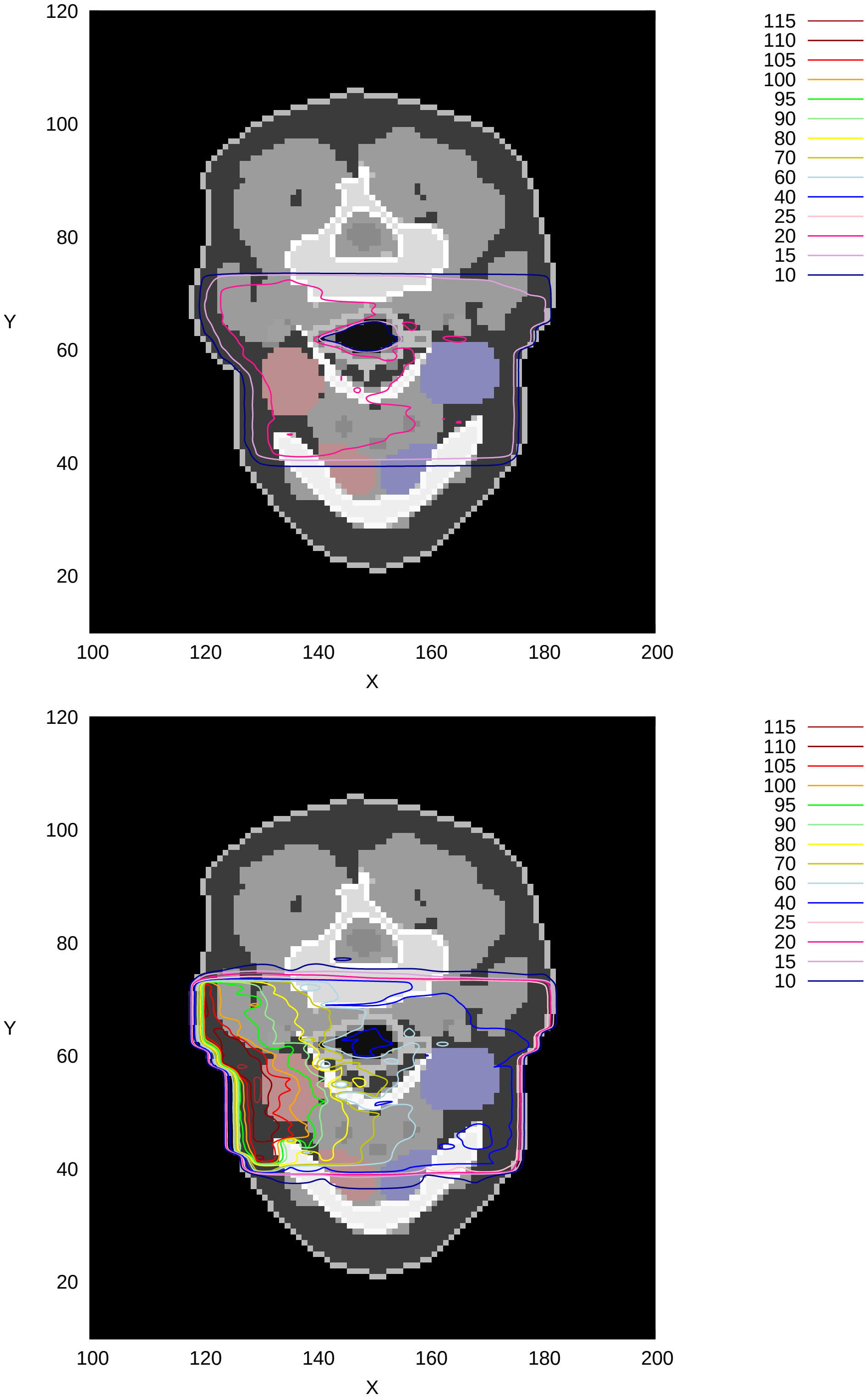

Figure 7.26: *Absorbed dose inside voxel phantom after 3 min irradiation with the* $6 \times 7\,\mathrm{cm}^2$ *FRM II beam and a total primary neutron flux of* $3.2 \cdot 10^8\, n/cm^2s$ *and a total primary photon flux of* $2.9 \cdot 10^8\, n/cm^2s$*; contourline as percentage of the prescribed dose of 2 Gy; slice 45; in red/blue, the right/left salivary glands are highlighted;*
top*: only primary photons;* ***bottom****: total absorbed dose;*

CHAPTER

8

Summary and conclusions

In this work, the basis for a computer-based neutron treatment planning system at the FRM-II in Garching is provided. In order to perform depth dose calculations, the Monte Carlo program GEANT4 was used for the first time as well as voxel patient phantoms. For neutrons, due to lack of previous benchmark calculations, extensive validation calculations were necessary. For example, the ambient dose equivalent, H*(10), inside the ICRU sphere was calculated and compared to results reported in literature. Excellent agreement was found for all relevant neutron energies from 10 meV to 20 MeV. Activation of gold foils inside PE spheres was also calculated with GEANT4 and compared to MCNP calculations. Again, excellent agreement was found. From these results, it is concluded that GEANT4 is now suitable for low energy neutron transport calculations.

The neutron spectrum at the medical beamline of the FRM-II was measured using a Bonner sphere spectrometer including gold foil detectors for neutron detection. For this purpose, the response matrix for this system was calculated with GEANT4 and the measured gold foil activation unfolded with the MSANDB code. The resulting neutron spectrum was close to that calculated with MCNP earlier which was adjusted to various threshold probes [16]. Thus, the neutron spectrum at the patient treatment position was independently measured and an experimental neutron spectrum is now available for this position.

Using this neutron spectrum as input, GEANT4 was used to calculate depth dose curves in a water phantom. The calculated dose distributions were compared to those measured earlier by means of ion chambers [65]. The agreement was perfect for all depths from 0 cm to 30 cm. These results showed again that GEANT4 is now suitable to be used for such neutron transport calculations.

Similar calculations were performed after having voxelised the water phantom and the resulting depth dose curves were almost identical to those for the unvoxelised phantom. This demonstrates that GEANT4 can now also be applied to voxel phantoms. A human voxel phantom was finally used as a model patient and neutron-photon depth dose calculations were performed for a beam geometry already used at the FRM II to treat salivary gland tumour patients. By means of 2D dose deposition plots, the resulting dose distributions within the head is visualised. It was demonstrated for example, that in a 3 minute irradiation, 50% of the submandibular gland in the voxel phantom get at least a dose of 2 Gy. Based on these calculations, a proper weighting for the increased relative biological efficiency of neutrons can be easily implemented if available. Using artificial RBE-LET-functions as examples, this was demonstrated by calculating weighted doses and visualising them in a 2D plot.
Returning to the initial requirements that a planning system for neutron treatment had to be established which is able to quantify the neutron dose as well as the biological reaction of tissues, the main points were implemented in this work. The patient geometry including an uneven surface as well as the different atomic compositions of the various tissues can be taken into account, resulting in a 3D matrix of the deposited dose where biological weighting is possible. When better radiobiological data is available, this can also be included in the calculations together with a dose-dependence of the efficiency. The data can contain radiation quality dependent dose effect curves for cell killing as well as for early complications and late effects. Tissue radiosensitivity, assessed by a physician, can also be taken into account as well as local oxygen enhancement ratios.

For the presented depth dose calculations performed using the human voxel phantom, $42 \cdot 10^6$ neutron histories in the beam profile were calculated, corresponding to 10^6 histories/cm^2. This required about $3 \cdot 10^6$ CPU-seconds with 20 processors on a (IBM Cluster 1350)-server with 2 GB RAM (each node has 2 processors: AMD Opteron Modell 250 (2,4 Ghz/1MB L2)). Therefore, with 20 processors available for the calculation, a 3D dose distribution with the phantom was finished after about 43h. Under these conditions, the resulting doses in the beam included 3% statistical uncertainty, which is normally required in patient treatment planning. Using more and faster computing power, a neutron treatment plan can be calculated in one night, which corresponds to the duration of Monte Carlo treatment planning for electron therapy used in many hospitals at the moment.

References

[1] Decay scheme of Au-198. `http://en.wikipedia.org/wiki/Decay_scheme`.

[2] Schematic view of the three salivary glands. `http://en.wikipedia.org/wiki/Image:Illu_quiz_hn_02.jpg`.

[3] The GNUplot plotting software. `http://www.gnuplot.info`.

[4] S. Agostinelli, J. Allison, K. Amako, and et. al. Geant4-a simulation toolkit. *Nucl. Instrum. Methods Phys. Res., Sect. A*, 506:250–303, 2003.

[5] A. V. Alevra and D. J. Thomas. Neutron spectrometry in mixed fields: multisphere spectrometers. *Rad. Prot. Dos.*, 107(1-3):37–72, 2003.

[6] A.V. Alevra and V.D. Plostinaru. Characterisation of the IPNE Bonner sphere spectrometer by comparison with the PTB system. *Nucl. Instrum. Methods Phys. Res., Sect. A*, 476:21–25, 2002.

[7] K. Amako, S. Guatelli, V. N. Ivanchenko, M. Maire, B. Mascialino, K. Murakami, P. Nieminen, Lu. Pandola, S. Parlati, M. G. Pia, M. Piergentili, T. Sasak, and L. Urban. Comparison of Geant4 electromagnetic physics models against the NIST reference data. *IEEE Trans. Nucl. Sci.*, 52(4):910–918, August 2005.

[8] K. Amgarou, V. Lacoste, H. Muller, and F. Fernández. Set-up of a passive bonner sphere system for neutron spectrometry at mixed fields with predominant photon component based on activation detectors. *Rad. Prot. Dos.*, 126(1-4):337–341, May 2007.

[9] G.W Barendsen. The relationship between RBE and LET for different types of Lethal damage in mammalian cells: biophysical and molecular mechanisms. *Radiat. Res.*, 139:257–270, 1994.

[10] R. Bedogni. Neutron spectrometry and dosimetry for radiation protection around a high energy electron/positron collider. Master's thesis, Universitat Autònoma de Barcelona, Facultat de Ciéncies, Departament de Física, July 2006.

[11] M. Belli, D. Bettega, P. Calzolari, F. Cera, R. Cherubini, M. Dalla Vecchia, M. Durante, S. Favaretto, G. Gialanella, and G. Grossi. Inactivation of human normal and tumour cells irradiated with low energy protons. *Int. J. Radiat. Biol.*, 76(6):831 – 839, June 2000.

[12] M. Belli, F. Cera, R. Cherubini, M. Dalla Vecchia, A. M. I. Haque, F. Ianzini, G. Moschini, O. Sapora, G. Simone, M. A. Tabocchini, and P. Tiveron. RBE-LET relationships for cell inactivation and mutation induced by low energy protons in V79 cells: further results at the LNL facility. *Int. J. Radiat. Biol.*, 74(4):501 – 509, October 1998.

[13] M. Belli, R. Cherubini, S. Finotto, G. Moschini, O. Sapora, G. Simone, and M. A. Tabocchini. RBE-LET relationship for the survival of V79 cells irradiated with low energy protons. *Int. J. Radiat. Biol.*, 55(1):93 – 104, January 1989.

[14] D. Bettega, P. Calzolari, R. Marchesini, G. L. Noris Chiorda, A. Piazzolla, L. Tallone, F. Cera, R. Cherubini, M. Dalla Vecchia, and S. Favaretto; P. Tiveron. Inactivation of C3H10T1/2 cells by low energy protons and deuterons. *Int. J. Radiat. Biol.*, 73(3):303 – 309, March 1998.

[15] H. Breitkreutz. Spektrale Charakterisierung des Therapiestrahls am FRM II. Diplomarbeit, Technische Universität München, September 2007.

[16] H. Breitkreutz, FM. Wagner, A. Röhrmoser, and W. Petry. Characterisation of the fast reactor neutron beam MEDAPP at FRM II. *Nucl. Instrum. Methods Phys. Res., Sect. A*, 593:466–471, 2008.

[17] C. Burman, G.J. Kutcher, B. Emami, and M. Goitein. Fitting of normal tissue tolerance data to an analytic function. *Int. J. Oncol. Biol. Phys.*, 21(1):123–135, 1991.

[18] J.-F. Carrier, L. Archambault, and L. Beaulieu. Validation of GEANT4, an object-oriented Monte Carlo toolkit, for simulations in medical physics. *Med. Phys.*, 31(3):484–492, March 2004.

[19] G.A.P. Cirrone, G. Cuttone, S. Donadio, V. Grichine, P. Guatclli, S.and Gumplinger, V. Ivanchenko, M. Maire, A. Mantero, B. Mascialino, P. Nieminen, L. Pandola, S. Parlati, A. Pfeiffer, M.G. Pia, and L. Urban. Precision validation of Geant4 electromagnetic physics. *IEEE Nuclear Science Symposium Conference Record*, 1:482– 485, 2003.

[20] Los Alamos Nuclear Database. ENDF/B-VI. `http://t2.lanl.gov`.

[21] C. Domingo, T. Bouassoule, K. Amgarou, M.J. García, J. Castelo, E. Morales, and F. Fernández. Bonner sphere spectrometer. In *Uncertainty Assessment in Computational Dosimetry: A Comparison of Approaches*. CONRAD WP4 workshop, October 2007.

[22] A.A. Edwards. The use of chromosomal aberrations in human lymphocytes for biological dosimetry. *Rad. Res.*, 148:39–44, 1997.

[23] B. Emami, J. Lyman, A. Brown, L. Coia, M. Goitein, J.E. Munzenrider, B. Shank, and L.J. Solinand M. Wesson. Tolerance of normal tissue to therapeutic irradiation. *Int. J. Oncol. Biol. Phys.*, 21(1):109–122, 1991.

[24] S. Endo, M. Hoshi, K. Shizuma, J. Takada, and D.T. Goodhead. Calculation of the neutron W value for neutron dosimetry below the MeV energy region. *Phys. Med. Biol.*, 45:947 953, 2000.

[25] R. Engenhart-Cabillic and A. Wambersie, editors. *Fast neutrons and high-LET part in cancer therapy.* Springer, 1998.

[26] F. Fernández, M. Bakali, M. Tomás, H. Muller, and J. L. Pochat. Neutron measurement in the Vandellòs II nuclear power plant with a Bonner sphere system. *Rad. Prot. Dos.*, 110(1-4):517–521, 2004.

[27] F. Fernández, T. Bouassoule, K. Amgarou, C. Domingo, M. J. Garcia, V. Lacoste, V. Gressier, and H. Muller. Monte Carlo calculations and validation of a gold foil-based bonner sphere system. *Rad. Prot. Dos.*, 13-26:366–370, May 2007.

[28] F. Fernández, C. Domingo, K. Amgarou, J. Castelo, T. Bouassoule, M. J. Garcia, and E. Luguera. Neutron measurements in a Varian 2100c linac facility using a bonner sphere system based on passive gold activation detectors. *Rad. Prot. Dos. adv. acc.*, doi:10.1093/rpd/ncm075:1–5, May 2007.

[29] A. Ferrari and M. Pelliccioni. On the ambient dose equivalent. *J. Radiol. Prot.*, 14(4):331–335, 1994.

[30] A. Ferrari and M. Pelliccioni. On the conversion coefficients from fluence to ambient dose equivalent. *Rad. Prot. Dos.*, 51(4):251–255, 1994.

[31] TUM Forschungsneutronenquelle Heinz Maier-Leibnitz (FRM II). `http://www.frm2.tum.de`.

[32] S. Garny, G. Leuthold, V. Mares, H.G. Paretzke, and W. Rühm. Verification of GEANT4 transport calculations for neutrons below 15 MeV. *submitted to: IEEE Trans. Nucl. Sci.*, 2009.

[33] S. Garny, V. Mares, H. Roos, W. Rühm, and F. Wagner. Measurement of the neutron spectrum and neutron dose at the FRM II therapy beamline with Bonner spheres. *In preparation.*

[34] S. Garny, V. Mares, and W. Rühm. Response functions of a bonner sphere spectrometer calculated with GEANT4. *accepted to be published by: Nucl. Instrum. Methods Phys. Res., Sect. A*, 2009.

[35] S. Garny, W. Rühm, M. Zankl, F. Wagner, and H. Paretzke. The MEDAPP therapy beamline at the FRM II research reactor, Garching, Germany - GEANT4-calculation of the depth dose distribution in a voxel phantom. *In preparation.*

[36] GEANT4. *GEANT4: Physics Reference Manual*, December 2006. `http://geant4.web.cern.ch/geant4/support/userdocuments.shtml`.

[37] GEANT4. *Geant4 User's Guide for Application Developers*, December 2006. `http://geant4.web.cern.ch/geant4/support/userdocuments.shtml`.

[38] D.T. Goodhead, M. Belli, A.J. Mill, D.A. Bance, L.A. Allens, S.C. Hall, F. Ianzani, G. Simone, D.L. Stevens, A. Stretch, M.A. Tabocchini, and R.E. Wilkinson. Direct comparison between protons and alpha-particles of the same LET: I. Irradiation methods and inactivation of asynchronous V79, HeLa and C3H 10T1/2 cells. *Int. J. Radiat. Biol.*, 61(5):611 – 624, May 1992.

[39] M. Hajek, T. Berger, W. Schöner, and N. Vana. Analysis of the neutron component at high altitude mountains using active and passive measurement devices. *Nucl. Instrum. Methods Phys. Res., Sect. A*, 476:69–73, 2002.

[40] E. Hall. *Radiobiology for the Radiologist.* J.B.Lippincott Company, Philadelphia, 2001.

[41] J R Harvey. The basis of a suggested instrumental approach to the surveying of neutron fields and the measurement of personal dose from neutrons. *Phys. Med. Biol.*, 26(2):253–267, 1981.

[42] J.S. Hendricks, S.C. Frankle, and J.D. Court. ENDF/B-VI Data for MCNP. Technical Report LA-12891, Los Alamos National Laboratory, 1994.

[43] J. Heufelder, K. Zink, M. Scholz, K.-D. Kramer, and K. Welker. Eine Methode zur automatisierten Bewertung von CT-basierten Bestrahlungsplänen in der perkutanen Strahlentherapie. *Z. Med. Phys.*, 13:231–239, 2003.

[44] A. Howard. Validation of neutrons in Geant4 using TARC data - production, interaction and transportation. In *Nuclear Science Symposium Conference Record*, volume 3, pages 1506–1510, San Diego, CA, November 2006.

[45] ICRP. RBE for deterministic effects. Report 58, International Commission on Radiation Units and Measurements, 1989.

[46] ICRP. Recommendations of the International Commission on Radiological Protection. Report 60, International Commission on Radiological Protection, 1990.

[47] ICRP. Basic anatomical and physiological data for use in radiological protection: reference values. Report 89, International Commission on Radiological Protection, 2002.

[48] ICRP. Recommendations of the ICRP. Report 103, International Commission on Radiological Protection, 2008.

[49] ICRU. Neutron dosimetry for biology and medicine. Report 26, International Commission on Radiation Units and Measurements, 1976.

[50] ICRU. Clinical neutron dosimetry part I: Determination of absorbed dose in a patient treated by external beams of fast neutrons. Report 45, International Commission on Radiation Units and Measurements, 1989.

[51] ICRU. Tissue substitutes in radiation dosimetry and measurement. Report 44, International Commission on Radiation Units and Measurements, 1989.

[52] ICRU. Prescribing, recording, and reporting photon beam therapy. Report 50, International Commission on Radiation Units and Measurements, 1993.

[53] ICRU. Stopping powers and ranges for protons and alpha particles. Report 49, International Commission on Radiation Units and Measurements, 1993.

[54] ICRU. Conversion coefficients for use in radiological protection against external radiation. Report 57, International Commission on Radiation Units and Measurements, 1998.

[55] ICRU. Fundamental quantities and units for ionizing radiation. Report 60, International Commission on Radiation Units and Measurements, 1998.

[56] ICRU. Prescribing, recording and reporting photon beam therapy. Supplement 62, International Commission on Radiation Units and Measurements, 1999.

[57] ICRU. Prescribing, recording and reporting electron beam therapy. Report 71, International Commission on Radiation Units and Measurements, 2004.

[58] ICRU. Stopping of ions heavier than helium. Report 73, International Commission on Radiation Units and Measurements, 2005.

[59] US National Cancer Institute. Tumor staging. `http://www.cancer.gov/cancertopics/factsheet/detection/staging`.

[60] F. James. A review of pseudorandom number generators. *Comput. Phys. Commun.*, 60:329344, 1990.

[61] ed. J.F. Briesmeister. MCNP - A general monte carlo n-particle transport code. Version 4B LA-12625-M, Los Alamos National Laboratory, 1997.

[62] H. Jiang and H. Paganetti. Adaptation of GEANT4 to Monte Carlo dose calculations based on CT data. *Med. Phys.*, 31(10):2811–2818, October 2004.

[63] S. Kampfer. Umfassende Charakterisierung eines Spaltneutronenstrahls. Diplomarbeit, Technische Universität München, Januar 2006.

[64] S. Kampfer, F.M. Wagner, B. Loeper, and P. Kneschaurek. Erste dosimetrische Ergebnisse an der neuen Neutronentherapieanlage am FRM II. In *37. Jahrestagung der Deutschen Gesellschaft für Medizinische Physik*, pages 318–319. L. Bogner, B. Dobler, September 2006.

[65] S. Kampfer, FM Wagner, B. Loeper-Kabasakal, and P. Kneschaurek. Die neue Neutronentherapieanlage am FRM II in Garching. *Strahlenther. Onkol.*, 183(Supplement 1:72), 2007.

[66] R. Katz, R. Zachariah, F. Cucinotta, and C. Zhang. Survey of cellular radiosensitivity parameters. *Rad. Res.*, 140:356–365, 1994.

[67] J. Kiefer. *Biological Radiation Effectcs*. Springer, 1990.

[68] H. Klein and D. Thomas. Quality assurence. *Rad. Prot. Dos.*, 107(1-3):175–188, 2003.

[69] D.E. Knuth. *The Art of Computer Programming*, volume 2, chapter Seminumerical algorithms. Addison-Wesley, Redding, MA, 1981.

[70] H. Krieger and W. Petzold. *Strahlenphysik, Dosimetrie und Strahlenschutz*, volume 1. Teubner Verlag, 1992.

[71] J. Kummermehr, V. Magaddino, and F.M. Wagner. Preclinical screening of the biological effectiveness of a therapeutic beam at SR10. Technical report, FRM II, Experiment no. 623, 2006.

[72] G.J. Kutcher, C. Burman, L. Brewster, M. Goitein, and R. Mohan. Histogram reduction method for calculating complication probabilities for 3D treatment planning evaluations. *Int. J. Oncol. Biol. Phys.*, 21(1):137–146, 1991.

[73] D. H. Lehmer. Mathematical methods in large-scale computing units. In *Proceedings of the Second Symposium on Large Scale Digital Computing Machinery*, pages 141–146, Cambridge, 1951. Harvard University Press.

[74] R. Lemrani, M. Robinson, V.A. Kudryavtsev, M. De Jesus, G. Gerbier, and N.J.C. Spooner. Low-energy neutron propagation in MCNPX and GEANT4. *Nucl. Instrum. Methods Phys. Res., Sect. A*, 560:454–459, 2006.

[75] G. Leuthold, V. Mares, W. Rühm, E. Weitzenegger, and H.G. Paretzke. Long-term measurements of cosmic ray neutrons by means of a Bonner spectrometer at mountain altitudes - first results. *Rad. Prot. Dos.*, 126(1-4):506–511, 2007.

[76] G. Leuthold, V. Mares, and H. Schraube. Calculation of the neutron ambient dose equivalent on the basis of the ICRP revised quality factors. *Rad. Prot. Dos.*, 40(2):77–84, 1992.

[77] H.W. Lewis. Multiple scattering in an infinite medium. *Phys. Rev.*, 78:526, 1950.

[78] P. lEcuyer. Efficient and portable combined random number generators. *Commun. ACM*, 31:742, 1988.

[79] R. E. MacFarlane. Data testing of ENDF/B-VI. In *International Conference on Nuclear Data for Science and Technology*, Los Alamos National Laboratory preprint LA-UR-94-1541, Gatlinburg, Tennessee, May 1994.

[80] V. Magaddino, F.M. Wagner, and J. Kummermehr. Preclinical screening of the biological effectiveness of a therapeutic neutron beam at SR10, FRM II. *Experimetelle Strahlentherapie und Klinische Strahlenbiologie*, 16:129–131, 2007.

[81] J. Magee and A. Chatterjee. *Kinetics of nonhomogeneous processes*, chapter Track reactions of radiation chemistry. John Wiley & Sons, 1987.

[82] V. Mares, G. Schraube, and H. Schraube. Calculated neutron response of a Bonner sphere spectrometer with ^{3}He counter. *Nucl. Instrum. Meth. A*, 307:398–412, 1991.

[83] G. Marsaglia. Random numbers fall mainly in the plains. *Proc. Nat. Acad. Sci. USA*, 61:25–28, 1968.

[84] G. Marsaglia, A. Zaman, and W.-W. Tsang. Toward a universalrandom number generator. *Stat. Prob. Lett.*, 9:35, 1990.

[85] M. Matzke. Unfolding procedures. *Rad. Prot. Dos.*, 107:155–174, 2003.

[86] F. Mauro, G. Arcangeli, L. D'Angelo, C. Marino, and M. Benassi. Mathematical models of cell survival after ionizing radiation: Application to radiotherapy planning. *Health Phys.*, 57(Sup. 1):355–361, 1989.

[87] W. N. McElroy, S. Berg, and T. Crockett. A computer-automated iterative method for neutron flux spectra determination by foil activation. Technical Report AFWL-TR-67-41, Sandia National Laboratories, Albuquerque, New Mexico, 1967.

[88] M.H. Moar, R.D. Errington, R.J. Caplan, and et al. Fast neutron therapy in advanced head and neck cancer: a collaborative international randomized trial. *Int. J. Radiat. Oncol. Biol. Phys.*, 32:599–604, 1995.

[89] A. Morhart and G. Burger. Specified dose equivalent quantities for neutrons in the ICRU sphere and their applicability. *Rad. Prot. Dos.*, 12:107–111, 1985.

[90] MPI. A Message-Passing Interface standard.
`http://www-unix.mcs.anl.gov/mpi`.

[91] National Research Counsil Canada. EGSnrc.
`http://www.irs.inms.nrc.ca/EGSnrc/EGSnrc.html`.

[92] National Institue of Standards and Technology. NIST Database. `http://www.nist.gov/srd/online.htm`.

[93] C.C. Orton and L. Cohen. A unified approach to dose-effect relationships in radiotherapy. I: Modified TDF and linear quadratic equations. *Int. J. Radit. Oncol. Biol. Phys.*, 14(3):549–556, 1988.

[94] H. Paganetti, H. Jiang, S.-Y. Lee, and H. M. Kooy. Accurate monte carlo simulations for nozzle design, commissioningand quality assurance for a proton radiation therapy facility. *Med. Phys.*, 31(7):2107–2118, July 2004.

[95] S. Paganini and E. Vilela. Evaluation of the fluence to dose conversion coefficients for high energy neutrons using a voxel phantom coupled with the GEANT4 code. *Braz. J. Phys.*, 35(3B):818–820, 2005.

[96] H. Paretzke. *Kinetics of nonhomogeneous processes*, chapter 3: Radiation Track Structure Theorie, pages 89–170. John Wiley & Sons, 1987.

[97] H. Paul and A. Schinner. Judging the reliability of stopping power tables and programs for heavy ions. *Nucl. Instrum. Methods Phys. Res., Sect. B*, 209:252–258, 2003.

[98] M. Pelliccioni. Overview of fluence-to-effective dose and fluence-to-ambient dose equivalent conversion coefficients for high energy radiation calculated using the fluka code. *Rad. Prot. Dos.*, 88(4):279–297, 2000.

[99] C.A. Perks, D.J. Thomas, B.R.L. Siebert, S. Jetzke, G. Hehn, and H. Schraube. Comparison of response function calculations for multispheres. *Rad. Prot. Dos.*, 44:85–88, 1992.

[100] A.-M. Perroche and M. Boutillon. Measurement of the ambient dose equivalent and directional dose equivalent in a Co-60 beam. *Rad. Prot. Dos.*, 27(3):139–148, 1989.

[101] E.B. Podgorsak. *Radiation oncology physics: A handbook for teachers and students.* International Atomic Energy Agency, 2005.

[102] E. Poon and F. Verhaegen. Accuracy of the photon and electron physics in GEANT4 for radiotherapy applications. *Med. Phys.*, 32(6):1696–1711, June 2005.

[103] I. Pshenichnov, I. Mishustin, and W. Greiner. Neutrons from fragmentation of light nuclei in tissue-like media: a study with the GEANT4 toolkit. *Phys. Med. Biol.*, 50:5493–5507, November 2005.

[104] I. Pshenichnov, I. Mishustin, and W. Greiner. Comparative study of depth-dose distributions for beams of light and heavy nuclei in tissue-like media. *Nucl. Instrum. Methods Phys. Res., Sect. B*, 266(7):1094–1098, April 2008.

[105] A.. Rosenfeld, A. Wroe, I. Cornelius, M.Reinhard, and D.Alexiev. Analysis of inelastic interactions for therapeutic proton beams using monte carlo simulation. *IEEE Trans. Nucl. Sci.*, 51(6):3019–3025, December 2004.

[106] R. Sauer. *Strahlentherapie und Onkologie.* Urban & Schwarzenberg, 1993.

[107] H. Schlattl, M. Zankl, and N. Petoussi-Henß. Organ dose conversion coefficients for voxel models of the reference male and female from idealized photon exposures. *Phys. Med. Biol.*, 52:2123–2145, 2007.

[108] E. Schmid, H. Schraube, and M. Bauchinger. Chromosome aberration frequencies in human lymphocytes irradiated in a phantom by mixed beam of fission neutrons and γ-rays. *Int. J. Radiat. Biol.*, 73/3:263–267, 1998.

[109] E. Schmid, F.M. Wagner, H. Romm, L. Walsh, and H. Roos. Dose-response relationship of dicentric chromosomes in human lymphocytes obtained for the fission neutron therapy facility MEDAPP at the research reactor FRM II. *Radiat Environ Biophys.*, 48(1):67–75, Feb. 2009.

[110] H. Schraube, W.G. Alberts, H. Brede, B. Burghardt, B. Drschel, H. Heinzelmann, A. Hess, M. Höfert, and E. Piesch. Die Bestimmung der Energiedosis eines Neutronenstrahls mit Hilfe von Ionisationskammern. Kompendium, gsf-Forschungszentrum für Umwelt und Gesundheit, 2003.

[111] H. Schuhmacher and B.R.L. Seibert. Quality factors and ambient dose equivalent for neutrons based on the new ICRP recommendations. *Rad. Prot. Dos.*, 40:85–89, 1992.

[112] B. Siebert. Letter to the editor. *Rad. Prot. Dos.*, 51(4):301–303, 1994.

[113] B.R.L. Siebert and R. Hollnagel. Intercomparison and evaluation of calculated neutron fluence to ambient dose equivalent conversion factors. *Rad. Prot. Dos.*, 12:145–149, 1985.

[114] B.R.L. Siebert and H. Schuhmacher. Quality factors, ambient and personal dose equivalent for neutrons, based on the new ICRU stopping power data for protons and alpha particles. *Rad. Prot. Dos.*, 58:177–183, 1995.

[115] G. Simmer, V. Mares, E. Weitzenegger, and W. Rühm. Iterative unfolding for bonner sphere spectrometers using the SAND code - sensitivity analysis and dose calculations. *Radiat. Meas.*, submitted, 2008.

[116] K. Sutherland, S. Miyajima, and H. Date. A simple parallelization of GEANT4 on a PC cluster with static scheduling for dose calculations. *J. Phys.: Conf. Ser.*, 74:8, 2007.

[117] D. J. Thomas, N. P. Hawkes, L. N. Jones, P. Kolkowski, and N. J. Roberts. Characterization and utilization of a bonner sphere set based on gold activation foils. *Rad. Prot. Dos.*, 126(1-4):229–233, 2007.

[118] D.J. Thomas and A.V. Alevra. Bonner sphere spectrometers-a critical review. *Nucl. Instrum. Methods Phys. Res., Sect. A*, 476:12–20, 2002.

[119] D.J. Thomas, A.G. Bardell, and E.M. Macaulay. Characterisation of a gold foil-based Bonner sphere set and measurements of neutron spectra at a medical accelerator. *Nucl. Instrum. Methods Phys. Res., Sect. A*, 476 (2002) 31-35:31–35, 2002.

[120] J. Torres, M. Buades, J. Almansa, R. Guerrero, and A. Lallena. Dosimetry characterization of 32p intravascular brachytherapy source wires using monte carlo codes PENELOPE and GEANT4. *Med. Phys.*, 31(2):296–304, February 2004.

[121] J. Turner. *Atoms, Radiation and Radiation Protection.* John Wiley & Sons, 1995.

[122] Y. Uwamino and T. Nakamura. Two types of multi-moderator neutron spectrometers: gamma-ray insensitive type and hight-efficiency type. *Nucl. Instrum. Methods Phys. Res., Sect. A*, 239:299–309, 1985.

[123] K. G. Veinot and N. E. Hertel. Effective quality factors for neutrons based on the revised ICRP/ICRU recommendations. *Rad. Prot. Dos.*, 115(1-4):536–541, 2005.

[124] M. Vilches, S. García-Pareja, R. Guerrero, M. Anguiano, and A.M. Lallena. Monte carlo simulation of the electron transport through thin slabs: A comparative study of penelope, geant3, geant4, egsnrc and mcnpx. *Nucl. Instrum. Methods Phys. Res., Sect. B*, 254(2):219–230, January Volume 254, Issue 2, January 2007, Pages 219-230.

[125] V. Vylet. Response matrix of an extended bonner sphere system. *Nucl. Instrum. Methods Phys. Res., Sect. A*, 476:26–30, 2002.

[126] F.M. Wagner, Th. Bücherl, S. Kampfer, A. Kastenmüller, and W. Waschkowski. Thermal neutron converter for irradiations with fission neutrons. *Nuclear Physics and Atomic Energy*, 3(21):30–36, 2007.

[127] F.M. Wagner, P. Kneschaurek, A. Kastenmller, B. Loeper-Kabasakal, S. Kampfer, H. Breitkreutz, W. Waschkowski, M. Molls, and W. Petry. The munich fission neutron therapy facility MEDAPP at the research reactor FRM II. *Strahlenther Onkol.*, 184(12):643–646, 2008.

[128] A. Wambersie, J. Hendry, J. Gueulette, R. Gahbauer, R. Pötter, and V. Grégoire. Radiobiological rationale and patient selection for high-LET radiation in cancer therapy. *Radiother. Oncol.*, 73(Sup.2):S1–S14, 2004.

[129] S. Webb and A.E. Nahum. A model for calculating TCP in radiotherapy including the effects of inhomogeneous distributions of dose and clonogenic cell density. *Phys. Med. Biol.*, 38:653–666, 1993.

[130] J.P. Wellisch. Geant4 hadronic physics status and validation for large HEP detectors. *Computing in High Energy and Nuclear Physics*, ePrint nucl-th/0306006:8, March 2003.

[131] H. Wu, M. Durante, K. George, and T.C. Yang. Induction of chromosome aberrations in human cells by charged particles. *Rad. Res.*, 148:102–107, 1997.

[132] M. Zankl, J. Becker, U. Fill, N. Petoussi-Henß, and K.F. Eckerman. GSF male and female adult voxel models representing ICRP reference man the present status. In *Proceedings of The Monte Carlo Method: Versatility Unbounded in a Dynamic Computing World*, La Grange Park, USA, 2005. American Nuclear Society.

APPENDIX

A

Description of radiobiophysical quantities

In the following sections some physical quantities used in radiation protection are explained.

A.1 Absorbed dose

The quantity absorbed dose D inside a volume element with mass dm is defined as:

$$\mathrm{D} = \frac{\mathrm{dE}}{\mathrm{dm}} \qquad \left[\frac{\mathrm{J}}{\mathrm{kg}}\right]$$

with dE being the deposited energy inside this volume:

$$\mathrm{dE} = \mathrm{T_{in}} - \mathrm{T_{out}} + \mathrm{Q_{\Delta m}}$$

T_{in} is the energy of all incoming particles, T_{out} is that of all particles leaving the volume (both exclusive rest mass) and $Q_{\Delta m}$ is the change of rest mass of all particles involved.

A.2 KERMA

The KERMA (= kinetic energy released per unit mass) is defined as:

$$\mathrm{KERMA} = \frac{\mathrm{dE_{trans}}}{\mathrm{dm}} \qquad \left[\frac{\mathrm{J}}{\mathrm{kg}}\right]$$

with dE_{trans} being the kinetic energy transferred from the primary particles to matter (e.g. by emitting secondaries) inside the volume with mass dm.

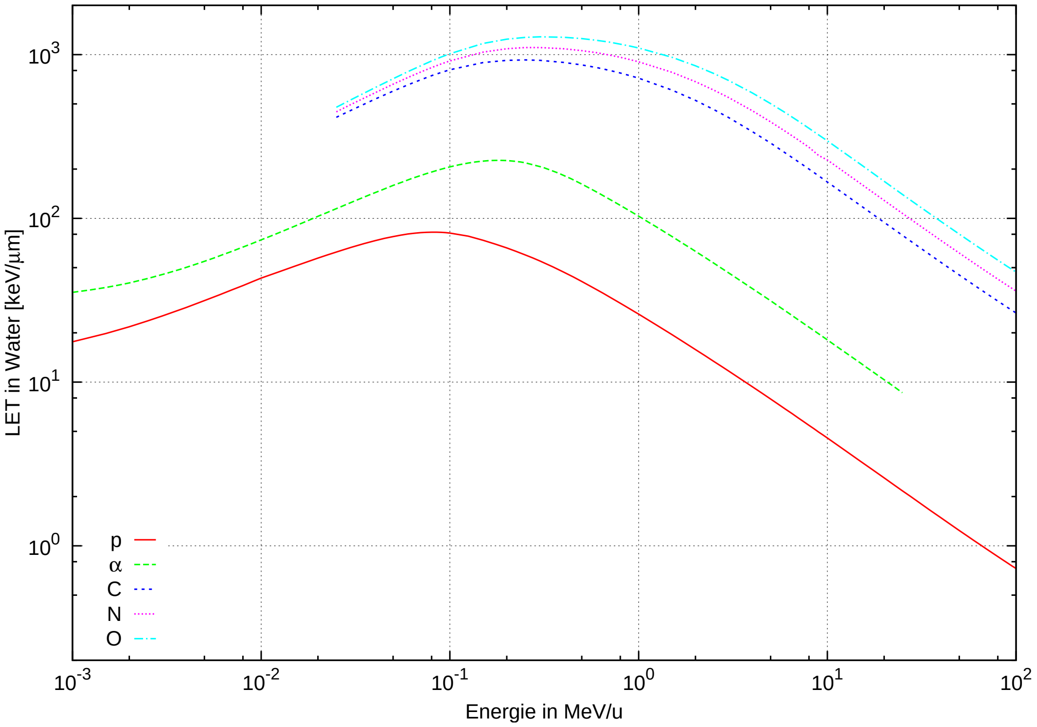

Figure A.1: *Linear energy transfer for different particles in water, data from ICRU 49 [53] and ICRU 73 [58]*

A.3 Ambient dose and ambient dose equivalent

The ambient dose equivalent is defined in ICRU 57 [54] as the dose equivalent in 1 cm depth of the standard ICRU-Phantom (which is a 30 cm sphere of tissue-equivalent material [54]), homogeneously illuminated by a parallel field of particles (geometry see figure 5.1). The dose equivalent is the deposited energy dose of every primary and secondary particle at this point. This value is multiplied by the quality factor of this particle (depending on the energy and the LET of the particle) in each step and summed over all particles to obtain the ambient dose equivalent:

$$H^*(10) = \sum_{particles,steps} Q(LET) \cdot D \tag{A.1}$$

In this context, the dose deposited in 1 cm depth without the quality factor is called ambient dose, D*(10).

A.4 Linear energy transfer (LET)

The linear energy transfer of a particle in matter is defined [55] as the local average of the ratio of the energy deposited between l and $l + dl$ divided by the steplength dl:

$$L_\Delta = \frac{dE_\Delta}{dl} \tag{A.2}$$

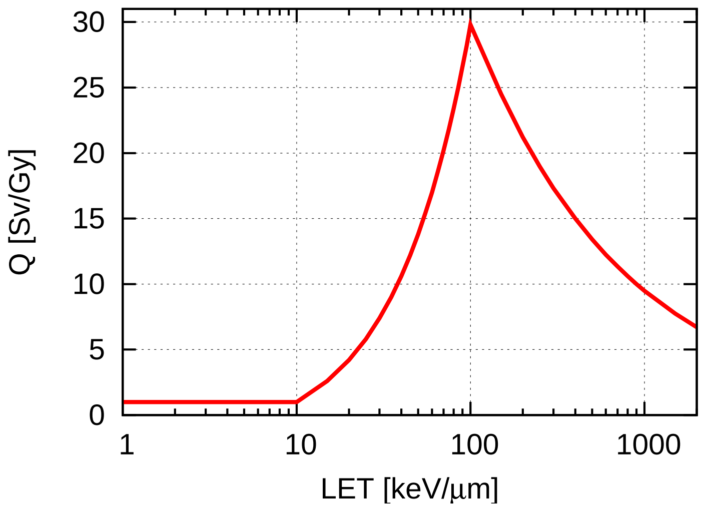

Figure A.2: *Dependency of the quality factor on LET, see table A.1*

The index Δ stands for a cut-off-level, meaning that only energy-losses below the cut off value are taken into account. This formaly separates the higher energy secondary particles from clusters along the primary track. Therefore, L_∞ is identical to the stopping power (see for example B.4.2). The symbol L without index denotes L_∞ unless otherwise stated.

A.5 Quality factor

The quality factor Q was introduced by the ICRU to take into account the efficiency of different kinds of radiation in matter to produce a certain biological effect. It is dependant on the linear energy transfer (LET, see A.4) of the particle. Q was defined by the ICRP Publication 60 [46] (which was not changed in ICRP 103 [48]) in the following way, see table A.1 and figure A.2.

LET [keV/μm] in water	Q
< 10	1
10 -100	$0,32 \cdot LET - 2,2$
> 100	$300/\sqrt{LET}$

Table A.1: *Quality-factor-LET-relationship as defined in* ICRU 57 [54] *and* ICRP 60 [46]

APPENDIX

B

Basic physics of primary and secondary particles in matter

In this chapter the interaction of the different primary and secondary particles which occur at the irradiation facility FRM II are described, focusing on energy deposition.

B.1 Photons

The main physical interactions of photons with matter are the photoelectric- (section B.1.2) and the Comptoneffect (section B.1.3). At higher energies pair production (section B.1.4) and photonuclear reactions (section B.1.5) also play a role (see figure B.1). At low energies elastic scattering (Thomson and Raleigh scattering, chapter B.1.1) occurs, but there is no energy deposition to the material involved, so it is only discussed briefly. Photons are indirectly ionising particles, thus the energy is not primarily transferred directly to the material, but to their secondary electrons, which then deposit most of the energy in small discrete amounts (see section B.3).

B.1.1 Elastic scattering

By elastic scattering of photons, almost no energy is transferred to the medium. There are two possible ways of interaction: Thomson scattering and Raleigh scattering.
Thomson scattering is a low-energy process of coherent Compton scattering. It is caused by a free electron which is stimulated to oscillate in response to the electromagnetic vector of a passing photon. The oscillation is promptly emitted in the form of a photon with adequate energy. Altogether, the incoming photon is deflected in angle

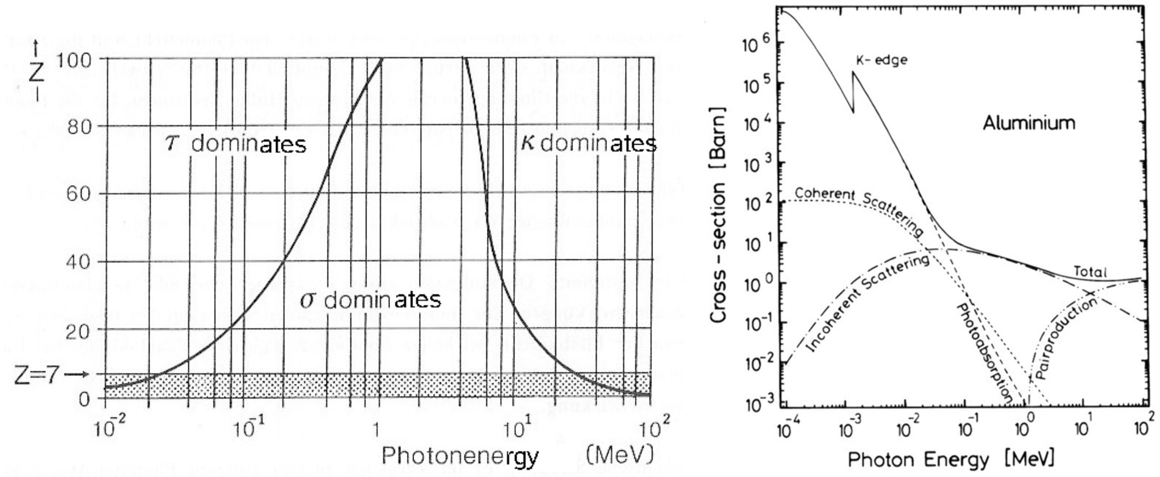

Figure B.1:
left: *dominating photon interaction probabilities as a function of photon energy and target atomic number (dotted: tissue-relevant atomic numbers): $\tau =$ photoelectric effect, $\sigma =$ Compton scattering, $\kappa =$ pair production [70]*
right: *photon cross section in the low Z-material aluminium as a function of photon energy [96]*

but very little energy is transferred to the medium.
Elastic scattering by a whole atom, consisting of a nucleus and several electrons, is called **Raleigh scattering**. Almost no energy is transferred and the photon is only slightly deflected. The change in momentum is compensated by the nucleus. The relative reaction probability for Raleigh scattering has its maximum at approximately 20 keV in water. But even there it is one order of magnitude smaller than both photoelectric effect and compton scattering (see figure B.2).

The cross section for this coherent Raleigh interaction is [96]:

$$\sigma_{Raleigh} \sim \rho \, \frac{Z^{1.5}}{(h\nu)^4}$$

with atomic number Z, density of target ρ and energy of incoming photons $h\nu$.

B.1.2 Photoelectric effect

The photoelectric effect is the dominant interaction process in water for photon energies smaller than 30 keV. The photon collides inelastically with an electron that is bound in the electromagnetic field of a nucleus with binding energy φ. The photon is totally absorbed and an electron (so called photoelectron) is emitted. The energy of the electron has to follow energy conservation:

$$E_{e^-,kin} = E_{photon} - E_{e^-,bond} = \hbar\omega - \varphi$$

The maximal kinetic energy that can be transferred is therefore:

$$E_{e^-,max} = \hbar\omega - \varphi_0$$

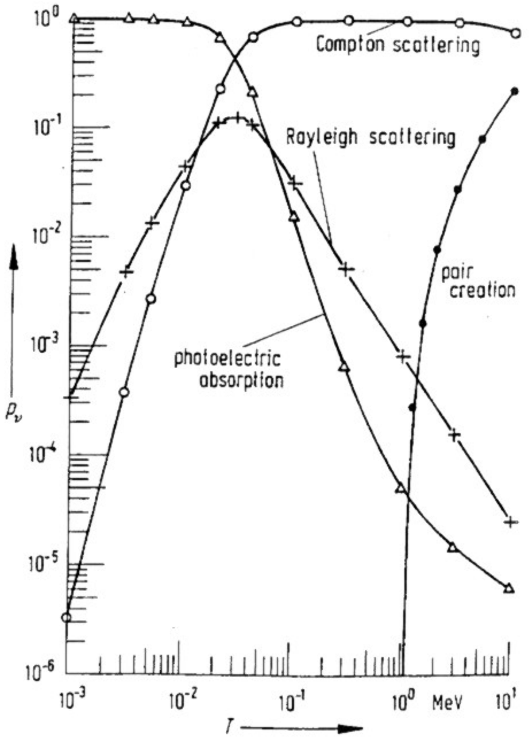

Figure B.2: *Relative interaction probability* p_ν *of photons with energy* T *in water for the different kinds of interactions (calculated with the Hubbell-model for scattering cross sections) [61]*

with φ_0 being the binding energy of the most weakly bound valence electron as interaction partner. The presence of the nucleus is required to absorb the remaining momentum. The deflection angle between the direction of the incoming photon and the resulting accelerated electron is depending on the energy of the photon. The higher the photon energy, the higher the probability that the electron is emitted in forward direction (see figure B.3). The photoelectric cross section strongly depends on the tar-

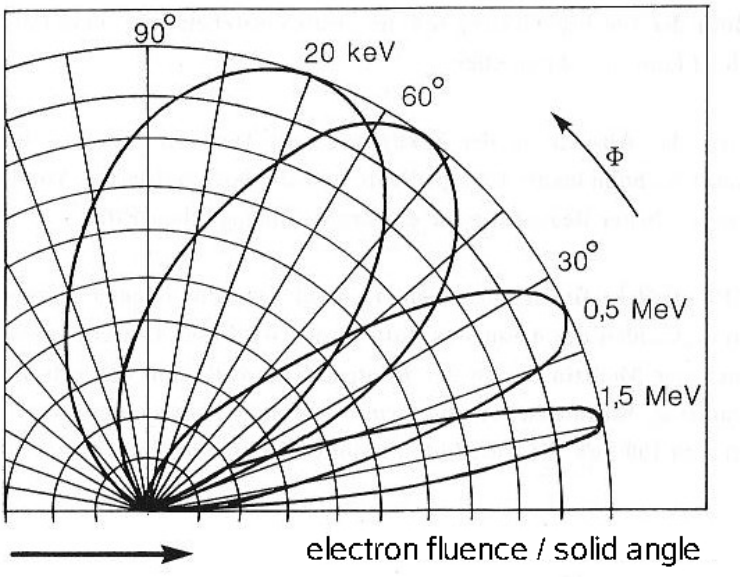

Figure B.3: *Relative angular distribution of photoelectrons depending on photoenergy and angle of emission* Φ *in relation to the direction of incidence (arrow) [70]*

get atomic number Z (density of target material ρ) and decreases with the cube of the photon energy.

$$\sigma \sim \rho \frac{Z^4}{(\hbar\omega)^3}$$

The absorption coefficient μ (defined by the absorption of energy inside matter, see B.1.6) reflects the atomic shell structure of the target atom which is visible as absorption edge(s) (see right side of figure B.1). The photon typically interacts with the innermost accessible electron possible ($E_{photon} > E_{e^-,bond} = \varphi_{shell}$). When the energy increases, at certain thresholds its energy is sufficient to ionise the electron of a more interior shell and the cross section rises ("jumps") abruptly. A byproduct of the process after relaxation is a charged, typically also excited ion. It relaxes afterwards by emitting one or more Auger electrons or a fluorescence photon. Photoionisation is the reason for an important effect in radiation therapy: the interface effect between materials with high atomic numbers. The photons and photoelectrons originating from the relaxation cascades of the ion have a defined range (see chapter B.3). Therefore, the energy deposited directly behind layers of high-Z-materials can be much higher than would be expected without the interface effect. For example in the human body, the dose deposited in bone surface cells around the calcium (Z=20)-rich bones is much higher than the dose in areas separated from high-Z-material by distances larger than the ranges of such secondary particles.

B.1.3 Compton effect

In materials with low atomic number Z, like those in the human body, the Compton effect plays an important role over a wide range of energy (see figure B.1). The incoming photon is scattered at a quasi-free electron, deflected and looses energy. The electron is recoiled and emitted from the atom (geometry see figure B.4). The energy of the

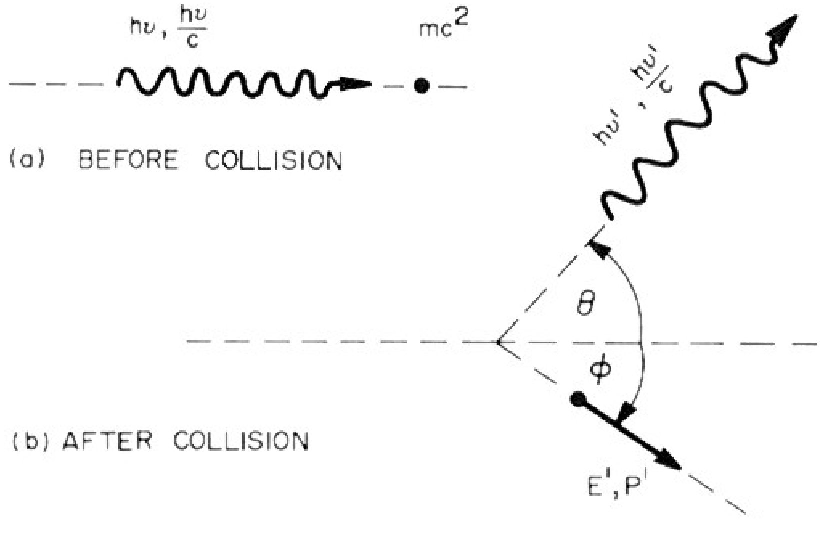

Figure B.4: *Geometry of the Compton scattering with scattering angle of the electron* ϕ *and of the photon* θ *[70]*

deflected photon ($h\nu\,'$, wave length $\lambda\,'$) is:

$$h\nu\,' = \frac{h\nu}{1+\frac{h\nu}{m_0c^2}\,(1-\cos\theta)}$$

with the primary photon energy $h\nu$ (wave length λ), electron mass m_0 and deflection angle of the photon from its former direction of flight θ. This relationship can be expressed in terms of the so-called Compton shift $\Delta\lambda$:

$$\Delta\lambda = \lambda\,' - \lambda = \frac{h}{m_0c}\,(1-\cos\theta)$$

The kinetic energy of the Compton electron is:

$$E_{kin,e^-} = h\nu - h\nu\,' - E_{e^-,bond} \approx h\nu\frac{(1-\cos\theta)}{\frac{m_0c^2}{h\nu}+(1-\cos\theta)}$$

where the binding energy of the bound valence electron, is often small compared to the photon energy and can therefore be neglected. The emission angle φ of the electron with respect to the direction of flight of the primary photon is:

$$\tan\varphi = \frac{\sin\theta}{(1+\frac{h\nu}{m_0c^2})(1-\cos\theta)}$$

The angular distribution of both the electron and the deflected photon strongly depend on the energy of the incoming photon. For small photon energies, even photon back reflection is possible, while for high energies, both are predominantly scattered in forward direction (see figure B.5). The energy of the Compton scattered photon is minimal for $\cos\theta = -1$, or $\theta = \pi$, but can take on all values between this minimum and the maximum, which is a function of the primary photon energy (see left side of figure B.6). The energy of the electron displays a complementary behaviour to the photon energy and has an upper limit: $\mathrm{E}^{\mathrm{max}}_{\mathrm{kin,e^-}} \approx \frac{(\mathrm{h}\nu)^2}{\mathrm{m_0c^2}}$ for the minimal $\cos\theta = -1$ photon energy (see right side of figure B.6). At low primary photon energies, the relative energy loss of the photon is smaller than at high energies (compare $E'_\gamma/E_\gamma \approx 0.7$ at 100 keV and $E'_\gamma/E_\gamma \approx 0.2$ at 1MeV). The electron energy, behaving complementary to the photon energy, can therefore be quite large for high photon energies. This results in electrons which have a range from zero up to several centimetres in tissue (see chapter B.3). So photons with higher energies can deposit their energy farther away from the main axis mediated by these high energy secondary electrons.

The probability of scattering ($d\sigma/d\Omega$) with deflection angle θ is given by the differential scattering cross section of Klein-Nishina [96] (see figure B.7):

$$\frac{d\sigma}{d\Omega} = \frac{r_0^2}{2}(1+\cos^2\theta)\left(\frac{1}{1+\alpha(1-\cos\theta)}\right)^2\left(1+\frac{\alpha^2(1-\cos\theta)^2}{[1+\alpha(1-\cos\theta)](1+\cos^2\theta)}\right)$$

with $\alpha = h\nu/m_ec^2$ and $r_0 = 2.82\cdot 10^{-15}m = \frac{e^2}{4\pi\epsilon_0\cdot m_ec^2}$ = "radius of the electron". The charged and excited ion relaxes subsequently, in the same way as after the photoelectrical effect.

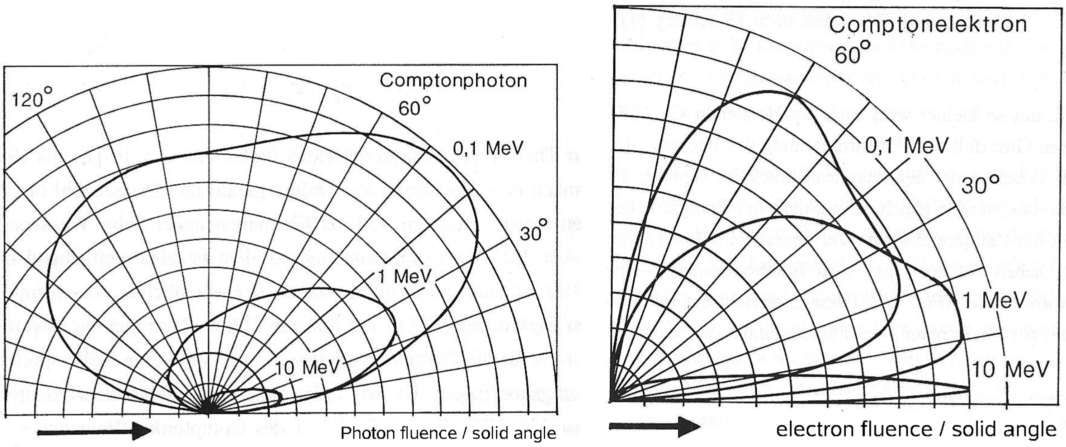

Figure B.5: *Distribution of the Compton-photon and -electron angle depending on the primary photon energy and angle to the direction of incidence (arrow) [70]*

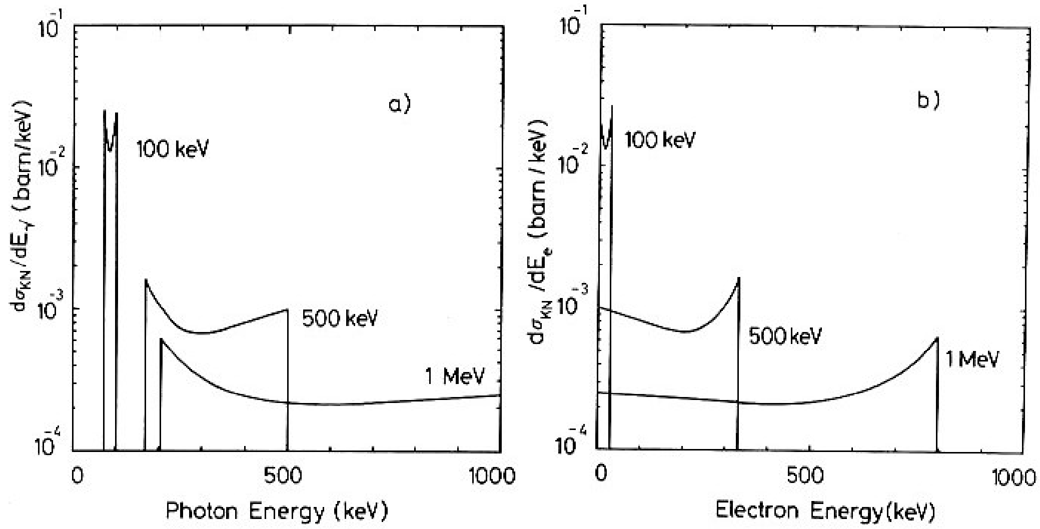

Figure B.6: *(a) Compton photon- and (b) electron-spectrum after Comptonscattering of 0.1, 0.5 and 1 MeV-photons [96]*

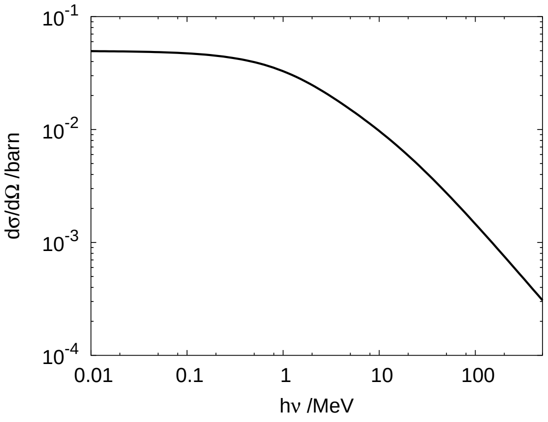

Figure B.7: *Total compton cross section $d\sigma/d\Omega$ per electron given by Klein-Nishina for a fixed photon scattering angle of $\theta = 30°$ [96]*

B.1.4 Pair production

Pair production in the electromagnetic field of a nucleus can only happen at energies above two times the rest energy of the electron:

$$2E_{rest} = 2m_0c^2 = 1,022MeV$$

It is not the dominating interaction at energies below rather high energies $E_\gamma > 10$ MeV (see figure B.1). In the coulomb field of a nucleus, the photon interacts electromagnetically and disappears into an electron-positron pair. Because the two particles have the same mass, the angle between the direction of flight of the electron and the positron is always 180° in the centre of mass system, while in the laboratory system, they are boosted in a more or less forward direction, depending on the energy and momentum of the photon. The energy surpassing twice the rest energy is distributed between the electron and the positron. They have an identical spectrum, with the maximum energy:

$$E_{max} = h\nu - 2m_0c^2$$

Both the electron and the positron release their energy in inelastic interactions with the material (see chapter B.3). When the positron has only very little kinetic energy left, the inverse process can happen. Together with an electron, it will annihilate and two 511 keV photons are emitted. This process is called annihilation (see chapter B.3.5). The two photons can again interact with the material, or escape without any changes. For the whole pair production process, the mass of the participating nucleus is so large that the absorption of momentum can typically be neglected. This is not the case for pair production in the field of an electron. Its momentum and energy absorption have to be taken into account. Therefore, this process is often called triplet production. It is rather improbable and physically it cannot happen unless the photon energy is larger than four times the rest energy of an electron ($E_\gamma > 4m_ec^2 = 2.044$ MeV).

B.1.5 Photonuclear reactions

Photons with very high energies can even interact with the nucleus, knocking out a neutron or proton. The remaining nucleus is frequently still exited and relaxes by emitting other particles. Like in the case of the photoelectric effect, the photon energy has to exceed at least the binding energy of the nucleon. This is identical to the energy which the knocked out particle needs to overcome the potential well, which is caused by the nuclear reaction in the case of neutrons. The photon energy has to be still higher in the case of a knocked out proton, because this has to overcome both the nuclear interaction and the coulomb barrier. The threshold for photonulear reaction is much higher than that for pair production, for most elements, the minimal energy is between 6 and 20 MeV, (see table B.1). Furthermore, the cross section at those energies is several orders of magnitudes smaller than the one of the photoelectric effect, compton scattering and pair production. Nevertheless, in high energy photon fields, like for example at modern high energy linear accelerators applied in hospitals with acceleration voltages higher than 15 MV, a measurable neutron flux is induced. Additionally, the photonuclear reaction can excite a nucleus, e.g. in the air of the treatment room.

reaction	**threshold [MeV]**	**decay**	$T_1/2$
$^{12}C(\gamma,n)^{11}C^*$	18.7	β^+,EC	20.4 min
$^{14}N(\gamma,n)^{13}N^*$	10.5	β^+	9.96 min
$^{16}O(\gamma,n)^{15}O^*$	15.68	β^+,EC	122 s
$^{16}O(\gamma,2n)^{14}O^*$	28.9	β^+,γ	70.6 s
$^{27}Al(\gamma,2n)^{26}Al^*$	12.7	β^+,γ,EC	6.4 s
$^{12}C(\gamma,p)^{11}B$	16.0	stable	-
$^{16}O(\gamma,p)^{15}N$	12.1	stable	-
$^{27}Al(\gamma,p)^{26}Mg$	8.3	stable	-

Table B.1: *Nuclear photo reactions for some atoms relevant in radiation therapy with decay properties of the daughter nuclei [121]*

The unstable nucleus relaxes into the ground state by subsequent decay, emitting β^+, β^- or photons or undergoing internal conversion. Therefore, operators of high energy accelerators are obliged to provide good air conditioning to reduce radiation exposure to the staff and patients by activated air particles.

B.1.6 Photon attenuation

The "range" of a photon in a specified material can be described as the exponential attenuation:

$$I(x) = I_0 \cdot e^{-\mu x} \quad \Rightarrow \quad d_{1/2} = \frac{\ln 2}{\mu} \quad , \quad d_{1/10} = \frac{\ln 10}{\mu}$$

with primary intensity I_0. The primary intensity $I(x)$ inside a material decreases exponentially with the material thickness x. The absorption coefficient μ is the sum of the absorption coefficients of the constituent photon reactions:

$$\mu = \mu_{coh} + \mu_{photo} + \mu_{compton} + \mu_{pair}$$

To give an estimate of the attenuation of a photon, the half value layer $d_{1/2}$ or the tenth value layer $d_{1/10}$ are used, which give the thickness of the layer that decreases the intensity to 50% and 10% respectively. For 1MeV photons in water $d_{1/10}$ is approximately 30 cm.

B.1.7 Depth dose curve

Photons entering into a material will interact elastically or inelastically, will be deflected and absorbed. The deposited energy of these processes can be described locally as absorbed dose (see chapter A.1). The depth dose curve is defined as the development of this dose with depth in material.

Photons are indirectly ionising particles and therefore the properties of the induced secondary electron radiation (see chapter B.3) are crucial for the energy deposition. A steep build-up is evoked by them behind an interface of materials with different densities followed by a shallow decline. The exact form of the curve depends strongly on the energy of the primary photons. At high energies, the dose maximum is shifted to greater depth, but the curve becomes shallower as "harder" radiation is more penetrating. In radiation therapy this effect is used to reduce dose to the skin, which is typically not the target volume. On the other hand, healthy organs behind the tumour get more dose when photons with higher energies are used.

B.2 Neutrons

Neutrons, like photons, are uncharged "indirectly ionising" particles. Neutrons are instable when not bound in a nucleus and decay with a half-life of 886 seconds into a proton, an electron and an antineutrino. Though uncharged, neutrons can also interact by electromagnetic forces with an electron. This is caused by the spin, the magnetic moment and the inhomogeneity in the distribution of charge inside the neutron. But the forces connected to these physical quantities are extremely small and can be neglected here.

Interaction with matter is mediated by the strong (nuclear) forces, which are typically confined to a very small radius of impact of some femtometers($= 10^{-15}$m). In material, the nuclei of the atoms do not lie closely to each other. Therefore, interaction of neutrons with the nuclei are scarce and neutrons have quite a large "range" (defined in a similar way as for photons) in matter, which is also called a high penetration capability.

Neutrons are normally classified by their kinetic energy. The energies relevant for this thesis are thermal neutrons (about 2 meV to 100 meV), epithermal neutrons (up to 1 eV), intermediate neutrons (up to 10 keV) and fast neutrons (up to 20 MeV). Thermal means that the neutrons are in thermal equilibrium with their surrounding. At room temperature, this can be described with a Maxwell- Boltzmann-distribution, with the most probable energy at 25 meV and the average energy at 38 meV. Thermal neutrons scatter elastically with the atoms of the material, gaining or losing energy in the process, until they are captured or leave the material.

Compared to charged particles like protons, neutrons penetrate deeply into matter. Monoenergetic neutron depth dose curves display a steeper decline than those of photons with the same energy when entering into dense biological matter. At greater depths, the secondary gamma-radiation entails the curve to flatten out. The depth dose curve can usually be fitted with a combination of two exponential declines, one originating from the neutrons, the other depending on the secondary photons. The depth dose distribution strongly depends on the exact atomic (even isotopic) composition of the material. Scattering with and without excitation of the nucleus and neutron capture with relaxation reactions of the nucleus afterwards are the main interaction types in tissue at neutron energies produced with the converter at the FRM II (see chapter 3.1). In figures B.9 and C.1-C.4, the cross sections of the different kinds of target atoms can be seen. Resonances are usually not found at lower energies, where capture and elastic scattering dominate (gold is an exception to this as can be seen

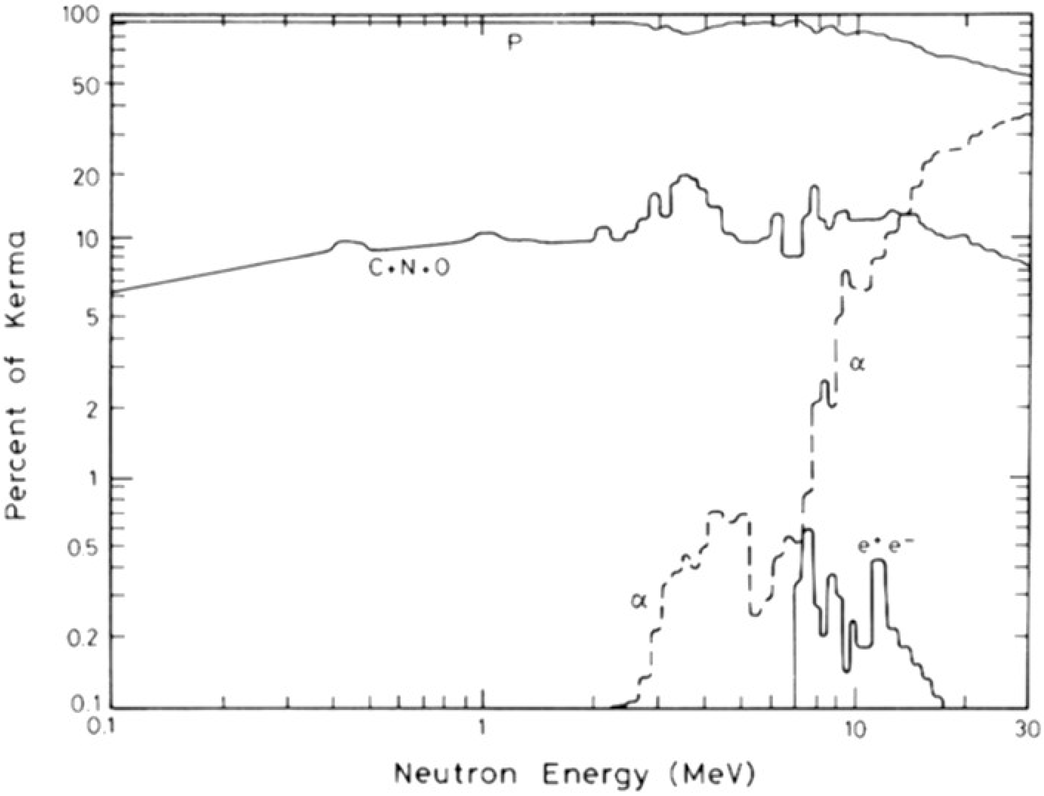

Figure B.8: *Fraction of* KERMA *going into different charged secondary particles of neutrons in tissue equivalent plastic (A 150)[96]*

in figure C.4). The main interaction partners in tissue are protons (see figure B.8), which have a very high elastic scattering cross section over a wide range of energies (10 times as high as that of other relevant atoms) a big abundance in most tissues, and can accept larger recoil energies. In the following sections, the different kinds of interaction are described separately.

B.2.1 Neutron production

Neutrons can be produced in different ways. In nuclear reactors, neutrons with a spectrum ranging from thermal energies up to around 15 MeV are generated by fission of ^{235}U. The average energy is 2 MeV. A moderator is needed to slow down the neutrons emanating from the uranium in order to keep the chain reaction going [121]. The exact spectrum of the neutrons depends on the materials (moderator, shielding, filters,...) between the core and the application. Particle accelerators can also produce neutrons, utilising specific reactions, like T(d,n)α. To avoid exited states of the product nucleus, light particles are preferred as target material of a proton or deuteron beam. The neutrons from these reactions are quasi-monoenergetic.
Alpha-particle emitters can also be used as particle source for a producing reaction like: $^9_4$Be(α,n)$^{12}_6$C [121]. Usually the alpha-source is radium, polonium or plutonium, mixed

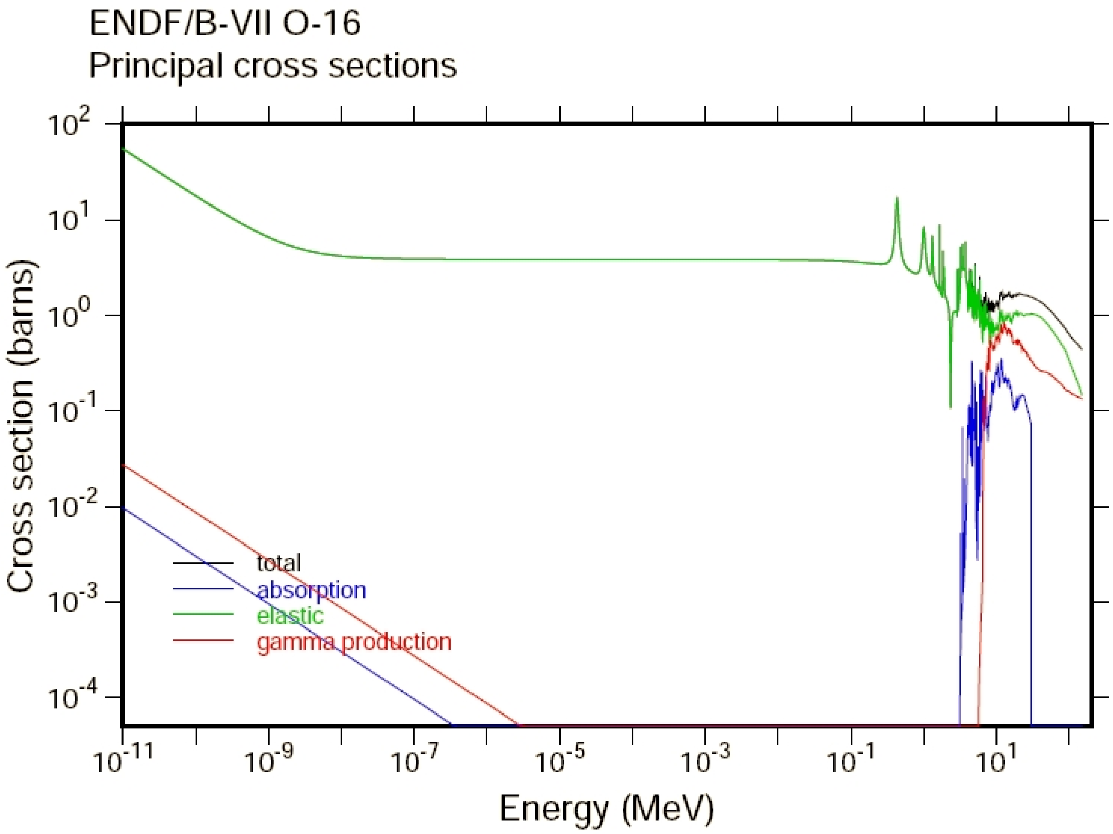

Figure B.9: *Interaction cross sections for neutrons in oxygen* ^{16}O *[79]*

with a light metal (beryllium, boron) to minimise the coulomb repulsion between α and nucleus. The emitted (monoenergetic) alpha particles slow down to different energies before they react and produce neutrons. On the other side, the transmitted energy, which is the Q-value of the (α,n)-reaction and the kinetic energy of the alpha before the interaction, is split between the neutron and the nucleus. Therefore, the neutrons produced have a wide energy spectrum. The intensity of this neutron production decreases with its driving force, the α-emitter decay.

A similar method is to use a photoneutron source, where a photon is captured and a neutron emitted afterwards (γ,n). This can be designed quasi-monoenergetic if a nucleus is selected as photon emitter which has only one single γ-line. Compared to an alpha particle, a photon with energies around 1 MeV has a very large range (about 10 cm half value layer in tissue; 5 MeV-α has 50 μm range) and the energy loss inside the source between its radiation and its capture can be neglected. The main drawback of the photoneutron sources is the very strong gamma-ray background. For every neutron produced, there are 1000 photons emitted simultaneously. Similar to the alpha-emitter source, the intensity decreases with the decay of the γ-producing nuclide. Both the alpha and the photonuclear source are designed in encapsulated form.

For calibration purposes, another radioactive source can be used: heavy nuclei (^{254}Cf, ^{252}Cf, ^{238}Pu, ...), which can decay by spontaneous fission. Their greatest advantage is

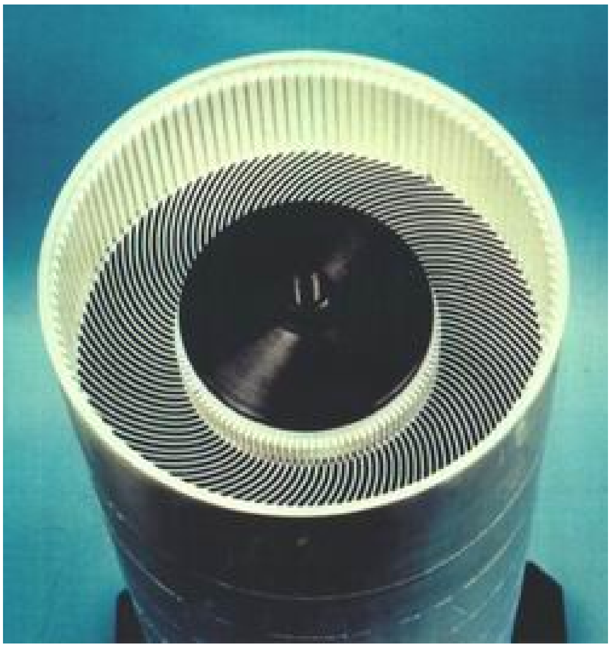

Figure B.10: *Picture from FRM II [31]: 113 fuel plates are welded inside the fuel element in evolvent form around the centre. The cooling slot is homogeneously 2.2 mm thick everywhere.*

their big half life which is usually much larger than that of the alpha-emitter-source. The energy of neutrons and the remaining nuclei are spectra like those in induced fission (see chapter B.2.5).

B.2.2 Elastic scattering

Elastic scattering dominates neutron interactions below 5 MeV in tissue. Since total energy is conserved, the kinetic energy loss of the neutrons in the interaction is equal to the kinetic energy gain of the secondary particles produced. Most important is elastic scattering of neutrons by hydrogen, which have approximately equal mass. Hydrogen elastic scattering in tissue amounts to 85% of KERMA (see figure B.8). The maximum energy that can be transferred from a neutron with kinetic energy E_n to a nucleus with mass number A can be derived from conservation of energy and momentum:

$$Q_{max} = \frac{4A}{(A+1)^2} E_n$$

In analogy to the collision of a billiard ball, a neutron hitting an hydrogen nucleus can transfer its whole energy to the interaction partner. The ratio of the proton energy after the collision to the kinetic energy of the neutron E_n can also be derived from conservation of energy and momentum:

$$\frac{Q}{E_n} = \cos^2\theta$$

with θ being the scattering angle of the proton, which adds with the neutron scattering angle to 90° (if non-relativistic). This is one way to measure the energy spectrum of a neutron beam: the so called proton-recoil spectrometer, where Q and θ are measured to derive E_n. In the centre-of-mass frame, the absolute value of the momenta does not change and the proton angle in the laboratory frame of reference θ depends on that in the centre-of-mass frame ω in the following way:

$$\omega = 2\theta$$

In the centre-of-mass frame, the scattering is isotropic. The probability that a proton is scattered in the area element dA is:

$$P_\omega(\omega)d\omega = \frac{dA}{4\pi R^2} = \frac{1}{2}\sin\omega d\omega$$

Transformed to the laboratory system,

$$P_\theta(\theta)d\theta = 2\sin\theta\cos\theta d\theta$$

and for the proton energy:

$$P(Q)dQ = \frac{1}{E_n}dQ$$

The isotropy of the spectrum still holds in the centre-of-mass frame even if the mass of the neutron and the nucleus are not equal. Thus, the average energy transferred to a nucleus is approximately one half of the maximum energy that can be transferred to the nucleus.

Thermal scattering is a special form of elastic scattering at very low energies (below 4 eV). There, the target atom cannot be assumed to be free, but the molecular binding has to be taken into account. The neutron scatters then on a bound atom, which has different properties of backscattering, etc. Special cross section data sets are needed for this kind of interaction. These are available from Los Alamos [79] for hydrogen in water and hydrogen in polyethylene. They are included in the GEANT4 dataset.

B.2.3 Inelastic scattering

In inelastic scattering, some of the energy transferred by the neutron is absorbed by the nucleus internally, which results in the excitation of the nucleus. The neutron is either scattered or absorbed in the process. The nucleus gets de-excited by emitting one or several photons or particles. The energy which these particles need to overcome the potential well has to be delivered by the neutron. The remaining energy transferred by the neutron is distributed to these secondary particles as kinetic energy. It can amount to several MeV. The two principal possibilities for this interaction, scattering or absorption of the neutron can be written in the following form :

$${}^{\mathrm{A}}_{\mathrm{Z}}\mathrm{X}(\mathrm{n},\mathrm{n}'){}^{\mathrm{A}}_{\mathrm{Z}}\mathrm{X}^* \quad \text{and} \quad {}^{\mathrm{A}}_{\mathrm{Z}}\mathrm{X}\ (\mathrm{n},\ {}^{\mathrm{a}}_{\mathrm{b}}\mathrm{x})\ {}^{\mathrm{A}+1-\mathrm{a}}_{\mathrm{Z}-\mathrm{b}}\mathrm{X}$$

An example for the first reaction is the inelastic scattering of neutrons on carbon:

$${}^{12}\mathrm{C}(\mathrm{n},\mathrm{n}'){}^{12}\mathrm{C}^*$$

with a threshold of 4.8 MeV and a cross section of 0.53 barn.

An example of the second reaction is the inelastic scattering of neutrons on ^{3}He:

$${}^{3}_{2}\mathrm{He}(\mathrm{n},\mathrm{p})\mathrm{T}$$

with a cross section of $5.33 \cdot 10^3$ barns and a Q-value of 765 keV. ^{3}He can be used as counter gas inside a Bonner sphere spectrometer for low intensity neutron fields. Another famous reaction is the inelastic neutron scattering on atmospheric nitrogen ^{14}N:

$$^{14}_{7}\mathrm{N(n,p)}^{14}_{6}\mathrm{C}$$

with $\sigma = 1.7\,\mathrm{barn}$ and $\mathrm{Q} = 626\,\mathrm{keV}$. Besides capture by hydrogen, this is another way neutrons can deposit significant energy to tissue. On the other hand, the concentration ratio of ^{14}C to ^{12}C can also be used to determine the age of materials which no longer take part in the natural carbon-cycle (because they are dead).
Many elastic and inelastic interactions (as well as capture reactions) are only possible if the neutron has a kinetic energy above a certain threshold. These characteristic energies can also be used to evaluate the properties of an unknown neutron spectrum by pre-calculating response functions and unfolding measured activations or secondary particles.

B.2.4 Neutron capture

Neutron capture is not very different from inelastic scattering. The neutron is absorbed by the nucleus ("captured") and the latter gets excited. To de-excite back into the ground state, one or more photons are emitted. They can have quite high energies and contribute considerably to the radiation exposure of healthy tissue inside a human body, particularly even outside the main beam of neutrons (for interaction properties of photons see figure B.1). In general:

$$^{\mathrm{A}}_{\mathrm{Z}}\mathrm{X}\ (\mathrm{n},\ \gamma)\ ^{\mathrm{A+1}}_{\mathrm{Z}}\mathrm{X}$$

The probability of neutron capture rises with the retention period of the neutron inside the sphere of the strong interaction field of the nucleus. Therefore, the cross section for neutron capture is much larger for thermal neutrons than for fast ones and, disregarding resonances, it often displays a $1/v$ decline (with $v =$ neutron velocity):

$$\sigma \sim \frac{1}{v} \sim \frac{1}{\sqrt{E}}$$

For low energies, capture is usually the leading interaction process for many atoms. One of the most important capture processes in tissue, though the cross section is not exceptionally big (0.33 barn), is the one on hydrogen:

$$^{1}_{1}\mathrm{H(n,}\gamma\mathrm{)d} \quad \text{with} \quad \mathrm{E}_\gamma = 2,225\mathrm{MeV}$$

The 2.225 MeV-photons contribute considerably to the γ-contamination of the neutron beam inside a hydrogen-containing target and to total energy deposition in an extended body. Another example is neutron capture by gold:

$$^{197}_{79}\mathrm{Au(n,}\gamma\mathrm{)}^{198}_{79}\mathrm{Au}$$

with $\sigma = 98.8\,\mathrm{barn}$ (thermal capture cross section). $^{197}_{79}$Au can be used for neutron detection by activation inside a Bonner sphere spectrometer at high intensity neutron fields (see also B.2.6).

B.2.5 Fission by neutrons

When a nucleus (heavier than iron) is fissioned into smaller fragments, energy is released because the binding energy per nucleon decreases with increasing atomic mass number. An example for this physical property is the alpha-particle decay, where a nucleus $^{\mathrm{A}}_{\mathrm{Z}}\mathrm{X}$ spontaneously emits an α-particle ($^{4}_{2}\mathrm{He}$) and is converted into $^{\mathrm{A-4}}_{\mathrm{Z-2}}\mathrm{Y}$. There are two kinds of fission: spontaneous (see chapter B.2.1) and induced. In nuclear reactors, the second kind is used to produce further neutrons for research or for maintaining the chain reaction and thereby producing heat/energy. Induced fission is triggered by a neutron, which is absorbed by the nucleus. This induces vibrations in the nucleus, which distends and splits because of electrostatic repulsion. The probability that a neutron is absorbed is much higher for thermal than for higher neutron energies. For example the thermal neutron fission cross section for ^{235}U is 530 barn whereas for 1 MeV neutrons it is only about 1 barn. Therefore, neutrons have to be moderated inside a reactor (for example by water), to enable an efficient and ongoing chain reaction. Fission strongly depends on the inner properties of the nucleus. Theoretically, it is possible also for “small nuclei” ($\mathrm{Z} > 56$). But for heavier nuclei the cross sections are much higher, because the strong force holding the nucleus together becomes smaller than the electrostatic repulsion between the nuclear protons. The latter decreases slower with distance than the strong force. Thus, the nuclei become more unstable. Additionally, the ratio of protons to neutrons inside the nucleus is also of importance. Nuclei with even-odd numbers of protons and neutrons are split more readily than those with odd or even number for both, because the energy released is higher. For the breakup, there are many different possibilities. For $^{235}_{92}\mathrm{U}$ for example there is:

$$^{1}_{0}\mathrm{n} +^{235}_{92}\mathrm{U} \rightarrow^{147}_{57}\mathrm{La} +^{87}_{35}\mathrm{Br} + 2\,^{1}_{0}\mathrm{n}$$

with an average kinetic energy of all secondary particles of 195 MeV and an average number of secondary neutrons of 2.5 (of which 99.36% are emitted promptly). There is a high probability that the masses of the produced secondaries are asymmetric, which leads to a bimodal mass distribution of the fragments. Most of the fragments are radioactive themselves and decay later on.

B.2.6 Neutron activation

Target atoms can become activated by different neutron interactions, mainly inelastic scattering and capture (see chapters B.2.3 and B.2.4). The activated nuclei decay with decay-constants λ into N daughter atoms. The rate of change in the number of daughter atoms during the irradiation can be calculated:

$$\frac{\mathrm{dN}}{\mathrm{dt}} = \Phi\sigma\mathrm{N_T} - \lambda\mathrm{N}$$

with the number of target atoms $\mathrm{N_T}$, the neutron capture cross section σ and a neutron beam flux Φ (in $\frac{\mathrm{neutrons}}{\mathrm{cm^2 s}}$). With the assumption that the flux rate is constant in time ($\Phi = \mathit{const}$) and that the primary number of target atoms is so large that their decrease by activation can be neglected ($\mathrm{N_T} = \mathrm{const}$), this equation can easily be solved. For

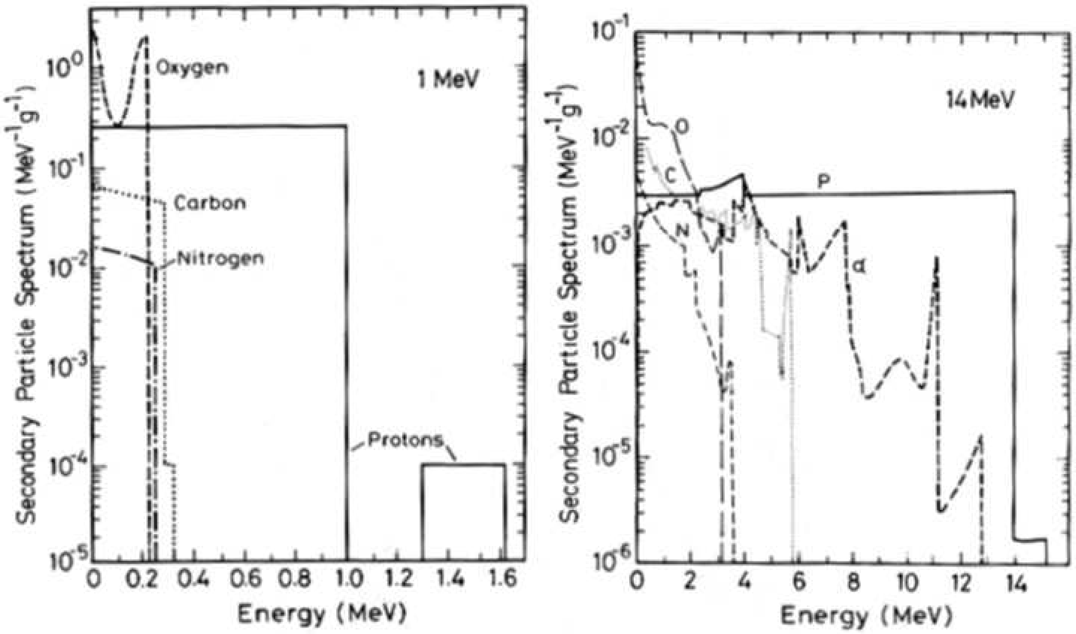

Figure B.11: *Secondary particle spectra of 1MeV and 14 MeV neutrons in ICRU tissue; protons at higher energies than primary neutrons from* $^{14}\mathrm{N(n,p)}^{14}\mathrm{C}$*-reaction [96]*

zero daughter atoms at the beginning of the irradiation (N(t = 0) = 0), the activity of the daughter λN is:

$$\lambda \mathrm{N} = \Phi\sigma \mathrm{N_T}(1 - \mathrm{e}^{-\lambda t})$$

$A_\infty = \Phi\sigma N_T$ is the saturation activity that is reached for infinite irradiation time (for shorter irradiation times see chapter E.1).
If the primary neutrons are not monoenergetic but spread over a certain range of energies, this equation can be solved e.g. for all necessary energy groups. Inside these energy groups, the cross section has to be averaged.

B.2.7 Secondary particle spectra

As was explained in chapter B.2, neutrons are indirectly ionising particles, which deposit their energy via secondary particles. For a better understanding of neutron action on tissue it is therefore important to have a certain knowledge about the secondary particle spectra. In figure B.11, the secondary particle spectra of two monoenergetic neutron beams in ICRU-tissue are plotted, namely for 1 MeV and for 14 MeV. For neutron energies above several MeV, the cross sections of many of the alpha-particle producing reactions are increasing (see also figures B.9 and C). Therefore, these particle start to play a role for energy deposition (see also fraction of KERMA curves in figure B.8). For low energy neutrons, secondary particles are mainly produced by elastic interaction, next to (n,p) and (nγ) reactions. For protons as interaction partners, this leads to a rectangular secondary particle spectrum (this was discussed in detail in chapter B.2.2). Furthermore, there are some protons with higher energy than that of the primary neutron. These are produced by the $^{14}N(n,p)^{14}C$-reaction. Heavier particles are also elastic scattering partners. Because of their larger mass, they have smaller energies after the interaction and are not so important for neutron energy deposition.

B.2.8 Neutron and photon track structures

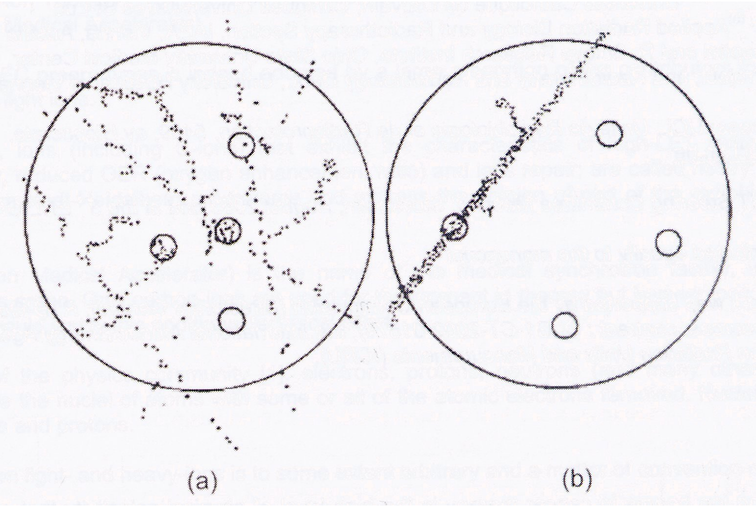

Figure B.12: *Distribution of ionisations in a medium irradiated by X-rays (a) and neutrons (b). The black dots represent ionisations produced along the tracks of secondary particles.[128]*

Though both neutrons and photons are indirectly ionising particles, the energy deposition on a microscopic level is quite different. As shown in figure B.12, photons (on the left side) are less densely ionising. Through their secondary particles, the electrons, the energy is deposited in smaller and more variable amounts. A hit of a cell nucleus does not always lead to a lethal event, often many tracks are required to achieve cell death [9]. On the other side, neutrons, together with their much more densly ionising secondary particles, protons and heavier ions, produce a track that is narrower. When a target is transversed by a particle track, a large amount of energy is deposited, which could lead to cell death. Comparison of microscopic spectra for equal absorbed dose values indicates that in subcellular volumes ($1-2\,\mu$m), the energy deposited is about 100 times higher for neutrons than for photons on average [128]. This leads to a different biological efficiency, depending on the radiation quality, which is further discussed in chapter 2.

B.3 Electrons and positrons

Electrons and positrons are charged particles interacting directly with atoms and molecules. Both can occur as secondary particles of many other kinds of incident particles. Compared with their usual interaction partners, they have small masses. Therefore they are subject to large changes in their directions of flight. Furthermore, they display relativistic behaviour already at low energies: electrons with a kinetic energy of 2.56 keV have a velocity of 0.1-times the velocity of light and therefore must be

considered relativistic. Electrons and positrons share some of their interaction properties with heavier charged particles (ions), but at high energies, they behave quite differently.
Basically, two kinds of interactions can be differentiated: collision and radiative energy loss. At low energies ($E_e < 1MeV$) excitation or ionisation of the atomic shell dominates the interaction events. The electron collides with the whole atomic shell or with a single electron. The electron can get electro-magnetically deflected in the field of the nucleus or one of the shell-electrons. It changes direction and releases energy in form of radiation (Bremsstrahlung).
Positrons interact very similar to electrons, with the only exception that they have a positive charge. This is most important in close collisions. Furthermore, being the antipartcles of electrons, they can "annihilate" at low energies.

B.3.1 Electron collisions

Electron collision can happen with the whole atomic shell or with a single shell electron. The first case dominates when the primary electron has relatively low energy ($\lessapprox 25\,keV$). The electron can be deflected elastically without loss of energy or it can excite/ionize the atom. The shell deexcites by emitting a secondary electron (Auger-electron) or photon (fluorescence photon). If the electron has higher energy, which corresponds to a smaller impact parameter, it can penetrate into another atomic shell and interact directly with single electrons there. The primary electron can excite other shell electrons to higher states of energy or even ionise them, followed by a series of relaxation mechanisms. The probability for ionisation in an inelastic collision increases

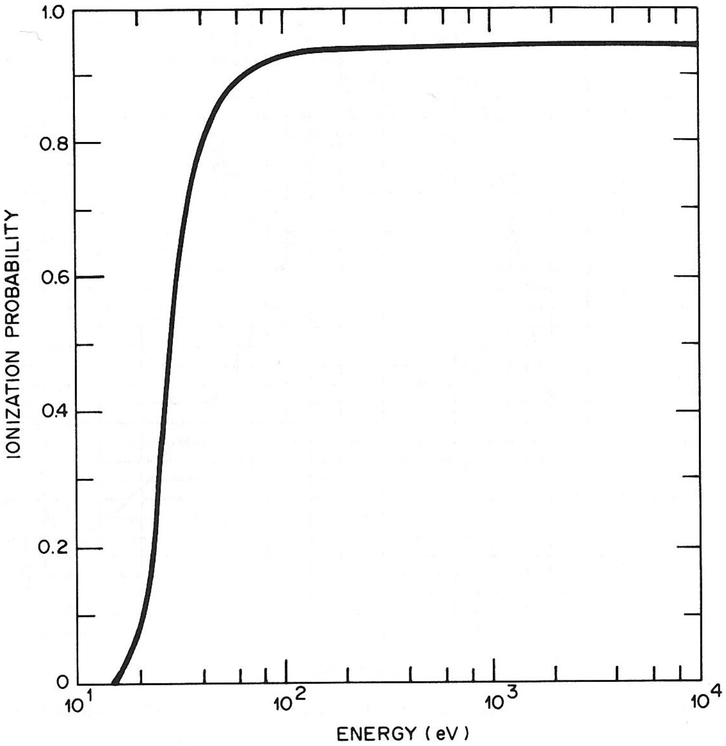

Figure B.13: *Probability of an energy loss causing ionisation and not excitation [121]*

steeply at low energies until reaching its maximum of about 95% at about 100 eV (see figure B.13). In contrary to the photoeffect, typically outer shell electrons (valence-electrons) are ionised. But inner electrons from the K- and L- shell can be hit, too. These interactions are the reason for the characteristic lines in the spectrum of an x-ray tube, for example.

The energies of the secondary electrons can get very big, but they are limited by definition to 50% of the primary electron energy. This is due to the indistinguishability of the two particles. Therefore, the particle which has more kinetic energy after the collision is defined as the primary projectile. The secondary electron can have enough energy to ionise further electrons (over about, say, 200 eV); it is then sometimes called δ-electron.

According to Bethe's theory, the total inelastic cross section can be written as [96]:

$$\sigma(\mathrm{E}) = \frac{\mathrm{A}}{\mathrm{E}} \ln \mathrm{E} + \frac{\mathrm{B}}{\mathrm{E}} + \frac{\mathrm{C}}{\mathrm{E}^2} + \cdots$$

with electron energy E, material-dependant probabilities for hard (close) collisions B and C and those for grazing (far) collisions A. Their cross section rises steeply until around 100eV to decline afterwards more shallowly (see figure B.14).

At higher energies, such collisions get more and more rare and bremsstrahlung begins to dominate. This can nicely be seen in the evolution of the mass collision and mass radiation stopping power[1](see figure B.15). Collision dominates for energies smaller than 1 MeV, while after a short transition phase, the main contribution of the interaction is bremsstrahlung above 10 MeV. Collision stopping power $\left(-\frac{dE}{dx}\right)^{\mp}_{col}$ can be described in the following way [121]:

$$\left(-\frac{\mathrm{dE}}{\mathrm{dx}}\right)^{\mp}_{\mathrm{col}} = \frac{4\pi \mathrm{k}_0^2 \mathrm{e}^4 \mathrm{n}}{\mathrm{mc}^2 \beta^2} \left[\ln \frac{\mathrm{mc}^2 \tau \sqrt{\tau + 2}}{\sqrt{2}\, \mathrm{I}} + \mathrm{F}^{\mp}(\beta)\right]$$

With $\tau = E^{e^-}_{kin}/mc^2$ and $\mathrm{F}^-(\beta)$ for electrons:

$$\mathrm{F}^-(\beta) = \frac{1-\beta^2}{2}\left[1 + \frac{\tau^2}{8} - (2\tau + 1)\ln 2\right]$$

and for positrons because of their difference in charge:

$$\mathrm{F}^+(\beta) = \ln 2 - \frac{\beta^2}{24}\left[23 + \frac{14}{\tau + 2} + \frac{10}{(\tau + 2)^2} + \frac{4}{(\tau + 2)^3}\right]$$

At very high, relativistic energies, collision stopping power rises again. This is due to the Lorentz contraction, which is called density-effect. It enables the interaction of particles that are farther away from each other. As a consequence, collision stopping power is not proportional to the density any more. Another effect is the polarisation effect, which causes the mass radiation stopping power of heavy materials to rise less steep with energy than that of lighter materials. This is caused by the density-dependence of the polarisation, which has the following origin. The target atoms get

---

[1] Dividing the stopping powers by the density ρ eliminates the dependence on the density

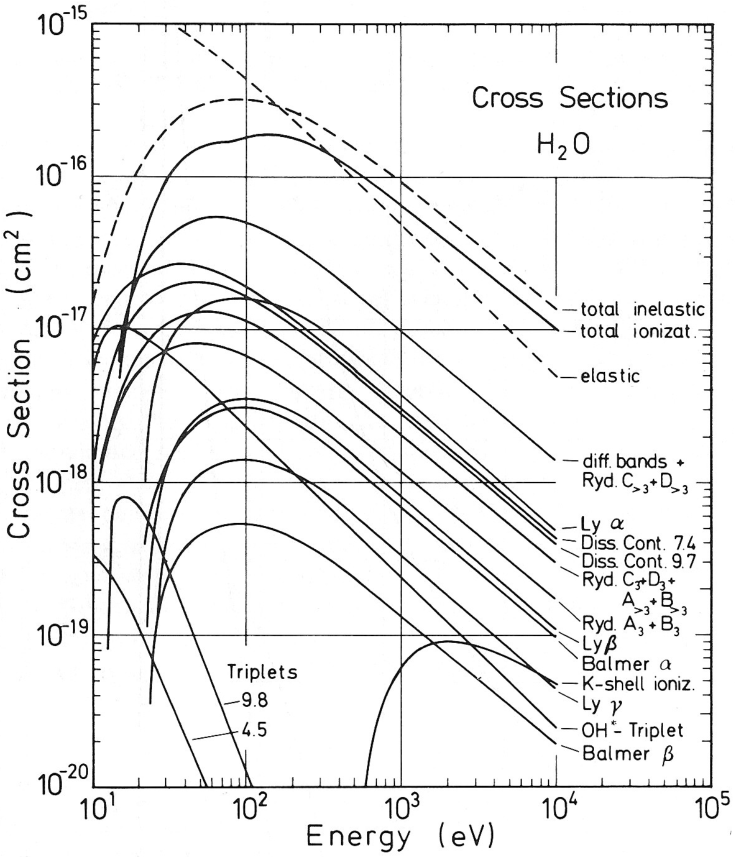

Figure B.14: *Electron cross section for elastic scattering, ionisation and excitation in water vapour at low energies [96]*

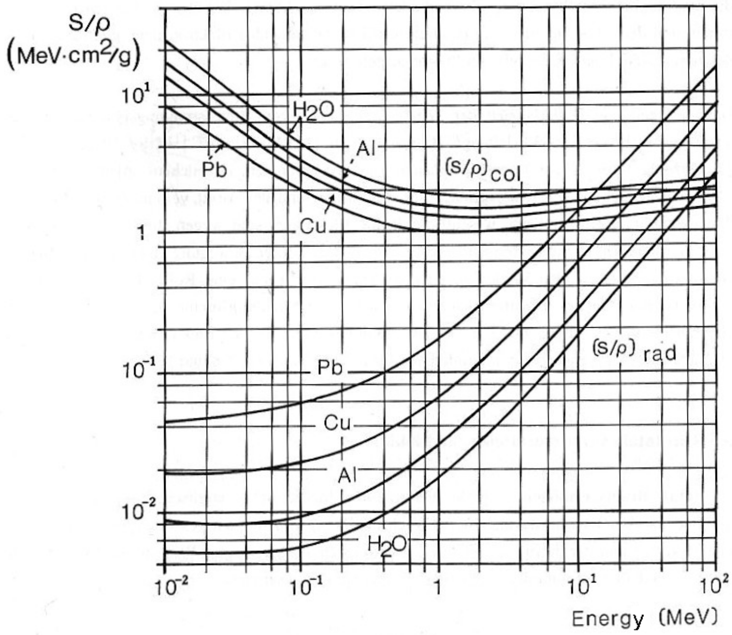

Figure B.15: *Mass collision* $(S/\rho)_{col}$ *and mass radiation* $(S/\rho)_{rad}$ *stopping power for electrons in water, aluminium, lead and copper at high energies [70]*

polarised in the electromagnetic field of the incoming primary electron. This polarisation depends on the local charge density which is proportional to the density of the target. At relativistic energies, the electromagnetic field of the primary electron gets more and more distorted. This, in turn, changes the polarisation of the target. But these polarised atoms shield the electrons from distant charges. So with less shielding, more interaction is possible.

B.3.2 Bremsstrahlung

When a primary electron is deflected, and therefore accelerated, in the more or less well shielded[2] Coulomb field of a nucleus or another electron, bremsstrahlung is emitted. The primary electron has to have sufficient energy to penetrate into the atom. There, an interaction with a single particle is possible. The momentum of the electron is changed by this deflection and the difference in momenta transferred to photons. These photons can have the same energy as the primary electron at most, the distribution of energy is homogeneous between zero and this value (see [121]). Deflection without energy loss is also possible in the limiting case of elastic scattering. The secondary photons tend to be emitted the more in forward direction the higher the primary electron energy. This property is used to produce synchrotron radiation. In one part of a synchrotron, the direction of flight of the electron is switched frequently (in the so called wiggler), to convert as much energy to bremsstrahlung (then called synchrotron radiation) as possible. This synchrotron radiation is emitted as a narrow beam in the direction of flight of the electrons. In an x-ray tube, bremsstrahlung is the so called continuous X-ray background.

There exists no closed analytical formula for the mass radiation stopping power, but it can be calculated numerically. An approximation for the ratio between collision and radiative stopping power of electrons with total energy E in an element with atomic number Z is (see [121]):

$$\frac{\left(-\frac{\mathrm{dE}}{\mathrm{dx}}\right)^-_{\mathrm{rad}}}{\left(-\frac{\mathrm{dE}}{\mathrm{dx}}\right)^-_{\mathrm{col}}} \approx \frac{\mathrm{Z} \cdot \mathrm{E[MeV]}}{800} \qquad (\mathrm{E_e} > 500\,\mathrm{keV})$$

The radiative energy loss increases with decreasing impact parameter and increasing deflection angle. Bremsstrahlung produced at high electron energies can penetrate deep into the material and produce tertiary electrons there, which can produce further photons or electrons on their part. In that way, cascade-showers of electrons and photons are generated.

B.3.3 Nuclear reactions

Nuclear reaction can be triggered by electrons with very high energies ($\mathrm{E_e} > 10\,\mathrm{MeV}$), mainly in target materials with high atomic numbers. The electrons are scattered at the nucleus and thereby convey a greater part of their kinetic energy. The exited nucleus emits particles and photons to de-excite into the ground state. With the energy threshold for electrons being so high, the effect is mostly irrelevant for radiation therapy and will not be discussed further.

---

[2] The surrounding shell electrons shield some fraction of the the nucleus field

B.3.4 Cerenkov-radiation

Another possible source for secondary photons is the formation of Cerenkov- radiation, produced when a charged particle (velocity v) moves faster than light can disperse inside the relevant material (velocity of light in matter c_{mat}, velocity in vacuum c_{vac}). The photons are emitted as linear polarised light with an angle δ to the direction of the electrons:

$$\cos\delta = \frac{\mathrm{c_{vac}}}{\mathrm{v \cdot n_m}}$$

with n_m = refraction index = $\frac{c_{vac}}{c_{mat}}$. However, the energy loss is very small (1 keV/cm in perspex in comparison to 2 MeV/cm for collisions, [70]); so it will be negelected here.

B.3.5 Positron annihilation

Apart from the interactions mentioned above, positrons display another kind of interaction. When the positron slows down to thermal energies at the end of its track, it can annihilate together with its antiparticle, the electron. In the centre-of-mass frame two photons are generated with an energy of 511 keV each and opposite momentum, the pair-momentum being randomly distributed between the angles zero and 2π. Depending on the residual kinetic energy of the positron before the annihilation, the angle between the two photons in the laboratory system gets distorted in the direction of flight of the positron, but usually the kinetic energy of the positron is so small that this effect can be neglected.

B.3.6 Total stopping power, range and LET

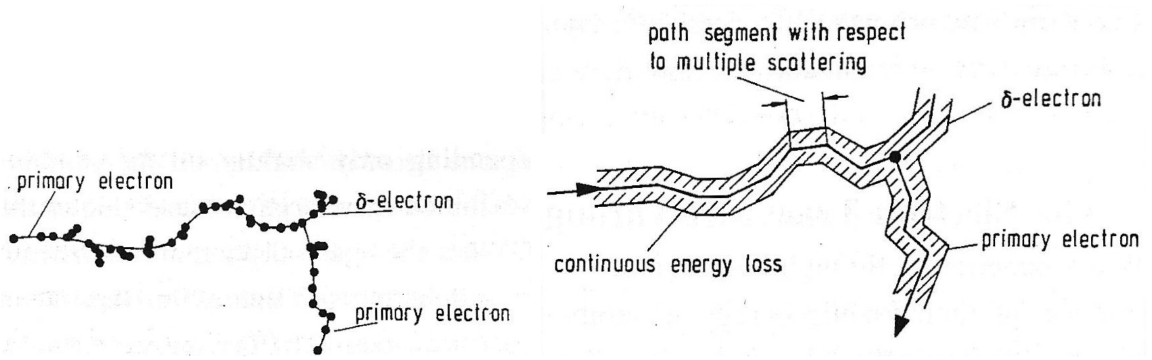

Figure B.16: *Schematic picture of a realistic electron track (left) and of the simulation with condensed-history-model (right) [61]*

The track of a high energy electron consists of pieces of strait tracks, where the energy loss is small and the deflection angle is negligible, and of scattering events with high energy loss and big scattering angles (see figure B.16). After a short distance, the energy of the electron decreases in a steep decline to thermal levels. Therefore, the maximum range of an electron can be directly defined, in contrary to that of uncharged particles (see figure B.17). The path length ℓ of an electron can be calculated using the total stopping power $S_{tot} = \left(\frac{dE}{dx}\right)_{tot} = S_{col} + S_{rad}$:

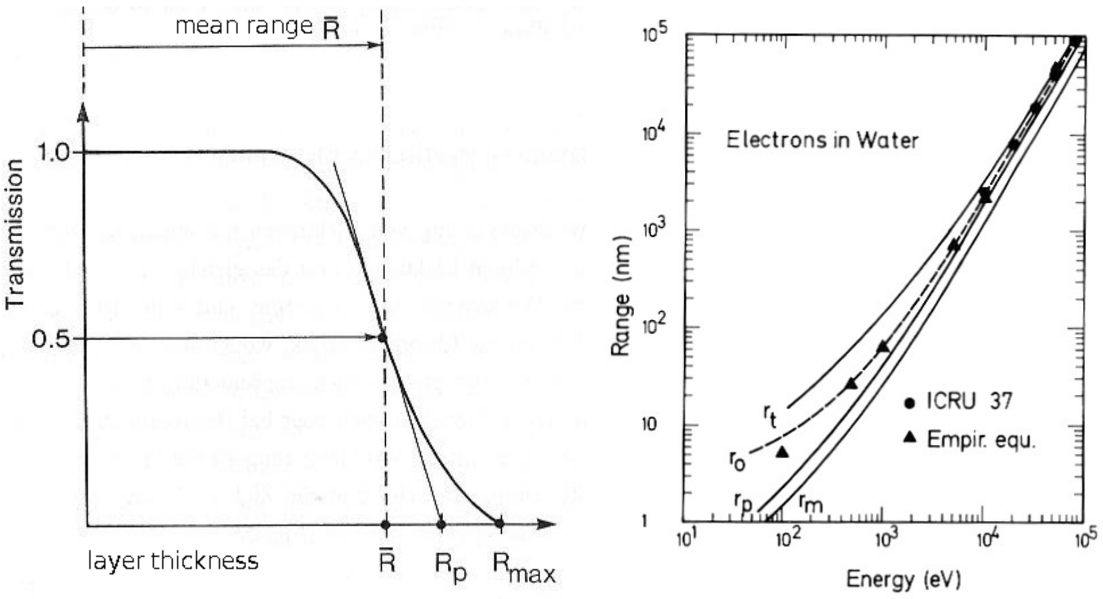

Figure B.17: *Range of electrons: schematic (left, [70]) and calculated/measured (right, [96]);* $\mathrm{R_{max}}$ *maximum range,* $\mathrm{r_t}$ *total track length,* $\mathrm{r_0}$ *mean track length,* $\mathrm{\bar{R} = r_m}$ *mean range,* $\mathrm{R_p = r_p}$ *practical range*

$$\ell = \int_0^{\mathrm{E_0}} \frac{1}{\mathrm{S_{tot}}} \, \mathrm{dE}$$

with E_0 = primary energy of the electron. But the real transmission through a material is shorter, because the track is not straight. With the help of a so-called detour factor X, the practical range R_p can be calculated from ℓ, giving an approximation for the penetration depth in direction of the beam [70]:

$$\mathrm{R_p} = \frac{\ell}{\mathrm{X}}$$

X depends on the primary electron energy and on the material composition. R_p is defined by the intersection of the tangent in the inflection point of the transmission (T)-depth curve with the (T = 0)-axis (see figure B.17). The mean range $\bar{R}$ is defined by the depth of the 50% transmission. It is, for example, 0.14 mm for 100 keV electrons or 15 mm for 3 MeV electrons, both in tissue. Along the track, the electrons are scattered often, sometimes with large scattering angles. Therefore, a narrow electron beam spreads out with increasing depth, so that in the depth x, the beam's width is approximately x (see figure B.18).

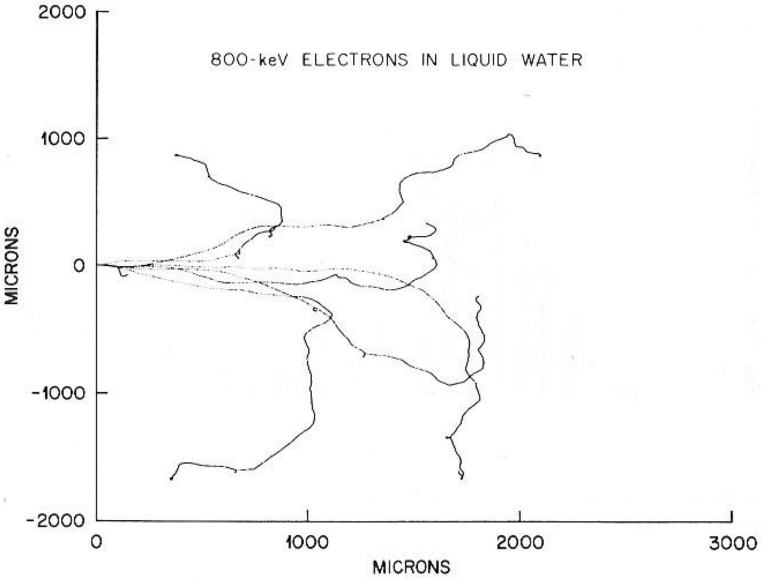

Figure B.18: *Calculated track of a 800 keV-electron in water [121]*

Another parameter to quantify energy loss is the linear energy transfer LET (see chapter A.4), which is directly linked to the stopping power:

$$\mathrm{LET} = \mathrm{S_{tot}} - \frac{\mathrm{dE_{brems}}}{\mathrm{dx}}$$

with dE_{brems} = energy loss by bremsstrahlung. At low energies, bremsstrahlung production is rare and energy loss due to it can be neglected. In this case LET and stopping power are equal. Sometimes a restricted LET_Δ is considered in which also energy losses above a cutoff-value Δ are not taken into consideration. The concept tries to account only for events along a particle track, where high energy density prevails.

B.4 Protons and heavier ions

Ions, like electrons, are charged particles and interact with atoms directly. They have a much higher mass (for proton: m_p=1836 m_e), which is the reason for their straighter tracks.

B.4.1 Elastic and inelastic Scattering

Direct collisions of ions with nuclei are rare because atoms are basically empty with only a tiny nucleus surrounded by few, even tinier electrons. This was shown long ago by Rutherford in his famous gold-foil experiment. But if an ion is scattered at the Coulomb field of a nucleus, the deflection from the direction of incidence can be very large as it is the scattering of two particles of similar mass. The number of such collisions with significant deflection can be assessed e.g. with the help of the radiation stopping power S_{rad} (with density ρ, target material atomic number Z and projectile charge ze, mass m and energy E):

$$\mathrm{S_{rad}} \sim \rho \mathrm{Z}^2 \left(\frac{\mathrm{ze}}{\mathrm{m}}\right)^2 \mathrm{E}$$

This effect, the production of bremsstrahlung, is also possible for electrons. But at energies and materials which are used in radiation therapy, it is not of great importance in tissue. Because of the $1/m^2$- dependence, it is even 6 orders of magnitudes smaller in the case of ions, so it can be neglected. Furthermore, the direct interaction of the ion with the nucleus, which leads to nuclear reactions like capture and emission of other small ions and photons, is of no importance in the relevant mass and energy range of radiation therapy by photons and fission neutrons.

Most of the collisions are interactions of the ion with the atomic shell. Electrons are at least three orders of magnitude lighter than ions. During the collision, the electrons are raised into higher atomic shells, which leads to the excitation of the target atom, or they are totally kicked out of the atom, which leads to its ionisation. The crucial quantity is again the impact parameter (see chapter B.3.2). If it is big (that means the ion's energy is small), the whole atomic shell is the interaction partner. It is polarised and deformed. The energy loss of such a scattering is small, the deflection of the projectile evanescent. With decreasing impact parameter, the ion can penetrate much deeper inside the atom and interact with single electrons. Sometimes, the ion is subject to so called binary collisions, where the transfer of energy to the secondary electron is quite large. This δ-electron can then efficiently excite or ionise further electrons. Because of the differences in mass, the ion with mass M_{Ion} and energy E before the scattering is practically not deflected and its maximum energy loss Q_{max} is small:

$$\mathrm{Q_{max}} = \frac{4\mathrm{m_e M_{Ion}}}{(\mathrm{M_{Ion}} + \mathrm{m_e})^2} \cdot \mathrm{E} \approx 4\frac{\mathrm{m_e}}{\mathrm{M_{Ion}}} \cdot \mathrm{E}$$

$$\mathrm{Q_{max}[keV]} \approx \frac{1}{500} \cdot \frac{\mathrm{E}}{\mathrm{M_{Ion}}} \left[\frac{\mathrm{MeV}}{\mathrm{u}}\right]$$

This was calculated using conservation of energy and momentum and assuming a free electron; Q_{max} for bound electrons can be higher

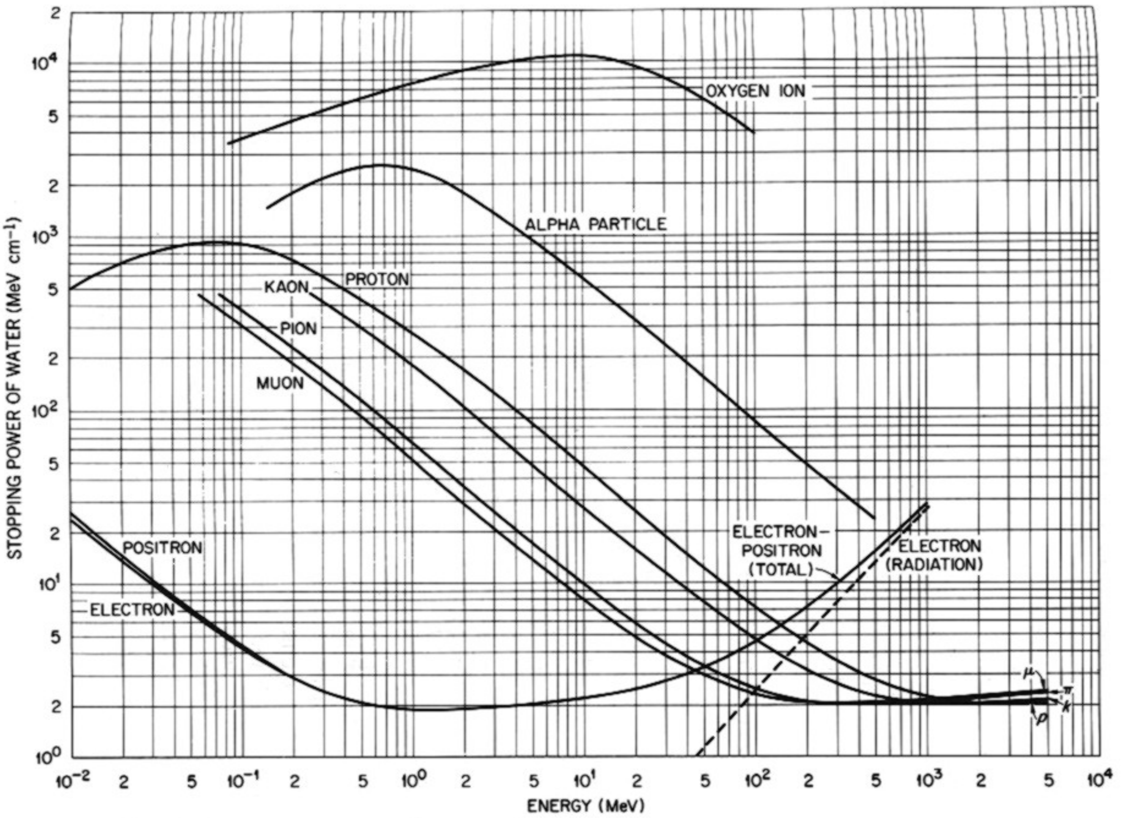

Figure B.19: *Stopping power of different particles in water [121]*

B.4.2 Mass stopping Power and LET

Ions follow straight tracks through material, depositing small quantities of energy along their way. Only at the very end of the track, the amount of deposited energy per unit pathlength increases steeply, until all of the ion's energy is deposited. Along the track, the ion gets just slightly deflected, because the mass difference of the interaction partners (electron versus ion) is very big (ratio of $> 10^3$). The ion-interactions and their energy loss can be described by the integral mean quantity stopping power ($-\frac{dE}{dx}$). It is equal to the linear energy transfer LET but including the energy loss by the production of bremstrahlung (see figure B.19). In a homogeneous material, Bethe and Bloch derived [96]:

$$-\frac{dE}{dx} \sim \frac{Z^2 e^4 n}{m_e c^2 \beta^2}\left[\ln\frac{2 m_e c^2 \beta^2}{I(1-\beta^2)} - \beta^2\right]$$

with atomic number of the ion Z, electron density of the material n, β=v/c and the Bethe-mean-excitation-energy I. For small values of Z, that is for light ions, the Bethe-excitation-energy I is between 20 to 100 eV.

Considerably less energy is deposited per unit steplength at high compared to low energies. This leads to the characteristic shape of the energy loss curve of heavy charged particles:

- at low energies , the stopping power increases with E

- at medium energies, it displays the characteristic $\frac{1}{E}\ln E$-decline due to electromagnetic interaction
- at high energies, relativistic effects take place: mass gain and Lorentz-contraction lead to a rise of the stopping power once again[3]. This effect is much more pronounced for electrons, where it is also displayed at lower energies.

At low energies (E[MeV]< $Z^2/2$) [70], the charge of the ion does not stay the same along the track. Electrons of the target are captured and lost again by stripping. In the formulae for the stopping power, the atomic number of the ion Z has to be replaced by an effective valency Z_{eff}, which can become considerably smaller than Z.

B.4.3 Ion range

Ion ranges are clearly defined by the distance between entering the material and coming to a stop. The ion track is composed of all individual interaction steps of the ion. In every step, the ion looses some of its energy, which is given by the stopping power $(-\frac{dE}{dx})$. The integral of the reciprocal stopping power over the primary ion energy to zero energy gives the range of the ion:

$$\mathrm{R(T)} = \int_0^{\mathrm{T}} \left(-\frac{\mathrm{dE}}{\mathrm{dx}}\right)^{-1} \mathrm{dE} \sim \frac{\mathrm{E}_0^2}{\rho\,\mathrm{m(Ze)}^2} \qquad \text{(for nonrelativistic energies)}$$

with E_0 = primary energy of the ion, Ze = charge of the ion. This approximation is only valid for nonrelativistic particles. If the mass stopping power is plotted versus the remaining range of an ion, the graph shows an almost flat beginning (plateau area) and a steep peak in greater depth, shortly before the end of the track. The Bragg-curve is often used in clinical practice, which results from the residual individual ion stopping power curves versus range, is broadend by the energy loss straggling of many particles i.e. there is no “Bragg-curve” of a single particle.

B.5 Particle tracks and relaxation of exited target atoms

Nuclei and atoms of the target material get exited by the different interaction processes explained in detail above. Nuclear excitation happens at very short time scales. On the one hand the nucleus can relax promptly after the excitation by emitting photons or small particles (these processes have already been considered above in the interaction processes). On the other hand, long-living nuclei can be produced which de-excite by decay into the ground state. The delayed radiation can be used for measurement purposes like for example gold activation and has to be taken into account for long lasting effects on healthy tissue surrounding an irradiated tumour.

The excitation or ionisation of the atomic shell, caused by passing charged particles, is

---

[3] Lorentz-contraction causes a distortion of the electromagnetic field. In this way, interactions with more target atoms are possible

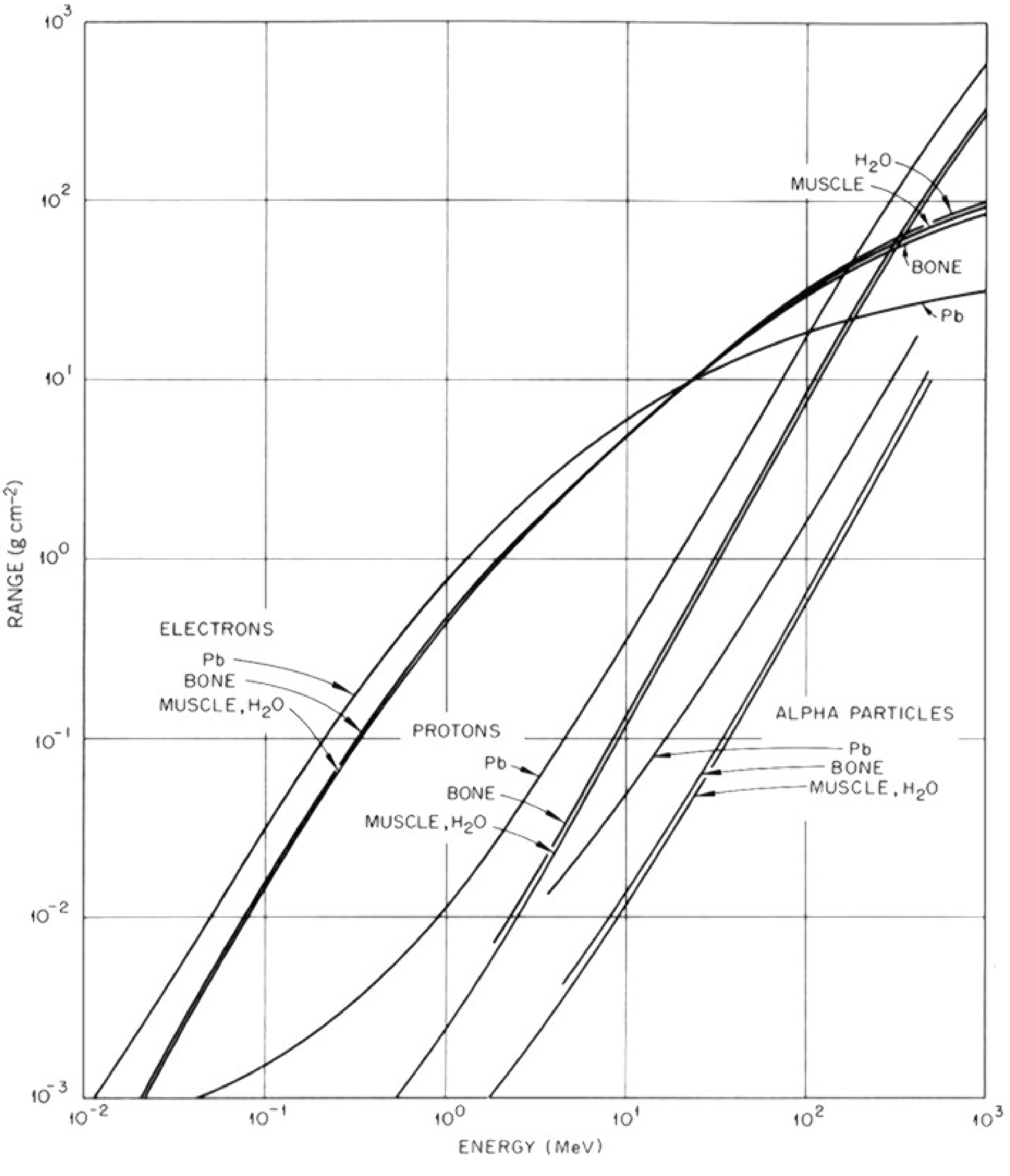

Figure B.20: *Range of electrons, protons and alphas in water, muscle, bone and lead [121]*

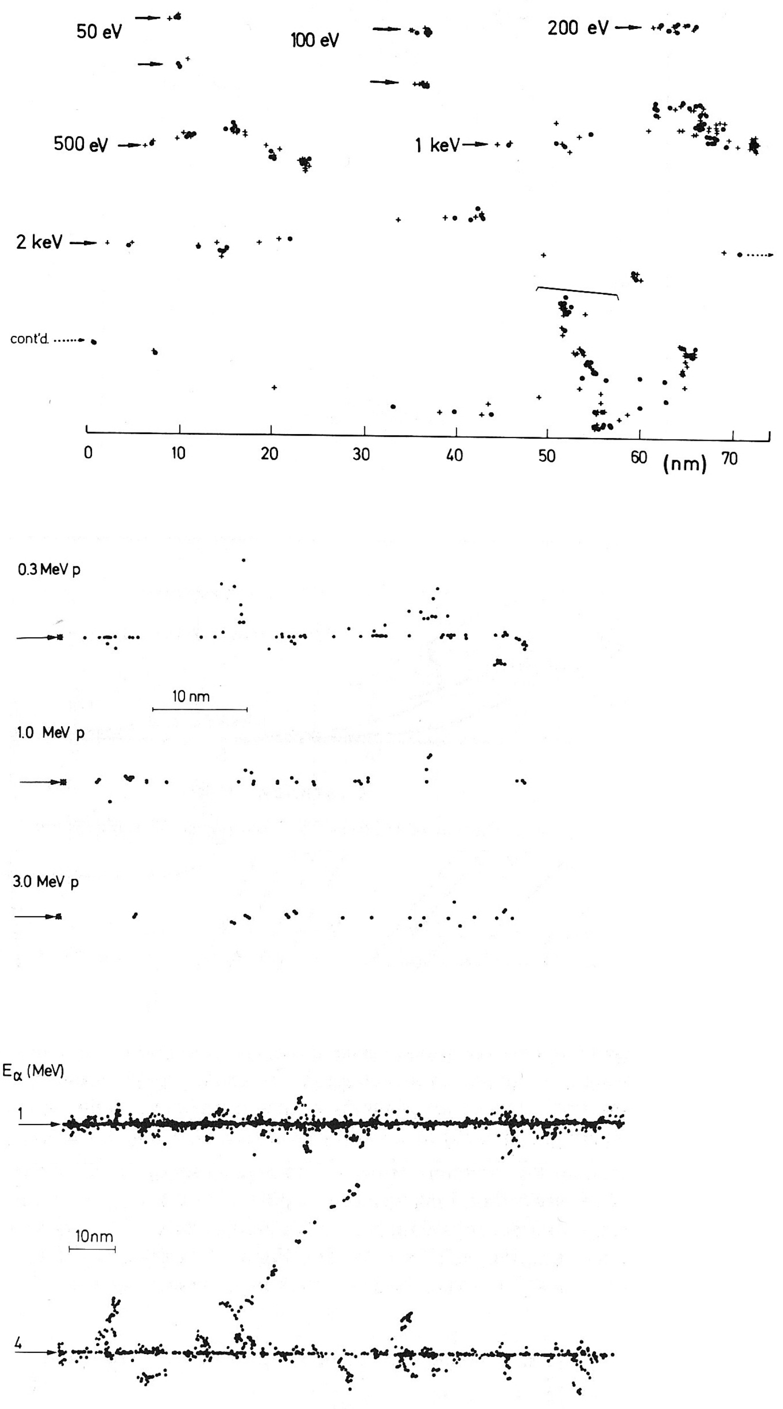

Figure B.21: *2D-projections of electron, proton and alpha tracks in water vapour (e^-) and water calculated with MOCA-8 or MOCA-14. For electrons two kinds of interaction are displayed: + for excitation; • for ionisation [96]*

different. Electrons of different atomic shells are lifted in higher states or completely removed from the atom. Afterwards, there is a vacancy in the relevant atomic shell, which can be a very instable energetic state. If the vacancy is in an inner shell, it is usually filled with an electron of the higher shells. The energy difference of the two states is emitted in the form of radiation (fluorescence) or transferred to another electron, which can itself get exited or even ionised (Auger-process). Both processes can lead to further exited states which have to relax. In target atoms with low atomic numbers, Auger-electron emission dominates whereas at higher ones fluorescence prevails.

Different kinds of interactions characterise the track structure of the different primary particles. Uncharged particles like photons or neutrons produce charged particles like electrons, positrons and ions that determine the track structures of such fields. The distance between two successive points of interaction is usually large compared to the range of the produced charged secondaries. A photon track spreads out more than a neutron track of comparable energy because the photons' secondaries, the electrons, have a greater range than the main secondaries of the neutrons, the ions. In addition, electron tracks spread more than ion tracks because of their lower mass (see chapter B.3.6). The frequency of occurrence of interactions along the track increases for charged particles with increasing proximity to the track end. These track properties can be seen in figure B.21.

APPENDIX

C

Cross sections

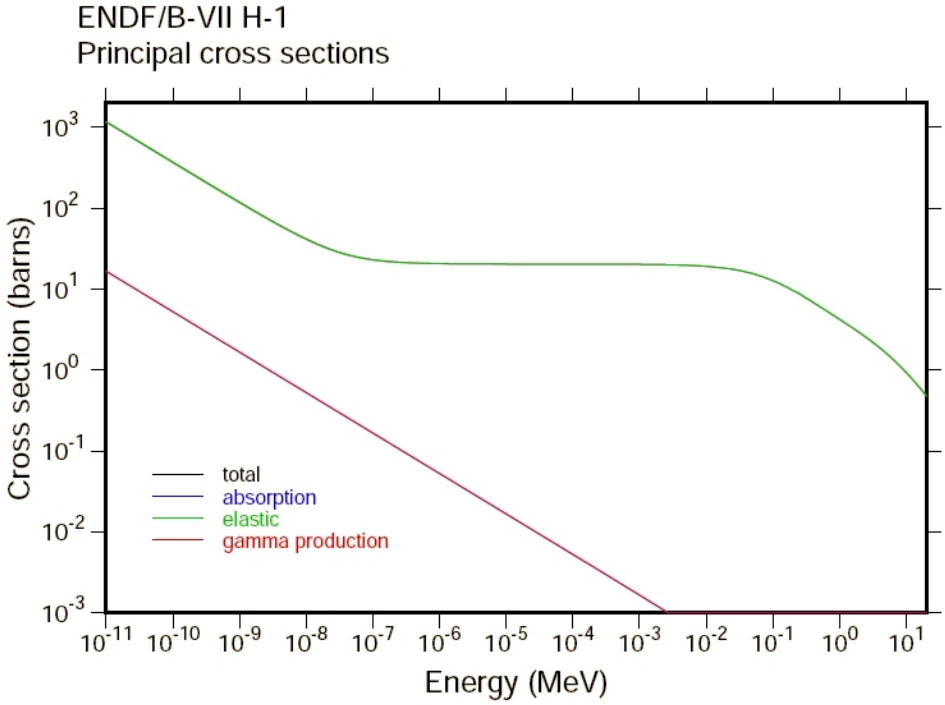

Figure C.1: *Interaction cross sections for neutrons in hydrogen [79]*

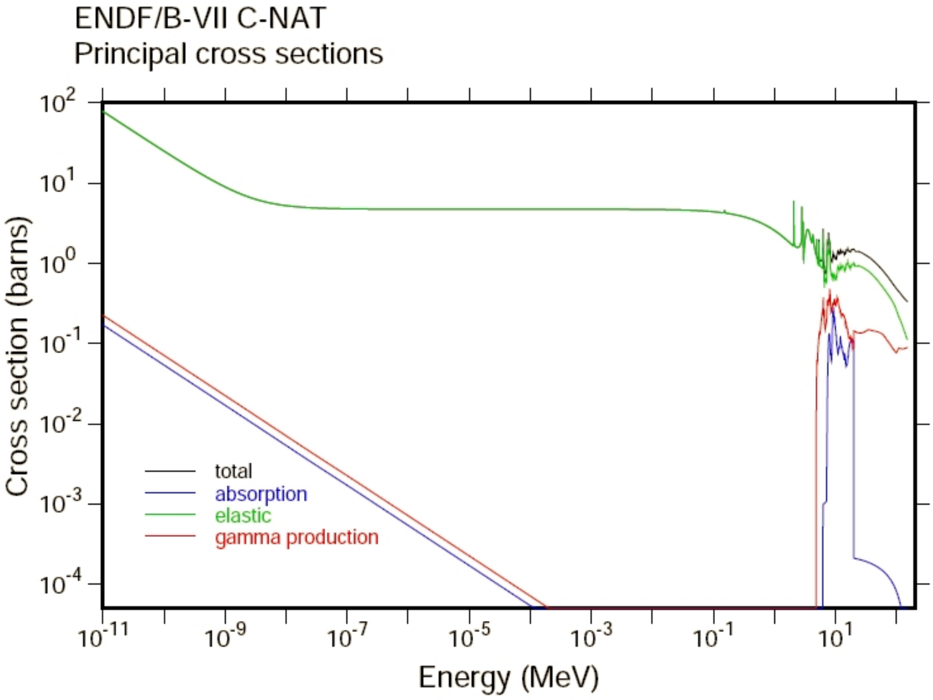

Figure C.2: *Interaction cross sections for neutrons in carbon (natural composition) [79]*

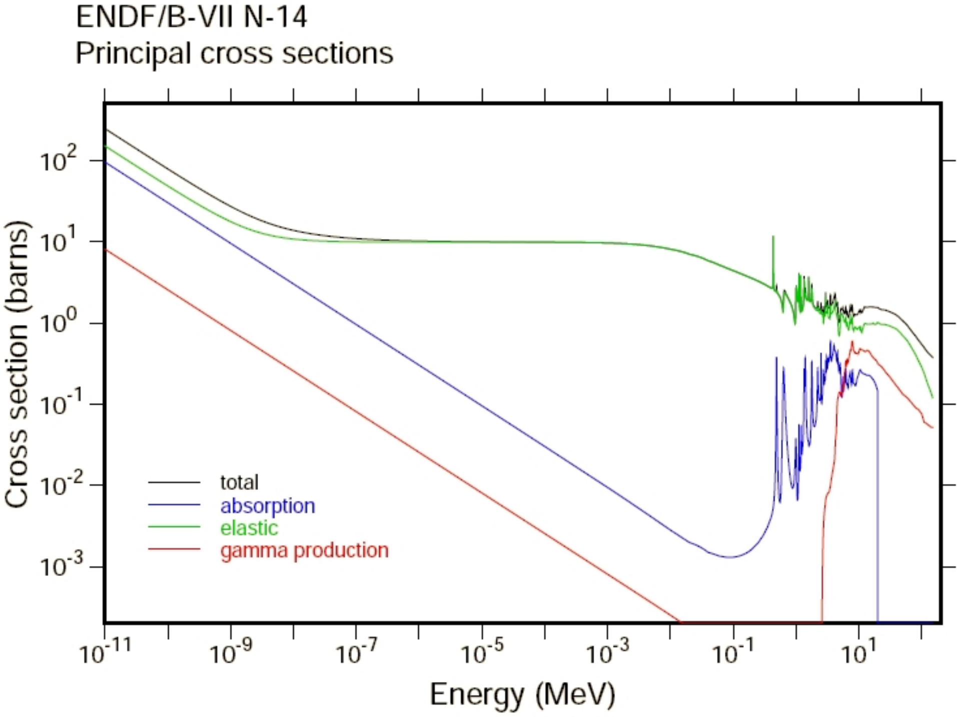

Figure C.3: *Interaction cross sections for neutrons in nitrogen* (^{14}N) *[79]*

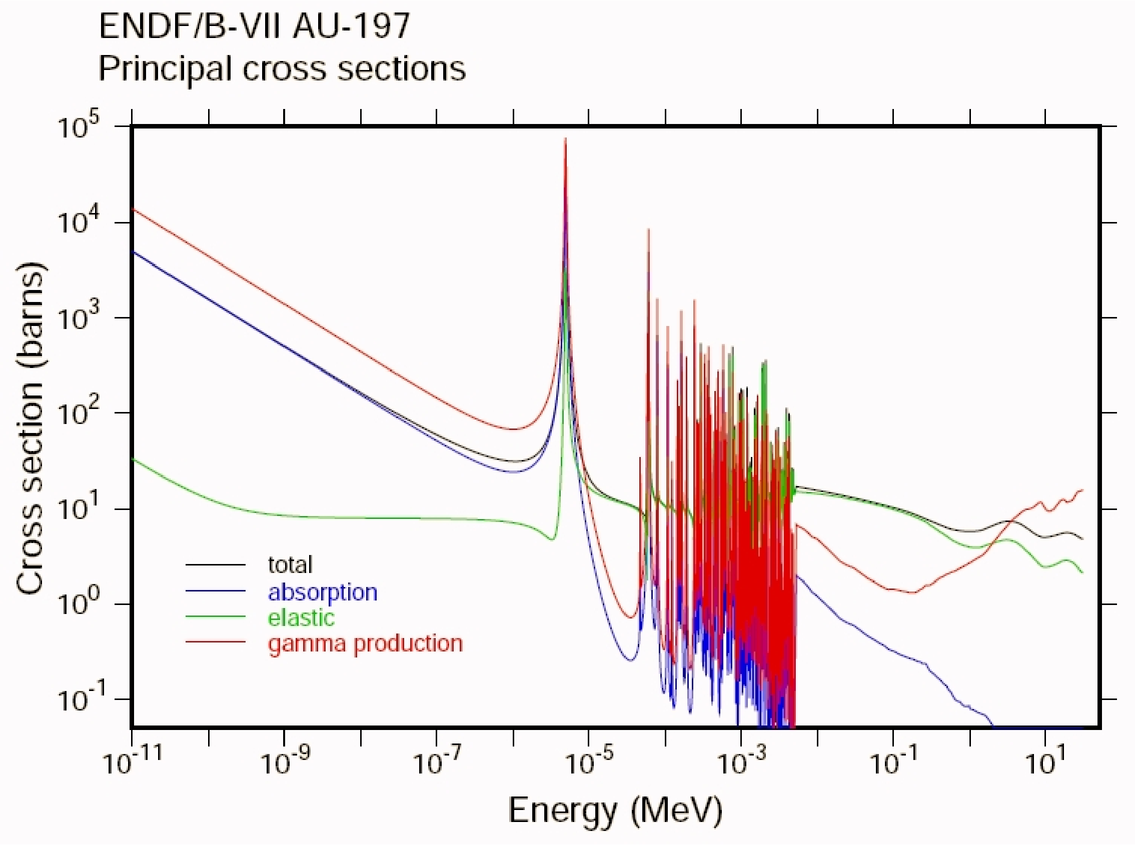

Figure C.4: *Interaction cross sections for neutrons in gold* (^{197}Au) *[79]*

APPENDIX

D

Energy rebinning of cross sections

CONBOLZ (Rühm, priv. com.) is a programm to rebin a cross section or a similar data structure. The programm needs a cross-section-energy-file $\sigma(E)$ and the energy structure $[E_i,E_{i+1}]$ that this is to be rebinned into. It is based on the following formular:

$$\int_{E_i}^{E_{i+1}} \frac{\partial\phi}{\partial E}\,\sigma(E)dE = \sigma_i^* \int_{E_i}^{E_{i+1}} \frac{\partial\phi}{\partial E}dE \qquad \text{for all i} \tag{D.1}$$

With σ_i^* being the mean cross section in the new bin-structure $[E_i,E_{i+1}]$ and the corresponding particle flux $\phi(E)$. This can be solved for one energy bin i:

$$\sigma_i^* = \frac{\int_{E_i}^{E_{i+1}} \frac{\partial\phi}{\partial E}\,\sigma(E)dE}{\int_{E_i}^{E_{i+1}} \frac{\partial\phi}{\partial E}\,dE} \tag{D.2}$$

Therefore, in order to calculate the optimum mean cross section, the characteristics of the particle flux have to be known or guessed. For neutrons this problem is normally solved by taking a so-called thermalized spectrum, with the Maxwell-Boltzmann-peak at thermal energies and a 1/E decline from there on (from 0.125 eV upwards). This is in most cases a good guess for the neutron spectrum behind a layer of hydrogen-containing matter of sufficient thickness (i.e. some centimeters). But it has to be thoroughly tested if this assumption is true. In the case of the gold-capture cross section, the disturbance of the flux by the gold cannot be neglected for the giant resonance at 5 eV, so the assumption of the 1/E-decline is not true there. For further discussion see chapter 5.2.2.

APPENDIX

E

Supplementary remarks to the Bonner sphere measurements

E.1 Derivation of the activation

In chapter B.2.6, the saturation activation of an irradiated foil after an infinitely long irradiation time was derived to be

$$A_\infty = \dot{\Phi}\sigma N_T$$

When the irradiation is stopped after a time $\mathrm{t_r}$, the activation of the foil is $A = A_\infty \left(1 - e^{-\lambda t_r}\right)$. The number of counts $\mathrm{Z \cdot t_m}$ (count-rate Z without background) is measured after an elapsed time $\mathrm{t_e}$ with a gamma-counter. The measurement takes time $\mathrm{t_m}$:

$$\mathrm{Z \cdot t_m = q\varepsilon \int_{t_r+t_e}^{t_r+t_e+t_m} Ae^{-\lambda(t-t_r)}dt = q\varepsilon \frac{Ae^{\lambda t_r}}{\lambda} \left(e^{-\lambda(t_r+t_e)} - e^{-\lambda(t_r+t_e+t_m)}\right)}$$

with photon emission probability q and detection efficiency ε. This can be solved to get the activation:

$$A = \frac{Z\lambda t_m}{q\varepsilon} \cdot \frac{e^{-\lambda t_r}}{e^{-\lambda(t_e+t_r)}(1 - e^{-\lambda t_m})}$$

Including the factor for not reaching full saturation (see above), the saturation activity A_∞ can be derived:

$$A_\infty = \frac{Z\lambda t_m}{q\varepsilon} \cdot \frac{e^{\lambda t_e}}{(1 - e^{-\lambda t_m})(1 - e^{-\lambda t_r})}$$

If the measurement time t_m and the irradiation time t_r are short compared to the half-life of the nucleus (in this case $T_{1/2}(^{198}Au) = 2.696d$) then $(1 - e^{\lambda t_x}) \xrightarrow{\lambda t_x << 1} \lambda t_x$ and:

$$A_\infty = \frac{Z \lambda t_m}{q\varepsilon} \cdot \frac{e^{\lambda t_e}}{\lambda t_m \cdot \lambda t_r} = \frac{Z}{q\varepsilon} \cdot \frac{e^{\lambda t_e}}{\lambda t_r}$$

This equation was used for the translation of the measured count-rates into activation values of the gold foil (see chapters 6.1 and 6.3.1).

E.2 Sum of Bonner sphere response

In figure E.1, the sum of all the response functions of the Bonner spheres simulated with GEANT4 are plotted. The response of the bare foil is excluded to represent the real situation of the unfolding with the measured data. All single response functions are plotted in figure 6.6.

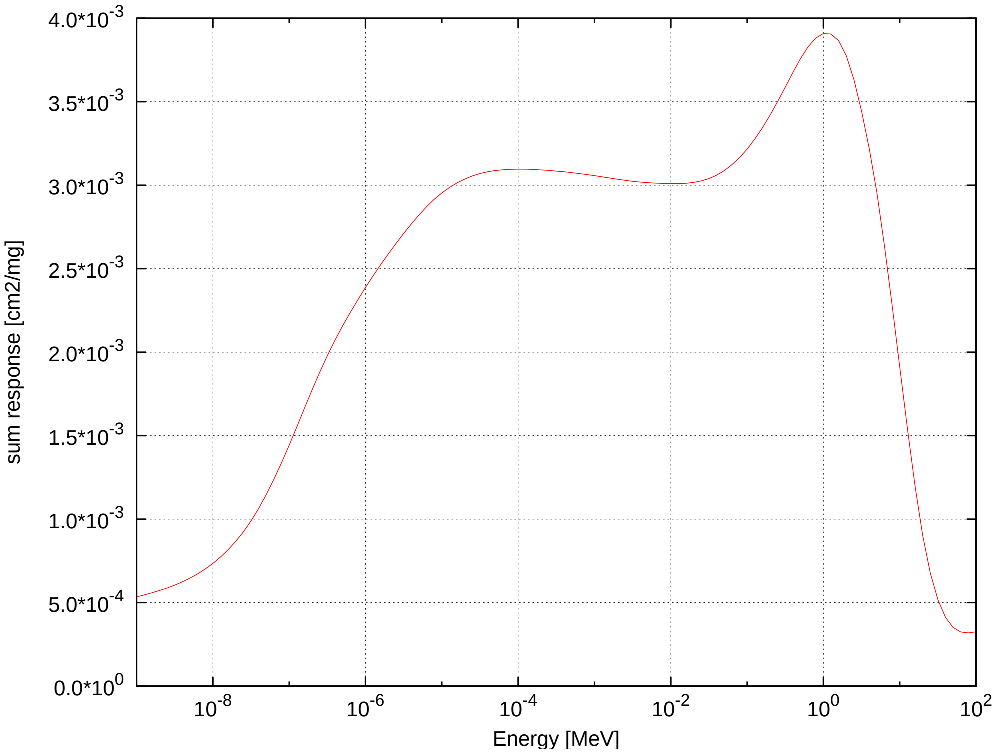

Figure E.1: *Sum of response functions of all 16 Bonner spheres (1.3 inch to 15 inch) without the bare gold foil*

E.3 Measurement vectors

Figures E.2 and E.3 display the two sets of gold foil activation, obtained with a Bonner sphere spectrometer in the FRM II in Garching in December 2006. Both results with and without Cd-tin around the gold foil are shown for the two measurement sites – patient treatment position and radiography site. For discussion, see chapter 6.3.2, for analysis of the unfolded spectrum see chapter 6.5.

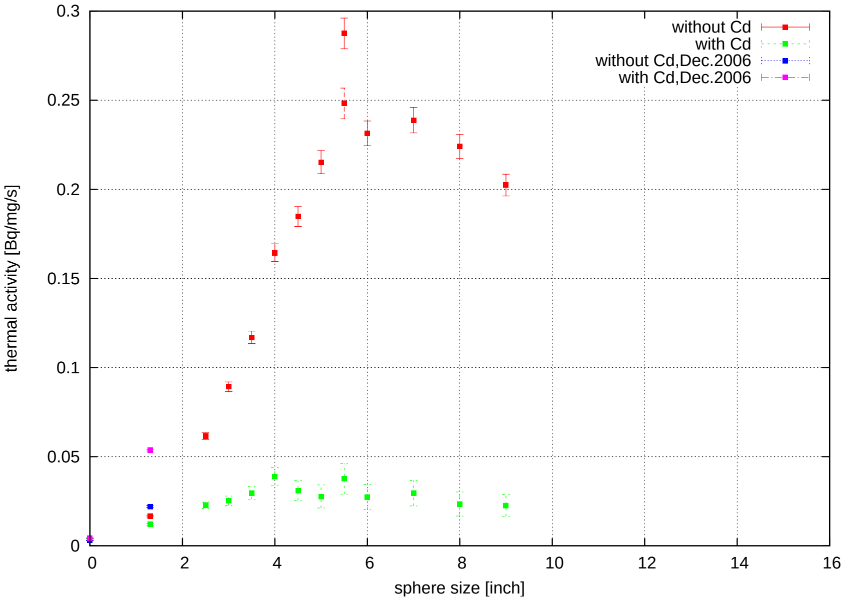

Figure E.2: *Specific activity vectors of the measurements at the patient treatment position*

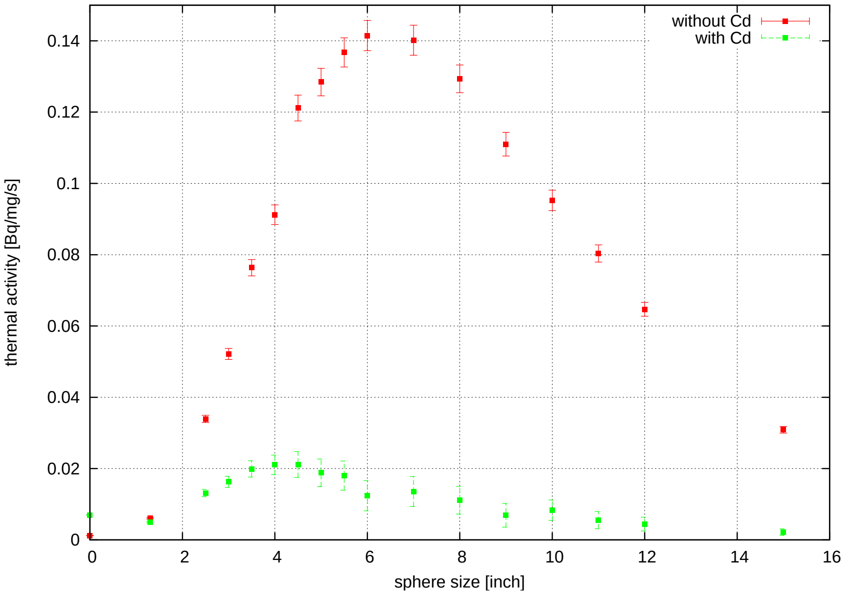

Figure E.3: *Specific activity vectors of the measurements at the radiography position*

E.4 Supplementary figures to the unfolding process

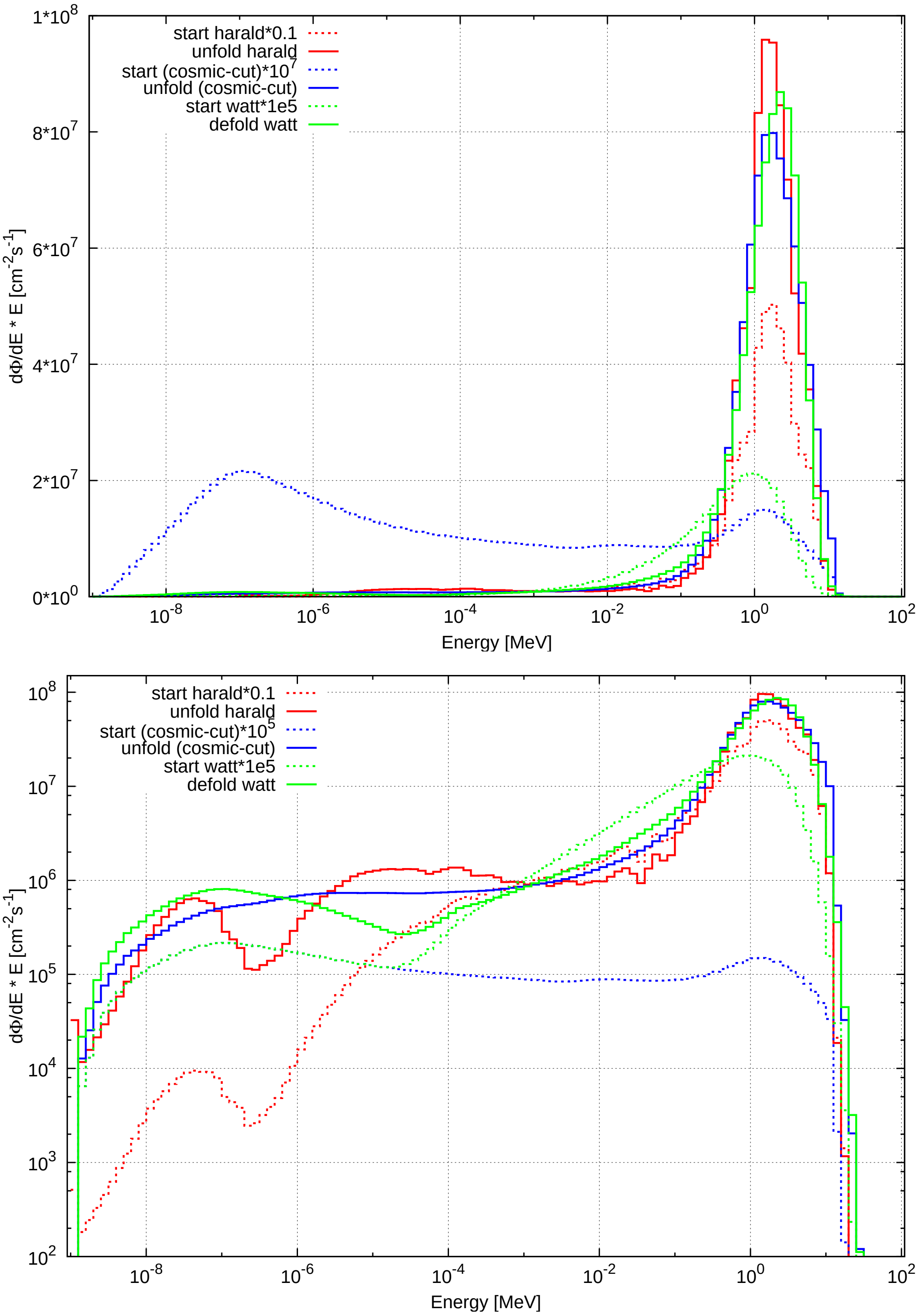

Figure E.4: *Neutron spectrum unfolded with MSAND. Three different start spectra are used as indicated: one is a thermalised neutron spectra from cosmic rays, cut at about 12 MeV to account for the edge of the fission spectrum, the second a fission or watt spectrum with an additional thermal peak, the third is the spectrum calculated and measured by Harald Breitkreutz [16]*

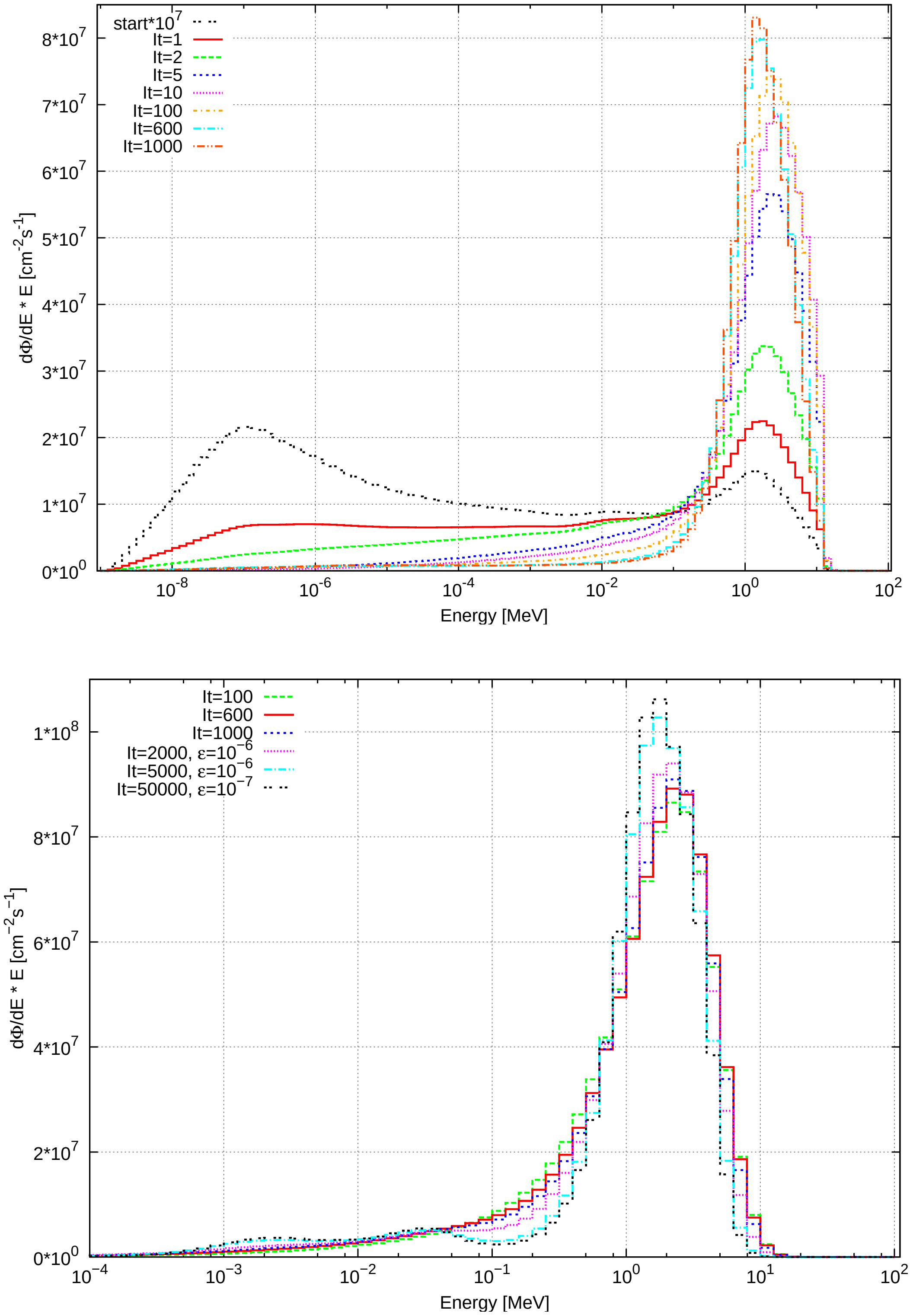

Figure E.5: *Neutron spectrum unfolded with MSAND, different numbers of iteration steps are used (depicted as numbers on the lines)*
top: *thermalised neutron spectra, cut at about 12 MeV as startspectrum (see figure 6.8)*
bottom: *fission (watt) spectrum with thermal peak as startspectrum*

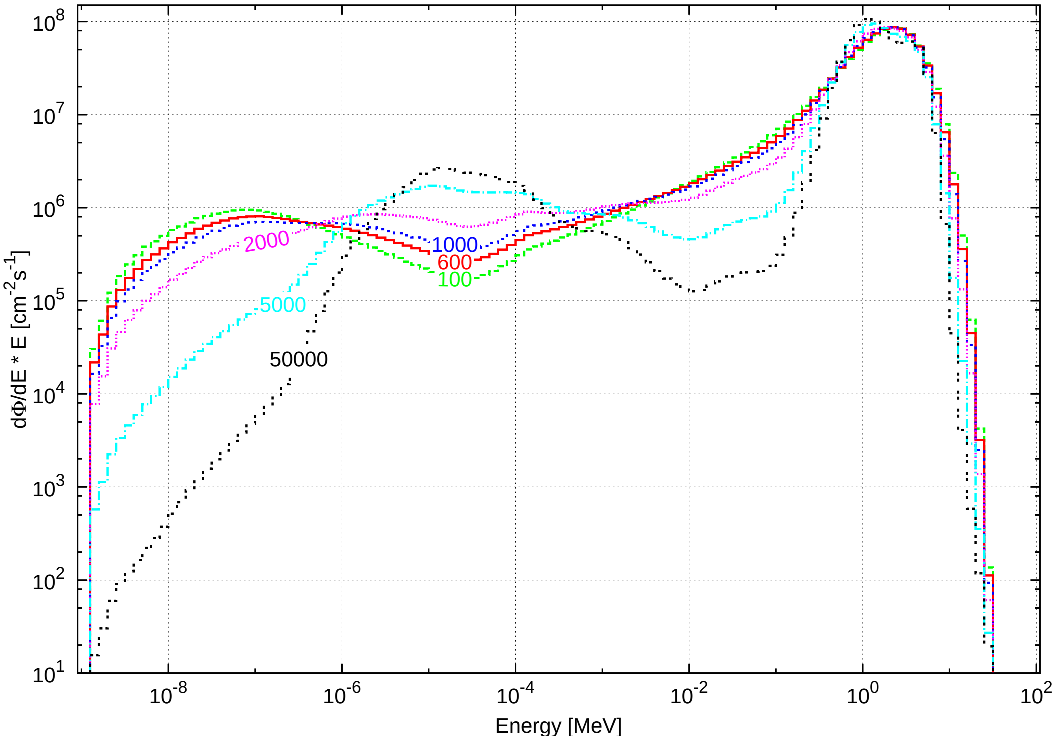

Figure E.6: *Neutron spectrum unfolded with MSAND, depending on different numbers of iteration steps (depicted as numbers on the lines); start spectrum = fission (watt) spectrum with thermal peak (see figure 6.8)*

E.5 The unfolded FRM II neutron spectrum

Table E.1: *The neutron flux measured inside the patient treatment room at the FRM II with a Bonner sphere spectrometer and unfolded with MSANDB;*
binned energy file: first lower bin border = 8.912e-10eV; upper energy bin borders given

energy [eV]	neutron-flux [n/cm2s]
1.122e-09	431788
1.413e-09	2.94519e+03
1.778e-09	5.8724e+03
2.239e-09	1.17251e+04
2.818e-09	1.75719e+04
3.548e-09	2.34334e+04
4.467e-09	2.93489e+04
5.623e-09	3.6312e+04
7.079e-09	4.14068e+04
8.912e-09	4.76357e+04
1.122e-08	5.50405e+04
1.413e-08	6.05849e+04
1.778e-08	6.74567e+04
2.239e-08	7.6252e+04
2.818e-08	8.30885e+04
3.548e-08	9.03276e+04
4.467e-08	9.73048e+04
5.623e-08	1.04097e+05
7.079e-08	1.10118e+05
8.912e-08	1.15332e+05
1.122e-07	1.19539e+05
1.413e-07	1.22622e+05
1.778e-07	1.25421e+05
2.239e-07	1.2811e+05
2.818e-07	1.31432e+05
3.548e-07	1.35665e+05
4.467e-07	1.40478e+05
5.623e-07	1.45694e+05
7.079e-07	1.5077e+05
8.912e-07	1.55445e+05
1.122e-06	1.59635e+05
1.413e-06	1.63173e+05
1.778e-06	1.65857e+05
2.239e-06	1.6768e+05
2.818e-06	1.6897e+05
3.548e-06	1.69478e+05
4.467e-06	1.69417e+05
5.623e-06	1.69349e+05
7.079e-06	1.69324e+05
8.912e-06	1.69604e+05
1.122e-05	1.69702e+05
1.413e-05	1.69716e+05
1.778e-05	1.69095e+05
2.239e-05	1.6844e+05
2.818e-05	1.67924e+05
3.548e-05	1.67895e+05
4.467e-05	1.68304e+05
5.623e-05	1.69363e+05
7.079e-05	1.70681e+05
8.912e-05	1.71971e+05
0.0001122	1.7335e+05
0.0001413	1.74612e+05
0.0001778	1.75626e+05
0.0002239	1.76617e+05
0.0002818	1.78431e+05
0.0003548	1.80538e+05
0.0004467	1.83575e+05
0.0005623	1.87798e+05
0.0007079	1.92201e+05
0.0008912	1.96932e+05

energy [eV]	neutron-flux [n/cm2s]
0.001122	2.02217e+05
0.001413	2.07957e+05
0.001778	2.13448e+05
0.002239	2.20062e+05
0.002818	2.27843e+05
0.003548	2.37679e+05
0.004467	2.48969e+05
0.005623	2.62868e+05
0.007079	2.79182e+05
0.008912	2.97448e+05
0.01122	3.18994e+05
0.01413	3.41274e+05
0.01778	3.67096e+05
0.02239	3.96531e+05
0.02818	4.33071e+05
0.03548	4.77639e+05
0.04467	5.30728e+05
0.05623	5.99897e+05
0.07079	6.90931e+05
0.08912	8.19631e+05
0.1122	1.00256e+06
0.1413	1.26724e+06
0.1778	1.65534e+06
0.2239	2.22402e+06
0.2818	3.05588e+06
0.3548	4.24682e+06

energy [eV]	neutron-flux [n/cm2s]
0.4467	5.9124e+06
0.5623	8.13177e+06
0.7079	1.09057e+07
0.8912	1.39883e+07
1.122	1.6734e+07
1.413	1.83374e+07
1.778	1.84104e+07
2.239	1.74058e+07
2.818	1.58278e+07
3.548	1.39098e+07
4.467	1.16727e+07
5.623	9.20611e+06
7.079	6.64088e+06
8.912	4.1955e+06
11.22	2.31526e+06
14.13	1.24601e+05
17.78	7.56236e+03
22.39	4.70008e+02
28.18	2.77621e+01
35.48	1.61983
44.66	9.32792e-03
56.23	5.48033e-05
70.78	3.54026e-07
89.11	2.56998e-09
112.2	2.01231e-09

E.6 The ^{3}He-BSS-response matrix

In figure E.7, the response matrix of a Bonner Sphere system with ^{3}He-detectors for the moderated thermal flux inside the spheres is plotted. For details on the caluclation and geometry see [82].

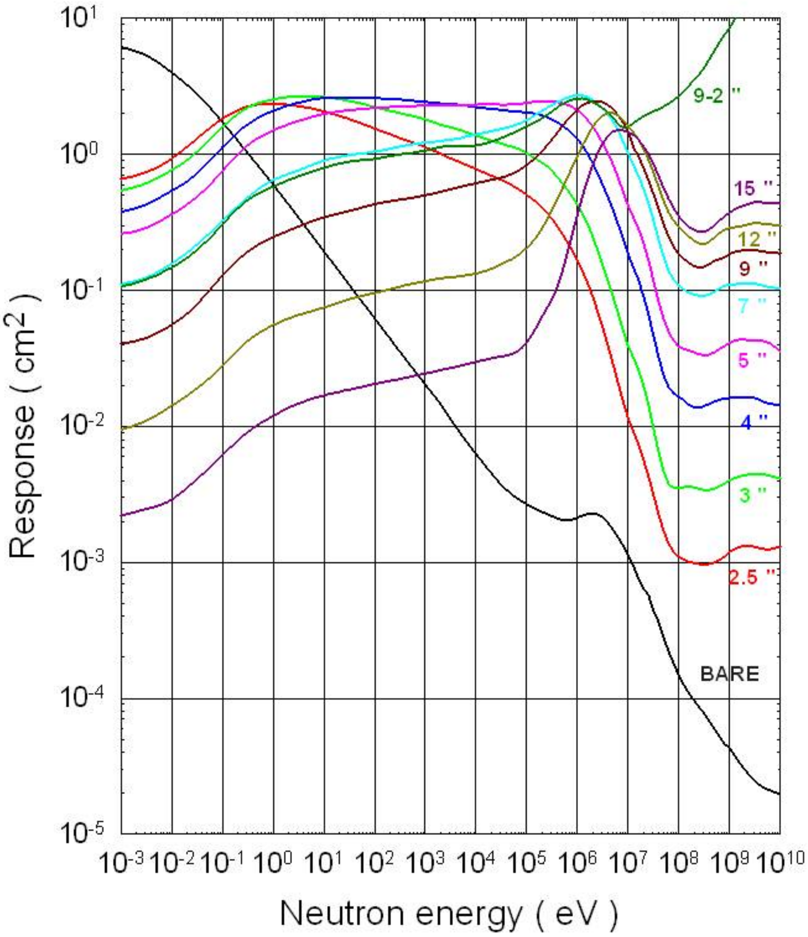

Figure E.7: ^{3}He-*BSS-response matrix, calculated with MCNP by Mares (priv. com.)*

APPENDIX

F

Supplementary remarks to calculations in the water phantom

F.1 Description of experiment

For ionisation chambers there are two borderline or “ideal” states. One displays secondary electron equilibrium where all particle produced in the gas are counted and where the size of the gas-volume is larger than the mean free path of the particles. The other works under Bragg-Gray or cavity chamber conditions where all measured particles are produced inside the thick chamber wall and only a small part of the energy is deposited in the gas. Real ionisation chambers cannot fulfill one of the two conditions exactly, but when approximations are accepted, one case can usually be chosen.
For the FRM II measurements, it can be assumed that cavity conditions are fulfilled. In this case, the dose in tissue is given by:

$$\mathrm{D_t} = \frac{\mathrm{Q}}{\mathrm{m}} \cdot \frac{\overline{\mathrm{W}}}{\mathrm{e}} \cdot (\mathrm{s_{w,g}}) \cdot \left[\frac{\mathrm{K_t}}{\mathrm{K_w}}\right]$$

with

- Q = corrected measured charge
- $\overline{\mathrm{W}}$= mean ionisation energy of an ion pair
- $(s_{w,g})$ = ratio of mass stopping powers in wall (w) and gas (g)
- $\left[\frac{K_t}{K_w}\right]$ = ratio of KERMA in tissue (t) to wall (w)

- m = mass of the gas.

Another factor which takes into account the point of origin of the particle (that crosses, stops, starts, or does both in the chamber (insider)) can usually be omitted for calibrated chambers. Conditions others than those at calibration are compensated for by further correction factors.
The calibration of both chambers was done in a photon reference beam, where the correction for the wall thickness and displacement of the actual measurement point from the geometric middle of the chamber was determined. Correction factors for air pressure and temperature and properties of the measurement gas and its supply were determined among others with the help of a test source.
The two measurement values $\mathrm{M_T}$ and $\mathrm{M_U}$ of the neutron sensitive (T=TE) and unsensitive chamber (U) are transformed to dose values $\alpha_\mathrm{x}\mathrm{R_x}$ ($\mathrm{x} = \mathrm{T}, \mathrm{U}$) with the calibration factor $\mathrm{N_k^x}$ which was determined in the photon field:

$$\alpha_\mathrm{x}\mathrm{R_x} = \mathrm{M_x} \cdot \mathrm{N_K^x}$$

This dose value $\alpha_\mathrm{x}\mathrm{R_x}$ can be expressed with the neutron $\mathrm{D_n}$ and photon $\mathrm{D_\gamma}$ dose and the neutron $\mathrm{k_x}$ and photon $\mathrm{h_x}$ response of the x-chamber ($\mathrm{x} = \mathrm{U}, \mathrm{T}$):

$$\alpha_\mathrm{T}\mathrm{R_T} = \mathrm{k_T} \cdot \mathrm{D_n} + \mathrm{h_T} \cdot \mathrm{D_\gamma} \quad , \quad \alpha_\mathrm{U}\mathrm{R_U} = \mathrm{k_U} \cdot \mathrm{D_n} + \mathrm{h_U} \cdot \mathrm{D_\gamma}$$

The neutron and photon dose can be calculated from this:

$$\mathrm{D_n} = \frac{\mathrm{h_U} \cdot (\alpha_\mathrm{T}\mathrm{R_T}) - \mathrm{h_T} \cdot (\alpha_\mathrm{U}\mathrm{R_U})}{\mathrm{h_U} \cdot \mathrm{k_T} - \mathrm{h_T} \cdot \mathrm{k_U}} \quad , \quad \mathrm{D_\gamma} = \frac{\mathrm{k_T} \cdot (\alpha_\mathrm{U}\mathrm{R_U}) - \mathrm{k_U} \cdot (\alpha_\mathrm{T}\mathrm{R_T})}{\mathrm{h_U} \cdot \mathrm{k_T} - \mathrm{h_T} \cdot \mathrm{k_U}}$$

which simplifies for equal photon sensitivities of both chambers ($\mathrm{h_t} = \mathrm{h_u}$) to:

$$D_n = \frac{(\alpha_T R_T) - (\alpha_U R_U)}{k_T - k_U} \quad , \quad D_\gamma = \frac{(\alpha_U R_U) - k_U \cdot D_n}{h_U}$$

with

$$\mathrm{k_T} = \frac{\mathrm{W_c}}{\overline{\mathrm{W}}_\mathrm{n}} \frac{(\mathrm{s_{w,g}})_\mathrm{c}}{(\mathrm{r_{w,g}})_\mathrm{n}} \left[\frac{\left(\frac{\mu_\mathrm{en}}{\rho}\right)_\mathrm{t}}{\left(\frac{\mu_\mathrm{en}}{\rho}\right)_\mathrm{w}} \right]_\mathrm{c} \left[\frac{\mathrm{K_w}}{\mathrm{K_t}} \right]_\mathrm{n}$$

where c denotes the calibration in the photon field and n the measurement with neutron irradiation. $\mathrm{W_c} = 29.3\mathrm{eV}$ is the energy necessary to produce an ion-pair inside the TE-gas filled TE-chamber in the calibration photon field. The mean $\mathrm{W_n}$ has to be calculated according to:

$$\overline{\mathrm{W}}_\mathrm{n} = \frac{\int \mathrm{W_n(E)} \cdot \mathrm{K}_\phi(\mathrm{E}) \cdot \phi(\mathrm{E})\mathrm{dE}}{\int \mathrm{k}_\phi(\mathrm{E}) \cdot \phi(\mathrm{E})\mathrm{dE}}$$

where the neutron flux $\phi(E)$ at the position of measurement has to be known or guessed. In this case, using a precalculated spectrum along with KERMA-coefficients $\mathrm{K}_\phi(\mathrm{E})$ from [51] and $\mathrm{W_n}$ values of [24], Kampfer [65] calculated $\overline{\mathrm{W}}_\mathrm{n}$ to be 31.5 eV and $\frac{\mathrm{W_c}}{\overline{\mathrm{W}}_\mathrm{n}} = 0.93$. This is in the range of other measurements ([24, 50]). The change of the neutron spectrum with depth was not considered in this case, but W_n is only weakly changing in the relevant energy range so that this assumption is likely to hold. Both the mass stopping power ratio $(s_{w,g})_c$ and the energy conversion ratio factor $(r_{w,g})_n$ were set to 1 and the ratio of the KERMA factor of the wall and the reference tissue $\left[\frac{K_w}{K_t}\right]_n$ was determined to be 1.03, which leads to $k_T = 0.958$. k_U was individually calibrated to be 0.02, which has already been used in earlier measurements [65].

F.2 Statistical analysis of depth dose curves

In figure F.1, the calculated and measured data are fit with an exponential decline and 2.5% to 97.5% confidence intervalls for the parameters of the fitted regression lines for the calculated and measured data were calculated. The geometry and calculation was discussed in detail in chapter 7.1.3 together with the results. The fit was done for doses in depths between 2 cm and 20 cm. The graphical display in figure F.1 gives no indication of significant deviations between the different calculations and the measurement. It is visible that the voxelised and simple geometry are almost equal and that the influence of the wall can be neglected. On a basis of the plot including confidence intervalls, the calculations with the two different spectra (MCNP+MSITER from [16] and that obtained with the Bonner Sphere spectrometer) can be said to agree.

Figure F.1: *Statistical analysis of depth dose curves: fit with 2.5%-97.5% confidence intervalls of the different calculations (with GEANT4) and the measurement (gray); used spectra for the calculations are: MCNP+MSITER [16](red), BSS-spectrum without walls (green) BSS-spectrum with walls (blue) and BSS-spectrum with walls in voxelised geometry (mean of 8 central voxels; black)*

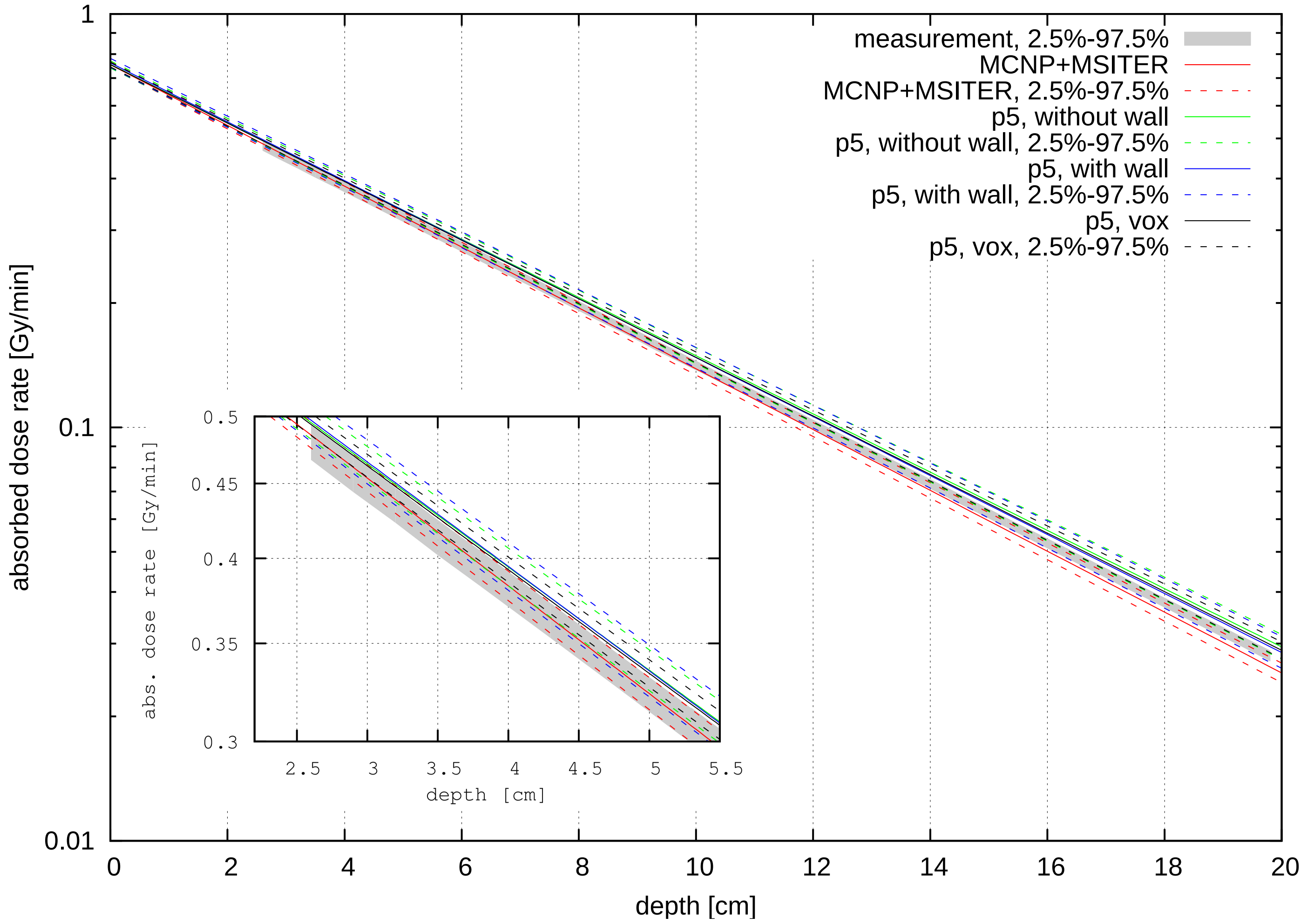

F.3 Neutron flux inside waterphantom

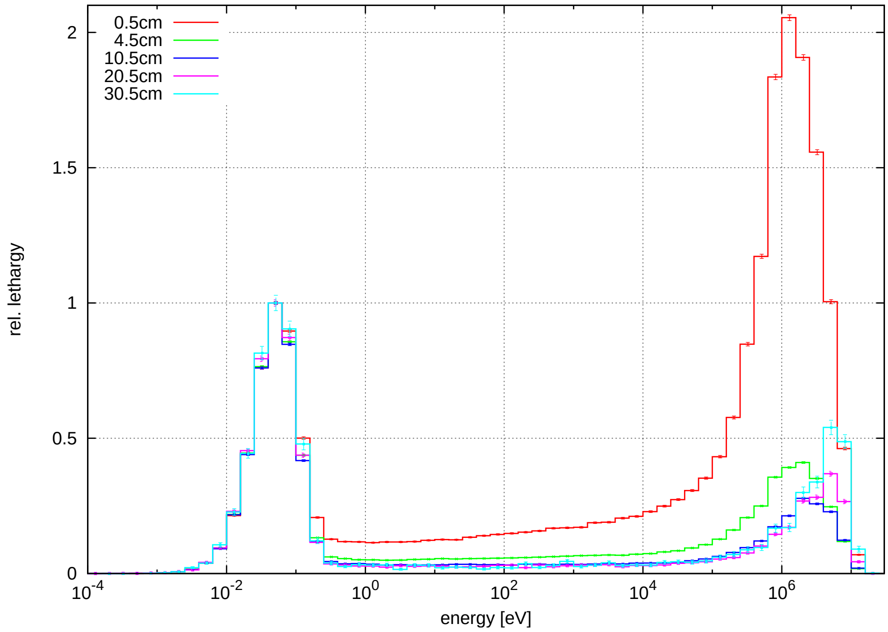

Figure F.2: *Neutron spectra in different depth of the water phantom with own primary unfolded neutron spectrum; normalized to the respective thermal peak heights*

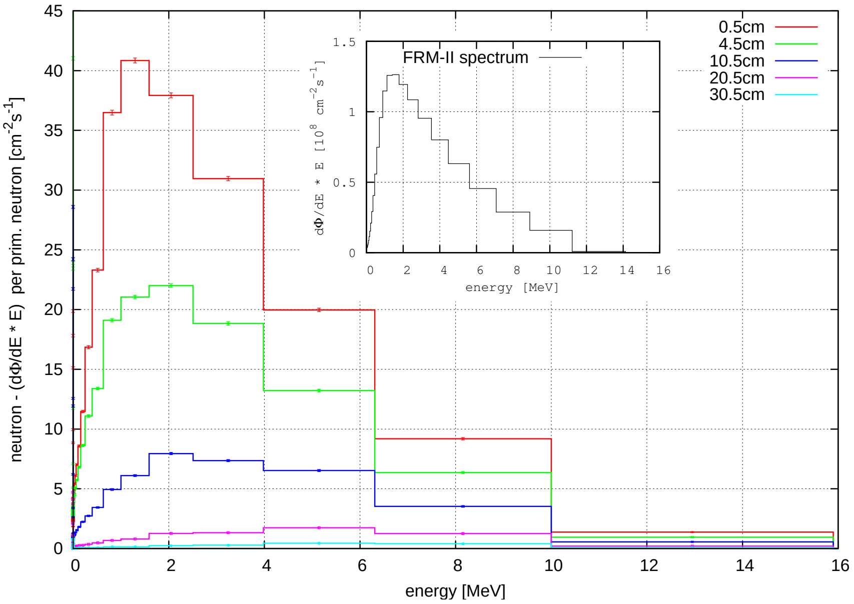

Figure F.3: *Neutron spectra in different depth of the water phantom with own primary unfolded neutron spectrum (see inset); normalised to incoming neutron flux*

APPENDIX

G

Supplementary data for calculations in the voxel phantom

Table G.1: *Atomic material composition; first column: material number, rest: fractionmass in percent of different atoms*

Z:	1	6	7	8	11	12	15	16	17	19	20	26
Atom:	H	C	N	O	Na	Mg	P	S	Cl	K	Ca	Fe
0	0.	0.	70.	30.	0.	0.	0.	0.	0.	0.	0.	0.
1	2.2	9.5	2.9	42.1	0	0.7	13.7	0	0	0	28.9	0
2	3.5	16	4.2	44.5	0.3	0.2	9.5	0.3	0	0	21.5	0
3	8.6	37.7	2.5	40.8	0.2	0.1	3.2	0.3	0	0	6.6	0
4	9.5	47.6	1.7	33.4	0.2	0	2.4	0.2	0	0	5	0
5	8.5	37.2	2.6	41	0.2	0.1	3.3	0.3	0	0	6.8	0
6	8	32.5	2.8	43.7	0.2	0.1	4	0.3	0.1	0	8.3	0
7	10.4	51.4	1.8	32.9	0.1	0.1	1.1	0.2	0	0	2	0
8	8.6	36.9	2.6	41.3	0.2	0.1	3.3	0.3	0	0	6.7	0
9	9.5	42.7	2.5	38.8	0.2	0.1	2	0.2	0	0	4	0
10	9.7	41.3	2.8	41.1	0.1	0.1	1.6	0.2	0	0	3	0.1
11	9.3	42.1	2.4	38.5	0.2	0.1	2.4	0.2	0	0	4.8	0
12	9.1	37.8	2.9	42.7	0.2	0.1	2.3	0.3	0	0	4.6	0
13	9.8	42.	2.8	40.8	0.1	0.1	1.4	0.2	0	0	2.7	0.1
14	8.7	35.2	3	44.	0.2	0.1	2.8	0.3	0	0	5.7	0
15	10.2	44.7	2.7	39.5	0.1	0.1	0.9	0.2	0	0	1.5	0.1
16	9.9	42.7	2.8	40.4	0.1	0.1	1.3	0.2	0	0	2.4	0.1
17	11.5	64.4	0.7	23.1	0.1	0	0.1	0.1	0	0	0	0
18	9.6	9.9	2.2	74.4	0.5	0	2.2	0.9	0.3	0	0	0
19	10	20.4	4.2	64.5	0.2	0	0.1	0.2	0.3	0.1	0	0
20	10.2	11	3.3	74.5	0.1	0	0.1	0.2	0.3	0.2	0	0.1
21	10.2	14.3	3.4	71	0.1	0	0.2	0.3	0.1	0.4	0	0
22	10.5	13.9	2.7	71.7	0.2	0	0.3	0.2	0.2	0.3	0	0
23	10.2	18.3	3.6	6.9	0.2	0	0.2	0.2	0.2	0.2	0	0
24	10.5	10.8	2.4	75.3	0.2	0	0.2	0.2	0.2	0.2	0	0
25	10.5	26.2	2.7	59.6	0.1	0	0.2	0.3	0.2	0.2	0	0
26	10.8	4.1	1.1	83.2	0.3	0	0	0.1	0.4	0	0	0
27	10.6	33.2	3	52.7	0.1	0	0.1	0.2	0.1	0	0	0
28	11.4	59.8	0.7	27.8	0.1	0	0.1	0.1	0	0	0	0
29	10.3	10.5	3.1	74.9	0.2	0	0.2	0.3	0.3	0.2	0	0

Table G.2: *Voxel-Organ-ID, Materialnumber of "Zankl" and in GEANT4, density ρ and organ name in GEANT4 and name of the organ/tissue*

Organ-ID	Mat-No	$\rho[g/cm^3]$	G4-Mat-No	Geant4-Name	Organ / Tissue
1	33	1.030	25	SoftTissue_4	Adrenal,left
2	33	1.03	25	SoftTissue_4	Adrenal,right
3	33	1.030	25	SoftTissue_4	Airways(and_mouth):Anterior_nasal_passage(ET1)
4	33	1.03	25	SoftTissue_4	Posterior_nasal_passage_down_to_larynx(ET2)
5	29	1.05	21	Muskel	Oral_mucosa,tongue
6	29	1.05	21	Muskel	Oral_mucosa,lips,cheeks
7	33	1.03	25	SoftTissue_4	Trachea
8	33	1.03	25	SoftTissue_4	Bronchi
9	28	1.060	20	Blut	Blood_vessels,head
10	28	1.06	20	Blut	Blood_vessels,trunk
11	28	1.06	20	Blut	Blood_vessels,arms
12	28	1.06	20	Blut	Blood_vessels,legs
13	2	1.920	2	HartKnochen	Humeri,upper_half,cortical
14	3	1.18	3	MischKnochen	Humeri,upper_half,spongiosa
15	22	0.98	17	BM_medulla	Humeri,upper_half,medullary_cavity
16	2	1.920	2	HartKnochen	Humeri,lower_half,cortical
17	4	1.12	4	BM_spongiosa	Humeri,lower_half,spongiosa
18	23	0.98	17	BM_medulla	Humeri,lower_half,medullary_cavity
19	2	1.920	2	HartKnochen	Ulnae_radii,cortical
20	5	1.12	4	BM_spongiosa	Ulnae_radii,spongiosa
21	24	0.98	17	BM_medulla	Ulnae_radii,medullary_cavity
22	2	1.920	2	HartKnochen	Wrists_hand,cortical
23	6	1.12	4	BM_spongiosa	Wrists_hand,spongiosa
24	2	1.920	2	HartKnochen	Clavicles,cortical
25	7	1.19	5	BM_clavicles	Clavicles,spongiosa
26	2	1.920	2	HartKnochen	Cranium,cortical
27	8	1.25	6	BM_cranium	Cranium,spongiosa
28	2	1.920	2	HartKnochen	Femora,upper_half,cortical
29	9	1.05	7	BM_femora	Femora,upper_half,spongiosa
30	22	0.98	17	BM_medulla	Femora,upper_half,medullary_cavity
31	2	1.920	2	HartKnochen	Femora,lower_half,cortical
32	10	1.12	4	BM_spongiosa	Femora,lower_half,spongiosa
33	23	0.98	17	BM_medulla	Femora,lower_half,medullary_cavity
34	2	1.920	2	HartKnochen	Tibiae_fibulae_patellae,cortical"
35	11	1.12	4	BM_spongiosa	Tibiae_fibulae_patellae,spongiosa
36	25	0.98	17	BM_medulla	Tibiae_fibulae_patellae,medullary_cavity
37	2	1.920	2	HartKnochen	Ankles_foot,cortical
38	12	1.12	4	BM_spongiosa	Ankles_foot,spongiosa
39	2	1.920	2	HartKnochen	Mandible,cortical
40	13	1.19	8	BM_mandible	Mandible,spongiosa
41	2	1.920	2	HartKnochen	Pelvis,cortical
42	14	1.11	9	BM_pelvis	Pelvis,spongiosa
43	2	1.920	2	HartKnochen	Ribs,cortical
44	15	1.09	10	BM_rib	Ribs,spongiosa
45	2	1.920	2	HartKnochen	Scapulae,cortical
46	16	1.13	11	BM_scapulae	Scapulae,spongiosa
47	2	1.920	2	HartKnochen	Spine_Cervical,cortical
48	17	1.14	12	BM_cervicalSpine	Cervical_spine,spongiosa

Organ-ID	Mat-No	$\rho[g/cm^3]$	G4-Mat-No	Geant4-Name	Organ / Tissue
49	2	1.920	2	HartKnochen	Thoracic_spine,cortical
50	18	1.08	13	BM_thoracicSpine	Thoracic_spine,spongiosa
51	2	1.920	2	HartKnochen	Lumbar_spine,cortical
52	19	1.17	14	BM_lumbarSpine	Lumbar_spine,spongiosa
53	2	1.920	2	HartKnochen	Sacrum,cortical
54	20	1.05	15	BM_sacrum	Sacrum,spongiosa
55	2	1.920	2	HartKnochen	Sternum,cortical
56	21	1.08	16	BM_sternum	Sternum,spongiosa
57	26	1.100	18	Knorpel	Cartilage,head
58	26	1.1	18	Knorpel	Cartilage,trunk
59	26	1.1	18	Knorpel	Cartilage,arms
60	26	1.1	18	Knorpel	Cartilage,legs
61	30	1.05	22	SoftTissue_1	Brain
62	36	0.950	28	Fett	Breast_left,adipose_tissue
63	35	1.02	27	Brust	Breast_left,glandular_tissue
64	36	0.95	28	Fett	Breast_right,adipose_tissue
65	35	1.02	27	Brust	Breast_right,glandular_tissue
66	31	1.050	23	SoftTissue_2	Eyes_lense,left
67	31	1.05	23	SoftTissue_2	Eye_bulb,left
68	31	1.05	23	SoftTissue_2	Eye_lense,right
69	31	1.05	23	SoftTissue_2	Eye_bulb,right
70	33	1.03	25	SoftTissue_4	Gall_bladder,wall
71	33	1.03	25	SoftTissue_4	Gall_bladder,contents
72	32	1.040	24	SoftTissue_3	Stomach_wall
73	32	1.04	24	SoftTissue_3	Stomach_contents
74	32	1.04	24	SoftTissue_3	Small_intestine_wall
75	32	1.04	24	SoftTissue_3	Small_intestine_contents
76	32	1.04	24	SoftTissue_3	Ascending_colon_wall
77	32	1.04	24	SoftTissue_3	Ascending_colon_contents
78	32	1.04	24	SoftTissue_3	Transverse_colon_wall,right
79	32	1.04	24	SoftTissue_3	Transverse_colon_contents,right
80	32	1.04	24	SoftTissue_3	Transverse_colon_wall,left
81	32	1.04	24	SoftTissue_3	Transverse_colon_contents,left
82	32	1.04	24	SoftTissue_3	Descending_colon_wall
83	32	1.04	24	SoftTissue_3	Descending_colon_contents
84	32	1.04	24	SoftTissue_3	Sigmoid_colon_wall
85	32	1.04	24	SoftTissue_3	Sigmoid_colon_contents
86	32	1.04	24	SoftTissue_3	Rectum_wall
87	30	1.050	22	SoftTissue_1	Heart_wall
88	28	1.06	20	Blut	Heart_contents=blood
89	30	1.050	22	SoftTissue_1	Kidneys_left,cortex
90	30	1.05	22	SoftTissue_1	Kidney_left,medulla
91	30	1.05	22	SoftTissue_1	Kidney_left,pelvis
92	30	1.050	22	SoftTissue_1	Kidney_right,cortex
93	30	1.05	22	SoftTissue_1	Kidney_right,medulla
94	30	1.05	22	SoftTissue_1	Kidney_right,pelvis
95	31	1.05	23	SoftTissue_2	Liver
96	28	1.060	20	Blut	Lungs_left,blood
97	37	0.38	29	Lunge	Lung_left,tissue

Organ-ID	Mat-No	$\rho[g/cm^3]$	G4-Mat-No	Geant4-Name	Organ / Tissue
98	28	1.060	20	Blut	Lung_right,blood
99	37	0.38	29	Lunge	Lung_right,tissue
100	34	1.030	26	Lymph	Lymphatic_nodes,extrathoracic_airways
101	34	1.03	26	Lymph	Lymphatic_nodes,thoracic_airways
102	34	1.03	26	Lymph	Lymphatic_nodes,head
103	34	1.03	26	Lymph	Lymphatic_nodes,trunk
104	34	1.03	26	Lymph	Lymphatic_nodes,arms
105	34	1.03	26	Lymph	Lymphatic_nodes,legs
106	29	1.050	21	Muskel	Muscle,head
107	29	1.05	21	Muskel	Muscle,trunk
108	29	1.05	21	Muskel	Muscle,arms
109	29	1.05	21	Muskel	Muscle,legs
110	33	1.03	25	SoftTissue_4	Oesophagus
111	32	1.040	24	SoftTissue_3	Ovaries,left
112	32	1.04	24	SoftTissue_3	Ovary,right
113	31	1.05	23	SoftTissue_2	Pancreas
114	33	1.03	25	SoftTissue_4	Pituitary_gland
115	33	1.03	25	SoftTissue_4	Prostate
116	36	0.950	28	Fett	Residual_tissue,head
117	36	0.95	28	Fett	Residual_tissue,trunk
118	36	0.95	28	Fett	Residual_tissue,arms
119	36	0.95	28	Fett	Residual_tissue,legs
120	33	1.030	25	SoftTissue_4	Salivary_glands,left
121	33	1.03	25	SoftTissue_4	Salivary_glands,right
122	27	1.090	19	Haut	Skin,head
123	27	1.09	19	Haut	Skin,trunk
124	27	1.09	19	Haut	Skin,arms
125	27	1.09	19	Haut	Skin,legs
126	33	1.03	25	SoftTissue_4	Spinal_cord
127	32	1.04	24	SoftTissue_3	Spleen
128	1	2.75	1	Zahn	Teeth
129	32	1.040	24	SoftTissue_3	Testis,left
130	32	1.04	24	SoftTissue_3	Testis,right
131	33	1.03	25	SoftTissue_4	Thymus
132	32	1.04	24	SoftTissue_3	Thyroid
133	29	1.05	21	Muskel	Tongue,inner_part
134	33	1.03	25	SoftTissue_4	Tonsils
135	33	1.030	25	SoftTissue_4	Ureter,left
136	33	1.03	25	SoftTissue_4	Ureter,right
137	32	1.04	24	SoftTissue_3	Urinary_bladder,wall
138	32	1.04	24	SoftTissue_3	Urinary_bladder,contents
139	33	1.03	25	SoftTissue_4	Uterus
140	38	1e-20	0	Air	Air_inside_body
141	0	1e-20	0	Air	Skin

Danksagung

Allen voran möchte ich Herrn Prof. Herwig G. Paretzke danken, der mir dieses interessante Thema als Doktorarbeit ermöglicht hat. Zusätzlich hat er sich dafür eingesetzt, daß ich einen Einblick in den Klinikalltag der Strahlentherapie am Klinikum Rechts der Isar werfen durfte. Ich danke auch Herrn Hoeschen und der Medizinphysikgruppe für die nette Unterstützung und Finanzierung meiner Stelle. Bei Frau Zankl möchte ich mich ganz speziell für die Bereitstellung des Voxelphantoms bedanken. Ein ganz besonderer Dank gilt Herrn Werner Rühm, der mich (obwohl ich nicht direkt zu seiner Arbeitsgruppe gehört habe), sehr unterstützt hat. Er hatte immer das Ziel vor Augen und hat vor allem auch die letzten Schritte der Fertigstellung sehr gut unterstützt. Ohne ihn wäre die Arbeit in dieser Form sicher nicht zustandegekommen. Ich möchte auch der Gruppe Personendosimetrie für die fruchtbaren Diskussionen danken und ganze besonders Herrn Vladimir Mares für die MCNP-Rechnungen, die er für mich ausgeführt hat und Herrn Peter Leuthold für so manchen Tipp aus seinem reichen Erfahrungschatz. Ein besonderer Dank gilt Herrn Franz Wagner, der die Messungen an der Forschungsneutronenquelle Heinz Maier-Leibnitz (FRM II) betreut und tatkräftig unterstützt hat. Bei meinen zahlreichen Fragen zum Reaktor hat er mir immer weitergeholfen. Auch Harald Breitkreutz hatte immer ein offenes Ohr für mich. Des weiteren danke ich Herrn Prof. A. Wambersie für die Literatur zur Neutronenbestrahlung. Herrn Bernhard Tandler danke ich für die Unterstützung bei den Clusterrechnungen. Dem GEANT4-Entwicklerteam vom CERN danke ich für die Unterstützung bei manchen GEANT4-Problemen, vor allem auch über ihr Forum. Speziell möchte ich mich bei Maria Grazia Pia und ihren Mitarbeiterinnen Barbara Mascialino und Susanna Guatelli sowie bei Alexander Howard und Koi Tatsumi bedanken.

Ich danke auch meinen Zimmergenossen Gregor Simmer und Christian Pioch sowie Frank Karinda für die nette Arbeitsatmosphäre und kleinen Auflockerungen zwischendurch. Ich hoffe, daß ihr Eure Arbeit auch gut abschließen könnt. Ein ganz herzlicher

Dank geht an Frau Pedone, mit der ich die letzten Jahre immer sehr kurzweilige und unterhaltsame Mittagspausen verbingen durfte.

Ein ganz besonderer Dank gilt meinem Freund Mathias, der immer für mich da war, um mich aufzubauen, wenn der Computer mal wieder nicht das gemacht hat, was ich von ihm wollte. Danke auch für die hilfreichen PC-Tipps. Ohne die schönen Sicherungsdateien hätte ich es sicherlich irgendwann geschafft alles zu löschen!
Ein ganz großer Dank gilt auch meinen Eltern und meiner Schwester Angelika, die mich immerzu toll unterstützt haben. Vielen Dank auch an meine Schwester für die Hilfe bei der statistischen Analyse.
Außerdem danke ich allen Helfern und Freunden die mich in den letzten Jahren auf viele Arten erfreut haben.